UNIVERSITY of CALIFORNIA
Santa Barbara

A path towards quantum supremacy with superconducting qubits

A dissertation submitted in partial satisfaction of the
requirements for the degree of

Doctor of Philosophy

in

Physics

by

Charles James Neill

Committee in charge:

John Martinis, Chair

Ben Mazin

Matthew Fisher

January 2018

The dissertation of Charles James Neill is approved:

Ben Mazin

Matthew Fisher

John Martinis, Chair

December 2017

Acknowledgements

This work would not have been possible without the help and kindness of my colleagues, in particular, Pedram Roushan, Yu Chen, and Anthony Megrant, for whom I have the utmost respect and gratitude. As well as my advisor, John Martinis, who showed me that amazing physics is the result of amazing engineering - a philosophy that will undoubtedly shape my career.

Curriculum Vitæ

Charles James Neill

Education

University of California, Santa Barbara (2011-2017)
Ph.D., Department of Physics

University of California, San Diego (2007-2011)
B.S. in Physics with specialization in materials Physics
Summa cum laude and departamental honors
Minor in Mathematics

Selected Publications

Charles Neill*, Pedram Roushan*, et al., "A blueprint for demonstrating quantum supremacy with superconducting qubits", *Submitted* (2017)

Pedram Roushan*, **Charles Neill***, et al., "Spectral signatures of many-body localization with interacting photons", *Accepted to Science* (2017)

Pedram Roushan*, **Charles Neill***, et al., "Chiral groundstate current of interacting photons in a synthetic magnetic field", *Nature Physics* 13, 146-151 (2017) †

Charles Neill*, Pedram Roushan*, et al., "Ergodic dynamics and thermalization in an isolated quantum system", *Nature Physics* 12, 1037-1041 (2016) †

Pedram Roushan*, **Charles Neill***, et al., "Observation of topological transitions in interacting quantum circuits", *Nature* 515, 241-244 (2014)

Yu Chen*, **Charles Neill***, et al., "Qubit architecture with high coherence and fast tunable coupling", *Phys. Rev. Lett.* 113, 220502 (2014)

Yu Chen, Pedram Roushan, Daniel Sank, **Charles Neill**, et al., "Emulating weak localization using a solid-state quantum circuit", *Nature Comm.* 5, 5184 (2014)

Charles Neill, Anthony Megrant, et al., "Fluctuations from edge defects in superconducting resonators", *Appl. Phys. Lett.* 103, 072601 (2013)

Anthony Megrant, **Charles Neill**, et al., "Planar Superconducting Resonators with Internal Quality Factors above One Million", *Appl. Phys. Lett.* 100, 113510 (2012)

Invited Talks

Invited Session at APS March Meeting, New Orleans, LA (March 2017).

Workshop on Quantum Simulation, Benasque, Spain (February 2015)

Institute for Quantum Science and Technology, Calgary, Canada (January 2015)

Condensed Matter Seminar, Boston University, Boston, MA (December 2014)

* Authors contributed equally

† Article featured on cover of the issue

Abstract

A path towards quantum supremacy with superconducting qubits

by

Charles James Neill

A key milestone on the path towards building a quantum computer will be the demonstration of an algorithm which exceeds the capabilities of any classical computer - achieving so called quantum supremacy. The challenge in developing such an algorithm lies in balancing computational complexity with experimental feasibility, particularly in the presence of errors. In this thesis, we design superconducting qubits and algorithms with the goal of finding such a balance. We implement a wide variety of control protocols, including parametric drive, adiabatic control, floquet evolution and time-domain spectroscopy. These tools are used to the study topological invariants, quantum chaos, quantum statistical mechanics, chiral symmetry breaking and many-body localization. We present experimental techniques for characterizing the complexity and fidelity of these algorithms and show that quantum supremacy is achievable using existing technology.

Contents

Chapter 1

Overview

1.1 Abstract

In this chapter, I introduce the basic physics of superconducting qubits. I show that these devices can realize computations whose complexity scales exponentially with the number of qubits. I present techniques for making these algorithms first-order insensitive to errors, allowing for more accurate computations. This chapter serves as an outline for how high-fidelity quantum computation may be achieved with superconducting qubits.

1.2 Quantum computing

Computers have revolutionized modern society. From cell-phones to super-computers, they are immensely powerful. However, even the most powerful computers grind to a halt when studying the behavior of quantum systems with only a few atoms. What is it

about quantum systems that make them so difficult to study on a classical computer?

To answer this question, lets consider the difference between classical and quantum bits. A classical bit is any system with two distinct states that can be reliably prepared and measured (typically denoted 0 and 1). Similarly, any quantum system with two distinct states can be used as a quantum bit or qubit (denoted $|0\rangle$ and $|1\rangle$).

In order to understand the advantage of qubits, lets consider a two bit example. Two classical bits can be in one of four states 00, 01, 10, or 11. Each one of these states contains two pieces of information - the state of the first bit and the state of the second bit. On the other hand, two quantum bits can be in a superposition of all four states

$$\alpha|00\rangle + \beta|01\rangle + \gamma|10\rangle + \delta|11\rangle \tag{1.1}$$

and contains four pieces of information (α, β, γ, δ). In general, a system with N classical bits contains N pieces of information (the state of each bit), whereas N quantum bits contain 2^N pieces of information (the probability amplitude for each basis state). The power of quantum computers comes from this exponential scaling of information with the number of qubits.

1.3 Superconducting qubits

Building a quantum computer is a massive challenge. The qubits need to interact with control wires, with one-another and with measurement circuits. All of this has to happen

while keeping the qubits sufficiently isolated that they retain their coherence.

Superconducting qubits are one of several potential candidates for building a quantum computer. Superconducting qubits benefit from the wealth of technology developed for integrated circuits. Their relatively large size is ideal for engineering coupling to control lines and coupling to one-another. An optical micrograph of a superconducting qubit is shown in Fig. F.1a. Gray regions correspond to a thin film of aluminum and dark regions are were the aluminum has been etched away to define features. The qubit consists of a large metal strip (red) and two small Josephson junctions (blue).

The junctions are superconducting wires separated by a thin insulating barrier. A simple approximate model for a junction is that of a non-linear inductor. For a linear inductor, the current I is proportional to the flux Φ through $\Phi = LI$. For a junction, the relationship is nonlinear and is given by $I = I_0 \sin(2\pi\Phi/\Phi_0)$ where I_0 is the critical current of the junction and Φ_0 is the flux quantum [178]. For small currents, we can Taylor expand the sin to first order giving $\Phi = \frac{\Phi_0}{2\pi}\frac{1}{I_0}I$; this allows us to define an effective inductance $L = \frac{\Phi_0}{2\pi}\frac{1}{I_0}$. This simple picture of a junction as a non-linear inductor provides intuition for understanding superconducting qubits.

A qubit combines a junction with a capacitor to form a nonlinear LC-oscillator, see Fig. F.1b&c. Similar to a linear inductor, the voltage across the junction is given by $V = d\Phi/dt$; this allows us to define the energy stored in the junction as $\int IV dt =$

$-\frac{\Phi_0}{2\pi} I_0 \cos(2\pi\Phi/\Phi_0)$[178]. The total energy of a qubit can then be written as

$$H = \frac{Q^2}{2C} - \left(\frac{\Phi_0}{2\pi}\right)^2 \frac{1}{L} \cos(2\pi\Phi/\Phi_0) \tag{1.2}$$

$$\approx \frac{Q^2}{2C} + \frac{\Phi^2}{2L} \tag{1.3}$$

where Q is the charge on the capacitor with capacitance C. By Taylor expanding the

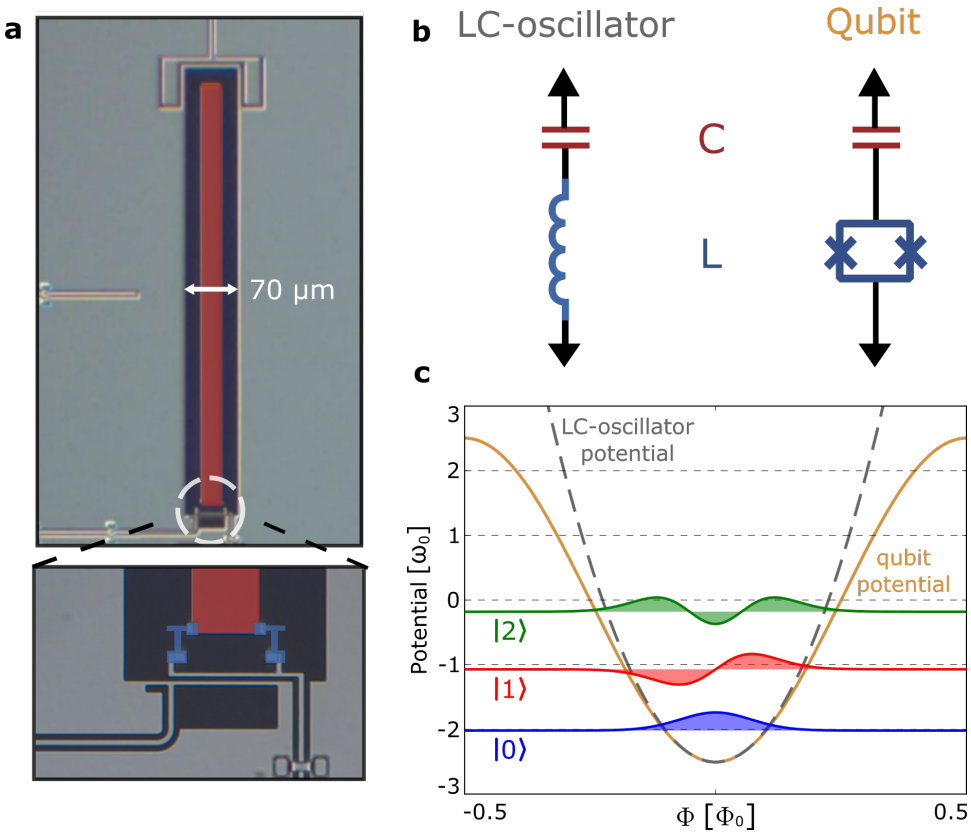

Figure 1.1: **Basics of superconducting qubits. a** Optical micrograph of a superconducting qubit. The capacitor has been falsely colored red and the junctions colored blue. Current through a control wire below the junctions is used to set the effective junction inductance and consequently the qubit frequency. **b** Schematic for an LC-oscillator (left) and a superconducting qubit (right). **c** The potential energy of the LC-oscillator (gray) and qubit (gold) are shown as a function of flux. The lowest three eigenstates of the qubit potential are overlaid.

cosine potential, we can reproduce the energy of an LC-oscillator (neglecting a constant offset). The energy levels of an oscillator are all equally spaced with separation $\omega_0 = 1/\sqrt{LC}$. In the supplementary material for Chapter 2, we show that the energy level spacing for the qubit is approximately ω_0 up to small corrections set by the impedance Z_0

$$E_n - E_{n-1} = \hbar\omega_0 \left(1 - n\lambda\right) \tag{1.4}$$

where $\lambda = Z_0/8.2\text{k}\Omega$ and $Z_0 = \sqrt{L/C}$. Typically, λ is designed to be a few percent.

Most of the qubit's properties can be understood intuitively by simply plotting the cosine potential. One period of the qubit's cosine potential is shown in Fig. F.1c along with the wave-function for three lowest energy-eigenstates. For states deep within the minima, the potential appears quadratic (dashed line) and states are separated in energy by the harmonic oscillator frequency ω_0. States high up in the well feel a potential which is wider than harmonic and thus have a lower energy. This non-linear spacing of energies allows us to isolate two levels and use them as a qubit.

When designing a qubit, one has to choose an impedance and a resonance frequency. Qubits with higher impedance have higher nonlinearity and therefore behave more like two-level systems. However, the impedance also sets the sensitivity to noise; see Chapter 2's supplementary material for details. Typically, the impedance is chosen between 300-400 Ω in order to balance a trade-off between nonlinearity and noise.

There is a similar trade-off when choosing the resonance frequency. Large resonance

frequencies are desired as they exponentially suppress unwanted thermal effects according to

$$e^{-\hbar\omega_0/k_bT} \tag{1.5}$$

where k_b is Boltzmann's constant and T is the temperature of the qubits (around 10 mK). However, choosing the frequency too high leads to issues with finding widely available and relatively inexpensive control electronics. Given these constraints, the qubit frequency is typically chosen between 4-8 GHz.

1.3.1 Coupling qubits

Any implementation of a quantum computer requires the qubits to interact with one-another in order to generate multi-qubit gates. In Fig. 8.1a, I consider two capacitively coupled qubits. In order to gain intuition for this device, lets neglect all nonlinear effects - these can be accounted for as a perturbation to the linear solution. In order to study the linear circuit, we replace the junctions with inductors, as shown in panel **b**.

The coupling between these two qubits can be understood by finding the normal modes of the coupled oscillators. A simple way to find the normal modes is to write down the capacitance matrix $\tilde{C}$ and the inductance matrix $\tilde{L}$. The frequencies of the normal modes can be found by solving

$$|\tilde{L}^{-1} - \omega^2\tilde{C}| = 0 \tag{1.6}$$

for ω, where $||$ is the determinant [176]. This is similar to finding the normal modes of masses coupled by springs using matrices of masses and spring constants.

The capacitance matrix can be found by replacing the inductors with ports (see panel **c**) and computing the admittance matrix Y; $\tilde{C}$ is defined through $Y = i\omega\tilde{C}$ [157]. The capacitance matrix for the two modes is given by

$$\tilde{C} = \begin{bmatrix} C + C_C & -C_C \\ -C_C & C + C_C \end{bmatrix} \tag{1.7}$$

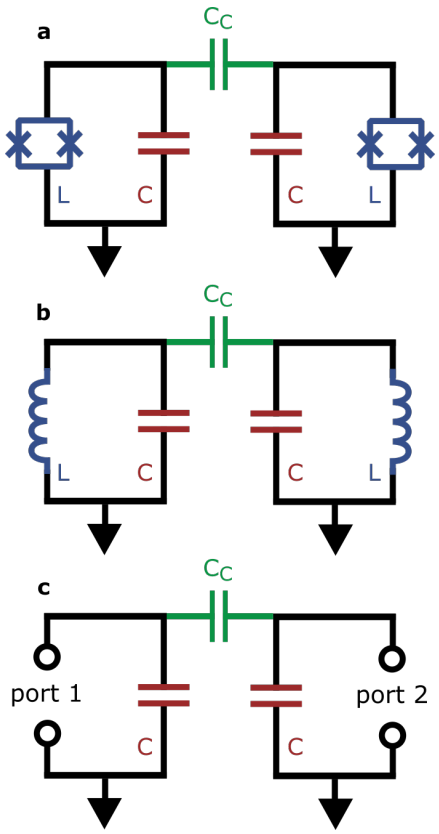

Figure 1.2: **Coupling qubits. a** Fixed capacitive coupling between two qubits. **b** The coupling between the two qubits can be understood (approximately) by replacing the junctions with inductors. **c** Replacing the inductors with ports allows us to construct the capacitance matrix and find the normal modes of the circuit.

and the inductance matrix is simply diagonal with elements L. The symmetric and anti-symmetric frequencies are given by

$$\omega_+ = \omega_0 \tag{1.8}$$

$$\omega_- = \frac{\omega_0}{\sqrt{1+2\kappa}} \tag{1.9}$$

where $\omega_0 = 1/\sqrt{LC}$ and $\kappa = C_C/C$ is the coupling efficiency. The coupling strength g is defined to be half the splitting between these two modes

$$g \equiv \frac{1}{2}\left(\omega_- - \omega_+\right) \tag{1.10}$$

$$\approx \kappa\frac{\omega_0}{2} \tag{1.11}$$

where the second equation is first order in κ. For inductive coupling, one arrives at the same expressions, except $\kappa = M/L$ where M is the mutual inductance.

Large coupling strengths are a resource for quantum computations as they set the speed limit at which information can go between qubits. A coupling efficiency of 1% allows information to swap between qubits in around 10 ns (roughly 1/1000 the coherence time). This relatively small coupling efficiency is straight forward to achieve in design.

Tunable coupling provides added flexibility when designing algorithms. A circuit diagram for tunable inductive coupling in shown in Fig. 1.3. All of the experiments in this thesis were performed using devices based on this schematic. The tunable coupling can be understood in a similar way to fixed coupling, however, the effective mutual

inductance is now given by $M_{\text{eff}} = \frac{M^2}{L_1+L_2}$. The coupling strength is tuned by putting flux into the coupler's loop; this flux changes the effective inductance of the coupler junction L_1 which changes the effective mutual inductance. A detailed description of this is provided in the next chapter along with some basic device characterization.

1.4 Control

Greater control over the qubits provides more options when trying to implement algorithms. For this reason, we design qubits with both tunable resonance frequencies and tunable interactions. By applying shaped control pulses to the qubits and couplers, we can vary matrix-elements in the control Hamiltonian over time. This can be used to generate a set of unitary operations (or gates) from which we can construct algorithms.

In order to gain intuition for the accessible gates, we can write down a model for coupled qubits in terms of the harmonic oscillator number operator n and creation (an-

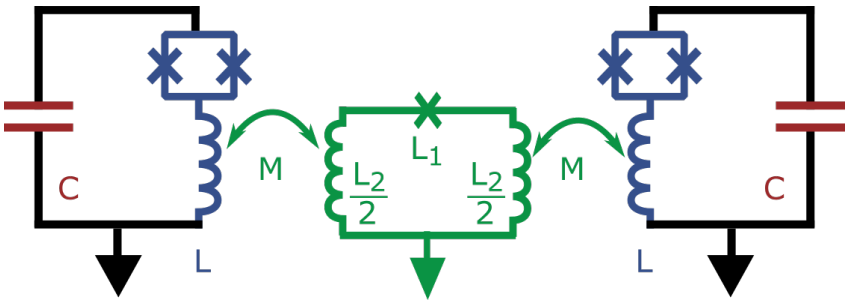

Figure 1.3: **Tunable inductive coupling.** Circuit diagram for two inductively coupled qubits. The coupling can be controlled by applying a flux to the coupler (green) which tunes the effective junction inductance.

nihilation) operators $a^\dagger$ (a)

$$H = \sum_i \omega_i(t)\, n_i + \frac{U_i}{2} n_i(n_i - 1) + \sum_i g_i(t) \left(a_i^\dagger a_{i+1} + a_i a_{i+1}^\dagger \right) \tag{1.12}$$

where the first term accounts for the harmonic oscillator energy and the second term accounts for the nonlinearity $U_i = \omega_i \lambda_i$. The second term is completely phenomenonlogical and is only valid for the first three levels (0,1,2); higher levels require more terms to reproduce the correct (nonlinear) spacing (Eq.1.4). The last term is an interaction which swaps an excitation between qubits; this results from both capacitive and inductive coupling. Time-dependent control over the first and last terms can be used to build a set of gates.

If the nonlinearity U is large compared to all other terms, the qubits can be approximated as two-level systems. The control Hamiltonian can be found by truncating the harmonic-oscillator operators to their two lowest levels. For a single qubit, this gives

$$H = -\frac{\omega_1}{2} \sigma_z \tag{1.13}$$

where σ_z is a Pauli operator. This term can be used to implement single-qubit rotations around the z-axis. For two qubits, the interaction term (truncated to the two lowest levels) can be represented as

$$H = g \left(\sigma_+^1 \sigma_-^2 + \sigma_-^1 \sigma_+^2 \right) \tag{1.14}$$

where σ_+ (σ_-) are the spin raising (lowering) operators. This term can be used to swap excitations between qubits.

Even when the nonlinearity U is large, the higher levels still affect the qubit dynamics dispersively. This effectively implements

$$H = J\sigma_z^1\sigma_z^2 \tag{1.15}$$

and can be used to generate controlled-phase gates [125]. Combining all of these terms gives us an effective control Hamiltonian

$$H = -\frac{1}{2}\sum_i \omega_i\sigma_z^i + \sum_i g_i\left(\sigma_+^i\sigma_-^{i+1} + \sigma_-^i\sigma_+^{i+1}\right) + J_i\sigma_z^i\sigma_z^{i+1} \tag{1.16}$$

In the next section, we consider numerical approaches for studying the complexity of computations which use this control model.

1.5 Computational complexity

When developing algorithms, one is required to carefully balance experimental feasibility with computational complexity. For example, faster algorithms are generally higher fidelity but lower complexity. When balancing this trade-off, a metric for quantifying complexity is a valuable tool. One very simple way of defining complexity is to ask how much memory does it take to store the state-vector in a classical computer. Once the memory requirements exceed roughly 1 petabyte, there simply does not exist a classical

computer capable of reproducing the result of the quantum computer. One petabyte of memory corresponds to a Hilbert-space dimension of roughly 2^{50}.

However, in order for this argument to apply, all 2^{50} states need to be important, otherwise theres the possibility that we could solve the problem keeping only a subset of the states. How can one determine if an algorithm meets such a criteria? The following method has been proposed as a test. Consider an algorithm which implements the unitary operation U on a set of qubits. The square of the matrix elements $|U_{nm}|^2$ correspond to measurable probabilities. For dynamics that uniformly explore all states, the distribution of these probabilities ρ is claimed to have the following exponential form [156, 28]

$$\rho = e^{-\text{Probability}\times N_{\text{states}}} \tag{1.17}$$

where N_{states} is the number of states in the Hilbert-space.

Lets work out a few simple numerical examples to see if this claim makes sense. Consider a hermitian matrix H where the elements are randomly generated from 0 to 2π. Since H is random it will have no symmetries and the unitary operator $U = e^{-iH}$ should uniformly sample all states. Fig. 1.4 shows a histogram of the transition probabilities $|U_{nm}|^2$ for a 1000 random operators of dimension 64 and 256; the width of the bars denotes the width of the bins used to construct the histogram. After scaling the probabilities by the number of states, the curves lie atop one another and decay exponentially as predicted by Eq. 1.17 (shown as a dashed gray line).

Now let's consider a numerical example that could potentially be implemented using

our qubits. A 1D array of qubits can be modeled approximately as

$$H = g \sum_i \left(\sigma_+^i \sigma_-^{i+1} + \sigma_-^i \sigma_+^{i+1} \right) + J \sum_i \sigma_z^i \sigma_z^{i+1} \tag{1.18}$$

as described in the previous section. We can generate random operations by evolving under this control Hamiltonian for some time and then applying Z operations on randomly selected qubits. Let's call this one cycle of evolution. The inset of Fig. 1.5 depicts 5 cycles of evolution on 6 qubits. The histogram of output probabilities is shown in green. Note that the evolution generated by Eq. 1.18 conserves the total number of excitations. If the initial state had three excitations, such as $|000111\rangle$, then all final states will have three

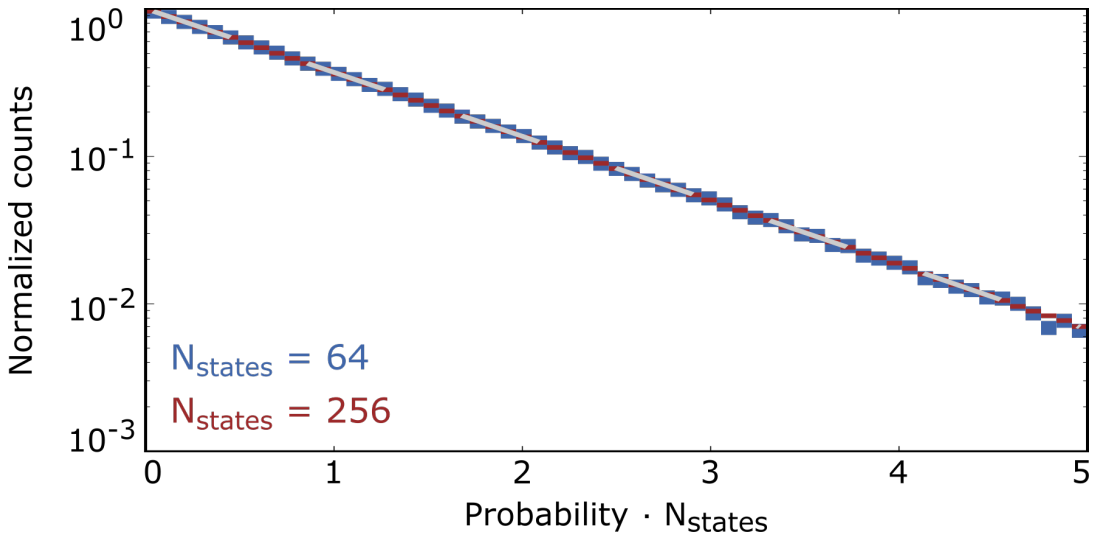

Figure 1.4: **Numerical simulation of uniform sampling.** Random hermitian matrices H are generated with elements ranging from 0 to 2π. These matrices are exponentiated in order to generate random unitary operators $U = e^{-iH}$. The figure shows a histogram of probabilities ($|U_{nm}|^2$) for both 64 and 256-dimensional matrices. The width of the bars denotes the width of the bins used to make the histogram. After weighting the probabilities by the dimension, these distributions lie atop one another and decay exponentially. A dashed gray line is overlaid and corresponds to Eq. 1.17.

excitations, such as $|101100\rangle$. In Fig. 1.5, only the probabilities associated with half the qubits being excited were used to construct the histogram. The exponential nature of the distribution suggests that this model may also be uniformly sampling all of the states in a manner similar to completely random evolutions. If so, the complexity of this gate sequence can be understood by simply asking how much classical memory does it take to store the state-vector.

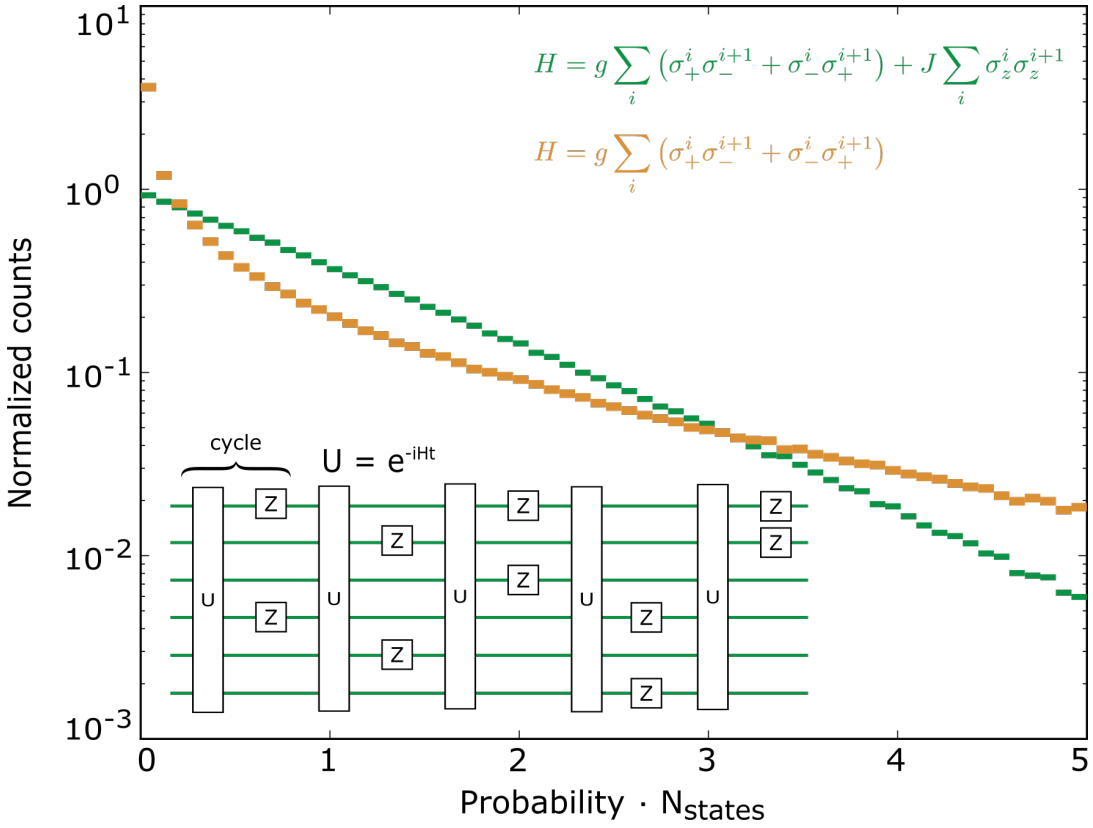

Figure 1.5: **Numerical simulation of two control protocols.** Consider the six-qubit gate-sequence shown inset. In green, we show a histogram of the transition probabilities for $gt = \pi$ and $Jt = \pi/4$. The width of the bars denotes the width of the bins used to make the histogram. The probabilities were taken from 10,000 random instances which were generated by placing the z-rotations in different places. The exponential form of the distribution suggests that this model uniformly samples states from the Hilbert-space. In contrast, the histogram for $J = 0$ is shown in gold and is not exponential.

In contrast to the two previous examples, let's consider an evolution which may be easy to simulate on a classical computer. In gold, we show the histogram of transition probabilities when $J = 0$. Here, we find a distribution that is clearly not exponential. This suggests that the complexity of these gate sequences may not require computational resources that scale with the full Hilbert-space dimension [28].

In Chapter 7, we experimentally measure similar histograms as a demonstration that our algorithm complexity scales exponentially with the number of qubits. As a numerical tool, studying these histograms allowed us to design better algorithms. The algorithm used in Chapter 7 was designed to be as easy to implement as possible while reaching high complexity with as few gates as possible. Finding such a compromise between experimental feasibility and computational complexity is important for achieving quantum supremacy with high fidelity.

1.6 Error detection

We are on the verge of realizing large arrays of 49 or more superconducting qubits. These devices will have the potential to outperform the most powerful supercomputers [28, 69]. However, these devices will not be large enough for error-correction [57]. This poses a fundamental challenge to develop algorithms that are both *computationally interesting* and *robust to errors*.

There are a wide variety of experimental errors that can lead to erroneous outcomes in a computation. While these errors are generally rather complicated, they are broadly

categorized as either phase-flip or bit-flip errors [57]. This model provides a simple zeroth-order picture of errors.

Lets consider an example of a bit-flip error. In an experiment, each measurement results in a single output state, such as $|01\rangle$. However, certain errors might yield the wrong answer, e.g. $|00\rangle$. This is an example of a bit-flip error and possible mechanisms include imperfect measurement.

Here is a simple method for detecting bit-flip errors. In the previous section, we considered algorithms which conserved the total number of excitations. For example, if we start in the state $|01\rangle$, then we only expect to measure the states $|01\rangle$ and $|10\rangle$. However, a measurement error might lead to an erroneous outcome, such as $|11\rangle$. If this happens, we can detect that an error has occurred and neglect this result. However, if two errors cancel one another, it is possible that they will go undetected. In this sense, we can be protected to first order against bit-flip errors. In Chapter 7, we demonstrate algorithms that take advantage of this observation.

In the final chapter of this thesis, I discuss a similar technique for identifying both phase-flip and bit-flip errors simultaneously. This has the potential to greatly improve the fidelity of future computations.

1.7 Overview of this thesis

In this chapter, we summarize the basic physics of superconducting qubits and outline a strategy for designing high fidelity algorithms. In Chapter 2, we build a two-qubit circuit

and characterize the basic performance. In Chapter 3, we build a three-qubit circuit and study quantum statistical mechanics using three-qubit swap-like gates. In Chapter 4, we study topological phase transitions using adiabatic state preparation. In Chapter 5, we study applications to fractional quantum hall by implementing parametrically-driven three-qubit gates. In Chapter 6, we study many-body localization by implementing a wide class of nine-qubit gates. In Chapter 7, we show that these nine-qubit gates can be implemented with such a high fidelity that quantum supremacy may be achievable using existing technology. In Chapter 8, the outlook, we propose a potential path towards higher coherence qubits and describe algorithms that are potentially less sensitive to errors. This thesis serves to document a long series of experiments pushing the control complexity of multi-qubit hardware and algorithms.

Chapter 2

Introduction to gmon qubits

2.1 Abstract

We introduce a superconducting qubit architecture that combines high-coherence qubits and tunable qubit-qubit coupling. With the ability to set the coupling to zero, we demonstrate that this architecture is protected from the frequency crowding problems that arise from fixed coupling. More importantly, the coupling can be tuned dynamically with nanosecond resolution, making this architecture a versatile platform with applications ranging from quantum logic gates to quantum simulation. We illustrate the advantages of dynamical coupling by implementing a novel adiabatic controlled-Z gate, with a speed approaching that of single-qubit gates. Integrating coherence and scalable control, the introduced qubit architecture provide a promising path towards large-scale quantum computation and simulation.

2.2 Introduction

The fundamental challenge for quantum computation and simulation is to construct a large-scale network of highly connected coherent qubits [139]. Superconducting qubits use macroscopic circuits to process quantum information and are a promising candidate towards this end [49]. Recent materials research and circuit optimization have produced significant progress in qubit coherence [127, 17, 146]. Superconducting qubits can now perform hundreds of operations within their coherence times, allowing the development of complex algorithms [18].

It is desirable to combine these high-coherence qubits with tunable inter-qubit coupling; the resulting architecture would allow both coherent local operations and dynamically varying qubit interactions. For quantum simulation, this would provide a unique opportunity to investigate dynamic processes in non-equilibrium phenomena [35, 78, 58]. For quantum computation, such an architecture would provide isolation for single-qubit gates yet enable fast multi-qubit gates that minimize decoherence errors.

Despite previous successful demonstrations [7, 24, 70, 74, 141, 183, 175, 25, 116, 152], these applications have yet to be realized due to the challenge of implementing tunable coupling without degrading the device performance. Serious control crosstalk arises when there is a DC path connecting the qubit and coupler junctions [7, 24, 70, 74, 141, 183]. Furthermore, the coupler circuit can introduce additional decay channels through which the qubit decoheres [24].

Here, we introduce a qubit architecture that incorporates fast tunable coupling, high

coherence and minimal crosstalk. In contrast to previous designs, our "gmon" device inductively couples transmon qubits at their low voltage node. This design strategy substantially reduces the qubit energy stored in the coupler, minimizing the influence of added loss and retaining the coherence of the transmon. In addition, it eliminates all DC connectivity between the qubit and the coupler junctions, dramatically reducing the control crosstalk of the circuit. With the coupling turned off, we demonstrate that our architecture is protected from the frequency crowding problems that arise from fixed coupling. By dynamically tuning the coupling, we implement a novel adiabatic controlled-Z gate at a speed approaching that of single-qubit gates.

2.3 Circuit diagram

A two-qubit unit cell with tunable coupling is shown in Fig. F.1(a). The qubits and control lines are defined by an aluminum film with cuts exposing the underlying sapphire substrate. Our circuit design is based on the Xmon qubit [17], consisting of a cross-shaped capacitor resonating with a nonlinear inductor $L_J = 9.0\,\mathrm{nH}$ from a DC SQUID. We modify the Xmon design to introduce a linear inductor $L_g = 200\,\mathrm{pH}$ from the junction to ground, with $L_g \ll L_J$ so the qubit nonlinearity is largely unaffected (see supplementary information). This inductor introduces a node where current from one qubit can be tapped off to interact with a neighboring qubit. A junction connecting the two nodes provides a tunable inductance L_c that controls the flow of this current and therefore the coupling.

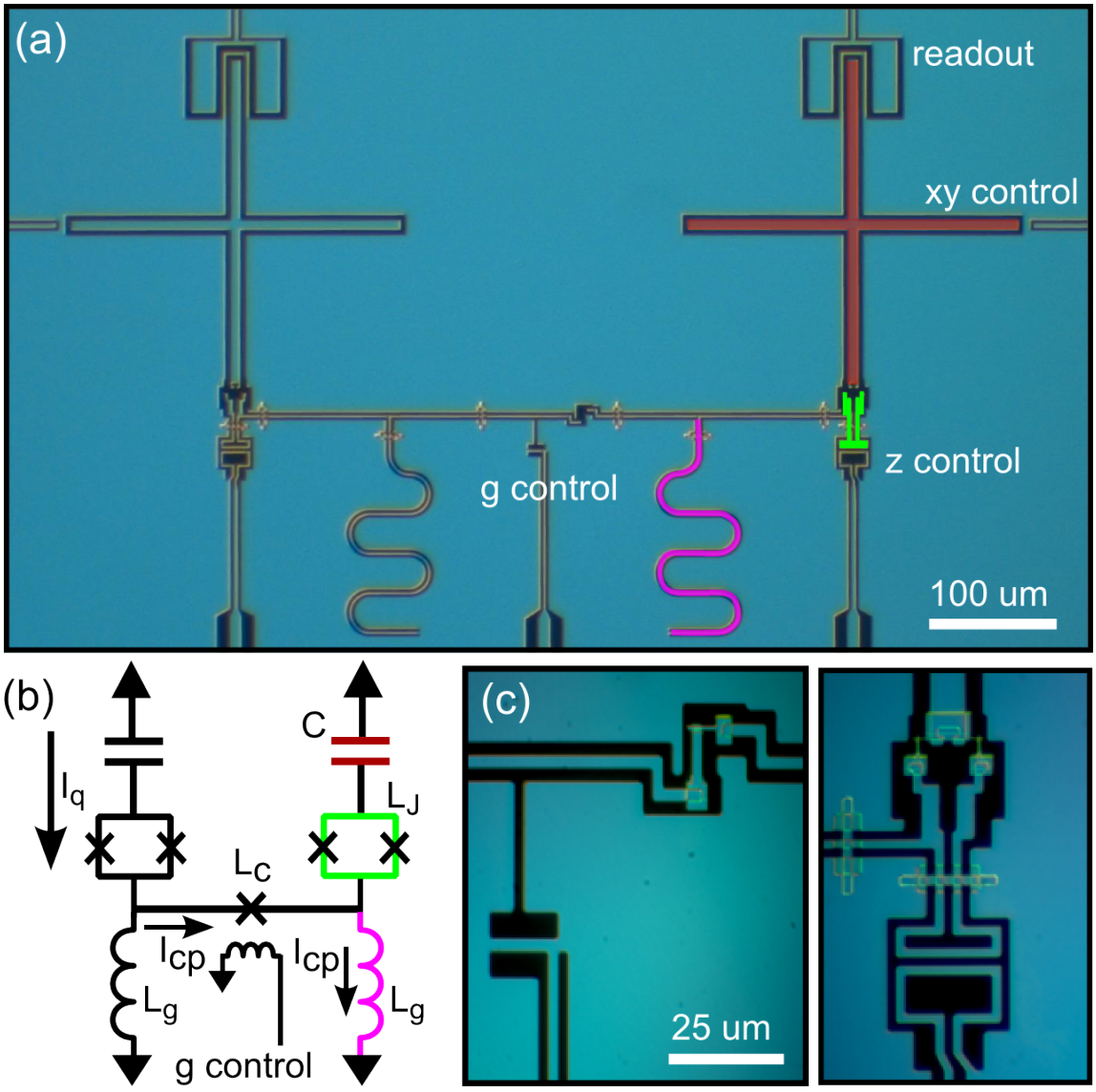

Figure 2.1: (a) Optical micrograph of two inductively coupled gmon qubits. The cross-shaped capacitors are placed in series with a tunable Josephson junction and followed by a linear inductor to ground. The circuit is depicted schematically in (b) with arrows indicating the flow of current for an excitation in the left qubit. The qubits are connected with a junction serving as a tunable inductor to control the coupling strength. (c) Micrographs of the coupler junction (left) and qubit SQUID (right). The bottom of each image shows a bias line to adjust the coupling strength (left) and qubit frequency (right, not shown in schematic).

The physics behind this tunable coupler is well explained using a simple linear model, since the coupling currents are much smaller than the critical current of the coupling junction $I_0 = 330\,\mathrm{nA}$; see Ref. [58] for a full quantum mechanical treatment. A circuit diagram for the device is given in Fig. F.1(b). An excitation current I_q in the first qubit mostly flows through L_g, with a small fraction $I_{\mathrm{cp}} = I_q L_g/(2L_g + L_c)$ flowing through the coupler to the second qubit. This current generates a flux in the second qubit $\Phi_2 = L_g I_{\mathrm{cp}}$. Ignoring parasitic inductance, the effective mutual inductance can be expressed as

$$M = \frac{\Phi_2}{I_q} = \frac{L_g^2}{2L_g + L_c} \quad . \tag{2.1}$$

Using this mutual inductance, the interaction Hamiltonian for the two qubits on resonance is

$$\hat{H}_{int} = -\frac{\omega_0}{2}\frac{M}{L_J + L_g}(\hat{a}_1^\dagger \hat{a}_2 + \hat{a}_1 \hat{a}_2^\dagger) \quad , \tag{2.2}$$

where ω_0 is the qubit resonance frequency. This equation uses the rotating wave approximation to express photon swapping with raising and lowering operators [152]. The coefficient of the interaction Hamiltonian gives the coupling strength

$$g = -\frac{\omega_0}{2}\frac{L_g}{L_J + L_g}\frac{L_g}{2L_g + L_{c0}/\cos\delta} \quad , \tag{2.3}$$

where we replaced L_c by the Josephson inductance $L_c = \Phi_0/(2\pi I_0 \cos\delta) \equiv L_{c0}/\cos\delta$.

Here δ is the phase difference across the coupler junction, set by applying a DC flux. The coupling g can be varied continuously from negative to positive, going smoothly through zero at $\delta = \pi/2$. This smooth transition ensures the existence of a bias where the coupling is completely negated, even with small stray coupling.

A critical part of our design is its compatibility with high coherence. The key concept to maintain coherence is the voltage divider created by L_J and L_g. Placing the coupling circuit at this low voltage node reduces capacitive losses to surface defects on coupler structure by a factor of $(L_J/L_g)^2$ - over 2000 in our design. For the gmon, we measure an energy relaxation time $T_1 \sim 7$–$10\,\mu$s, independent of the coupling strength (see supplementary information). This is comparable to that of Xmon devices with similar capacitor geometry ($8\,\mu$m center trace, $4\,\mu$m gap) and aluminum deposition conditions (high vacuum e-beam evaporation). Devices grown with molecular beam epitaxy and with optimized capacitor geometry have demonstrated lifetimes exceeding $40\,\mu$s [17].

In addition to the energy dissipation, the coupler circuit may introduce additional dephasing to the qubits. In order to minimize dephasing, we have designed the gmon circuit in a way that the qubit frequency has a weak dependence on the coupler bias, only a few tens of MHz per flux quantum. Near the optimal bias point, we have measured a dephasing time T_φ of $3 \sim 4\,\mu$s, , over the entire range of coupling strength from zero to its maximum value (see supplementary information). This is comparable to that of the Xmon qubit, indicating that the dephasing rate of the qubit is unaffected by the coupler circuit.

2.4 Tunable coupling

The core functionality of the gmon coupler is demonstrated in Fig. 8.1. In panel (a) we show the variation of coupling strength as a function of the coupler flux bias when the two qubits are brought into resonance at frequency $\omega_0/2\pi = 5.67\,\mathrm{GHz}$. Here for one qubit we sweep the microwave drive frequency and measure the qubit excited state probability P_1. We observe two distinct resonances at frequencies $\omega_0 + g$ and $\omega_0 - g$, resulting from the coupling-induced energy level splitting. The total splitting is twice the coupling strength, ranging from 0 to 110 MHz. This range can be further increased by modifying the coupler junction critical current. Note that we have compensated for the small changes in the qubit frequency ($\sim g$) that occur as L_c is varied. These compensations are small because DC control currents flow only through the coupler and not through the qubit junctions as the qubit capacitor acts as a DC block. The supplementary information gives details on how the qubit and coupler controls are effectively made orthogonal.

In Fig. 8.1(b), we set the the coupling strength to its maximum value and rapidly exchange an excitation between the two qubits. We excite the first qubit (Q_1), turn on the coupling, wait a variable delay time, and then measure the excited state probability of Q_1. We vary the frequency of Q_1 while fixing that of the second qubit (Q_2). The interaction produces the expected chevron pattern [76]. The strong coupling allows the excitation to swap between the qubits in 5 ns, consistent with the 110 MHz splitting measured above. At this rate, a $\sqrt{i\mathrm{SWAP}}$ gate could generate a Bell state in 2.5 ns, whereas a non-adiabatic CZ could be implemented in 10 ns [190]. We have also performed

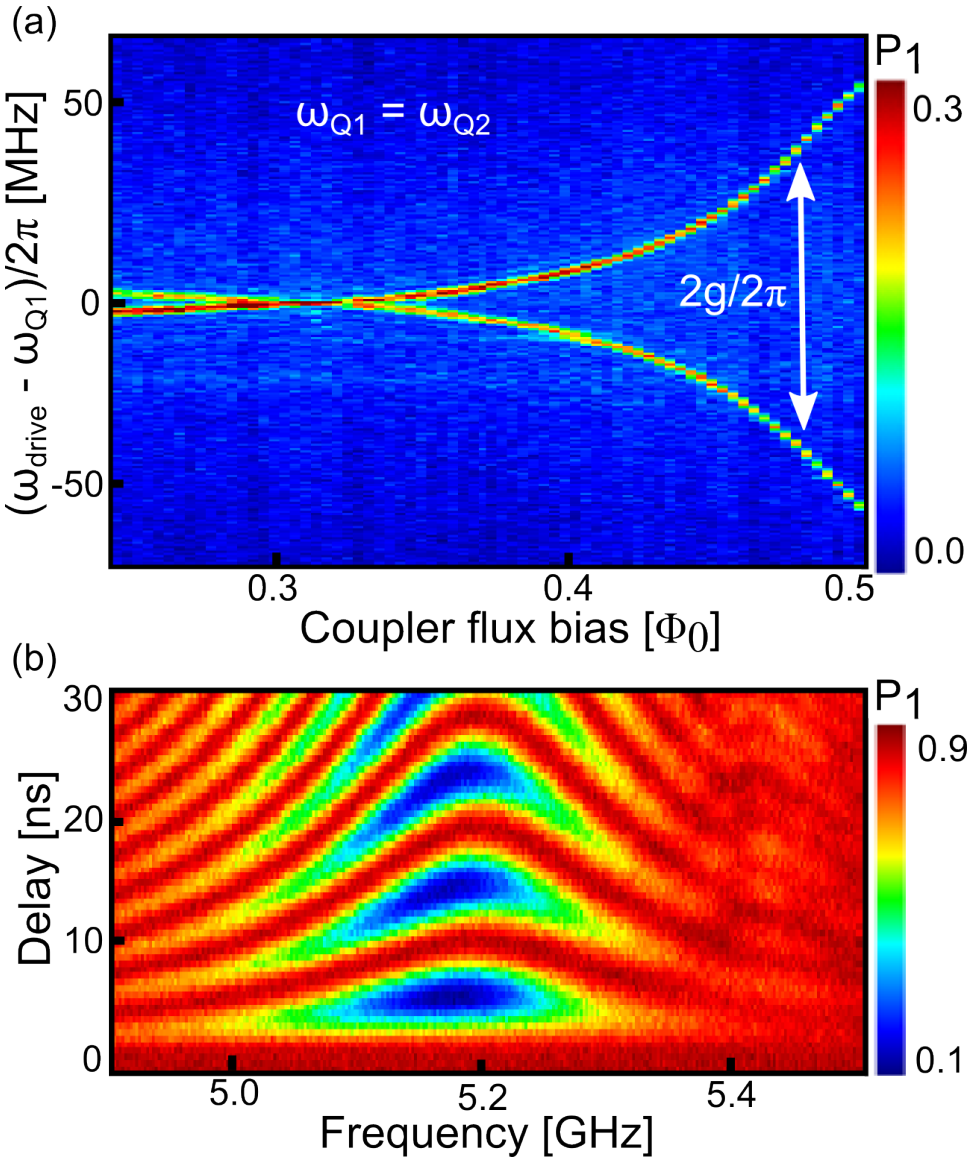

Figure 2.2: (a) The dependence of coupling strength on the coupler flux bias while the two qubits are on resonance, with $\omega_{Q1}/2\pi = \omega_{Q2}/2\pi = 5.67\,\text{GHz}$. For each value of the coupler flux bias, we sweep the microwave drive frequency and measure the excited state probability P_1 (colorbar) of Q_1. There are two distinct peaks in the spectroscopy resulting from the qubit energy level splitting. The frequency splitting is twice the coupling strength $g/2\pi$ and ranges from 0 to 110 MHz. (b) Q_1 excited state probability (colorbar) versus Q_1 frequency (horizontal axis) after exciting Q_1 and waiting a variable delay time (vertical axis). Q_2 is fixed at 5.18 GHz and the coupling set to 55 MHz. On resonance, the two qubits swap an excitation in 5 ns.

the same measurement with nominally zero coupling (see supplementary information). and observe no indication of swapping after 6 μs. This places an upper bound on the residual coupling of 50 kHz, providing an on/off ratio>1000.

2.5 Single-qubit gates

By incorporating tunable coupling with high coherence, our architecture provides a viable platform for both quantum computation and simulation. We applied this device to quantum simulation in a separate experiment where we demonstrated an interaction-driven topological phase transition [163]. Here, we focus on applications in quantum computation by implementing elementary logic gates. This architecture offers two distinct advantages: decoupling qubits for local single-qubit gates and dynamically tuning the interaction for fast two-qubit gates.

We characterize gate performance using a simplified form of randomized benchmarking [104, 123], using a series of Pauli gates. These gates belong to a subset of the Clifford group and are generated with microwave pulses corresponding to Bloch sphere rotations of angle π and $\pi/2$ around the X- and Y-axes. From this set we randomly choose m gates and apply these to the qubit, including a final gate that ideally maps the qubit back into the ground state. The probability of finding the qubit in the ground state is called the sequence fidelity F_{seq}, which decays exponentially with the number of gates as $F_{\mathrm{seq}} = Ap^m + B$. Here A, B and p are fit parameters; A and B relate to state preparation and measurement. We are interested in the average error per gate r, determined through

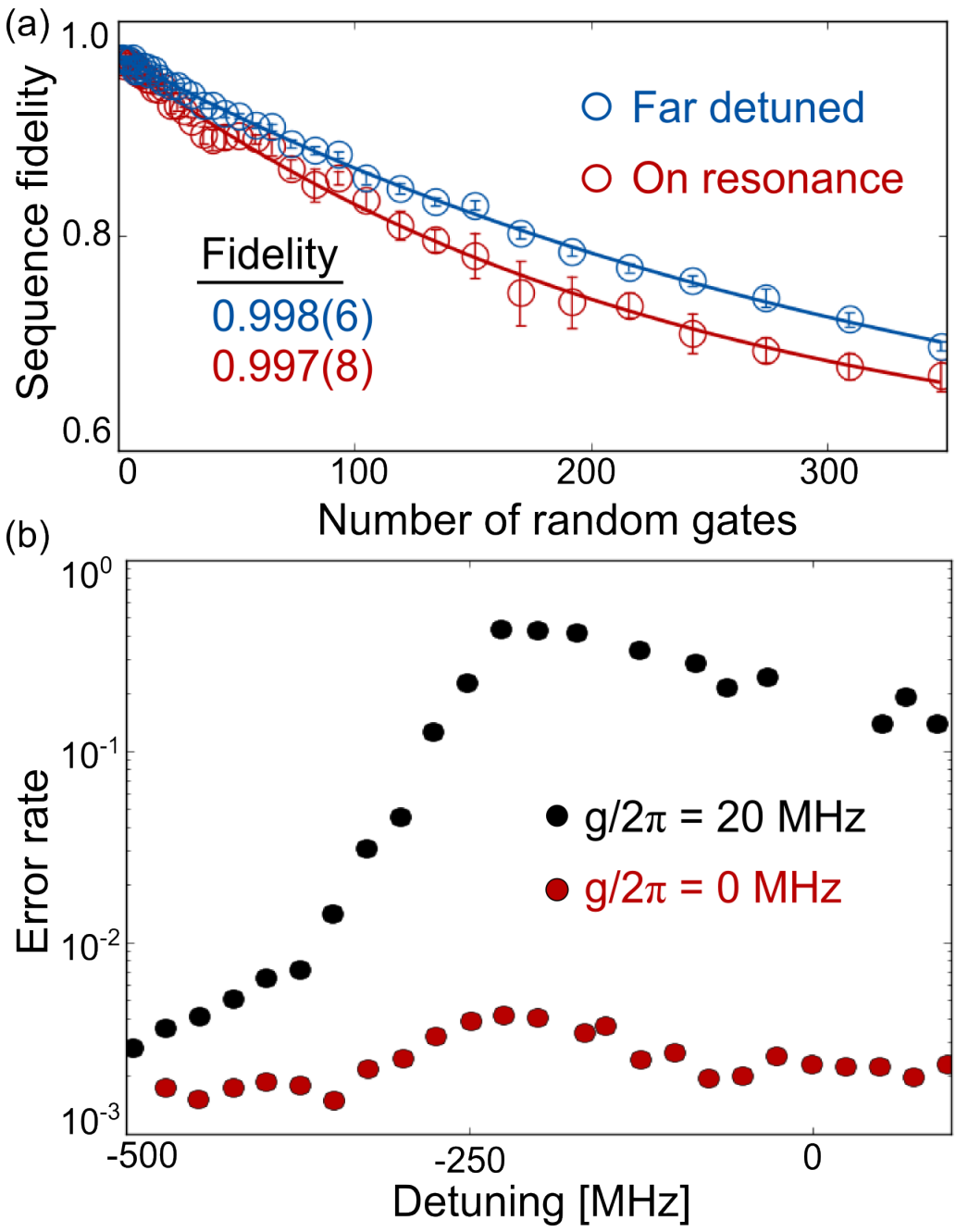

Figure 2.3: Simultaneous single-qubit randomized benchmarking. (a) Raw benchmarking data for Q_1 when Q_2 is far detuned (blue) and on resonance (red) with random gates applied to both qubits. Operating the qubits on resonance degrades the gate performance by $< .1\%$. Lines are fits to a decaying exponential. (b) The average error rate for Q_1 as a function of detuning between the two qubits, shown for nominally zero (red) and 20 MHz (black) coupling.

the relation $r = (1-p)(d-1)/d$ where $d = 2^{N_{\text{qubits}}}$. We note that Pauli gates do not fully depolarize errors, hence the extracted gate fidelities are only indicative.

The ability to isolate individual qubits for local operations is one advantage offered by a tunable coupling architecture. A metric to quantify this isolation is single-qubit gate fidelity $1-r$. For a baseline, we perform randomized benchmarking on the first qubit while the second qubit is far detuned and effectively decoupled. The sequence fidelity is plotted in Fig. 2.3(a) and displays the expected exponential decay with the number of random gates. Fitting the decay curve yields an average single-qubit gate fidelity of 99.86%. The two qubits are then placed on resonance with $g = 0$ and the measurement is repeated on both qubits; data for the first qubit is shown. Simultaneously operating the two qubits on resonance reduces the gate fidelity by $< 0.1\%$. The slightly increased error rate results from two sources: residual inter-qubit coupling, resulting from an imperfect choice of the zero coupling bias, and imperfect cancellation of microwave crosstalk between control signals.

In panel (b), we repeat this measurement as a function of frequency separation of the two qubits, demonstrating that our architecture can resolve the frequency crowding issues from fixed coupling. The average error rate is plotted in Fig. 2.3(b) for both $g/2\pi = 0$ and 20 MHz. Even for this relatively weak interaction, the single-qubit gate fidelity undergoes a significant reduction for detunings less than 500 MHz. The ability to turn off the coupling g results in a nearly flat error rate, with an on-resonance value two orders of magnitude lower than for fixed coupling. We note the slight degradation near

the qubit nonlinearity (220 MHz).

A concern in transmon design is the cross-coupling of qubits. One solution is to use 3D devices where qubits are shielded in enclosing cavities [146]. Here we directly demonstrate that cross-coupling effects can be made small for planar integrated circuits, while still allowing for strong direct coupling for multi-qubit operations.

2.6 Two-qubit gates

Control over the interaction strength with nanosecond resolution provides a unique tool to construct fast two-qubit gates. In Fig. 2.4(a) we illustrate the use of dynamical coupling to implement a fast controlled-Z (CZ) gate, with minimal non-adiabatic leakage errors. The straight lines correspond to the $|11\rangle$- and $|02\rangle$-state energies of the uncoupled system. Turning on the interaction pushes the energy levels apart, with the energies of the coupled system plotted as curved lines. Adiabatically turning on and off the coupling, as depicted with arrows, causes the $|11\rangle$ eigenstate to accumulate a dynamic phase. By calibrating the length of the interaction the phase shift can be set to π for a CZ gate.

In Fig. 2.4(b) we use a Ramsey measurement to verify that the gate produces the desired results. We first apply a $\pi/2$ pulse to Q_1, perform a CZ, apply a second $\pi/2$ pulse with varying phase, and then measure the Q_1 excited state probability. We then repeat the experiment with a π-pulse applied to Q_2 and overlay the data. The solid lines are fits to cosine oscillations. As expected, the π phase shift is observed only when both qubits are excited; otherwise the phase accumulation is zero.

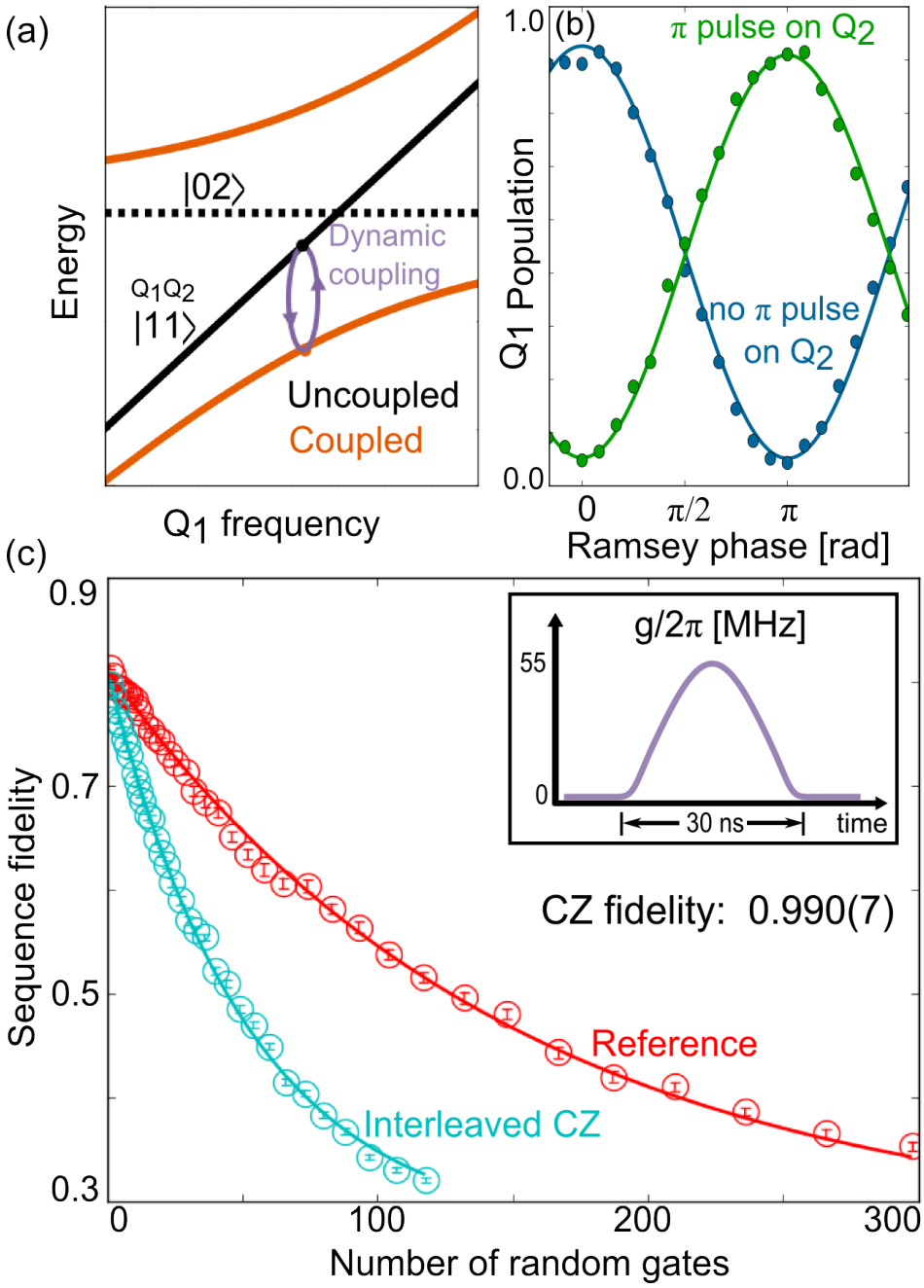

Figure 2.4: (a) Energy level diagram, illustrating a CZ gate using tunable coupling. Black (orange) lines are the uncoupled (coupled) two-photon eigenenergies. As the coupling is tuned on and off (depicted in purple), the energy levels repel and the states accumulate a dynamic phase. (b) Ramsey data demonstrating zero phase shift for single-photon states and a π phase shift for the two-photon state. (c) Randomized benchmarking results for a CZ gate utilizing the pulse shape (inset). We achieve 99.07% fidelity with a 30 ns gate.

We extract the fidelity of this CZ gate using interleaved randomized benchmarking, where we insert a CZ between random single-qubit Pauli gates. A reference curve without the interleaved CZ is measured and plotted in Fig.2.4(c) along with the interleaved sequence fidelity. Fitting these two curves allows us to extract an average CZ gate fidelity of 99.07%. The dominant error ($\sim$ 0.66%) comes from decoherence, measured by interleaved randomized benchmarking on the two qubit idle gate (see supplementary information). Surprisingly, despite the short gate time, the non-adiabatic error resulting from leakage to the $|02\rangle$ state is small ($\sim$ 0.25%), measured with the Ramsey error filter technique (see supplementary information) [120]. This results from using an optimized adiabatic trajectory based on a theory of optimal window functions [125]. The adiabatic trajectory used to vary the coupling strength is shown inset in panel (c).

High-fidelity gates have previously been demonstrated using Xmon qubits with fixed coupling [18]. We believe that gate fidelities can be further improved by instead employing tunable coupling. This will require incorporating lower loss materials, optimized capacitor geometry and characterization using the full Clifford group; this is currently in progress.

Chapter 3

Applications to quantum statistical mechanics

3.1 Abstract

Statistical mechanics is founded on the assumption that all accessible configurations of a system are equally likely. This requires dynamics that explore all states over time, known as ergodic dynamics. In isolated quantum systems, however, the occurrence of ergodic behavior has remained an outstanding question [48, 174, 162, 154]. Here, we demonstrate ergodic dynamics in a small quantum system consisting of only three superconducting qubits. The qubits undergo a sequence of rotations and interactions and we measure the evolution of the density matrix. Maps of the entanglement entropy show that the full system can act like a reservoir for individual qubits, increasing their entropy through

entanglement. Surprisingly, these maps bear a strong resemblance to the phase space dynamics in the classical limit; classically chaotic motion coincides with higher entanglement entropy. We further show that in regions of high entropy the full multi-qubit system undergoes ergodic dynamics. Our work illustrates how controllable quantum systems can investigate fundamental questions in non-equilibrium thermodynamics.

3.2 Introduction

Imagine air molecules in a room. They move around with all possible velocities in all directions. Attaining the exact knowledge of these trajectories is a daunting and an unrealistic task. Statistical mechanics, however, claims that exact knowledge of individual trajectories is not required and systems can be accurately described using only a few parameters. What is the essential property of these systems that allows for such a simple description?

Ergodic dynamics provide an explanation for this simplicity. If the dynamics are ergodic, then the system will uniformly explore all microscopic states over time, constrained only by conservation laws. Ergodicity ensures that

$$\langle O \rangle_{\text{time}} = \langle O \rangle_{\text{states}} \tag{3.1}$$

where O is any macroscopic observable and brackets denote averaging. In the limit of many particles, macroscopic observables such as pressure or density approach equilibrium and are stationary, therefore at any time $O(t) = \langle O \rangle_{\text{time}}$. These two equations imply that macroscopic observables can be predicted by uniformly averaging over all states and

this forms the foundation for all thermodynamic calculations.

In classical systems, it is chaotic motion which drives the system to ergodically explore the state space [144]. Quantum systems, however, are governed by Schrodinger's equation which is linear and consequently forbids chaotic motion [64]. This poses fundamental questions regarding the applicability of statistical mechanics in isolated quantum systems [48, 174, 162, 154]. Do quantum systems exhibit ergodic behavior in the sense of Eq. 3.1? Do quantum systems act as their own bath in order to approach thermal equilibrium? Extensive experimental efforts have been made to address these fundamental questions [100, 102, 40, 179, 108, 161, 169].

3.3 Large-spin model

Here we investigate ergodic dynamics by considering a simple quantum model whose classical limit is chaotic [184, 61, 118, 37, 65]. This model describes a collection of spin-1/2 particles whose collective motion is equivalent to that of a single larger spin with total angular momentum j governed by the Hamiltonian

$$\mathcal{H}(t) = \frac{\pi}{2\tau} J_y + \frac{\kappa}{2j} J_z^2 \sum_{n=1}^{N} \delta(t - n\tau) \tag{3.2}$$

where J_y and J_z are angular momentum operators. The sum over delta functions implies N applications of J_z^2 each at integer time steps. The angular momentum operators can be expressed in terms of the constituent spin-1/2 Pauli operators, e.g. $J_z = \frac{\hbar}{2} \sum_i \sigma_z^{(i)}$. Setting $\tau = 1$, the first term in $\mathcal{H}$ causes each spin to rotate around the y-axis by an

angle $\pi/2$. The second term couples every spin to every other spin with strength $\kappa/2j$. This can be seen by expanding J_z^2 in terms of z operators, where terms like $\sigma_z^{(1)}\sigma_z^{(2)}$ and all other combinations appear.

The classical dynamics, being simple to visualize and interpret, can provide valuable intuition for studying the quantum limit. The classical limit of this model occurs when j is very large and quantization effects become negligible. In this limit, the system behaves like a classical spinning top with dynamics which are known to be chaotic [184, 61, 118, 37]. The parameter κ sets the chaoticity and takes the dynamics from regular to chaotic as κ increases; at intermediate values, the system exhibits a rich mixture of both regular and chaotic motion.

3.4 Pulse-sequence

Experimentally realizing this model requires a high degree of control over both local terms and interactions in a multi-qubit Hamiltonian. This led to the design of a three-qubit ring of planar transmons with tunable inter-qubit coupling (see supplement) [17, 38, 58]. The rotations around the y-axis (J_y) are performed using shaped microwave pulses that are resonant with the qubit transition. The simultaneous and symmetric three-qubit interaction (J_z^2) is turned on and off using a tunable coupling circuit controlled by three separate square pulses. The qubit-qubit interaction energy g and the duration of the interaction pulses T set κ through the relation $\kappa = 3gT/\hbar$. We measure the strength of the interaction energy κ by determining the time it takes for an excitation to swap

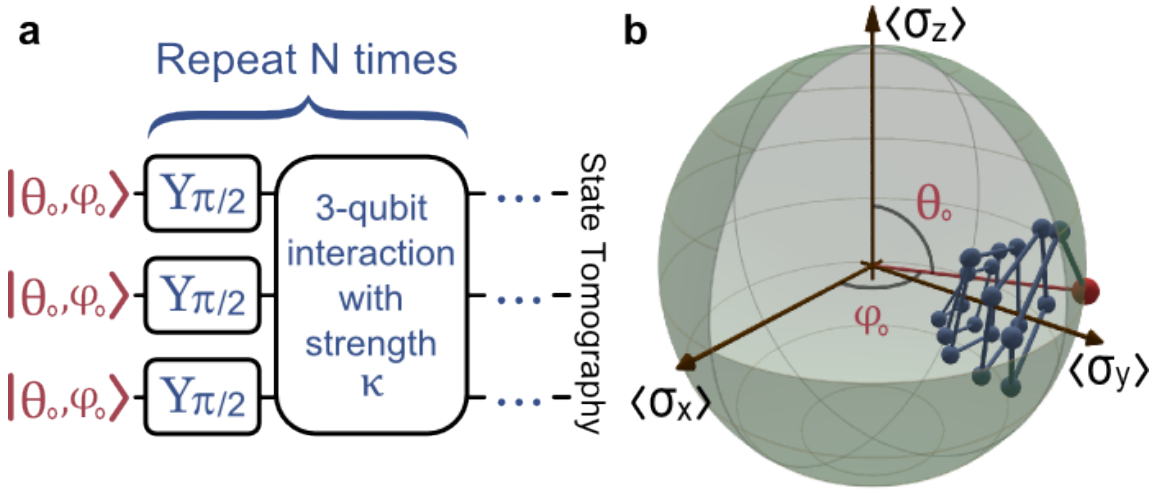

Figure 3.1: **Pulse sequence and the resulting quantum dynamics. a,** Pulse sequence showing first the initial state of the three qubits (Eq. 3.4) followed by the unitary operations for a single time step (Eq. 3.3). These operations are repeated N times before measurement. Single qubit rotations are generated using shaped-microwave pulses in 20 ns; the three-qubit interaction is generated using a tunable coupling circuit controlled using square pulses of length 5 ns for $\kappa = 0.5$ and 25 ns for $\kappa = 2.5$. **b,** The state of a single qubit is measured using state tomography and shown in a Bloch sphere. The initial state is shown in red with subsequent states shown in blue for $N = 1$ to 20.

between the qubits (see supplement).

The periodic nature of $\mathcal{H}$ allows us to write down the unitary evolution over one cycle as

$$U = e^{-i\frac{\kappa}{2j\hbar}J_z^2} e^{-i\frac{\pi}{2\hbar}J_y} \tag{3.3}$$

shown schematically in Fig. 3.1a. We begin by initializing each qubit in the state

$$|\theta_0, \varphi_0\rangle = \cos(\theta_0/2)\,|+\sigma_z\rangle + e^{-i\varphi_0}\sin(\theta_0/2)\,|-\sigma_z\rangle \tag{3.4}$$

where θ_0 and φ_0 are angles describing the orientation of the single qubit states. This state is known as a spin coherent state and is the most classical spin state in the sense of minimum uncertainty and zero entanglement. After preparing the initial state, we

rotate each qubit around the y-axis by an angle $\pi/2$. Next, we allow all of the qubits to interact with one another for a duration which sets the value of κ. We repeat these two steps N times and then tomographically reconstruct the resulting density matrix [138]. For details regarding the pulse sequence see supplementary information.

We visualize the evolution of the system by depicting the single-qubit state as a vector inside of a Bloch sphere, shown in Fig. 3.1b. Each Bloch vector is constructed by measuring the expectation values of the x, y, and z Pauli operators after evolving the system according to Eq. 3.3. As the dynamics are symmetric under qubit exchange, the qubits undergo nominally identical evolution and we plot the average behavior (see supplement). The chosen initial state is shown in red with the Bloch vector after subsequent steps shown in blue. After each step, there are two qualitative changes: a rotation and a change in the length. The orientation is analogous to the orientation of the classical spin. The change in length, however, describes entanglement amongst the qubits.

3.5 Entanglement and chaos

Entanglement can be characterized using the entanglement entropy S,

$$S = -\operatorname{Tr} \rho_{\mathrm{sq}} \log_2 (\rho_{\mathrm{sq}}) \tag{3.5}$$

where ρ_{sq} is the density matrix of a single qubit. Writing the trace as a sum reproduces the familiar definition of entropy $-\sum p_i \log (p_i)$, where p_i is the probability of being in the ith microstate. If the qubit is in a pure state, then the single-qubit state is completely known and the entropy is zero. However, if the qubits are entangled with one another,

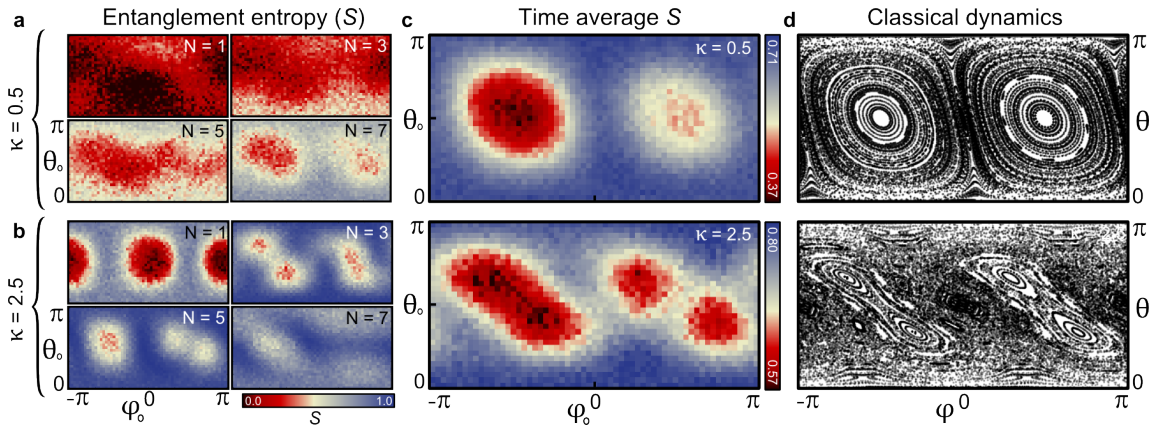

Figure 3.2: **Entanglement entropy and classical chaos. a,b,** The entanglement entropy (color) of a single qubit (see Eq. 3.5) averaged over qubits and mapped over a 31 x 61 grid of initial state, for various time steps N and two values of interaction strength κ. The entanglement entropy of a single qubit can range from 0 to 1. **c,** The entanglement entropy averaged over 20 steps for $\kappa = 0.5$ and over 10 steps for $\kappa = 2.5$; for both experiments the maximum pulse sequence is ≈ 500 ns. The left/right asymmetry is the result of experimental imperfections and is not present in numerical simulations (see supplement). **d,** A stroboscopic map of the classical dynamics is computed numerically and shown for comparison. The map is generated by randomly choosing 5,000 initial states, propagating each state forward using the classical equations of motion, and plotting the orientation of the state after each step as a point. We observe a clear connection between regions of chaotic behavior (classical) and high entanglement entropy (quantum).

then ρ_{sq} is a statistical mixture of states and the entropy is non-zero.

In Fig. 3.2a we show the entanglement entropy between a single qubit and the rest of the qubits at several instances in time. The entanglement entropy is measured by performing state tomography on the individual qubits [138] and then directly applying Eq. 3.5 to the reconstructed density matrix. In each panel we prepare various initial states $|\theta_0, \varphi_0\rangle$, evolve the system for N steps and plot the entanglement entropy; different panels correspond to different N. Initial states prepared close to the y-axis have low entropy (red) which remains low as the system evolves. States prepared farther away from the y-axis gain higher entropy (blue) given sufficient time. We perform the same set of experiments for stronger interaction, $\kappa = 2.5$, shown in Fig. 3.2b. At stronger interactions, the entropy increases rapidly and regions of low entropy are no longer isolated to near the y-axis.

In Fig. 3.2 a,b we see that the entropy fluctuates over time. In small quantum systems, there are fluctuations or revivals that vanish when the system size is taken to infinity (known as the thermodynamic limit). For finite systems, averaging the entropy over time is commonly used to estimate the equilibrium value approached by larger systems. In Fig. 3.2c we show the entanglement entropy averaged over time (N) for both values of interaction strength κ. The corresponding classical dynamics are shown in Fig. 3.2d. Note that the left-right asymmetry in Fig. 3.2c is not contained within the equations of motion and is the result of errors in the control signals.

We find a striking resemblance between the average entanglement in the quantum

system and chaotic dynamics in the classical limit. The regions of classical phase space where the dynamics are chaotic correspond to high entropy (blue) in the quantum system; regions that are classically regular correspond to low entropy (red), including bifurcation at large κ. The results shown in Fig. 3.2b have been predicted by recent theoretical works [98, 122]. The connection between chaos and entanglement has been of theoretical interest for quite some time [16, 107, 130]. However, these studies focused on very large systems near the border of quantum and classical physics [32, 31]. Here, we show that the results hold deep in the quantum limit. It is interesting to note that chaos and entanglement are each specific to their respective classical and quantum domains and any connection is counterintuitive. The correspondence is even more unexpected given that our system is so far from the classical limit [64, 23].

In Fig. 3.2b, the entanglement entropy in the blue regions approaches 0.8, close to the maximum attainable value of 1.0 for a single qubit. The value of 0.8 is very close to the value one would obtain by uniformly averaging over all states, 0.73 [145]. In Eq. 7.1, the Hamiltonian depends on time and, as a result, energy is not conserved. Therefore, statistical mechanics would predict the values of observables using an ensemble with maximum entropy or, equivalently, an infinite temperature ensemble. The observed density matrix approaching maximum entropy suggests that even small quantum systems undergoing unitary dynamics can appear to thermalize [167, 153, 162].

In the supplement, we numerically compute the evolution for larger systems and show that fluctuations decrease with increasing system size, as expected for finite-size systems

approaching thermal equilibrium. Additionally, we compute the behavior at larger values of κ and show that all initial states obtain near maximal entropy, as opposed to the mixed phase space shown in Fig. 3.2. This further supports the idea that what we see in the experiment is the onset of thermalization in a small quantum system.

3.6 Multiqubit correlations

The observed single-qubit entropy can originate from two sources: entanglement with the other qubits and entanglement with the environment (decoherence). In Fig. 3.3 we show that the contrast between high and low entropy results from entanglement amongst the qubits, confirming our assumption that the system is well isolated. In order to distinguish these two effects, we measure the three-qubit density matrix. Using these measurements, we compute the expectation values of all combinations of Pauli operators. The first nine columns in Fig. 3.3 contain operators only on a single qubit and thus provide information about local properties. The remaining columns contain products of two- and three-qubit operators and describe correlations between the qubits.

In the top panel we consider an initial state whose entropy has increased by the least amount (most red), shown inset. After ten time-steps, we see that each qubit is oriented along the y-axis as indicated by the first three peaks. The qubits pointing along the same direction leads to classical correlations, as indicated by the remaining peaks among the two- and three-qubit correlations. In the lower panel we consider an initial state whose entropy has increased by the largest amount (most blue). In addition

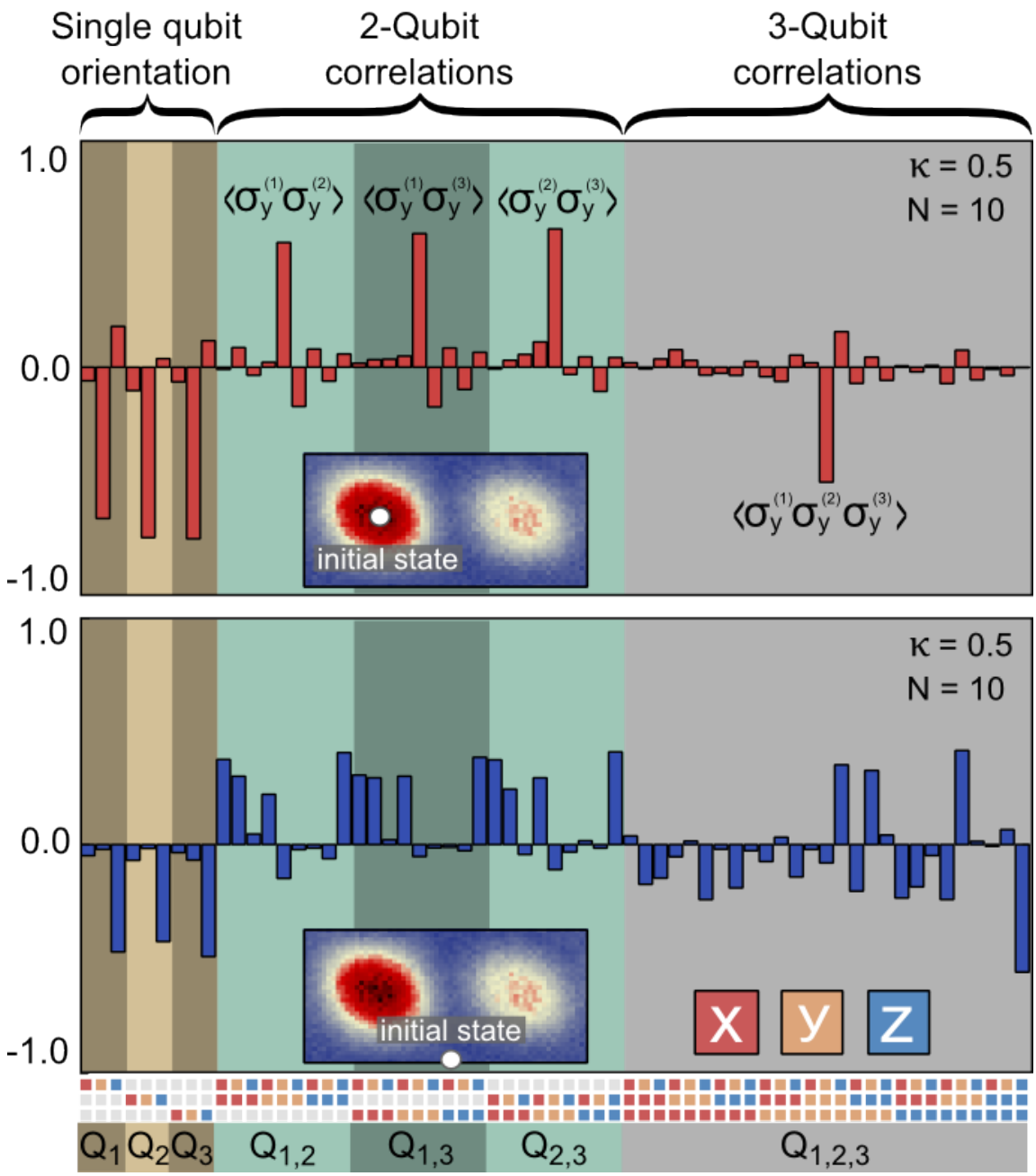

Figure 3.3: **Multi-qubit entanglement.** We represent the three-qubit density-matrix for two initial states shown inset, one where the entropy was low (top) and one where the entropy was high (bottom). In both cases, the initial state was evolved for N = 10 time-steps and $\kappa = 0.5$. Each bar indicates the expectation value of one possible combination of Pauli operators on the three qubits, the corresponding operator is shown using colored squares. The increase in multi-qubit correlations in the lower panel signifies that the contrast between high and low entropy is the result of entanglement.

to the qubit orientations and classical correlations, we also find many significant peaks among the multi-qubit correlations. These non-classical correlations are clear signatures of entanglement amongst the qubits. Additionally, we find that the three-qubit state purity, a measure of decoherence, is equal for both of these states, showing that the contrast between high and low entropy is entirely the result of inter-qubit entanglement (see supplement). This finding is in contrast to previous studies which found that, for initial states with high entropy, the system displayed a hypersensitivity to perturbations, such as environmental decoherence [37].

3.7 Ergodic dynamics

The advantage of studying statistical mechanics in a small quantum system is that we can directly check for ergodic motion in the three-qubit dynamics. Using measurements of the full multi-qubit density matrix, we investigate the connection between ergodic dynamics in the full system and entropy production in subsystems. Note that the full system is ideally in a pure state whose entropy is zero and stays zero as the system evolves - this is in stark contrast to subsystems which gain entropy over time through entanglement. While the full system cannot thermalize in the sense of reaching maximum entropy, it can undergo ergodic motion (time averages being equal to state-space averages). In statistical mechanics, a uniform average over states is given by the microcanonical ensemble. In Fig. 3.4 we plot the overlap of the time-averaged density matrix $\bar{\rho}$ with a microcanonical

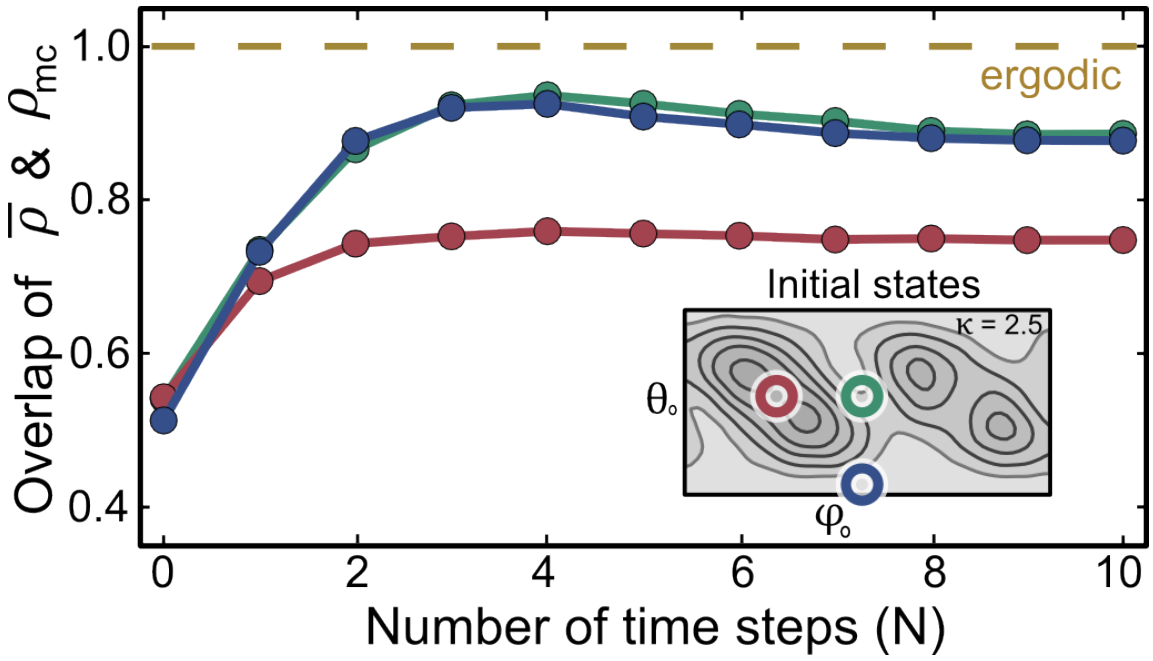

Figure 3.4: **Ergodic dynamics.** The overlap of the time-averaged three-qubit density matrix with a microcanonical ensemble (see Eq. 3.6) versus number of time steps N, for $\kappa = 2.5$. We choose three different initial states, shown inset. A value of 1.0 indicates that the dynamics are fully ergodic.

ensemble $\rho_{\rm mc}$, given by

$$\text{Overlap} = \text{Tr}\sqrt{\sqrt{\rho_{\rm mc}}\,\bar{\rho}\,\sqrt{\rho_{\rm mc}}} \tag{3.6}$$

Here $\rho_{\rm mc}$ is an 8-by-8 density matrix which attributes equal probability to all of the accessible states. The overlap of these two distributions approaching 1 would imply that time averages are equivalent to state-space averages for all measurable quantities.

We choose three different initial states: two are chosen from regions where subsystems had high entropy (blue & green) and one from a region that had low entropy (red). After just three steps, initial states where subsystems had high entropy approach a microcanonical ensemble to within 94%. Numerical simulations indicate that ideally the overlap plateaus at 98% - deviations from this ideal behavior are primarily due to deco-

herence. We find that initial states where subsystems had low entropy fail to approach a microcanonical ensemble. The strong overlap between time averages and state-space averages demonstrates that the three-qubit dynamics are ergodic and further supports the statistical mechanics framework for understanding the entropy production in single qubits.

Previous experiments have investigated the signatures of classical chaos in quantum systems [112, 37]. Here, using our ability to generate arbitrary product states, we establish a clear signature across the entire phase space. Our unique measurement capabilities allow us to go beyond previous works by directly connecting our observations to entanglement amongst the qubits, as opposed to environmental decoherence. Together, these tools allow us to demonstrate ergodic dynamics and show that superconducting qubits can be used to study fundamental concepts in statistical mechanics.

It is interesting to know the generality of our results as they could provide a generic framework for studying quantum dynamics. Numerical results suggest that ergodic behavior breaks down only when the evolution is highly constrained by conservation laws, such systems are referred to as integrable and represent models that are fine tuned and consequently rare [162]. Our choice of Hamiltonian was motivated by the lack of conserved quantities where only the total spin is conserved - not even energy is conserved. We believe that our simple and clear descriptions of thermalization merely lay the foundation upon which many fundamental questions in non-equilibrium thermodynamics can be experimentally investigated.

Chapter 4

Applications to topological phase transitions

4.1 Abstract

Topology, with its abstract mathematical constructs, often manifests itself in physics and plays a pivotal role in our understanding of natural phenomena. Notably, the discovery of topological phases in condensed matter systems has changed the modern conception of phases of matter [103, 180, 21, 71, 132]. The global nature of topological ordering, however, makes direct experimental probing an outstanding challenge. Present experimental tools are mainly indirect and as a result inadequate for studying the topology of physical systems at a fundamental level. Here, we employ the exquisite control afforded by state-of-the-art superconducting quantum circuits to investigate topological

properties of various quantum systems. The essence of our approach is to infer geometric curvature by measuring the deflection of quantum trajectories in the curved space of the Hamiltonian [63]. Topological properties are then revealed by integrating the curvature over closed surfaces, a quantum analog of the Gauss-Bonnet theorem. We benchmark our technique by investigating basic topological concepts of the celebrated Haldane model [68] after mapping the momentum-space of this condensed matter model to the parameter-space of a single qubit Hamiltonian. In addition to constructing the topological phase diagram, we are able to visualize the microscopic spin texture of the associated states and their evolution across a topological phase transition. Going beyond non-interacting systems, we demonstrate the power of our method by studying topology in an interacting quantum system. This required a new qubit architecture [59, 38] that allows for simultaneous control over every term in a two-qubit Hamiltonian. By exploring the parameter-space of this Hamiltonian, we discover the emergence of an interaction-induced topological phase. Our work establishes a powerful, generalizable experimental platform to study topological phenomena in quantum systems.

4.2 Introduction

Since the first observations of topological ordering in quantum Hall systems in the 1980s [103, 180], experimental studies of topological phases have mainly been performed with a limited number of primarily indirect measurement techniques. For instance, transport measurements are the predominant tool used to study the quantum Hall effect, where

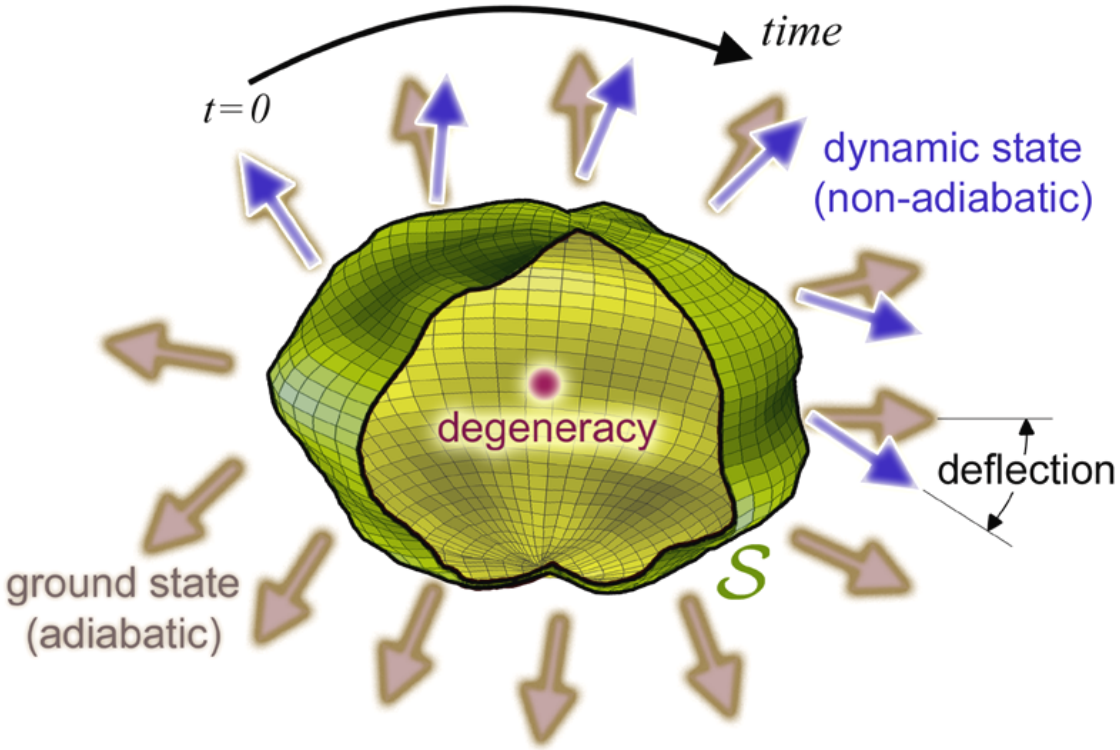

Figure 4.1: **Dynamical measurement of Berry curvature and $\mathcal{Ch}$.** In this schematic drawing, brown arrows represent the ground states (adiabatic limit) for given points on a closed manifold $\mathcal{S}$ (green enclosure, interrupted by an opening for the sake of illustration) in the Hamiltonian's parameter-space, and the blue arrows are the measured states during a non-adiabatic passage. According to (4.2), the Berry curvature $\mathbf{B}$ can be calculated from the deviation from adiabaticity. Integrating $\mathbf{B}$ over $\mathcal{S}$ gives the Chern number $\mathcal{Ch}$, which corresponds to the total number of degeneracies enclosed.

interpretations [177] are required to infer topological properties from the measurements. Consequently, topological studies in quantum systems where transport measurements cannot be carried out have remained elusive.

In principle, topological properties can be explored in *any* quantum system where the Hamiltonian can be written in terms of a set of parameters. Topological phases are characterized by topological invariants, such as the first Chern number $\mathcal{C}\hbar$, whose discrete jumps indicate transitions between different topologically ordered phases [186, 20]. For a quantum system, $\mathcal{C}\hbar$ is defined as the integral over a closed manifold $\mathcal{S}$ in the parameter-space of the Hamiltonian as

$$\mathcal{C}\hbar \equiv \frac{1}{2\pi} \oint_{\mathcal{S}} \mathbf{B} \cdot dS, \tag{4.1}$$

where $\mathbf{B}$ is the vector form of the Berry curvature [22]. As illustrated in Fig. 1 and shown in the supplementary information, $\mathbf{B}$ can be viewed as an effective magnetic field with points of ground state degeneracy acting as its sources, i.e., magnetic monopoles [187]. Using Gauss's law for the Berry curvature (magnetic field), $\mathcal{C}\hbar$ simply counts the number of degenerate energy eigenvalues (magnetic monopoles) enclosed by the parameter manifold $\mathcal{S}$. $\mathcal{C}\hbar$, which is invariant under perturbations to the shape of $\mathcal{S}$, is a topological number that reflects a property of the manifold of states as a whole and not a local property of parameter-space.

In previous works, topological properties of highly symmetric quantum systems have been measured [137, 111, 11]. However, since these earlier studies relied on interference, these methods are not readily generalizable. To circumvent this, Gritsev *et al.* [63] pro-

posed a general method to directly measure the local Berry curvature. The underlying physics of their idea is that motion in a curved space will be deflected from a straight trajectory; in other words, curvature reveals itself as an effective force, analogous to a charged particle moving in a magnetic field experiencing the well-known Lorentz force. Similarly, Gritsev *et al.* showed that in a region of the parameter-space with Berry curvature $\mathbf{B}$, if we "move" a quantum system by changing a parameter of its Hamiltonian with rate $|\mathbf{v}|$, then the state of the system feels a force $\mathbf{F}$ given by

$$\mathbf{F} \propto \mathbf{v} \times \mathbf{B} + \mathbf{O}(\mathbf{v^2}). \tag{4.2}$$

This force leads to deviations of the trajectory from the adiabatic path, which can be detected through measurements of the observables of the system (Fig. 1). As long as the ramping of parameters is done slowly, but not necessarily adiabatically, the deviation is directly proportional to $\mathbf{B}$. Since the adiabatic limit is generally hard to achieve, this relation has the important advantage of needing only a moderately slow change of state and only requires that the linear term dominates the response.

Direct measurement of $\mathbf{B}$ provides an alternative means to study topological phases that differs significantly from conventional approaches. In condensed matter systems an instantaneous realization of the entire phase space manifold, such as the Fermi surface, is required. In our approach, the local curvature of the space is dynamically "sensed" and topological invariants, such as $\mathcal{C}\hbar$, are inferred by integrating these measurements. Implementing this dynamical procedure requires the ability to continuously change the system Hamiltonian. In fully controllable quantum systems, where this can be achieved,

this method provides a powerful means to probe topological properties.

4.3 Measuring the Chern number

To elucidate this dynamical method, we demonstrate a basic implementation in quantum circuits with superconducting qubits [124, 78, 35]. The quantum state of a single qubit [17] is equivalent to a spin-1/2 particle in a magnetic field. Its Hamiltonian in the rotating frame can be written as

$$\mathcal{H}_S = -\frac{\hbar}{2}\mathbf{H}\cdot\boldsymbol{\sigma}, \tag{4.3}$$

where $\boldsymbol{\sigma} = (\sigma^x, \sigma^y, \sigma^z)$ are the Pauli matrices, and $\mathbf{H} = (H_X, H_Y, H_Z)$ is analogous to a control magnetic field. Full control over the parameters of this Hamiltonian is achieved by microwave pulses that control H_X and H_Y, and an applied flux through the qubit's SQUID loop which controls H_Z. We measure $\mathcal{C}\hbar$ for spherical ground state manifolds in $\mathbf{H}$-parameter-space (Fig. 2). We use θ and ϕ as spherical coordinates and consider the parameter trajectory that starts at the north pole at $t = 0$ and ramps along the $\phi = 0$ meridian ($H_Y = 0$) with constant velocity $v_\theta = d\theta/dt$ until it reaches the south pole at $t = T_f$. To realize motion on a spherical manifold, the control sequences of H_Z and H_X are chosen such that the control magnitude $|\mathbf{H}| = H_r$ is constant. In the adiabatic limit, the wavefunction would remain in the instantaneous ground state of $\mathcal{H}_S$, i.e. the $\phi = 0$ meridian on the Bloch sphere. For non-adiabatic ramps, instead, a deviation from the meridian is observed, as shown in Fig. 2(b). Here the Bloch vector is measured at each point in time by interrupting the ramp and performing state tomography. Note that this

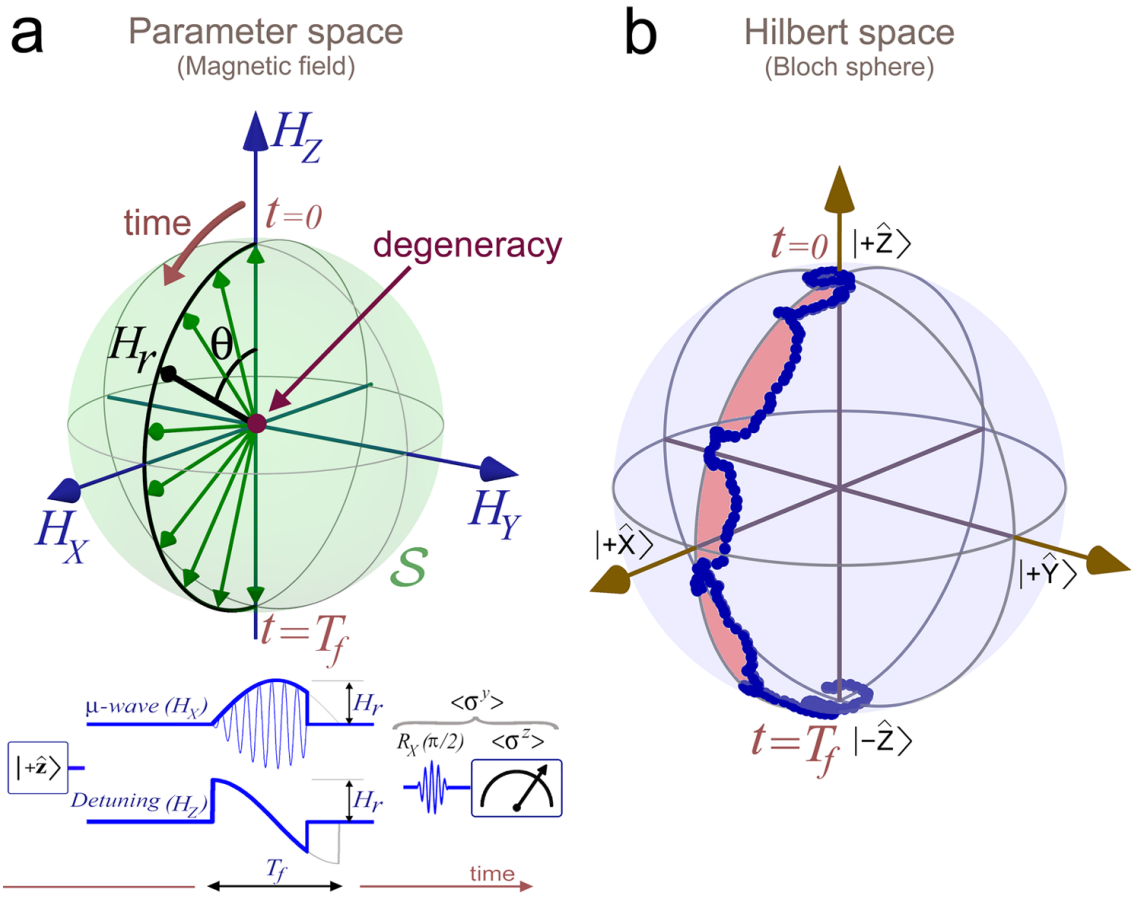

Figure 4.2: **Dynamical measurement of $\mathcal{CH}$. a.** A simultaneous microwave pulse $H_X(t) = H_r \sin(\pi t/T_f)$ and detuning pulse $H_Z(t) = H_r \cos(\pi t/T_f)$ are applied to construct a parameter-space trajectory. The pulse sequence results in a parameter-space motion along the $\phi = 0$ meridian ($H_Y = 0$ plane) on $\mathcal{S}$. **b.** The state of the qubit during this ramp ($H_r/2\pi = 10$ MHz and $T_f = 600$ ns) is determined using tomography, and shown (blue dots) on the surface of the Bloch sphere.

deviation is not due to noise, but rather is the expected non-adiabatic response due to local Berry curvature. For this trajectory, the force $\mathbf{F}$ takes the form $f_\phi = \frac{\hbar}{2} H_r \langle \sigma^y \rangle \sin\theta$, and integrating over the resulting deflection (shaded light red in Fig. 2(b)) gives $\mathcal{C}\hbar = 1 \pm 0.05$. Given the symmetry of this Hamiltonian, a line integral is sufficient for measuring the surface integral of $\mathcal{C}\hbar$ [170, 189]. A value of unity is expected, as the qubit ground state has a degeneracy at $\mathbf{H} = 0$, corresponding to a single monopole enclosed by the parameter sphere $\mathcal{S}$. We demonstrate the robustness of $\mathcal{C}\hbar$ by deforming the surface manifold $\mathcal{S}$ in the supplementary information.

4.4 The Haldane phase

The generality of our approach allows us to connect our measurements to certain condensed matter systems and their core topological features, such as topological phase transitions and the geometric winding of state vectors. This can be done by establishing a mapping from the real or momentum-space of the model condensed matter system to the parameter-space of the controllable quantum circuit. We choose what is perhaps the simplest theoretical model of topological behavior, the Haldane model [68], to benchmark our approach. This model serves as a foundation for other topological insulator models [21, 71, 132]. To show that the quantum Hall effect could be achieved without a global magnetic field, Haldane introduced a non-interacting Hamiltonian [68] given by

$$\mathcal{H}_G(k_x, k_y) = \hbar v_F (k_x \sigma^x + k_y \sigma^y) + (m_0 - m_t)\sigma^z, \tag{4.4}$$

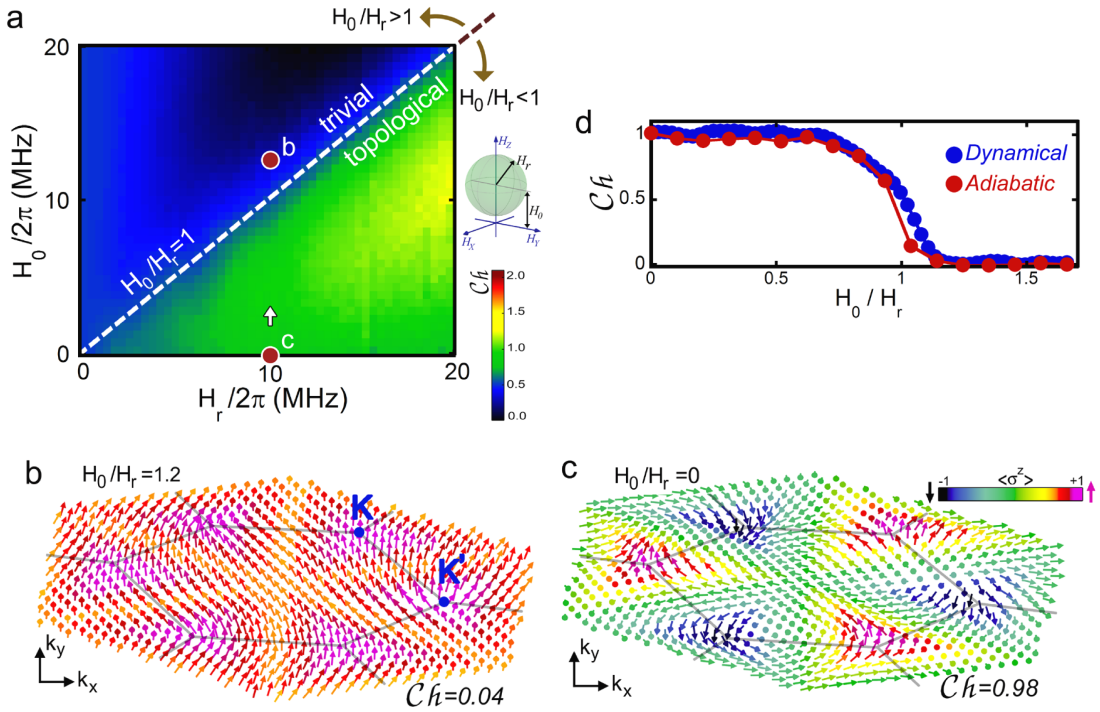

Figure 4.3: **Dynamic measurement of the topological phase diagram and adiabatic visualization of phases. a.** Dynamical determination of the phase diagram. First $\langle\sigma^y\rangle$ was measured during ramps similar to those in Fig 2(a), and then $\mathcal{C}\hbar$ was calculated. The dashed line is the expected phase boundary at $H_0 = H_r$. The ramp speed was $T_f = 1000\,\text{ns}$. **b**,**c.** With adiabatic state preparation, the state of the qubit was prepared and measured over a grid on the surface of the parameter sphere and then mapped to the hexagonal momentum-space plane. The ground states are presented as Bloch vectors, whose colors indicate their $\langle\sigma^z\rangle$ values. $H_0/H_r = 1.2$ for **b** and $H_0/H_r = 0$ for **c**. The gray lines show the FBZ of the honeycomb lattice and high symmetry points **K** and **K′** are marked. Each adiabatic sequence took $T_f = 1000\,\text{ns}$. **d.** The measured $\mathcal{C}\hbar$ from the adiabatic and dynamical (white arrow in **a**) methods are plotted vs. H_0/H_r.

where m_0 is the effective mass, and m_t corresponds to a second-neighbor hopping in a local magnetic field. The key prediction of the Haldane model is that if $m_0/m_t > 1$ the system is in a trivial insulating phase, and otherwise in a topological phase. Using a confocal mapping (supplementary information) one can recast Eq. (C.1) into the single-qubit Hamiltonian (C.32). If we consider spherical manifolds $\mathcal{S}$ of radius H_r displaced from the origin in the z direction by H_0 , then H_0/H_r in the qubit system plays the same role as m_0/m_t in the Haldane model.

In Fig. 3(a) we plot the results of this measurement, showing $\mathcal{C}\hbar$ as a function of H_r and H_0, which shows plateaus at values 0 and 1 separated by a phase transition boundary line at $H_r = H_0$. This transition can be easily understood: when $H_0 < H_r$ the degeneracy at $\mathbf{H} = 0$ lies within $\mathcal{S}$ giving $\mathcal{C}\hbar = 1$, whereas for $H_0 > H_r$ it lies outside $\mathcal{S}$ giving $\mathcal{C}\hbar = 0$.

In Haldane model, the topological and trivial phase each has its own signature spin texture in momentum space. Microscopic structure of these phases can be revealed by the conventional adiabatic method. We again consider spherical surfaces $\mathcal{S}$ and adiabatically ramp the control parameters to their final values on $\mathcal{S}$. The resulting Bloch vectors are then tomographically measured. With a confocal mapping (see supplementary information), $\mathcal{S}$ can be mapped to the first Brillouin zone (FBZ) of the honeycomb lattice. Therefore, the adiabatically measured ground state vectors on $\mathcal{S}$ can be depicted in the FBZ. Fig. 3(b) and (c) show the results for two manifolds with $H_0/H_r = 1.2$ and 0, corresponding to trivial and topological phases, respectively. By following the orientation

of the state-vector along any path starting at $\mathbf{K}$ and moving to $\mathbf{K}'$ (corners of the FBZ) and back to $\mathbf{K}$ one can see that in the topological case the state vector wraps around and makes one full rotation, while in the trivial case it only tilts away from vertical and then returns, without completing a rotation. These spin texture maps can also be used to extract local Berry curvature. As shown in Fig. 3(d), the resulting $\mathcal{C}\hbar$ from this adiabatic method shows good agreement with the dynamical method of measurement.

4.5 Interaction driven topological phase

Some of the most fascinating topological phenomena in quantum systems emerge in the presence of interaction. Compared to non-interacting systems, interactions impose a greater experimental challenge in studying topological properties. Nevertheless, the method outlined here stands out in its ability to provide insight into the topology of such systems. To illustrate this, we consider the most basic unit of interaction and measure $\mathcal{C}\hbar$ in a coupled two-qubit system. One significant experimental challenge here is the need for full control over the entire parameter-space of the Hamiltonian. Here we achieve this by using a new design for our superconducting qubits, which includes the ability to continuously vary the inter-qubit coupling strength g [59, 38]. The Hamiltonian of this system in a frame rotating with the qubits is given by

$$\mathcal{H}_{2Q} = -\frac{\hbar}{2}[H_0\sigma_1^z + \mathbf{H_1}\cdot\boldsymbol{\sigma_1} + \mathbf{H_2}\cdot\boldsymbol{\sigma_2} - g(\sigma_1^x\sigma_2^x + \sigma_1^y\sigma_2^y)], \tag{4.5}$$

where 1 and 2 refer to qubit 1 (Q1) and qubit 2 (Q2) respectively, and the biasing field H_0 is now only applied to Q1. In this design, we can access all regions of the 7-dimensional

parameter-space of this Hamiltonian.

We explore spherical manifolds with fixed $(H_0, |\mathbf{H_1}|, |\mathbf{H_2}|, g)$, analogous to the single-qubit experiment. We perform experiments where both $\mathbf{H_1} = \mathbf{H_2} = \mathbf{H_r}$ are ramped simultaneously with magnitude $|\mathbf{H_r}| = H_r$ (supplementary information). The measured $\mathcal{CH}$ is shown in Fig. 4(b) and (c) for three distinct cuts though this parameter-space.

We begin in panel (b) by exploring the simplest case, $g = 0$, where the qubits behave independently and the physics can be understood using the single qubit results. Since only Q1 is subject to H_0, its $\mathcal{CH}$ changes by 1 through the transition $H_0 = H_r$. In contrast, in the absence of a biasing field, $\mathcal{CH}$ of Q2 remains equal to 1. As the qubits are independent, the $\mathcal{CH}$ of the system is simply the summation of the individual $\mathcal{CH}$, leading to two phases with $\mathcal{CH} = 1$ and $\mathcal{CH} = 2$.

With the non-interacting limit of our system understood, we now focus on the effects of interaction by examining regions of parameter-space where $g \neq 0$. Considering manifolds with constant $g/2\pi = 4\,\mathrm{MHz}$, we observe a new phase with $\mathcal{CH} = 0$ (blue) when $H_r \lesssim g$, as shown in Fig. 4(b). To gain more insight into this new phase, we continuously vary g and examine the evolution of the $\mathcal{CH} = 0$ region. As shown in Fig. 4(c), this phase appears when $g \approx H_r$, and monotonically expands as g increases. These observations and the fact that this phase is absent when $g = 0$ indicate that the $\mathcal{CH} = 0$ phase is indeed driven by interaction.

In certain limits, the three phases could approximately be characterized by the dominance of the global field ($\mathcal{CH} = 2$), of local fields (disorder) ($\mathcal{CH} = 1$), and of interaction

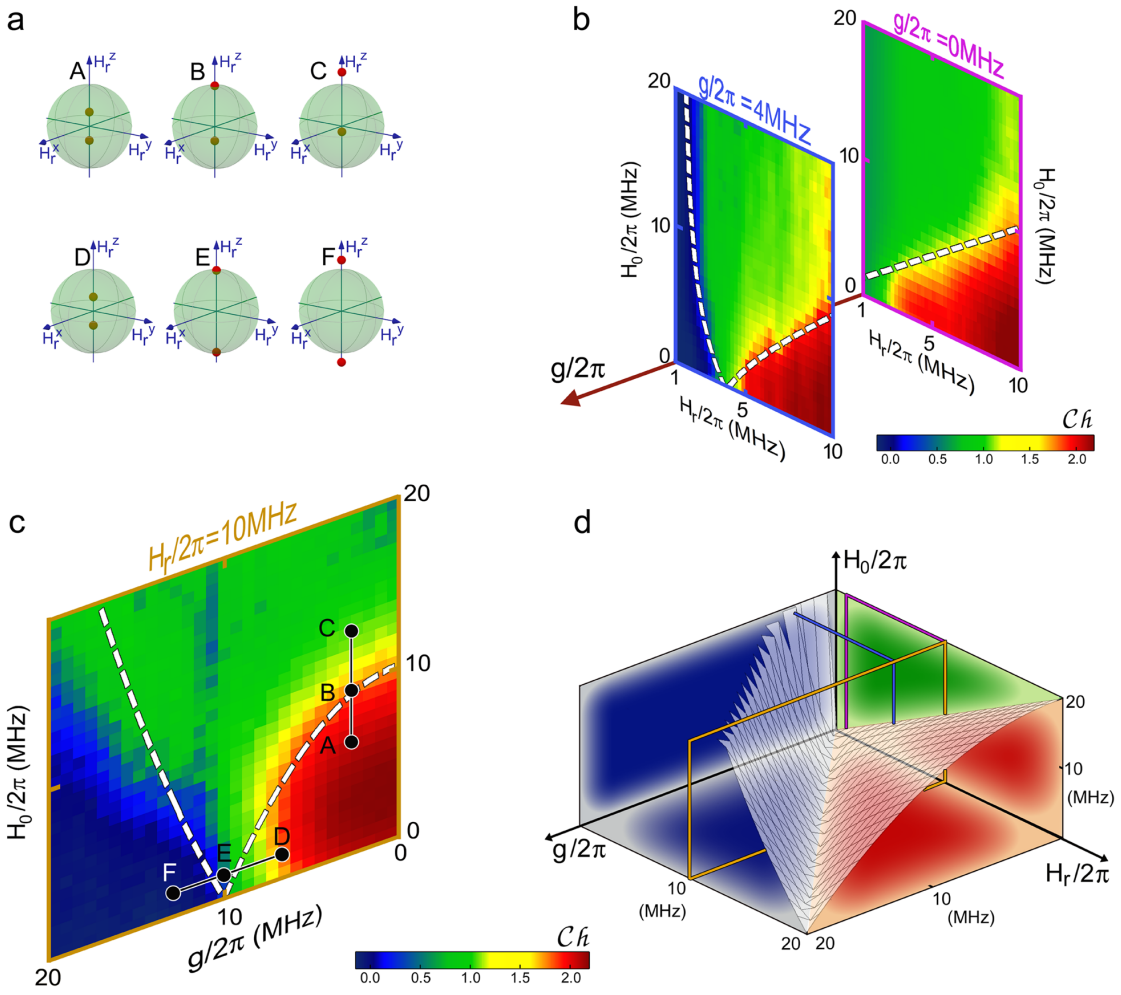

Figure 4.4: **Topological phase diagram of an interacting system. b,c.** The topological phase diagram of Eq. (4.5). In panel **b**, $\mathcal{C}\hbar$ was measured for two fixed $g/2\pi$ values of 0 and 4 MHz. In panel **c**, $\mathcal{C}\hbar$ was measured for fixed $H_r/2\pi$ =10 MHz. Dashed lines are topological transitions calculated analytically. **d.** The analytically calculated phase diagram showing three distinct $\mathcal{C}\hbar$ volumes and the separatrix plane. The phase diagram cuts in **b, c** are indicated by colored slices. **a.** The position of the monopoles in H-space are also shown for the points A through F shown in panel **c**, with a spherical manifold of radius $H_r/2\pi = 10$ MHz.

($\mathcal{C}\hbar = 0$). Interestingly, they also show some signature entanglement entropies (see supplementary information). The linear entropy of the states, averaged over the manifold, qualitatively hints toward a similar phase diagram in certain regions, where the phase with lowest $\mathcal{C}\hbar$ appears when the highest entanglement allowed in the system has been reached. However, since $\mathcal{C}\hbar$ is a global property, information about it cannot be deduced by the nature of any single ground state. While the interplay of fields and interactions provides hints to anticipate the various topological phases in this system, they are incapable of capturing the entire underlying physics that leads to quantized $\mathcal{C}\hbar$ values. Therefore, by reflecting topological attributes of the system, $\mathcal{C}\hbar$ remains distinct and irreplaceable.

As the analogy with the Gauss's law suggests, a concrete understanding of the phases can be obtained by considering how the singularities of the system move in the parameter-space. Given the relatively small size of the Hilbert space, analytic solutions can be obtained and the phase diagram can be predicted by calculating when points with degenerate ground states cross the spherical manifold. The points of ground state degeneracy are located on the z-axis of the $\mathbf{H_r}$-space. Sub-figures A, B and C in panel (a) correspond to the dots on Fig. 4(c), where g is small. In this limit, H_0 affects only one qubit, and increasing it moves only one monopole past the surface (C). For D, E, and F where instead H_0 is small, increasing g furthers the monopole separation, eventually moving both monopoles outside the surface (F). The result of a full analytical study are plotted in Fig. 4(d) which shows three distinct regions and their phase boundaries. There is a

direct 0 to 2 transition when $H_0 = 0$, but at finite values the system first goes through the green $\mathcal{C}\hbar = 1$ region. This latter behavior is seen in Fig. 4(c). The dashed lines in panels (b) and (c) are from this analytic solution, which uses no free parameters, and are in good agreement with the measurements. The deviations are mainly systematic errors, due to crosstalk between simultaneous control pulses.

The generality of our method is aligned with Feynman's original idea of quantum simulation [54], where a controllable quantum system is used to investigate otherwise inaccessible quantum phenomena. In the absence of other experimental approaches, the full controllability of our superconducting circuits will provide a unique platform for the exploration of topological phases of more complex quantum systems, perhaps most notably interacting spin systems where tantalizing evidence for fractionalization has been found [63]. Larger spin systems have smaller energy gaps, and longer ramps will be needed to remain close to the ground state manifold. A path forward is therefore to improve coherence in multi-qubit systems, research which is currently underway.

Chapter 5

Applications to fractional quantum hall

5.1 Abstract

The intriguing many-body phases of quantum matter arise from the interplay of particle interactions, spatial symmetries, and external fields [45]. Generating these phases in an engineered system could provide deeper insight into their nature and the potential for harnessing their unique properties [35, 44, 26, 10, 78, 60]. However, concurrently bringing together the main ingredients for realizing many-body phenomena in a single experimental platform is a major challenge. Using superconducting qubits, we simultaneously realize synthetic magnetic fields and strong particle interactions, which are among the essential elements for studying quantum magnetism and fractional quantum Hall (FQH)

phenomena [180, 110]. The artificial magnetic fields are synthesized by sinusoidally modulating the qubit couplings. In a closed loop formed by the three qubits, we observe the directional circulation of photons, a signature of broken time-reversal symmetry. We demonstrate strong interactions via the creation of photon-vacancies, or "holes", which circulate in the opposite direction. The combination of these key elements results in chiral groundstate currents, the first direct measurement of persistent currents in low-lying eigenstates of strongly interacting bosons. The observation of chiral currents at such a small scale is interesting and suggests that the rich many-body physics could survive to smaller scales. We also motivate the feasibility of creating FQH states with near future superconducting technologies. Our work introduces an experimental platform for engineering quantum phases of strongly interacting photons and highlight a path toward realization of bosonic FQH states.

5.2 Introduction

It is commonly observed that when the number of particles in a system increases, complex phases can emerge which were absent in the system when it had fewer particles, i.e. the "more is different" [9]. This observation drives experimental efforts in synthetic quantum systems, where the primary goal is to engineer and utilize these emerging phases. However, it has generally been overlooked that these sought-after phases can only emerge from simultaneous realization and control of particle numbers, real-space arrangements, external fields, particle interactions, state preparation, and quantum measurement. The

simultaneous realization of all these ingredients makes synthesizing many-body phases a holistic task, and hence constitutes a major experimental challenge. Engineering these factors, in particular synthesizing magnetic fields, have been performed in several platforms [26, 114, 131, 6, 88, 67, 160, 119, 181, 140]. However, these ingredients have not been jointly realized in any system thus far. To provide a tangible framework, we discuss realization of these key elements in the context of quantum Hall physics, and show when these ingredients come together they can construct a basic building block for creating FQH states.

The FQH states are commonly studied in 2-dimensional electron gases, a fermionic condensed matter system [180, 110]. However, many of the recent advancements in engineered quantum systems are taking place in bosonic platforms [60, 26, 44, 10, 78, 35]. Theoretical studies suggest the existence of rich phases for bosonic FQH systems, similar to their femionic counterparts [148, 41, 73, 151, 66]. In particular, bosonic FQH states are known to host non-Abelian anyons, which could implement quantum logic operations through braiding [136]. Among the prerequisites for realizing bosonic FQH states are (i) strong artificial gauge fields, leading to nearly flat single particle bands, (ii) strong interactions, (iii) low disorder, and (iv) a mechanism for accessing the many-body ground state. In this work, we engineer a modular unit cell consisting of three coupled qubits in a ring, which when tiled can be used to realize FQH phases (Fig. 1**(a)** and **(b)**) [85, 93]. We concurrently demonstrate tunable gauge fields, strong interactions, and adiabatic groundstate preparation in a low loss and disorder platform, where we have full state

preparation and quantum correlation measurement capabilities.

5.3 Synthesizing an artificial gauge field

When electrons hop between lattice sites of a crystal placed in a magnetic field, the wavefunction accumulates a path-dependent phase. The interference of electrons traveling along different paths is the fundamental origin of many rich many-body phases seen in correlated systems. However, due to the charge neutrality of photons, they are not affected by physical magnetic fields; therefore, an effective magnetic field has to be synthesized for quantum platforms with bosonic excitations [87, 26, 114, 72, 131, 6, 88, 105, 142]. One practical idea, proposed in various settings, suggests that artificial magnetic fields can be created by periodic modulation of the photon hopping strength between the lattice sites [52, 91, 66]. When the on-site energies of two lattice sites differ by Δ, then sinusoidal modulation of a tunneling term with frequency Δ and phase φ results in an effective complex hopping, where the photon's wavefunction picks up phase φ (Fig. 1**(c)**). This phase is analogous to the Peierls phase $e \oint \mathbf{A} \cdot d\mathbf{r}$ that is accumulated by a particle of charge e tunneling in an external magnetic vector potential $\mathbf{A}$. This idea can be implemented in a superconducting qubit platform, where qubits play the role of the lattice sites and modulating the strength of the inter-qubit couplings g sets the microwave photon hopping rate.

We place three transmon superconducting qubits in a ring (Fig. 1**(b)**), where each qubit is coupled to its neighbors via an adjustable coupler that can be dynamically

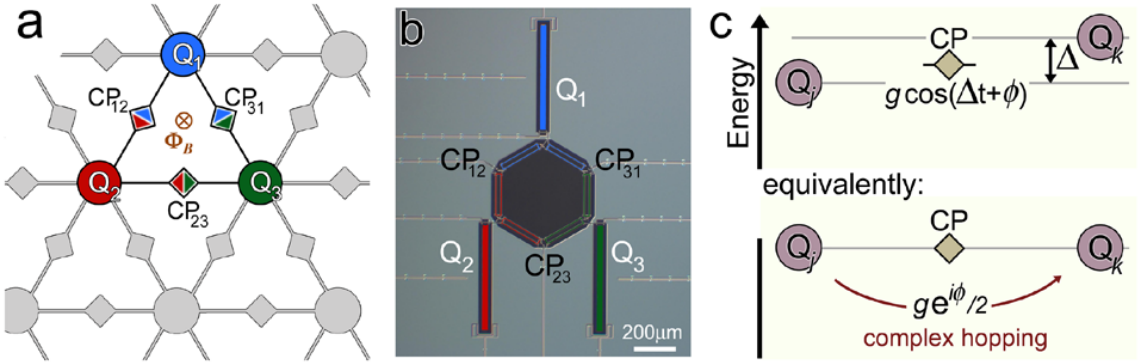

Figure 5.1: **The unit cell for FQH and synthesizing magnetic fields.** **(a)** A schematic illustration of how qubits and their couplers can be tiled to create a 2D lattice. The 3-qubit unit cell of this lattice, which is realized in this work, is highlighted. **(b)** An optical image of the superconducting circuit made by standard nano-fabrication techniques. It consist of three superconducting qubits Q_j connected via adjustable couplers CP_{jk}. Together, they form a triangular closed loop. **(c)** A parametric modulation approach is used for synthesizing magnetic fields. If the frequency difference of two qubits is Δ, then the sinusoidal modulation of the coupler connecting them with frequency Δ and phase φ results in an effective resonance hopping ($\Delta = 0$) with a complex hopping amplitude between the two qubits.

modulated on nano-second timescales [38]. The Hamiltonian of the system is

$$H(t) = \hbar \sum_{j=1}^{3} \omega_j (\hat{n} + 1/2) + \hbar \sum_{j,k} g_{jk}(t)(a_j^\dagger a_k + a_j a_k^\dagger) + H_{\text{int}}, \tag{5.1}$$

where $a^\dagger(a)$ are bosonic creation (annihilation) operators, ω_j is frequency of qubit Q_j, $\hat{n} = a_j^\dagger a_j$ is the particle number operator, and g_{jk} is the strength of the inter-qubit coupling between qubits Q_j and Q_k. H_{int} captures the interaction between bosons and is set by the non-linearity of the qubits. This term does not affect the dynamics in the single-photon manifold, and we will discuss its role in the two-photon manifold in more detail later. We modulate g of each coupler according to $g_{jk}(t) = g_0 \cos(\Delta_{jk} t + \varphi_{jk})$, and choose Δ_{jk} to be the difference between the frequencies of the two qubits that the coupler connects, i.e. $\Delta_{jk} = \omega_j - \omega_k$ (Fig. 2**(b)**). If $|g_{jk}| << |\omega_j - \omega_k|$, then, in the rotating

frame, the effective Hamiltonian of the system becomes

$$H_{\text{eff}}(\Phi_B) = \frac{\hbar}{2}\sum_{j,k} g_0(e^{i\varphi_{jk}}a_j^\dagger a_k + e^{-i\varphi_{jk}}a_j a_k^\dagger), \tag{5.2}$$

where $\Phi_B \equiv \varphi_{12} + \varphi_{23} + \varphi_{31}$ is the effective magnetic flux and is gauge-invariant (see supplement). One can intuitively understand the origin of the gauge invariance of Φ_B by noting that the three qubits in our case form a closed loop, and the accumulated phase needs to be single-valued when going around this loop. In other words, if the qubits' loop were open, Φ_B would not be gauge-invariant (see supplement for details).

5.4 Time-reversal symmetry breaking

Based on this idea, we construct a protocol (Fig. 2**(b)**) and study the dynamics of single microwave photons in our system. At $t = 0$, we create a microwave-photon which occupies Q_1 ($\psi_0 = |100\rangle$), and measure P_{Q_j}, the photon occupation probability of Q_j, as a function of time. As shown in the middle panel of Fig. 2**(c)**, the photon has a symmetric evolution for $\Phi_B = 0$. It propagates from Q_1 to Q_3 and Q_2 simultaneously, then back to Q_1, and then repeats the pattern with no indication of any preferred circulation direction (blue $\rightarrow$ $\begin{matrix}\text{red}\\ \text{green}\end{matrix}$ $\rightarrow$ blue $\rightarrow$ ...). Setting $\Phi_B = \pi/2$ leads to fundamentally different dynamics, where the photon propogation shows a preferred circulation direction and marches in a clockwise order from Q_1, to Q_3, to Q_2, eventually back to Q_1, and then repeating the pattern (blue $\rightarrow$ green $\rightarrow$ red $\rightarrow$ blue $\rightarrow$ ...). Choosing $\Phi_B = -\pi/2$ leads to counter-clockwise circulation, demonstrating that the synthetic flux Φ_B behaves quite similarly to physical magnetic flux (see supplement).

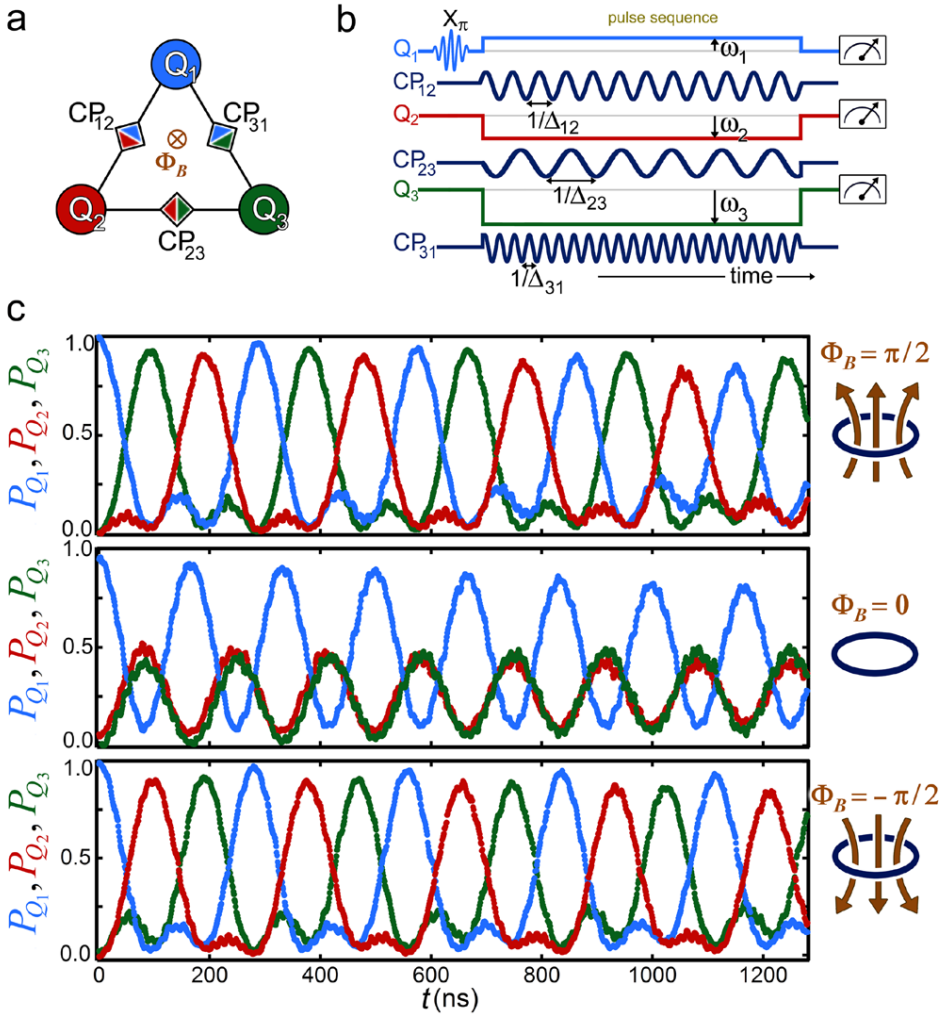

Figure 5.2: **Single-photon circulation resulting from the TRS breaking. (a)** Schematic of the three qubits and their couplers placed in a triangular closed loop.**(b)** The pulse sequence used for generating and circulating a microwave photon shows that qubits frequencies ω_j can be chosen to have arbitrary values, but each coupler is needed to modulate with frequency Δ_{jk}, set to the difference in the qubit frequencies that it connects $\omega_j - \omega_k$. The periodic modulation of each coupler can also has a phase φ_{jk}, where $\Phi_B \equiv \varphi_{12} + \varphi_{23} + \varphi_{31}$. **(c)** A microwave photon is created by applying a π-pulse to Q_1, at $t = 0$ ($\psi_0 = |100\rangle$). While applying the pulse sequence shown in **(b)**, the probability of photon occupying each qubit P_{Q_j} as a function of time is measured for three values of $\Phi_B = \pi/2, 0, -\pi/2$. We use $g_0 = 4\,\mathrm{MHz}$, $\omega_1 = 5.8\,\mathrm{GHz}$, $\omega_2 = 5.8\,\mathrm{GHz}$, $\omega_3 = 5.835\,\mathrm{GHz}$, $\Delta_{12} = 0$, $\Delta_{23} = 35\,\mathrm{MHz}$,$\Delta_{31} = 35\,\mathrm{MHz}$, $\varphi_{12} = 0$, $\varphi_{23} = 0$, and φ_{31} was used to set Φ_B.

The hallmark of magnetic fields in a system is the breaking of time reversal symmetry (TRS). Commonly, TRS preserving evolution of the state is defined as $\psi(t) = \psi(-t)$. Verifying TRS breaking based on this relation in a real experiment can be difficult, since reversing the flow of time is generally not feasible. However, the dynamics considered here is periodic with period $T = 280\,\text{ns}$ for $\Phi_B = \pm\pi/2$ and $T = 170\,\text{ns}$ for $\Phi_B = 0$ case. This periodicity allows us to arrive at a practical definition for TRS, which is $\psi(t) = \psi(T - t)$; e.g., one could follow the evolution of state from $t = T$ backward and see if it is the same as going forward from $t = 0$. It can be seen in Fig. 2**(c)** that TRS is preserved for $\Phi_B = 0$ and is broken when $\Phi_B = \pm\pi/2$. These observations establish TRS breaking for $\Phi_B = \pm\pi/2$ and further illustrate that the synthetic flux Φ_B indeed behaves akin to physical magnetic flux. The quantum nature of the circulation is manifested through quantum correlation measurements which show entanglement between qubits(see supplement for data). The measured entanglement makes our experiment distinct from others which are based on classical wave mechanics or those where the time-scales are much longer than the quantum coherence of the system, i.e. are in semi-classical limit [52, 53, 51, 95, 67, 159, 185, 160, 97, 119, 181, 140].

5.5 Interacting photons

We next focus on signatures of strong interactions, which are vital for realizing FQH states, as the many-body gap is set by the smaller of g and U. The typical weakness of interactions between bosons makes studying many-body quantum phenomena a major

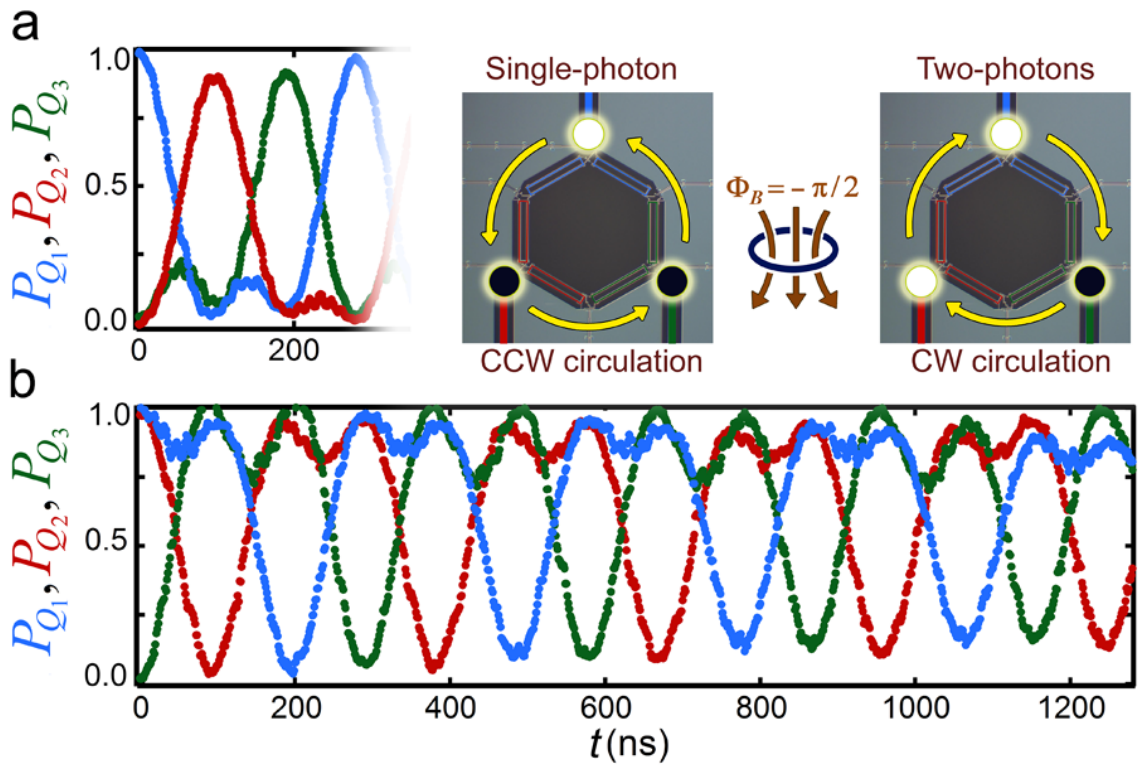

Figure 5.3: **Signature of strong interaction.** **(a)** The single-photon circulation data for $\Phi_B = -\pi/2$, which is shown in Fig. 2**(c)**, is partially shown for the ease of comparison with the two-photon data shown in **(b)**. **(b)** At $t = 0$, two photons are created and are occupying Q_1 and Q_2 sites. They are generated by applying a π-pulse to Q_1 and Q_2 and exciting them ($\psi_0 = |110\rangle$). The parameters used, pulse sequence, and the measurements are similar to Fig. 2. While the single-photon circulates in counter-clockwise direction, the photon-vacancy circulates in the clock-wise direction. The counter circulation of the two-photons case compared with the single-photon case is the direct consequence of strong interactions in the system. In the absence of interactions, the direction of circulation would have been the same. These findings are schematically demonstrated in panel **(a)**. The yellow arrows indicate the direction of circulation of the single-photon or single-vacancy case, where photons and vacancies are depicted by bright and dark disks, respectively, and shown on top of the optical image of the circuit used.

engineering challenge [148]. Superconducting qubits, however, naturally overcome this challenge and provide a platform where microwave photons can have strong interactions. Systems of coupled qubits can be understood with a Bose-Hubbard model, where the on-site interaction U originates from the expansion of qubit's confining cosine potential:

$$H_{\text{int}} = -\frac{U_2}{2}\sum_j \hat{n}_j(\hat{n}_j - 1) + \frac{U_3}{6}\sum_j \hat{n}_j(\hat{n}_j - 1)(\hat{n}_j - 2) + ... \tag{5.3}$$

In our system $U_2 \approx U_3 \sim 200\,\text{MHz}$ which sets the energy difference between single and double photon occupancy; e.g. the $|200\rangle$ to $|110\rangle$ transition. The hopping "bandwidth" in each manifold is set by g and is a few MHz. Therefore $U \gg g$ and qubits effectively form a hard core boson system.

The signature of strong interactions can be seen in the two-photon circulation as shown in Fig. 3**(b)**. In the absence of interactions one expects that two photons to circulate freely with the same chirality as a single photon. However, two-photon circulation in our system displays the opposite chirality, indicating that, as a result of strong interactions, photons do not move freely. Consequently, given that our system has three sites, when two photons are injected it is more natural to consider the motion of the photon-vacancy. Similar to the physics of holes in an electron band, the photon-vacancies have the opposite "charge", and hence circulate in the opposite direction compared to photons.

5.6 Chiral currents in the groundstate

In condensed matter systems, one is generally interested in finding the groundstate of a many-body system and probing its properties. In particular, the key signature of

FQH states is the appearance of groundstate chiral edge currents. As the many-body Chern number of an FQH phase can be extracted from the DC conductivity tensor, the capability to measure ground state currents is especially valuable. Although the evolution of $|100\rangle$ or $|110\rangle$, as discussed so far, provides an intuitive understanding of the response of the system to this synthetic gauge, these data do not directly reflect the groundstate properties of the system, because these initial states are not eigenstates of the Hamiltonian. To study ground state properties, we adiabatically prepare groundstates of Eq.(2) and examine breaking the TRS by measuring the chiral current in the groundstates (see Fig. 4**(a)** for pulse sequence). Analogous to the continuity equation in classical systems, a current operator $\hat{I}$ can be defined by equating the current in and out of a qubit site to the change of the photon number operator on that site ($\hat{I}_{in} - \hat{I}_{out} = d\hat{n}/dt$) (see supplement). From the continuity equations, we define the chiral current operator to be

$$\hat{I}_{\text{chiral}} \equiv \sum_{j,k} \hat{I}_{Q_j \to Q_k} = i \sum_{j,k} (e^{i\varphi_{jk}} a_j^\dagger a_k - e^{-i\varphi_{jk}} a_j a_k^\dagger). \tag{5.4}$$

Since $\hat{I}_{\text{chiral}}$ flips sign under TRS, we expect that its ground state expectation value will be zero whenever the Hamiltonian is TRS preserving, and nonzero otherwise. This equilibrium current is distinct from the commonly measured non-equilibrium particle imbalance [79, 96, 12], as experimental measurement of $\hat{I}_{\text{chiral}}$ require access to the groundstate.

To measure $\langle \hat{I}_{\text{chiral}} \rangle$ in the single-photon manifold, initially we prepare $\psi_0 = |100\rangle$ followed by a ramp up of the Hamiltonian parameters to generate Eq.(2) for various Φ_B

values (olive color, Fig. 4**(b)**). For preparing groundstates in the two-photon manifold, we initially create $\psi_0 = |110\rangle$ by exciting two qubits, followed by a similar ramp and measurements (maroon color, Fig. 4**(b)**). Note that due to large U/g ratio, the two-photon manifold with and without double occupancies are almost entirely separate. Because of the three-fold symmetry of the system, measuring the current operator between any pair of qubits, e.g. $\hat{I}_{Q_1 \to Q_2}$, suffices for knowing $\langle \hat{I}_{\text{chiral}} \rangle$. The solid lines are from numerical computations assuming perfect adiabaticity. For a given Φ_B, the measured $\langle \hat{I}_{\text{chiral}} \rangle$ on single- and two-photon manifold show almost exactly opposite values indicating that photons and photon-vacancies have opposite chiralities. On both manifolds and away from the origin, $\langle \hat{I}_{\text{chiral}} \rangle$ rather abruptly become non-zero with opposite values for $\Phi_B > 0$ and $\Phi_B < 0$, showing a quantum transition. Additional interesting points are $\Phi_B = \pm\pi$, where $\langle \hat{I}_{\text{chiral}} \rangle$ goes to zero on both one-photon and two-photon manifolds, and in contrast to $\Phi_B = 0$, the measured chiral current close to $\Phi_B = \pm\pi$ is smooth.

The vanishing of $\langle \hat{I}_{\text{chiral}} \rangle$ at $\Phi_B = 0, \pm\pi$ can be understood by noticing that the Hamiltonian of the system is real at these points and hence cannot break the TRS, whereas for other values it is irreducibly complex. Several feature of the data can be understood by computing the gap between the groundstate and the first excited state(background color of Fig. 4**(b)**). For $\Phi_B = 0$, $\langle \hat{I}_{\text{chiral}} \rangle$ is discontinuous, as the ground state is degenerate at $\Phi_B = 0$ and any finite Φ_B breaks this degeneracy and leads to chiral currents, effectively producing a first-order phase transition. On the other hand, for $\Phi_B = \pm\pi$, the ground state is not degenerate and there is a large gap to the excited

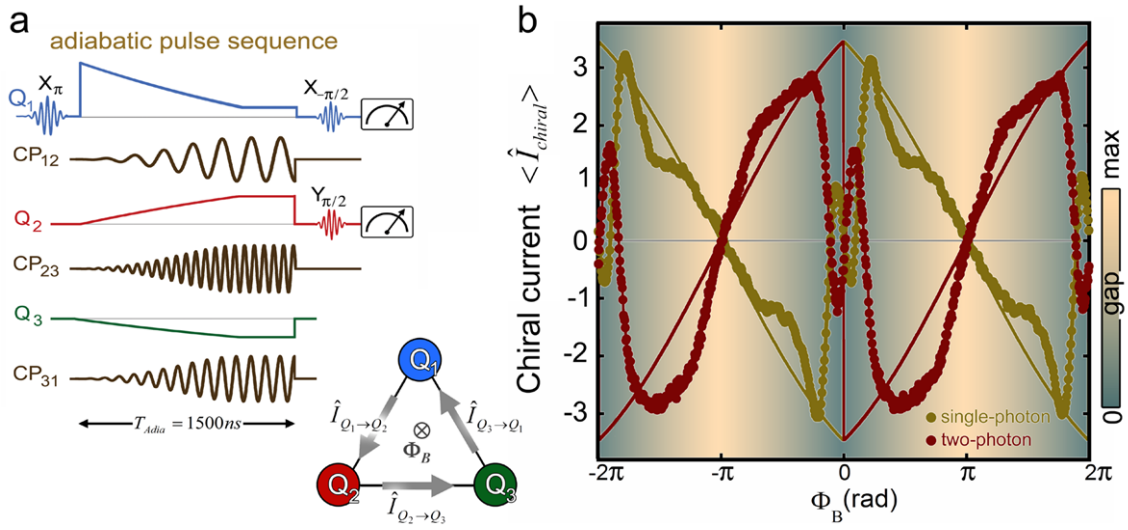

Figure 5.4: **Chiral currents in the groundstate.** **(a)** The pulse sequence for adiabatically preparing the groundstate of Eq.(2). For groundstates in the single-photon manifold, Q_1 is excited at $t = 0$ ($\psi_0 = |100\rangle$), and in the two-photon manifold, Q_1 and Q_2 are excited ($\psi_0 = |110\rangle$). To measure $\hat{I}_{Q_1 \to Q_2}$ at the end of parameter ramping, Q_1 and Q_2 are rotated, allowing for measurements of $\langle \sigma^X_{Q1} \sigma^Y_{Q2} \rangle$ and $\langle \sigma^Y_{Q1} \sigma^X_{Q2} \rangle$ (see supplement for details). **(b)** The measured values of $\langle \hat{I}_{\text{chiral}} \rangle$ in the single-photon (olive-color) or two-photon manifolds (maroon-color). The solid lines are computations for $T_{\text{adia}} \to \infty$. The energy gap of the Hamiltonian of the system (Eq.(2)) as a function of Φ_B is numerically computed and is shown as the background of the data. The gap closes at $\Phi_B = 0, \pm 2\pi$ and the groundstate become degenerate (green regions). The maximum gap size is $3g_0$, which here is 12 MHz.

states, and $\langle \hat{I}_{\text{chiral}} \rangle$ must therefore smoothly cross zero as Φ_B crosses $\pm\pi$. The origin of the oscillatory behavior close to $\Phi_B = 0$ is also due to gap closing, as a result of which the adiabatic ramps become incapable of providing correct results.

Our experiment highlights the strengths of superconducting qubits for synthesizing many-body phases of quantum matter. The inherent simplicity of the coupling modulation method also played a key role in this first demonstration of synthetic gauge fields with superconducting qubits; frequently, synthetic gauge field proposals for superconducting circuits demand challenging new architectures and are susceptible to charge noise. The scheme we employed avoids these issues, can be generally applied for other applications [91], and highlights a path forward beyond these proof of principle experiments to the direct realization of FQH states. To realize FQH physics, the system must be large compared to the magnetic length l_B of the Hamiltonian. If we choose the Kapit-Mueller Hamiltonian [93] as a basis, a flux per plaquette $\Phi_B = 1/3$ yields $l_B = 0.69$, which suggests an $L \times L$ lattice with $L \geq 6$ as an appropriate host for FQH physics. Further, a $2 \times L$ ladder with nearest and next nearest neighbor hopping can host a nearly exact Laughlin ground state that displays many of the properties of its $L \times L$ parent state. These include a local excitation gap, fractionalized excitations and a topological degeneracy which manifests as charge density wave order in ladder systems [56]. For both host systems, the Laughlin ground state is resilient against local phase noise, and it can be prepared through adiabatic evolution or resonant sequential photon injection, or stabilized indefinitely through engineered dissipation [92]. Thus, simply increasing the

size of our system provides a near-term experimental path for generating FQH states of light.

Chapter 6

Applications to many-body localization

6.1 Abstract

Statistical mechanics is founded on the assumption that a system can reach thermal equilibrium, regardless of the starting state. Interactions between particles facilitate thermalization, but, can interacting systems always equilibrate regardless of parameter values ? The energy spectrum of a system can answer this question and reveal the nature of the underlying phases. However, most experimental techniques only indirectly probe the many-body energy spectrum. Using a chain of nine superconducting qubits, we implement a novel technique for directly resolving the energy levels of interacting photons. We benchmark this method by capturing the intricate energy spectrum predicted for

2D electrons in a magnetic field, the Hofstadter butterfly. By increasing disorder, the spatial extent of energy eigenstates at the edge of the energy band shrink, suggesting the formation of a mobility edge. At strong disorder, the energy levels cease to repel one another and their statistics approaches a Poisson distribution - the hallmark of transition from the thermalized to the many-body localized phase. Our work introduces a new many-body spectroscopy technique to study quantum phases of matter.

6.2 Introduction

Consider a system of interacting particles isolated from the environment. Imagine it is initially prepared in a very low entropy state far from equilibrium. It is often observed that the system acts as its own thermal reservoir and approaches the equilibrium state. In this thermal phase the system shows ergodic behavior, where it uniformly explores all accessible states over time. Recent works discuss the emergence of another phase for the system in certain parameter regime where ergodicity breaks down and thermal equilibrium becomes unattainable [19, 135, 8, 191, 169, 173, 94, 42]. This finding is rather surprising, since intuitively one may think that interacting systems are always able to thermalize themselves. This phase is referred to as the many-body localized (MBL) phase [147, 36, 171, 101, 172, 15, 82, 81]. The conventional quantum phase transitions, e.g. from para- to ferro-magnetic, are characterized by changes in the groundstate of the system. However, the signatory differences between the thermalized and MBL phases are in dynamical behaviors, indicating that the transition involves change in the properties

of all many-body eigenstates of the system. Hence the physics goes beyond the ground-state and requires study of the entire energy spectrum, which constitutes an experimental challenge.

In classical physics, the characteristic (eigen) frequencies of the system and the shape of these vibrational modes are fundamental for understanding and designing mechanical structures and electrical circuits. Similarly, in quantum physics, the quantized eigen-energies and their associated wave-functions provides extensive information for predicting the chemistry of molecules or physics of condensed matter systems. Regardless of the underlying mechanism, creating local perturbations and recording the subsequent vibrational response of the system as a function of time can reveal the characteristic modes of that system. Our method for measuring the energy spectrum of a Hamiltonian is based on this and is extremely simple. For fixed Hamiltonians, the state of a system evolves according to Schrödinger equation

$$|\psi(t)\rangle = \sum_{\alpha} C_{\alpha} e^{-iE_{\alpha}t/\hbar} |\phi_{\alpha}\rangle, \tag{6.1}$$

where E_{α} is an eigen-energy of the Hamiltonian and $|\phi_{\alpha}\rangle$ is the corresponding eigenstate. Eqn. (6.1) implies that $\{E_{\alpha}\}$ and $\{C_{\alpha}\}$ determine the frequencies and the amplitudes of the modulations in $\psi(t)$, respectively. The similarity of Eqn. (6.1) and a Fourier transform (FT) relation suggests that the *frequencies* observed in the FT of the evolution could in principle reveal $\{E_{\alpha}\}$. In addition, the *magnitudes* of FT terms provide $\{C_{\alpha}\}$; these coefficients set the relative contribution of each $|\phi_{\alpha}\rangle$ to a given dynamics.

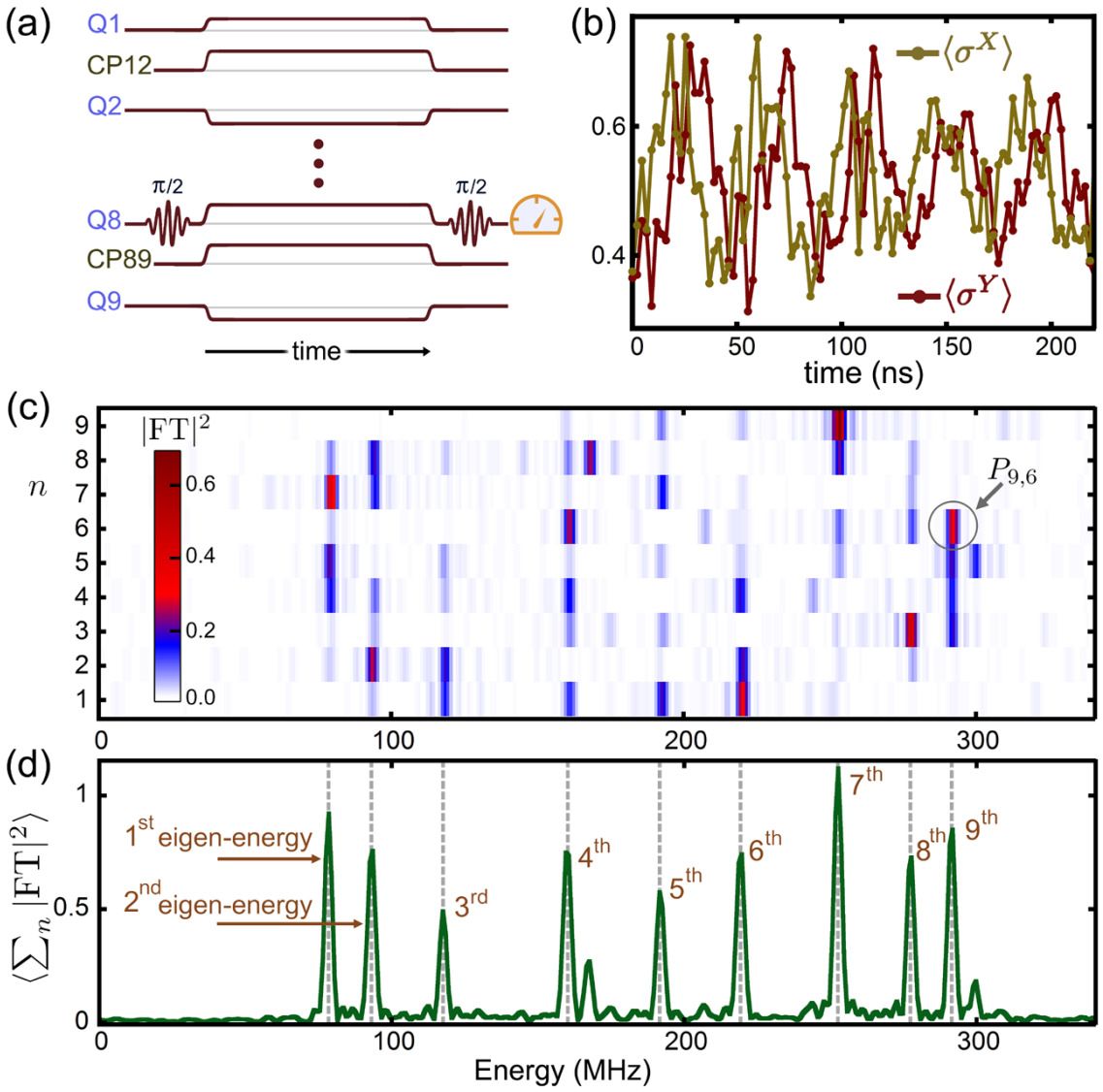

Figure 6.1: **Time-domain spectroscopy**.**(a)** Pulse sequence used to measure eigenvalues of a time-independent Hamiltonian, Eqn. (2) with $J/2\pi = 50\,\text{MHz}$, $U = 0$, and $\mu_n/2\pi$ randomly chosen from $[0, 100]\,\text{MHz}$. Initially, all the qubits are in the $|0\rangle$ state. Using a microwave pulse, one of the qubits is then placed on the superposition of $|0\rangle$ and $|1\rangle$ state ($Q8$ depicted here). The coefficients in the Hamiltonian are set by applying square pulses on the qubits $\{Qn\}$ and couplers $\{CP\}$. After the evolution, a microwave $\pi/2$ pulse is applied to the qubit in order to measure $\langle\sigma_n^X\rangle$ or $\langle\sigma_n^Y\rangle$. **(b)** Typical dataset showing $\langle\sigma_n^X\rangle$ and $\langle\sigma_n^Y\rangle$ versus time. **(c)** The FT of $\chi_1(n) = \langle\sigma_n^X\rangle + i\langle\sigma_n^Y\rangle$ for $n \in \{1, 2, ..., 9\}$. The peaks in the FT correspond to the eigenvalues of the Hamiltonian. The probability of a Fock state on $Q6$ to be in the 9^{th} eigenstate $P_{9,6}$ is highlighted. **(d)** Average of the FT amplitudes shown in **(c)**. Averaging is done to show all 9 peaks in one curve.

Using 9 superconducting qubits, we constructed a 1D bosonic lattice and implement a spectroscopy method based on the above-mentioned fundamental postulate of quantum mechanics. Each of our qubits can be thought of as a nonlinear oscillator. The Hamiltonian of the chain can be described by the Bose-Hubbard model

$$\begin{aligned} H_{BH} &= \sum_{n=1}^{9} \mu_n a_n^\dagger a_n + \frac{U}{2} \sum_{n=1}^{9} a_n^\dagger a_n (a_n^\dagger a_n - 1) \\ &+ J \sum_{n=1}^{8} a_{n+1}^\dagger a_n + a_n^\dagger a_{n+1}, \end{aligned} \tag{6.2}$$

where $a^\dagger$ (a) denotes the bosonic creation (annihilation) operator, μ_n is the on-site potential, J is the hopping rate between nearest neighbour lattice sites, and U is the on-site interaction. The qubit frequency, the nearest neighbor coupling, and nonlinearity set μ_n, J, and U, respectively. In our system, we can vary the first two in ns time-scales, but U is fixed.

In Fig. 1 we show how to identify the eigen-energies of Eqn. (2) when it describes hopping of a single photon in a disordered potential. In the beginning of the sequence there is no photon in the system and all the qubits are in $|0\rangle$ state. Then, we place the n^{th} qubit Qn in the superposition of $|0\rangle$ and $|1\rangle$ state (Fig. 1**(a)**). We measure the evolution of $\langle\sigma_n^X\rangle$ and $\langle\sigma_n^Y\rangle$, where σ^X and σ^Y are Pauli operators (acting on the $|0\rangle$ and $|1\rangle$ sub-space) (Fig. 1**(b)**). From the $\langle\sigma_n^X\rangle$ and $\langle\sigma_n^Y\rangle$ measurements we construct $\chi_1(n) \equiv \langle\sigma_n^X\rangle + i\langle\sigma_n^Y\rangle$. Next, we vary n from 1 to 9 to assure that the energy spectrum is fully resolved. By varing n the initial states form a complete basis, and then every energy eigen-state is certain to have some overlap with one of the initial states and hence

can be detected. Fig. 1**(c)** shows the FTs of $\chi_1(n)$ for each Qn in which distinct peaks can be readily identified. The result of averaging the FTs is depicted in Fig. 1**(d)**, where 9 peaks appear and their frequencies are the 9 eigen-energies of the Hamiltonian. The particular choices of initial states and the observables are made to avoid appearance of undesired energy peaks in the spectrum (see supplement).

6.3 Simulating 2D electrons

Next, we demonstrate our capability to accurately set the terms in a specific Hamiltonian and resolve the corresponding eigen-energies. We simulate the problem of Bloch electrons on a 2D lattice subject to a perpendicularly applied magnetic field B [77, 87, 155, 46, 80, 131, 6]. The magnetic length ($l_B = \sqrt{\hbar/eB}$) and lattice constant a characterize the electron's motion, and their interplay sets the physics. The resulting energy spectrum was first calculated by Hofstadter and resembles a butterfly [77]. For typical crystals, the magnetic field required to 'squeeze' one flux quantum through the unit cell is of the order of several tens of thousands of Tesla, too high to be experimentally feasible.

The Hofstadter energy spectra can be parameterized by a single dimensionless magnetic field $b = a^2eB/h$ which counts the number of magnetic flux quanta per unit cell. In the tight binding approximation the Schrödinger equation takes the form of 1D Harper Hamiltonian [77]

$$H_{\text{Harper}} = \Delta \sum_{n=1}^{9} \cos(2\pi n b) a_n^\dagger a_n + J \sum_{n=1}^{8} a_{n+1}^\dagger a_n + a_n^\dagger a_{n+1}. \tag{6.3}$$

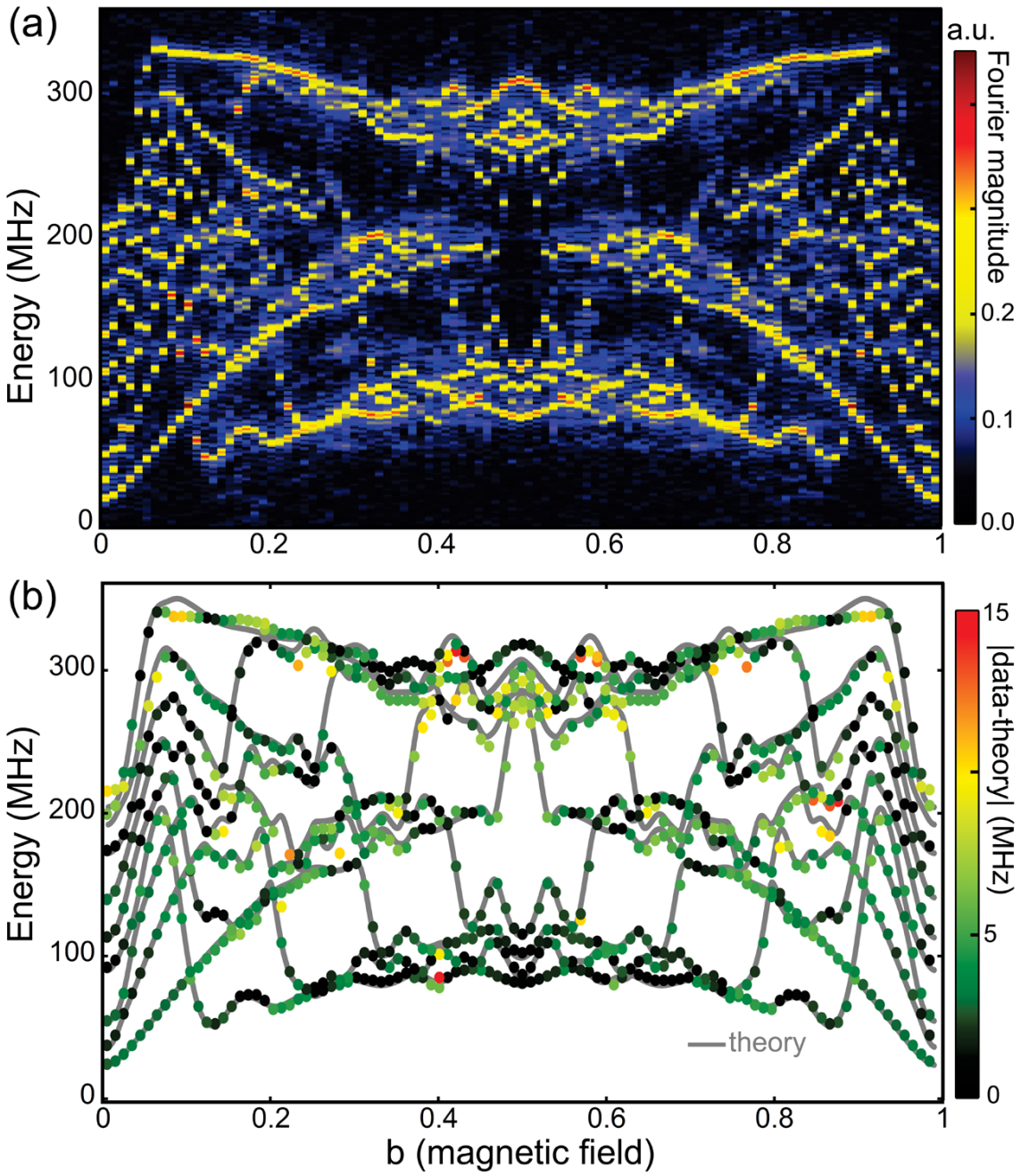

Figure 6.2: **Hofstadter butterfly**. In Eq. (3), we set on-site potentials $\Delta/2\pi = 50\,\text{MHz}$ and coupling $J/2\pi = 50\,\text{MHz}$. **(a)** Data similar to Fig. 1**(d)** is shown for 100 values of dimensionless magnetic field b ranging from 0 to 1. **(b)** For each b value, we identify 9 peaks and plot their location as a colored dot. The numerically computed eigenvalues of Eq. (2) are shown with gray lines. The color of each dot is the difference between the measured eigenvalue and the numerically computed one.

The H_{Harper} is the special case of H_{BH}, reached by setting $\mu_n = \Delta\cos(2\pi nb)$ and exciting only one photon in the system, i.e. $U = 0$. Note that in this limit the fermionic or bosonic nature of the particle does not matter. In Fig. 2, we vary b from 0 to 1 and realize 100 different H_{Harper}. Similar to Fig. 1, for each b value, initial states with n^{th} qubit excited are created and the evolution of $\langle\sigma_n^X\rangle$ and $\langle\sigma_n^Y\rangle$ are measured, and n is varied from 1 to 9. For each b value, Fig. 2**(a)** shows the magnitude summation of the FT of $\{\chi_1(n)\}$.

For large lattices with many energy levels, it is theoretically known that for rational b all energy bands split into sub-bands, and for irrational b the spectra become fractal and form a Cantor set. Since we have only 9 levels, what we see in Fig. 2**(a)** are the remnants of those bands. Nevertheless, the overall measured spectrum still resembles a butterfly. We focus on this featureful pattern of level crossings and meanderings and ask how well the measurements match simulation. In Fig. 2**(b)**, we present the numerically computed eigen-energies with solid gray lines and the measured peaks in **(a)** with colored dots. The color of the dots shows the distance in MHz of the peaks from the simulation values. The average deviation is 3.5 MHz. This implies we can set the matrix elements of the Hamiltonian, which in this case includes 17 terms, with $< 2\%$ error. This unprecedented capability in controlling a large quantum system is achieved through careful modeling of the qubits as non-linear resonators.

By placing two photons in the system, we next study the simplest interacting cases ($U \neq 0$). The rest of data presented in this work is taken by using the following procedure

(2-photon protocol). We realize a quasi-periodic potential by setting $\mu_n = \Delta\cos(2\pi nb)$. In total, 4 different irrational values of $b \in [0, 1]$ are chosen and the corresponding results are averaged. The irrational choice of b assures that the periodicity of the potential and lattice are incommensurate. In Eqn. (2), we set $J/2\pi = 50\,\mathrm{MHz}$, which results in $U/J = 3.5$. The initial states are made by placing two qubits (Qn and Qm) in the superposition of the $|0\rangle$ and $|1\rangle$ states. We measure two-point correlations and construct $\chi_2(n, m) \equiv \langle\sigma_n^X\sigma_m^X\rangle - \langle\sigma_n^Y\sigma_m^Y\rangle + i\langle\sigma_n^X\sigma_m^Y\rangle + i\langle\sigma_n^Y\sigma_m^X\rangle$. The peaks observed in the FT of $\chi_2(n, m)$ are the eigen-energies of H_{BH} in the two-photon manifold (see supplement).

6.4 Energy level statistics in an interacting system

Perhaps the most direct way of examining ergodic dynamics and its breakdown is by studying the distribution of the energy levels [143, 13, 27]. Using the 2-photon protocol, we measure the evolution of $\chi_2(n, m)$ for various strengths of disorder Δ. We identify the peaks in the FT of $\chi_2(n, m)$ as the energy levels E_α. Let $s_\alpha = E_{\alpha+1} - E_\alpha$ be the nearest-neighbor spacings (illustrated Fig. 3**(a)**), and level separation uniformity $r_\alpha \equiv \min\{s_\alpha, s_{\alpha-1}\}/\max\{s_\alpha, s_{\alpha-1}\}$. From our measured $\{E_\alpha\}$ we compute the associated $\{r_\alpha\}$ and construct their probability distribution (PD, Fig. 3**(b)**). For low disorder, the PD is mainly centered around the r_α values close to half, and with increase of disorder the histogram's peak shifts toward smaller r_α values.

It has been postulated that in the ergodic phase the statistics of levels is the same as the ensemble of real Hermitian random matrices, which follow the Gaussian Orthogonal

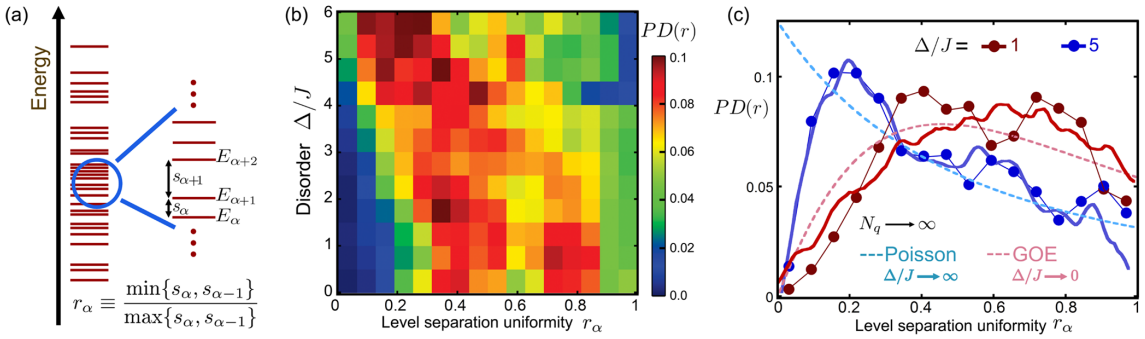

Figure 6.3: **Level statistics and transition from GOE to Poisson**. In Eqn. (2), we set hopping to $J/2\pi = 50\,\mathrm{MHz}$ which fixes $U/J = 3.5$. In total, 4 different irrational values of $b \in [0, 1]$ are chosen and the results are averaged. **(a)** The schematic of energy levels shows how r_α is defined. **(b)** The measured histogram of $P(r)$ measured for various Δ/J values is presented in color. **(c)** The measured histogram $P(r)$ of $\{r_\alpha\}$ for $\Delta/J = 1$ and 5. The dashed lines are plots of P_{Poisson} and P_{GOE} according to Eqn. (5), and the solid lines are numerical simulations. The change from GOE toward Poisson is indicative of vanishing of level repulsion when Δ becomes larger.

ensemble (GOE) [27]. In the localized phase, the energy levels become uncorrelated due to disorder and hence it is expected to show a Poisson distribution in energy landscape. The probability distribution of $\{r_\alpha\}$ for the ergodic and many-body localized phases, respectively, are

$$PD_{\mathrm{GOE}}(r) = \frac{27}{4}\frac{r + r^2}{(1 + r + r^2)^{5/2}}, PD_{\mathrm{Poisson}}(r) = \frac{2}{(1 + r)^2}. \tag{6.4}$$

In Fig. 3**(c)**, we focus on $\Delta/J = 1$ and 5, showing the measured histograms with dots and the numerical simulations with solid lines. The dashed lines are plots of Eqn. (5), providing the expected behavior in the thermodynamic limit (number of sites $N_q \to \infty$), and for limiting values of Δ/J. In contrast to these cases, the finite size of our chain results in features that can be seen in both data and simulation. When disorder is small, the energy eigenstates are extended across the chain (we will show this in Fig. 4,) and

hence the energy levels repel each other. Consequently, there are strong correlations between the levels and an equidistant distribution of levels would be favorable. When Δ becomes larger, the eigenstates become localized in space and unaware of each others presence at a given energy and level repulsion ceases. Therefore, the levels independently distribute themselves, showing a Poisson distribution in the energy landscape. The exact realization of Poisson distribution takes place only when $J/\Delta \to 0$; in our case $J/\Delta = 0.2$, which is where the peak in the histogram appears. Since the Poisson distribution is the signature of independent events, we conclude that the transition from ergodic to localized phase is associated with vanishing correlations in energy levels.

6.5 Spatial extent of eigenstates

A key signature of transition from ergodic to MBL phase is the change in the localization length of the system from being extended over entire system to localized over a few lattice sites. This physics can be studied by measuring the probability of each energy eigen-state being present at each lattice site $\{P_{\alpha,n}\}$ (see supplement). In our method, the frequencies of the FT signal give the eigen-energies, and from the magnitude of the FT terms $\{P_{\alpha,n}\}$ can be measured. For instance, $P_{9,6}$ is highlighted in Fig. 1**(c)**. In the study of metal-insulator transition [3, 83], a common way to quantify the extension in real-space or energy landscape is via the second moment of the probabilities, defined by Participation Ratio (PR)

$$PR_{\text{Space}}(\alpha) \equiv 1/\sum_n P_{\alpha,n}^2,\ PR_{\text{Energy}}(n) \equiv 1/\sum_\alpha P_{\alpha,n}^2. \tag{6.5}$$

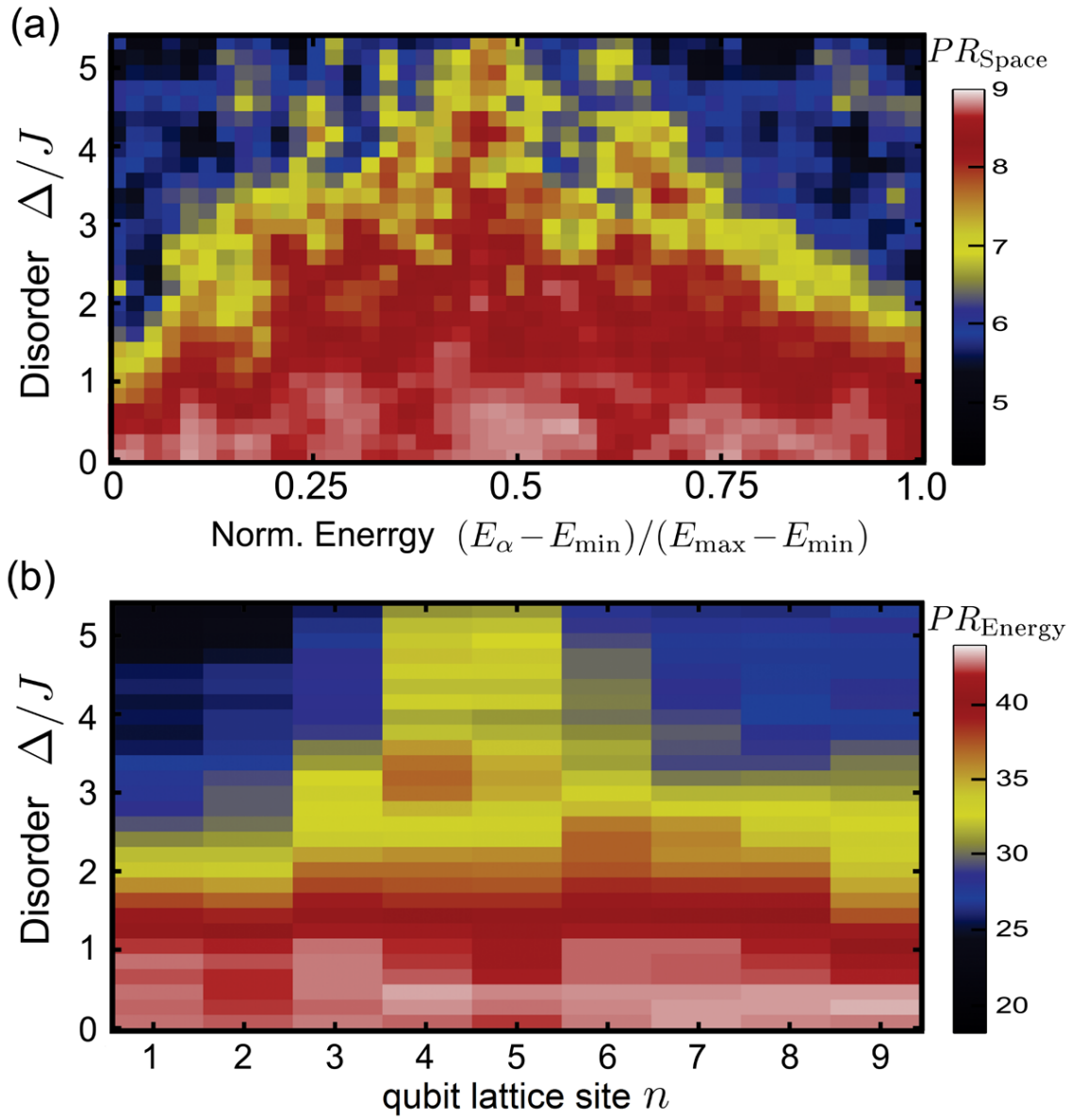

Figure 6.4: **Participation ratio and Mobility edges**. In Eqn. (2), we set $b = (\sqrt{5}-1)/2$, $J/2\pi = 50\,\text{MHz}$, which results in $U/J = 3.5$.We measure the evolution of $\chi_2(n,m) = \langle\sigma_n^X\sigma_m^X\rangle + \langle\sigma_n^Y\sigma_m^Y\rangle + i\langle\sigma_n^X\sigma_m^Y\rangle + i\langle\sigma_n^Y\sigma_m^X\rangle$ for all pairs of $n, m \in \{1, 2, ..., 9\}$ as a function time for various strengths of disorder Δ. From the magnitude of the peaks seen in the FT of the data the probabilities relating the positions of two-photon Fock states to energy eigenstates $\{P_{\alpha,n}\}$ are extracted. See supplement for details. The computed **(a)** PR_{Space} and **(b)** PR_{Energy} based on Eqn. (4) are plotted. The $E_{\max} - E_{\min}$ is the width of the energy band at a given Δ.

PR_{Space} indicates the number of sites over which an energy eigenstate $|\phi_\alpha\rangle$ has an appreciable magnitude. Similarly, PR_{Energy} measures how many energy eigenstates have significant presence on lattice site n. Note that the first moment of the probability distributions is normalization conditions $\sum_\alpha P_{\alpha,n} = 1$ and $\sum_n P_{\alpha,n} = 1$.

Demonstrated that we can fully resolved the energy spectrum of the two-photon energy manifold, we now extract $\{P_{\alpha,n}\}$. In Fig. 4**(a)**, we compute PR_{Space} for various disorder strengths and present them in the order of increasing energy. In this energy manifold, there are 36 single (e.g. $|001000100\rangle$) and 9 double occupancy states (e.g. $|000020000\rangle$), which gives $\binom{9}{2} + \binom{9}{1} = 45$ energy levels. For low disorder ($\Delta/J < 1$), PR_{Space} is about 8, indicating almost all energy eigenstates are extended over the entire chain of 9 qubit lattice sites. As the strength of disorder increases, the eigenstates with their energies close to the edge of the energy band start to shrink, while eigenstates with energies in the middle of the band remain extended at larger disorders. This is consistent with the notion that localization begins at the edges of the band, and a mobility edge forms (the yellow hue) and approaches the center of the band as disorder becomes stronger [3]. In Fig. 4**(b)**, we plot the PR_{Energy}, which shows that as the disorder becomes stronger, the number of eigenstates present at a given lattice site reduces, indicating that eigenstates are becoming localized on lattice sites. Furthermore, with increasing disorder, the eigenstates are avoiding the edges of the chain and more eigenstates have presence toward the center of the chain. The changes in PR_{Space} and PR_{Energy} are the fastest

near $\Delta/J = 2$, suggestive of a phase transition that has been smeared out due to finite size effects. Nevertheless, we emphasize that the quantum phase transition to the MBL phase is only defined in the thermodynamic limit ($N_q \to \infty$) [82]. Given the finite size of our system and the presence of only two interacting particles, it is interesting that we see several signatures associated with the MBL phase transition.

6.6 Quantum correlations

To provide a comprehensive picture of the transition to the localized phase, we study two-site quantum correlations $\mathcal{S}_{m,n}$ as a function of disorder strength Δ and distance between lattice sites $|m-n|$. We measure $\mathcal{S}_{m,n} \equiv |\langle \sigma_m^1 \sigma_n^2 \rangle - \langle \sigma_m^1 \rangle \langle \sigma_n^2 \rangle|$, where $\sigma^1, \sigma^2 \in \{\sigma^X, \sigma^Y\}$ and $m, n \in \{1, 2, ..., 9\}$, for all m and n combinations and Pauli operators. Fig. 5**(a)** shows $\tilde{\mathcal{S}}_{m,n}$, computed by averaging $\mathcal{S}_{m,n}$ over time and all possible combinations with the same $|m-n|$. For Δ up to $\Delta/J \approx 2$, $\tilde{\mathcal{S}}_{m,n}$ is rather symmetric in $|m-n|$, and for $\Delta/J > 2$ it exponentially decays with $|m-n|$. Intuitively, strong Δ creates large potential barriers that wave-functions cannot tunnel through and consequently correlations cannot develop. Interestingly, for $|m-n| < 3$, as disorder becomes stronger, $\tilde{\mathcal{S}}_{m,n}$ becomes larger, indicating that correlations cannot propagate far and locally build up in the potential 'puddles'. These observations are consistent with the signatures of the transitions from the metallic phase, where correlations are distance independent, to the localized phase where they decay rapidly with distance.

Our work demonstrates the novel information about various phases that can be ex-

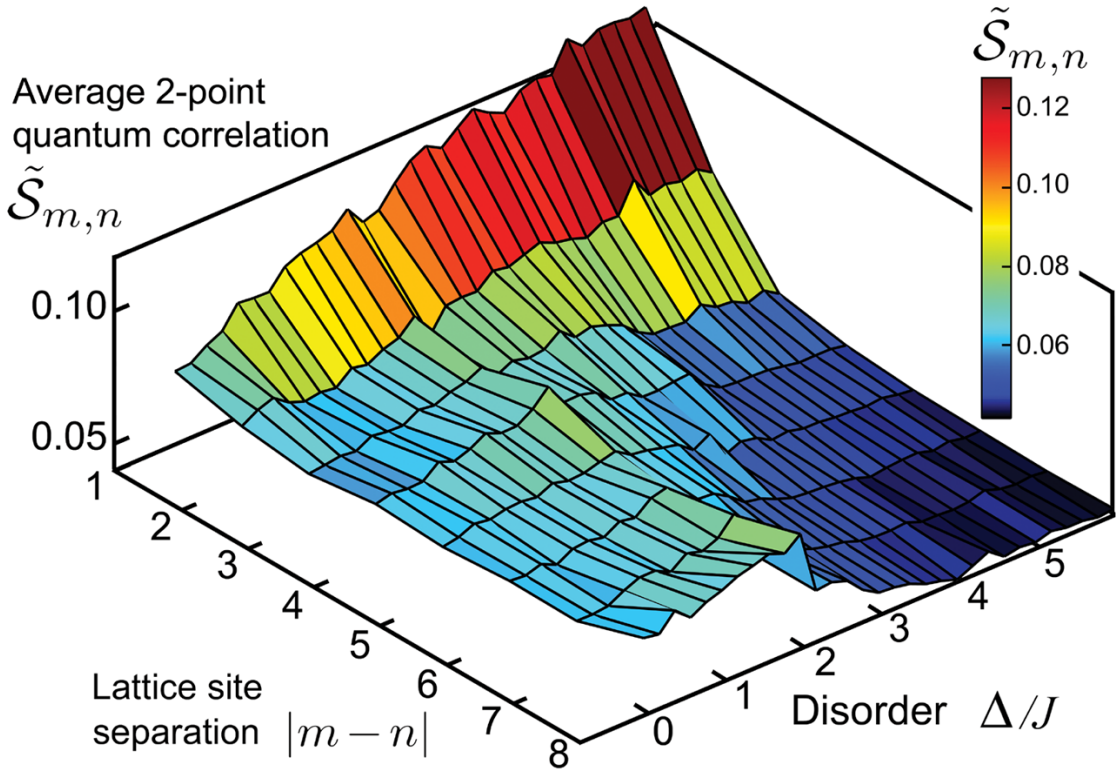

Figure 6.5: **Quantum correlations**. In Eqn. (2), we set $b = (\sqrt{5}-1)/2$, $J/2\pi = 50\,\mathrm{MHz}$, and $U/2\pi = 175\,\mathrm{MHz}$. We measure $\mathcal{S}_{m,n} = |\langle\sigma_m^1\sigma_n^2\rangle - \langle\sigma_m^1\rangle\langle\sigma_n^2\rangle|$ as a function time for various strengths of disorder Δ, where $\sigma^1, \sigma^2 \in \{\sigma^X, \sigma^Y\}$ and $m, n \in \{1, 2, ..., 9\}$. All $\binom{9}{2} = 36$ possible pairs of qubits are excited. The color shows $\mathcal{S}_{m,n}$ averaged over time (from 0 to 250 ns) and combinations with the same $|m-n|$. The change of correlations from almost uniform to exponentially decaying is consistent with change in behavior from ergodic to localized.

tracted if one directly resolves the energy levels of a system. Our findings signifies the generality of the MBL phenomena and the fact that its underlying physics prevails regardless of the details of the system.

Chapter 7

A blueprint for quantum supremacy

7.1 Abstract

Fundamental questions in chemistry and physics may never be answered due to the exponential complexity of the underlying quantum phenomena. A desire to overcome this challenge has sparked a new industry of quantum technologies with the promise that engineered quantum systems can address these hard problems. A key step towards demonstrating such a system will be performing a computation beyond the capabilities of any classical computer, achieving so-called quantum supremacy. Here, using 9 superconducting qubits, we demonstrate an immediate path towards quantum supremacy. By individually tuning the qubit parameters, we are able to generate thousands of unique Hamiltonian evolutions and probe the output probabilities. The measured probabilities obey a universal distribution, consistent with uniformly sampling the full Hilbert-space. As the number of qubits in the algorithm is varied, the system continues to explore

the exponentially growing number of states. Combining these large datasets with techniques from machine learning allows us to construct a model which accurately predicts the measured probabilities. We demonstrate an application of these algorithms by systematically increasing the disorder and observing a transition from delocalized states to localized states. By extending these results to a system of 50 qubits, we hope to address scientific questions that are beyond the capabilities of any classical computer.

7.2 Introduction

A programmable quantum system consisting of merely 50 to 100 qubits could revolutionize scientific research. While such a platform is naturally suited to address problems in quantum chemistry and materials science [54, 35, 109, 150], applications range to fields as far as classical dynamics [128] and computer science [89, 29, 117, 47]. A key milestone on the path towards realizing these applications will be the demonstration of an algorithm which exceeds the capabilities of any classical computer - achieving quantum supremacy [158]. Sampling problems are an iconic example of algorithms designed specifically for this purpose [1, 149, 34, 28]. A successful demonstration of quantum supremacy would prove that engineered quantum systems, while still in their infancy, can outperform the most advanced classical computers.

Consider a system of coupled qubits whose dynamics uniformly explore all accessible states over time. The complexity of simulating this evolution on a classical computer is easy to understand and quantify. Since every state is equally important, it is not

possible to simplify the problem, using a smaller truncated state-space. The complexity is then simply given by asking how much classical memory does it take to store the state-vector. Storing the state of a 46-qubit system takes nearly a petabyte of memory and is at the limit of the most powerful computers [69, 28]. Sampling from the output probabilities of such a system would therefore constitute a clear demonstration of quantum supremacy. Note that this is only an upper bound on the number of qubits required - other constraints, such as computation time, may place practical limitations on even smaller system sizes.

Here, we experimentally illustrate a blueprint for demonstrating quantum supremacy. We present data characterizing two basic ingredients required for any supremacy experiment: *complexity* and *fidelity*. First, we demonstrate that the qubits can uniformly explore the Hilbert-space, providing a direct measure of algorithm complexity. Next, we compare the measurement results with the expected behavior and show that the algorithm can be implemented with high fidelity. Experiments for probing complexity and fidelity provide a foundation for demonstrating quantum supremacy.

7.3 Device

The more control a quantum platform offers, the easier it is to embed diverse applications. For this reason, we have developed superconducting gmon qubits with tunable frequencies and tunable interactions. A photograph of the device used in this experiment is shown in Fig. F.1. The device consists of three distinct sections: control (bottom), qubits (center)

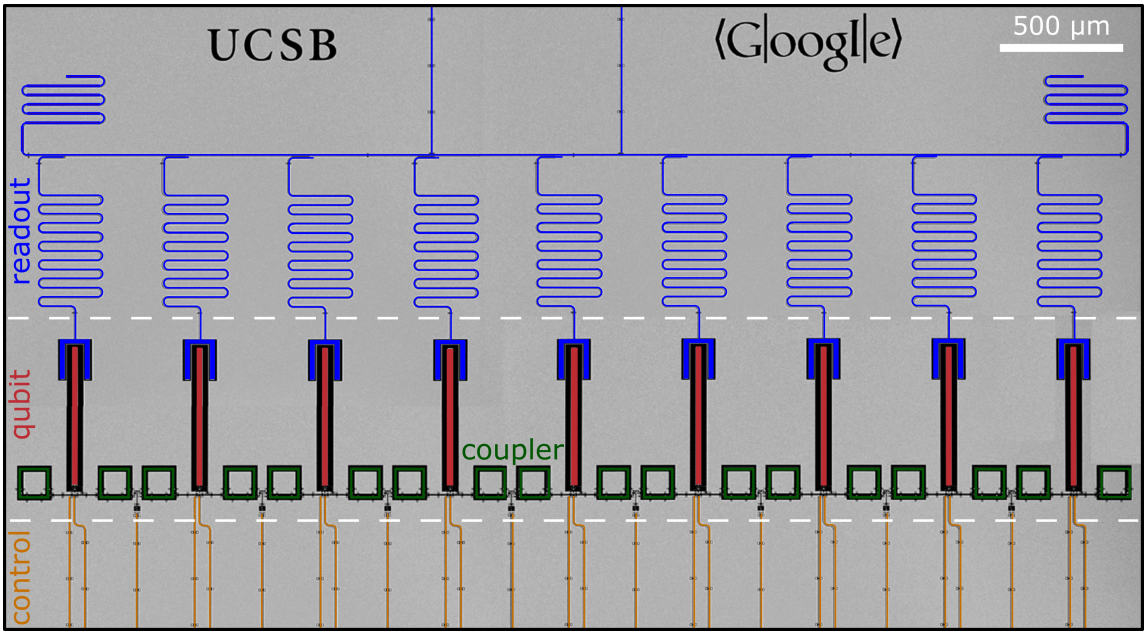

Figure 7.1: **Device: nine-qubit array.** Optical micrograph of the device. Gray regions are aluminum, dark regions are where the aluminum has been etched away to define features. Colors have been added to distinguish readout circuitry, qubits, couplers and control wiring.

and readout (top). A detailed circuit diagram is provided in the supplementary material.

Each of our gmon qubits can be thought of as a nonlinear oscillator. The Hamiltonian for the device is given by

$$\mathcal{H} = \sum_{i=1}^{9} \delta_i \hat{n}_i + \frac{\eta_i}{2} \hat{n}_i \left(\hat{n}_i - 1\right) + \sum_{i=1}^{8} g_i \left(\hat{a}_i^\dagger \hat{a}_{i+1} + \hat{a}_i \hat{a}_{i+1}^\dagger\right) \tag{7.1}$$

where $\hat{n}$ is the number operator and $\hat{a}^\dagger$ ($\hat{a}$) is the raising (lowering) operator. The qubit frequency sets the coefficient δ_i, the nonlinearity sets η_i and the nearest neighbor coupling sets g_i. The two lowest energy levels ($|0\rangle$ and $|1\rangle$) form the qubit subspace. The higher energy levels of the qubits, while only virtually occupied, substantially modify the dynamics.

7.4 Pulse sequence

In Fig. F.2 we outline the experimental procedure and provide two instances of the raw output data. Panel **a** shows a five-qubit example of the pulses used to control the qubits. First, the system is initialized (blue) by placing half of the qubits in the excited state, e.g. $|10100\rangle$. The dynamics result from fixing the qubit frequencies (red) and simultaneously ramping all of the nearest neighbor interactions on and then off (green). The shape of the coupling pulse is chosen to minimize leakage out of the qubit subspace [125]. After the evolution, we simultaneously measure the state of every qubit. Each measurement results in a single output state, such as $|10010\rangle$; the experiment is repeated many times in order to estimate the probability of every possible output state. We then carry out this procedure for randomly chosen values of the qubit frequencies, the coupler pulse lengths, and the coupler pulse heights. The probabilities of the various output states are shown in panel **b** for two instances of the evolution after 10 coupler pulses (cycles). The height of each bar represent the probability with which that output state appeared in the experiments.

It is important to note that the Hamiltonian in Eq. 1 conserves the total number of excitations. This means that because we start in a state with half the qubits excited, we should also end in a state with half the qubits excited. However, most experimental errors do not obey this symmetry, allowing us to identify and remove erroneous outcomes. While this helps to reduce the impact of errors, it slightly reduces the size of the Hilbert-space. For N qubits, the number of states is given by the permutations of N/2 excitations

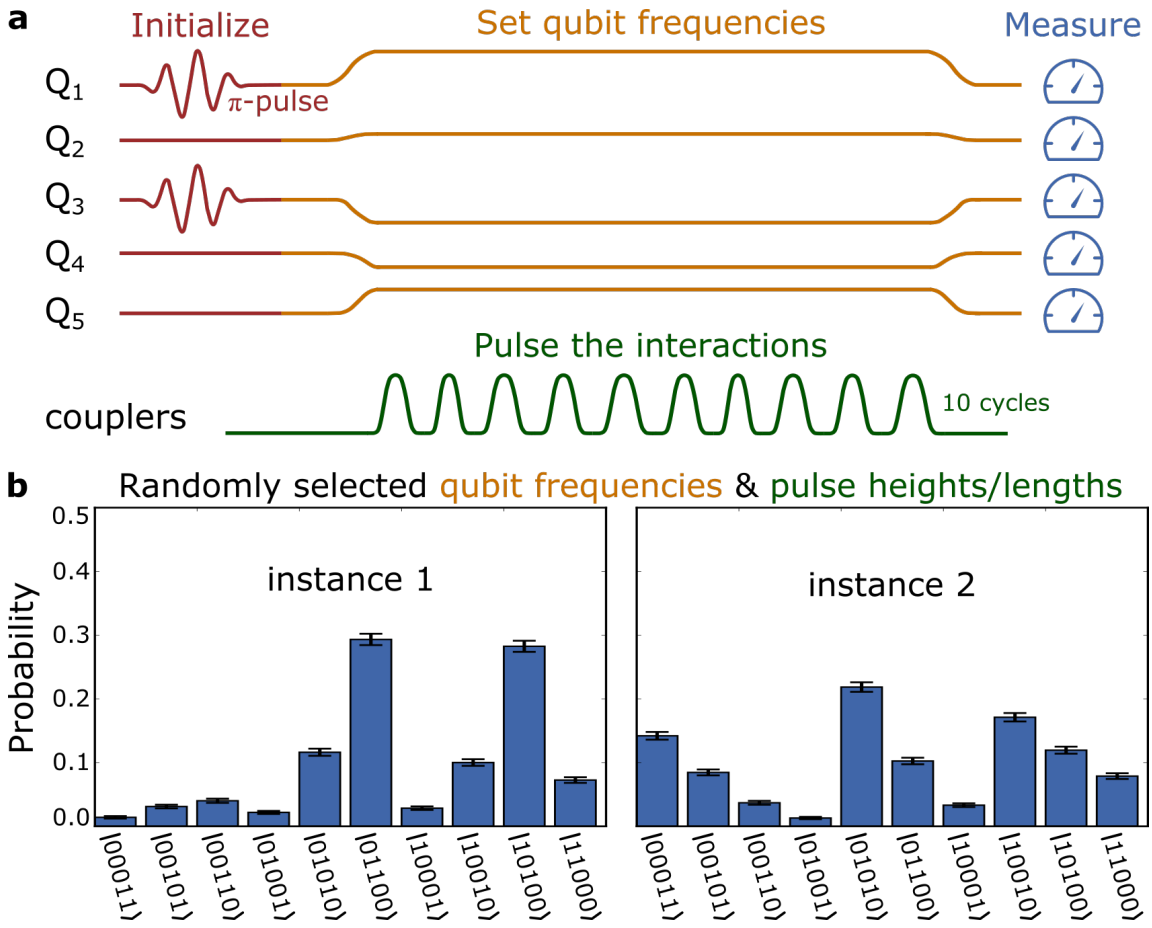

Figure 7.2: **Protocol: pulse sequence & raw data a** Five qubit example of the pulse sequences used in these experiments. First, the qubits are initialized using microwave pulses (blue). Half of the qubits start in the ground state $|0\rangle$ and half start in the excited state $|1\rangle$. Next, the qubit frequencies are set using rectangular pulses (red). During this time, all the couplings are simultaneously pulsed (green); each pulse has a randomly selected duration. Lastly, we measure the state of every qubit. The measurement is repeated many times in order to estimate the probability of each output state. **b** We repeat this pulse sequence for randomly selected control parameters. For each instance, the qubit frequencies, coupling pulse heights and lengths are varied. Here, we plot the measured probabilities for two instances after 10 coupler pulses (cycles). Error bars (± 3 standard deviations) represent the statistical uncertainty from 50,000 samples.

in N qubits and is approximately $2^N/\sqrt{N}$. As an example, a 64 qubit system would access roughly 2^{61} states under our protocol.

The measured probabilities, while they appear largely random, provide significant insight into the quantum dynamics. A key feature of these datasets are the rare, taller-than-average peaks. These highly-likely states are like a fingerprint of the underlying evolution and provide a means for verifying that the desired evolution was properly generated. The distribution of these probabilities provides evidence that the dynamics coherently and uniformly explore the Hilbert-space.

7.5 Measuring complexity

In Fig. F.3 we use the measured probabilities to show that the dynamics uniformly explore the Hilbert-space for experiments ranging from 5 to 9 qubits. We begin by measuring the output probabilities after 5 cycles for between 500 and 5000 unique instances. In order to compare experiments with different number of qubits, the probabilities are weighted by the number of states in the Hilbert-space. Fig. F.3a shows a histogram of the weighted probabilities where we find nearly universal behavior. Small probabilities (less than $1/\mathrm{N_{states}}$) appear most often and probabilities as large as $4/\mathrm{N_{states}}$ show up with a frequency of around 1%. In stark contrast to this, we observe a tall narrow peak centered around 1 for longer evolutions whose duration is comparable to the coherence time of the qubits.

A quantum system which uniformly explores all states is expected to have an expo-

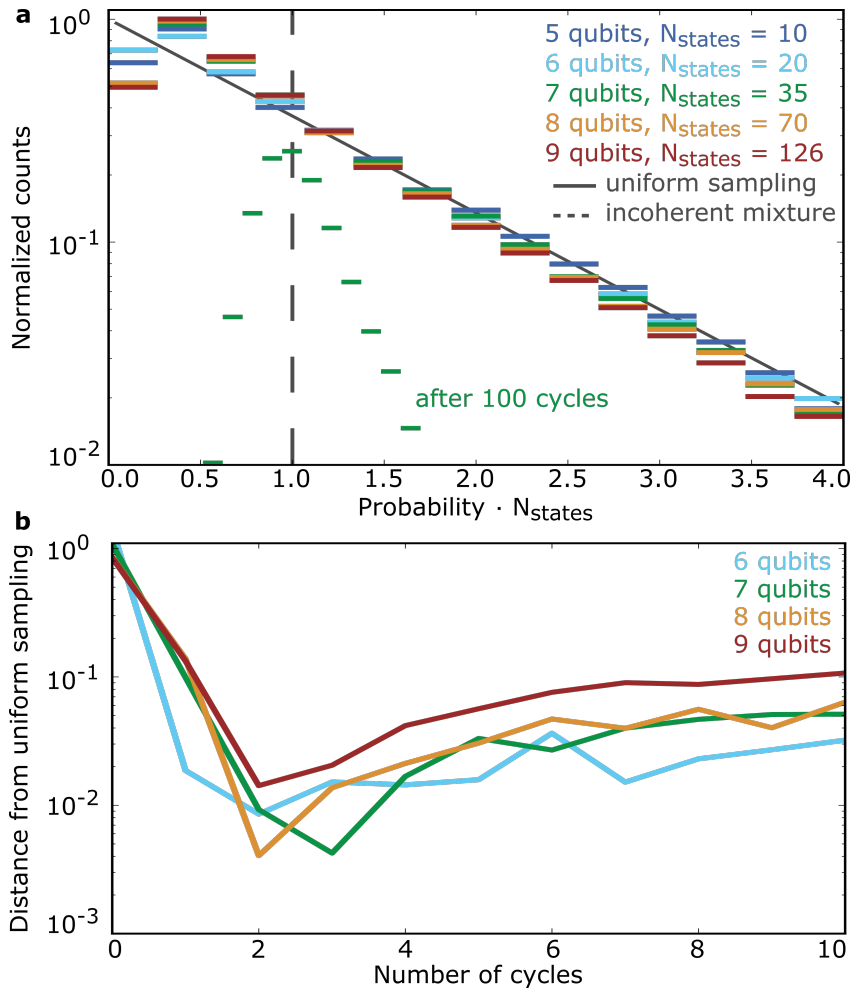

Figure 7.3: **Complexity: uniform sampling of an exponentially growing state-space. a** Histograms of the raw probabilities (see Fig. 1b) for 5 to 9 qubit experiments, after five cycles of evolution. Before making the histogram, probabilities are weighted by the number of states in the Hilbert-space, this places all of the curves onto a universal axis. The width of the bars represents the size of the bins used to construct the histogram. The data is taken from over 29.7 million experiments. For dynamics which uniformly explore all states, this histogram decays exponentially; an exponential decay is shown as a solid line for comparison. For contrast, we plot a histogram of the probabilities for 7 qubits after 100 cycles. Here, decoherence dominates and we observe a tall narrow peak around 1. **b** In order to measure convergence of the measured histogram to an exponential distribution, we compute their distance as a function of the number of cycles. Distance is measured using the KL-divergence (see Eq. 2). We find that a maximum overlap occurs after just two cycles, after which decoherence increases their distance.

nential distribution of weighted probabilities. The dark solid line in Fig. F.3a corresponds to such a distribution and is simply given by $e^{-\text{probability}\times\text{N}_{\text{states}}}$; this is also referred to as a Porter-Thomas distribution [28, 156]. The universal and exponential behavior of the data leads us to conclude that the dynamics are uniformly exploring the state-space. Deviations from an exponential distribution are the result of decoherence which drives the output states to appear with equal probability; this is the behavior that we observe at long times. This demonstration of dynamics that take advantage of the full exponentially growing number of states (a direct measurement of computational complexity) is a key ingredient for experimentally demonstrating quantum supremacy.

In Fig. F.3b we study the number of cycles it takes for the system to uniformly explore all states by comparing the measured probabilities to an exponential distribution. After each cycle, we compare the measured histogram to an exponential decay. The distance between these two distributions is measured using the KL-divergence D_{KL},

$$D_{KL} = S(\rho_{\text{measured}}, \rho_{\text{exponential}}) - S(\rho_{\text{measured}}) \tag{7.2}$$

where the first term is the cross-entropy between the measured distribution ρ_{measured} and an exponential distribution $\rho_{\text{exponential}}$, and the second term is the self-entropy of the measured distribution. The entropy of a set of probabilities is given by $S(P) = -\sum_i p_i \log(p_i)$ and the cross-entropy of two sets of probabilities is given by $S(P,Q) = -\sum_i p_i \log(q_i)$. Their difference, the KL-divergence, is zero if and only if the two distributions are equivalent.

We find that the experimental probabilities closely resemble an exponential distribu-

tion after just two cycles. For longer evolutions, decoherence reduces this overlap. These results suggests that we can generate very complex dynamics with only two pulses - a surprisingly small number.

7.6 Measuring fidelity

In addition to demonstrating an exponential scaling of complexity, it is necessary to characterize the algorithm fidelity. Determining the fidelity requires a means for comparing the measured probabilities P_{measured} with the probabilities expected from the desired evolution P_{expected}. Based on the proposal outlined in Ref. [28], we use the cross-entropy to quantify the fidelity

$$\frac{S\left(P_{\text{incoherent}}, P_{\text{expected}}\right) - S\left(P_{\text{measured}}, P_{\text{expected}}\right)}{S\left(P_{\text{incoherent}}, P_{\text{expected}}\right) - S\left(P_{\text{expected}}\right)} \tag{7.3}$$

where $P_{\text{incoherent}}$ stands for an incoherent mixture with each output state given equal likelihood - this is the behavior that we observe after many cycles. When the distances between the measured and expected probabilities is small, the fidelity approaches 1. When the measured probabilities approach an incoherent mixture, the fidelity approaches 0.

In Fig. 7.4a we show that the desired evolution can be implemented with high fidelity. We find that at short times the fidelity decays linearly with increasing number of cycles, fits to the data are shown as dashed lines. The slope of these lines measures the error per cycle; this slope is displayed inset for each number of qubits. We find that the error scales with the number of qubits at a rate of around 0.4% error/qubit/cycle. If such an

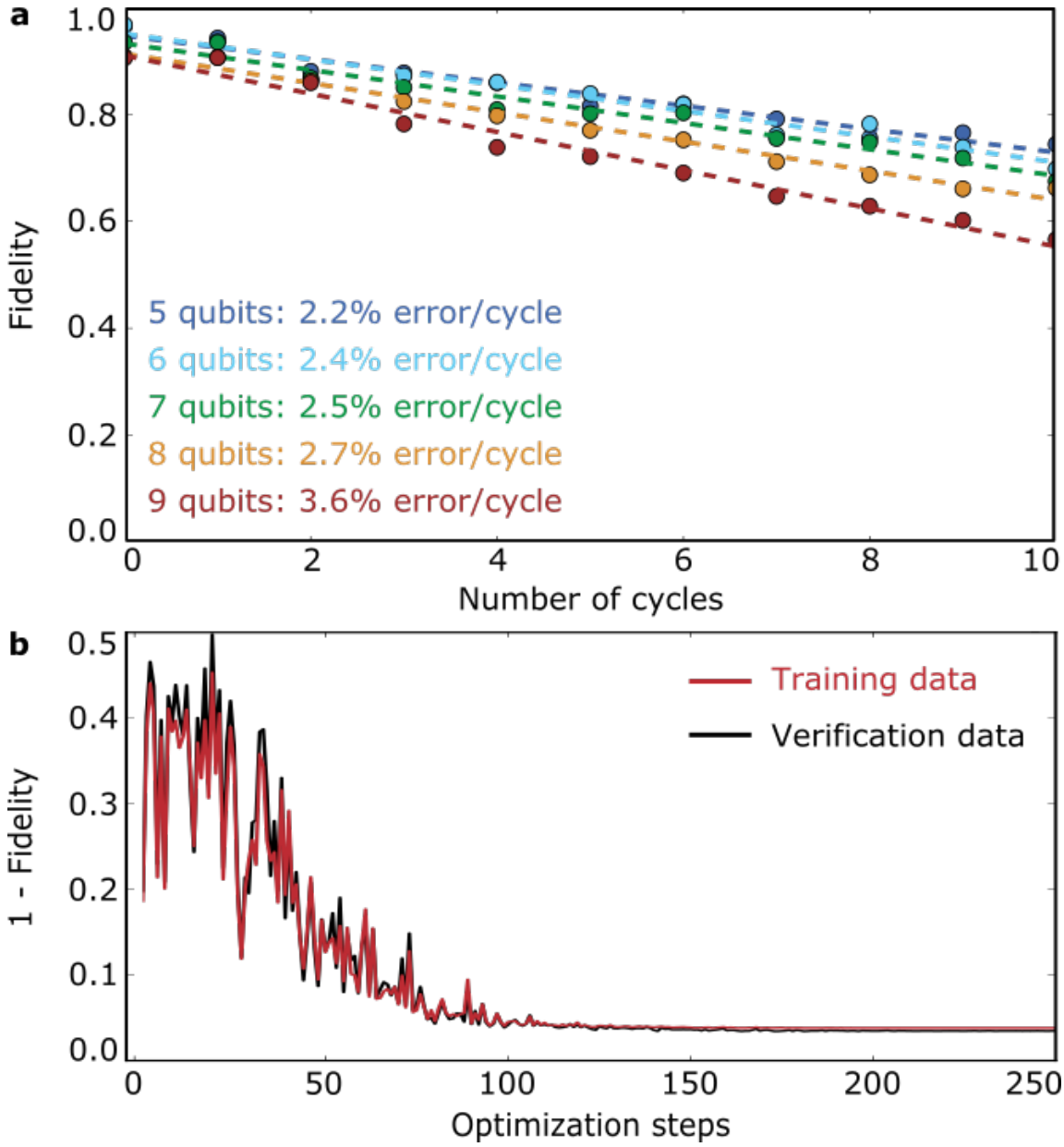

Figure 7.4: **Fidelity: learning a better control model.** **a** Average fidelity decay versus number of cycles for 5 to 9 qubit experiments (circles). The fidelity is computed using Eq. 3. The error per cycle, presented inset, is the slope of the dashed-line which best fits the data. **b** Using the fidelity as a cost-function, we learn optimal parameters for our control model. Here, we take half of the experimental data and use this to train our model. The other half of the data is used to verify this new model, the optimizer does not have access to this data. The corresponding improvement in fidelity of the verification set provides evidence that we are indeed learning a better control model.

error rate extends to larger systems, we will be able to perform 60 qubit experiments of depth 2 while still remaining above 50% total error. These results provide promising evidence that quantum supremacy may be achievable using existing technology.

Predicting the expected probabilities is a major challenge. First, substantial effort has been taken to accurately map the control currents to Hamiltonian parameters; the detailed procedure for constructing this map is outlined in the supplementary materials. Second, when truncating the Hamiltonian to qubits with two-levels, we find poor agreement both theoretically and experimentally. We find a 3-level description must be used to account for virtual transitions to the second excited state during the evolution. When including these states, truncating to a fixed number of excitations lowers the size of the computational Hilbert space from 3^N to approximately 0.15×2.42^N (see Table 1 in supplement): thus a nine-qubit experiment requires accurately modeling a 414-dimensional unitary operation. Determining how many of these states are needed for sufficient accuracy depends on the magnitude of the coupling and is an open question, but should scale somewhere between 2.0^N and 2.5^N.

In Fig. 7.4b we show how techniques from machine learning were used to achieve low error rates. In order to set the matrix-elements of the Hamiltonian, we build a physical model for our gmon qubits. This model is parameterized in terms of capacitances, inductances and control currents. The parameters in this model are calibrated using simple single qubit experiments (see supplement). Here, we use a search algorithm to find offsets in the control model which minimize the error (1 - Fidelity). Figure 7.4b shows the er-

ror, averaged over cycles, versus the number of optimization steps. Prior to training the model, the data is split into two halves - a training set (red) and a verification set (black). The optimization algorithm is only provided access to the training set, the verification set is used only to verify the optimal parameters.

We find that the error in both the training set and the verification set fall significantly by the end of the optimization procedure. The high degree of correlation between the training and verification data suggests that we are genuinely learning a better physical model. Optimizing over more parameters does not further reduce the error. This suggests that the remaining error is not control but results from decoherence. Using the cross-entropy as a cost function for optimizing the parameters of a physical model was the key to achieving high-fidelity control in this experiment.

7.7 Applications

Ideally, in addition to exponential complexity and high fidelity, a quantum platform should offer valuable applications. In Fig. 7.5 we consider applications of our algorithms to many-body physics where the exponential growth in complexity is a significant barrier to ongoing research [169, 19, 147, 166, 162, 154]. By varying the amount of disorder in the system, we are able to study disorder-induced localization. We study localization using 2-body correlations

$$|\langle \hat{n}_i \hat{n}_j \rangle - \langle \hat{n}_i \rangle \langle \hat{n}_j \rangle| \tag{7.4}$$

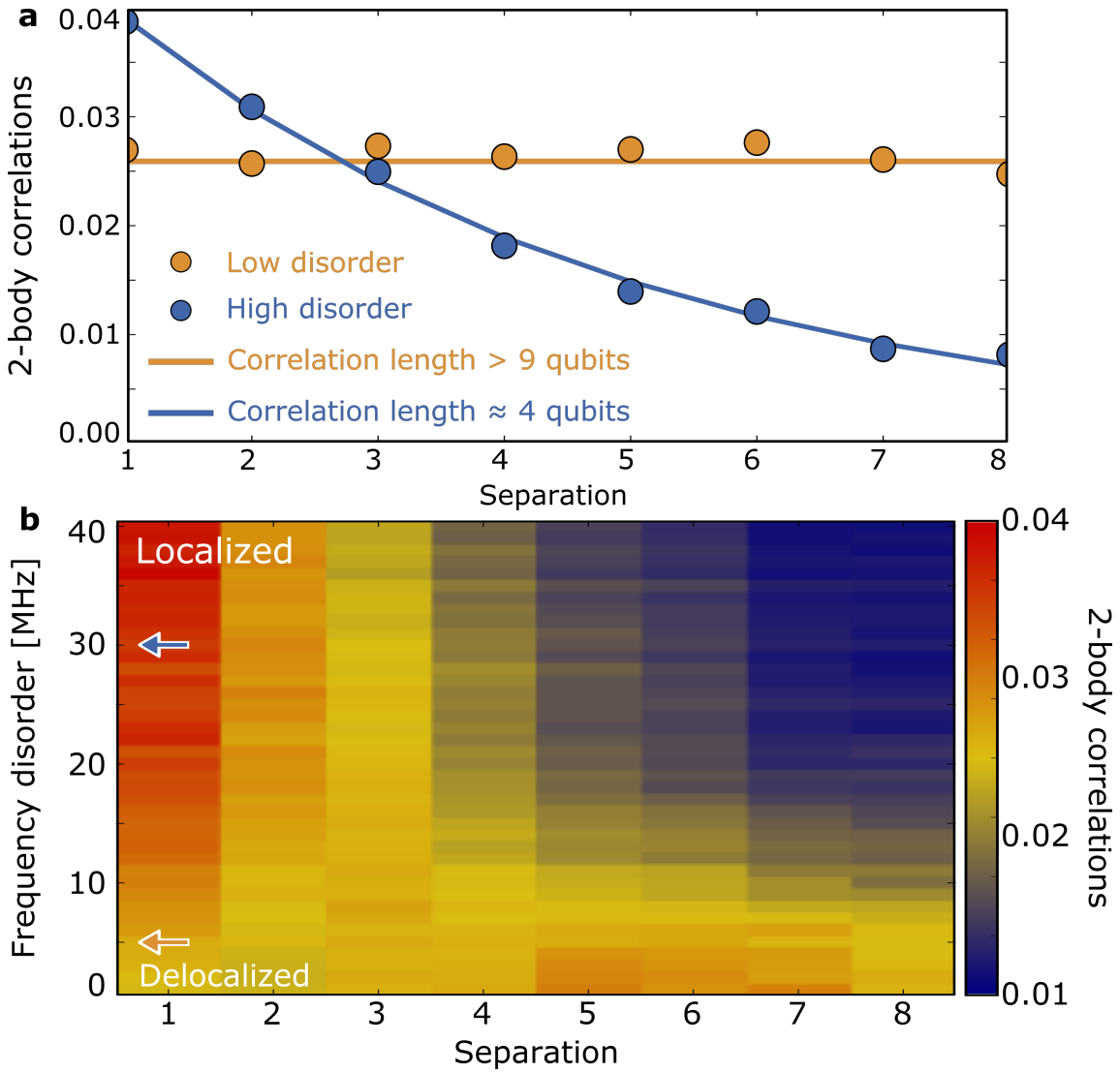

Figure 7.5: **Applications: localization & delocalization. a** Average 2-body correlations (see Eq. 4) as a function of the separation between qubits. The data is shown for two values of disorder strength. At low disorder (gold) the qubit frequencies are set over a range of ± 5 MHz and the 2-body correlations are independent of separation (i.e. qubits at the ends of the chain are just as correlated as nearest neighbors). At high disorder (blue) the qubit frequencies are set over a range of ± 30 MHz and we find an exponential decay in correlations as a function of separation. **b** We map out the correlations as a continuous function of the frequency disorder. Arrows indicate the location of line cuts used in panel **a**. We observe a clear transition from delocalization to localization.

which we average over qubit-pairs, cycles and instances. In panel **a**, we plot the average 2-body correlations versus the separation between qubits. This experiment is performed for both low and high disorder in the qubit frequencies, shown in gold and blue respectively. In panel **b**, this experiment is carried out as we continuously vary the amount of disorder.

At low disorder, we find that the correlations are independent of separation - qubits at opposite ends of the chain are as correlated as nearest neighbors. At high disorder, the correlations fall off exponentially with separation. The rate at which this exponential decays allows us to determine the correlation length. A fit to the data is shown in Fig. 7.5a as a solid blue line allowing us to extract a correlation length of roughly 4 qubits. The study of localization and delocalization in interacting systems provides a promising application of our algorithms.

Here, we have demonstrated an immediate path towards quantum supremacy. We show that the algorithm complexity scales exponentially with the number of qubits and can be implemented with high fidelity. If similar error rates are achievable in future devices with around 50 qubits, we will be able to explore quantum dynamics that are inaccessible otherwise.

Chapter 8

Outlook

8.1 Abstract

In Chapter 7, we demonstrate a 9-qubit algorithm whose complexity is exponential in the number of qubits and has an error of 1% per qubit. For the most part, the technology exists to build a 7x7 array and repeat this algorithm. If we can improve the fidelity by a factor of 4, then we can implement 49-qubit algorithms with a total error close to 10%. This would constitute an impressive realization of a quantum computer.

In order to achieve this goal, dedicated effort will need to be spent on improving coherence and algorithms. In this chapter, we introduce an alternative coupler design which is calculated to have similar performance to our typical devices but with the potential for higher coherence. In addition, we discuss algorithms where both phase-flip and bit-flip errors can be detected; this has the potential to take us a significant step towards our target error rates. The potential for high-fidelity algorithms on a 7x7 array

is an exciting goal for ongoing research.

8.2 Two approaches for coupler design

Tunable coupling offers greater flexibility when designing algorithms but comes at the cost of greater device complexity. It is important to engineer the coupling circuit in such a way that the impact on qubit coherence is minimal. In Fig. 8.1 I show two possible designs for tunable coupling. The top panel shows a circuit for tunable capacitive coupling. The lower panel shows the same tunable inductive coupling circuit from Chapter 1, however, now we include the capacitance of the coupler in our understanding of the circuit.

Despite the rather significant differences between these two designs, we can understand their behavior in a similar way. Using the same techniques as in Chapter 1, we can construct the capacitance and inductance matrices for these two circuits. For the tunable capacitive coupler (panel **a**), the capacitance matrix is given by

$$\tilde{C} = \begin{bmatrix} C_q + C_{qq} + C_{qc} & -C_{qc} & -C_{qq} \\ -C_{qc} & 2C_{qc} + C_c & -C_{qc} \\ -C_{qq} & -C_{qc} & C_q + C_{qq} + C_{qc} \end{bmatrix} \tag{8.1}$$

and the inductance matrix is simply diagonal with elements $\{L_q, L_c, L_q\}$. For the tunable

inductive coupler, the inductance matrix is given by

$$\tilde{L} = \begin{bmatrix} L_q - M_{\text{eff}} & \frac{M}{L_2} L_c & -M_{\text{eff}} \\ \frac{M}{L_2} L_c & L_c & \frac{M}{L_2} L_c \\ -M_{\text{eff}} & \frac{M}{L_2} L_c & L_q - M_{\text{eff}} \end{bmatrix} \tag{8.2}$$

where $M_{\text{eff}} = \frac{M^2}{L_1+L_2}$, $L_c = \frac{L_1 L_2}{L_1+L_2}$ and the capacitance matrix is diagonal with elements $\{C_q, C_c, C_q\}$.

Despite the apparent complexity of Eqs. 8.1 and 8.2, the resulting coupling is quite easy to understand. The top right matrix element is a direct coupling between the qubits and the strength of the interaction can be found using the results in Chapter 1. The effect

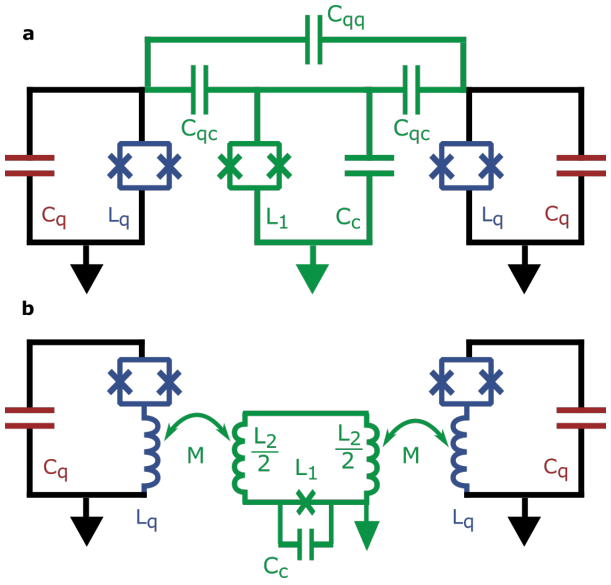

Figure 8.1: **Coupling qubits.** Two implementations of tunable coupling. **a** Tunable capacitive coupling. **b** Tunable inductive coupling. Note that L_q refers to the series inductance of the qubit junctions and linear inductance. In both cases, the coupling is controlled by an applied flux which tunes the effective junction inductance of the coupler.

of the coupler's mode can be understood by looking at the eigenvalues of the coupled system when $C_{qq} = 0$. For identical qubits and a high frequency coupler, the symmetric and anti-symmetric modes have eigenvalues

$$\omega_+ = \omega_q \tag{8.3}$$

$$\omega_-^2 = \frac{1}{2}\frac{1}{1-2\kappa_{qc}^2}\left(\omega_q^2 + \omega_c^2 - \sqrt{\left(\omega_q^2 - \omega_c^2\right)^2 + 8\kappa_{qc}^2\omega_q^2\omega_c^2}\right) \tag{8.4}$$

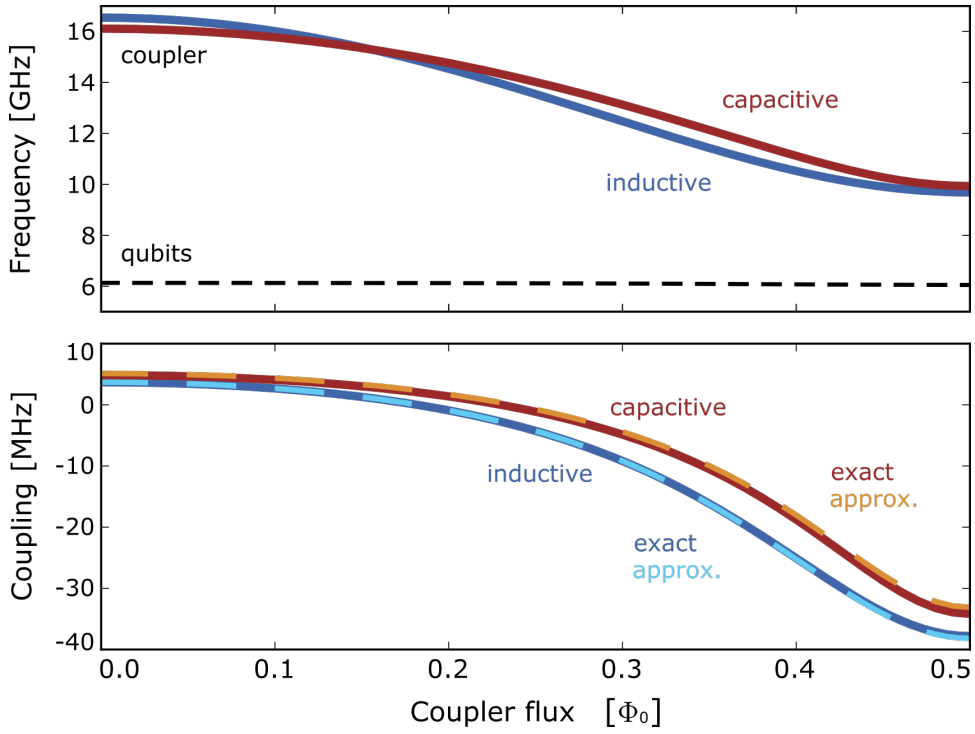

Figure 8.2: **Numerical simulations of tunable coupling circuits.** Coupler-mode frequency versus control flux for both the capacitive and inductive circuits is shown in the top panel; the resulting coupling is shown in the lower panel. The exact solution is calculated by finding the eigenvalues of the 3x3 matrices. The approximate solution is calculated by summing Eq. 8.5 and with the direct coupling.. Circuit parameters for the capacitive circuit: $L_q = 7\,\text{nH}$, $C_q = 90\,\text{fF}$, $L_1 = 2.1\,\text{nH}$, $C_c = 20\,\text{fF}$, $C_{qc} = 10\,\text{fF}$, $C_{qq} = 0.75\,\text{fF}$. Circuit parameters for the inductive circuit: $L_q = 7\,\text{nH}$, $C_q = 90\,\text{fF}$, $L_1 = 1.0\,\text{nH}$, $L_2 = 2.0\,\text{nH}$, $C_c = 140\,\text{fF}$, $M = 0.2\,\text{nH}$. Note that for the capacitive design, the coupler has been modeled with asymmetric junctions so that the mode has a minimum frequency - this makes the comparison simpler.

where ω_q is the frequency of the qubits, ω_c is the frequency of the coupler and κ_{qc} is the coupling efficiency between the qubit and the coupler. The coupling strength between the qubits is defined by half the frequency splitting of these two modes

$$g = \frac{1}{2}\left(\omega_- - \omega_+\right) \tag{8.5}$$

$$\approx \frac{g_{qc}^2}{\omega_q - \omega_c}\frac{\omega_q}{\omega_c}\frac{2\omega_q}{\omega_q + \omega_c} \tag{8.6}$$

where g_{qc} is the direct coupling between the qubit and the coupler. The second line is the lowest order expansion in κ_{qc}. The first term is the typical expression for off-resonance coupling of two-level systems and the last two terms are a correction of order 1.

The total coupling be can found (approximately) by summing the direct and indirect contributions. This approximate model and the exact solution (found by computing the eigenvalues of the 3x3 matrices) are plotted in Fig. 8.2. Both circuits achieve similar performance. Which design should be used therefore depends on which can implemented with the highest coherence.

For all of the experiments described in this thesis, we have used the tunable inductive coupling circuit. This scheme has the advantage that the direct matrix element is tunable and therefore can be designed without relying on lossy capacitive circuit elements. However, inductive coupling requires a long thin wire shunting the qubit. This wire can lead to loss as well as fabrication defects. These issues become of even greater concern in a 2D array where a single thin wire needs to connect each qubit to 4 couplers, spanning a distance of roughly 2 mm. There are additional concerns regarding the viability of the

inductive design for differential qubits, a possible future direction. Alternatively, one can choose tunable capacitive coupling. The advantage of capacitive coupling lies in the simplicity of the circuit design - the large features are generally low loss. However, this design relies heavily on the coupler's mode and dissipation in this circuit can damp the qubit (this can be understood treating it as a Purcell effect). The trade-off between these two designs needs to be understood carefully in the context of high-fidelity multi-qubit gates in a 2D architecture.

8.3 Error detection

High fidelity algorithms on small arrays (with 50 to 100 qubits) may allow for commercially viable applications prior to the realization of large error corrected arrays (with 100,000 to 1,000,000 qubits)[28, 57]. Developing error mitigation strategies for small scale systems could take us a significant step towards realizing such a goal. In Chapter 7 we demonstrate algorithms which are first order insensitive to bit-flip errors. In this section, we develop an algorithm which is first order insensitive to both bit-flip and phase-flip errors.

8.3.1 Phase-flip error detection

In Fig. 8.3, we present a technique for detecting phase-flip errors. Similar to the gate sequence described in the introductory chapter to this thesis, we numerically simulate

the evolution of 6 qubits under the control Hamiltonian

$$H_z = \sum_i \frac{g}{2}\left(\sigma_x^i \sigma_x^{i+1} + \sigma_y^i \sigma_y^{i+1}\right) + J\sigma_z^i \sigma_z^{i+1} \tag{8.7}$$

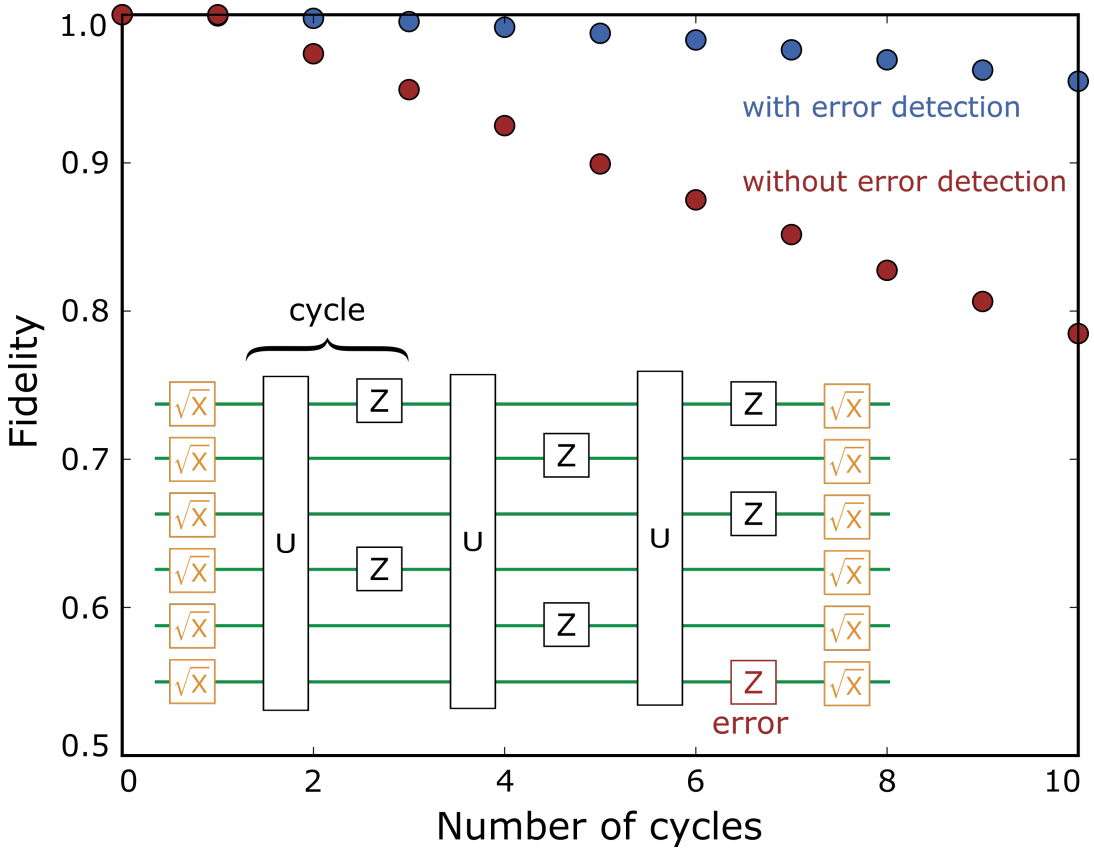

Figure 8.3: **Numerical simulations of error detection scheme.** The gate sequence (shown inset) begins and ends with a 90-degree x-rotations on all six qubits. One cycle of evolution is given by evolving Eq. 8.7 for $gt = \pi$ and $Jt = \pi/4$, followed by z-rotations on an even number of qubits. This is the ideal evolution. Errors are introduced by placing z-rotations after each cycle on every qubit with probability 0.005. The ideal probabilities and the erroneous probabilities (averaged over random instances of errors) can be compared to get a fidelity. The fidelity was computed using the cross-entropy (see Chapter 7 for details). Probabilities from 500 random instances of evolution were used (generated by placing the z-rotations in different places). Given that the evolution conserves parity (and single z-errors change the parity), instances where a single error occurred can be removed from the averaging process. The fidelity with this error detection is shown in blue. The fidelity without the x-rotations is shown in red. Without the x-rotations, phase-flip errors go undetected and the error rate is larger.

and then apply z-rotations on an even number of randomly selected sites (see inset). This procedure is repeated several times. In order to detect phase-flip errors, we start and end with a 90-degree x-rotation on every qubit. An intuitive way of understanding the effect of this rotation is to treat it as a change of basis taking $\sigma_z \to \sigma_y$, $\sigma_y \to -\sigma_z$ and $\sigma_x \to \sigma_x$. In this basis, the control Hamiltonian takes the form

$$H_x = \sum_i \frac{g}{2}\left(\sigma_x^i \sigma_x^{i+1} + \sigma_z^i \sigma_z^{i+1}\right) + J\sigma_y^i \sigma_y^{i+1} \tag{8.8}$$

Terms like $\sigma_x^i \sigma_x^{i+1}$ and $\sigma_y^i \sigma_y^{i+1}$ can change the number of excitations by 2 (they flip pairs of bits). In the original basis, excitation number was conserved because these two terms had the same coefficient (this cancels out the 2-excitation transitions). Now that they are different, we no longer have excitation number conservation, but instead we have parity conservation (or excitation number conservation modulo 2). If we start with an even or odd parity state, we expect the output states to have the same parity. However, if a phase-flip occurs, the z-rotation becomes an x-rotation and changes the parity. Errors of this form can then be detected and removed. Note that the number of z-rotations is chosen to be even so as to have no net effect on the parity.

In Fig. 8.3, we simulate errors in the evolution and quantify the impact on the algorithm's fidelity. After each cycle, a phase-flip is applied to each qubit with a certain probability. The desired evolution can be compared to the erroneous evolution (averaged over random error instances) in order to obtain a fidelity. The fidelity versus number of cycles is shown with and without the error detection scheme. We find that the error is

improved by a significant factor. The degree of protection as a function of error rates and number of qubits is an important area of ongoing study.

8.3.2 Bit- and phase-flip error detection

While the previous algorithm is protected from phase-flip errors, it is important to ask if it is simultaneously protected from bit-flip errors. The answer to this depends on our model of the errors. For example, if the bit-flips are modeled as random σ_y operations, then $\sigma_y \rightarrow -\sigma_z$ implies that these errors will go undetected. On the other hand, σ_x errors would still be σ_x errors and would be detectable. Measurement errors would occur after the rotations and would simply change the excitation number by 1 and would be easily detected. Energy relaxation is best modeled as $\sigma_- = (\sigma_x - i\sigma_y)/2$; after rotating the basis, these errors will only be detected 50% of the time. This suggests that by using this scheme we may be able to detect (and eliminate to first order) phase-flip errors and measurement errors, as well as reduce errors from photon loss by a factor of 2.

Appendix A

Supplementary Information for Chapter 2

A.1 Calibration

A key aspect of our design is the independent control of the qubit frequency and inter-qubit coupling. The resonance frequency of the individual qubits depends on the impedance of the coupling circuit; this is true for any coupling scheme. In our design, the total qubit inductance L is given by

$$\begin{aligned} L &= L_J + L_g||(L_g + L_c) \\ &= L_J + L_g - M \end{aligned} \tag{A.1}$$

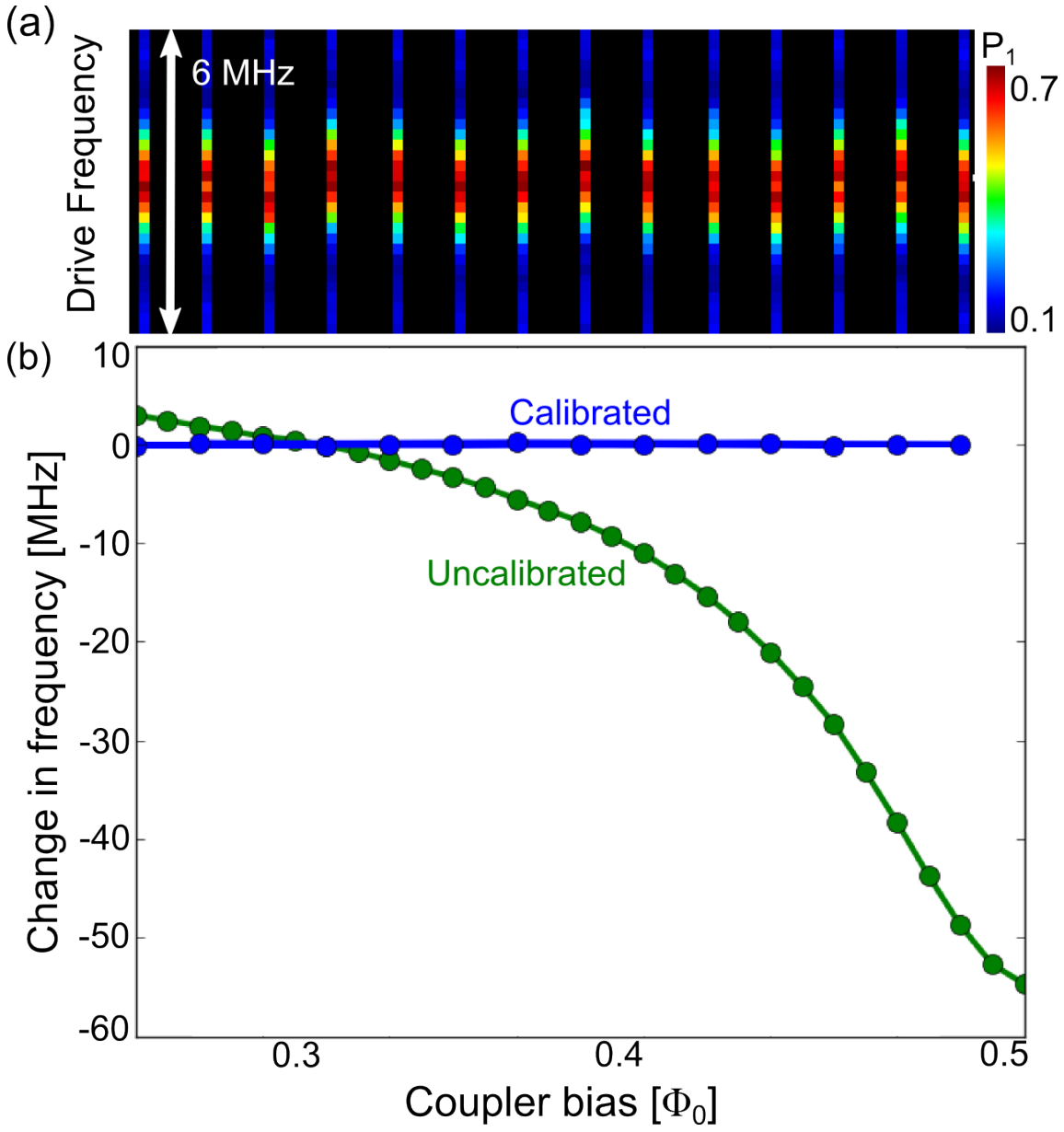

Figure A.1: (a) The frequency of Q_1, as a function of the coupler flux bias while the second qubit is far detuned. For each value of the coupling strength, we compensate the frequency shift due to the change in inductance, sweep the microwave drive frequency and measure the qubit excited state probability P_1. Each line is fit for a peak, with the results plotted in panel (b) in blue. The associated standard deviation is 110 kHz. The same experiment is performed without the calibration and overlayed in green.

where —— stands for "in parallel with" and M is the mutual inductance given in Eq. (1) of the main text. Changing the inter-qubit coupling is achieved by changing the mutual inductance, which additionally shifts the qubit's resonance frequency. We are able to compensate for this change in inductance using the tunable inductance of the qubit junction L_J. The compensation is achieved by first measuring the qubit frequency ω as a function of the qubit flux bias Φ_Q and then as a function of coupler bias Φ_C. The qubit frequency is given by $\omega = 1/\sqrt{LC} - \alpha$ where C is the qubit capacitance and α is the anharmonicity. Solving this expression for L and using the measured data for ω yields $L(\Phi_C)$ and $L(\Phi_Q)$. From the first expression we determine the change in inductance ΔL due to a change in Φ_C. Using the second expression we calculate the qubit flux bias required to shift L by $-\Delta L$. Summing these two terms yields zero net change in the qubit inductance. Note that the number of measurements required to compensate for the frequency shift scales linearly with the number of qubits and couplers.

The results of this compensation protocol are shown in Fig. A.1(a). For each value of the coupler flux bias, we sweep the microwave drive frequency and measure the excited state probability P_1. The frequency is almost completely independent of the coupler bias, with a standard deviation of 110 kHz. We fit each vertical column of data for a peak and plot the results in blue in Fig. A.1(b). We perform an identical measurement without calibration and overlay the results in green. We see that the qubit frequency shifts by over 60 MHz ($\sim g/2\pi$) as we vary the coupler bias.

A.2 Coherence

The most important part of constructing this tunable coupling architecture is to maintain the coherence inherent in the Xmon design. There are two primary sources of loss associated with the modifications that we have made: capacitive coupling to surface defects on the coupling structure and inductive coupling to the added bias line. The voltage divider created by L_J and L_g reduce capacitive losses by a factor of over 2000. The coupler bias line has a mutual inductance to the junction loop of 1 pH; this 1 pH coupling to a 50 Ohm line introduces a decoherence source with an associated T_1 of greater than 200 μs at 80 MHz of coupling. We measure T_1 as a function of the qubit frequency and plot the results in Fig. A.2(a). These results are comparable to the performance of previous Xmon devices with similar capacitor geometry and growth conditions. We observe no indication that the T_1 is reduced as we vary the coupling strength, with data shown in Fig. A.2(b).

It is important to ensure that the coupling circuit does not introduce additional dephasing to the qubits. As discussed in the Ref [126] and [165], the dephasing rate can be minimized by reducing the sensitivity of the qubit frequency to the coupler flux bias, i.e., $df_{10}/d\varphi_{Coupler}$. We have designed our gmon with $df_{10}/d\varphi_{Coupler} < 0.1\,\mathrm{GHz}/\Phi_0$, nearly two orders of magnitude less than that of the qubit flux bias $df_{10}/d\varphi_{Qubit}$. As a consequence, near the qubit optimal bias point, we achieved a T_φ of $3 \sim 4\,\mu$s over the full range of coupler bias, with data shown in Fig. A.2(c). The measured coherence times are comparable to that of Xmon qubits and are independent of the coupler bias. These

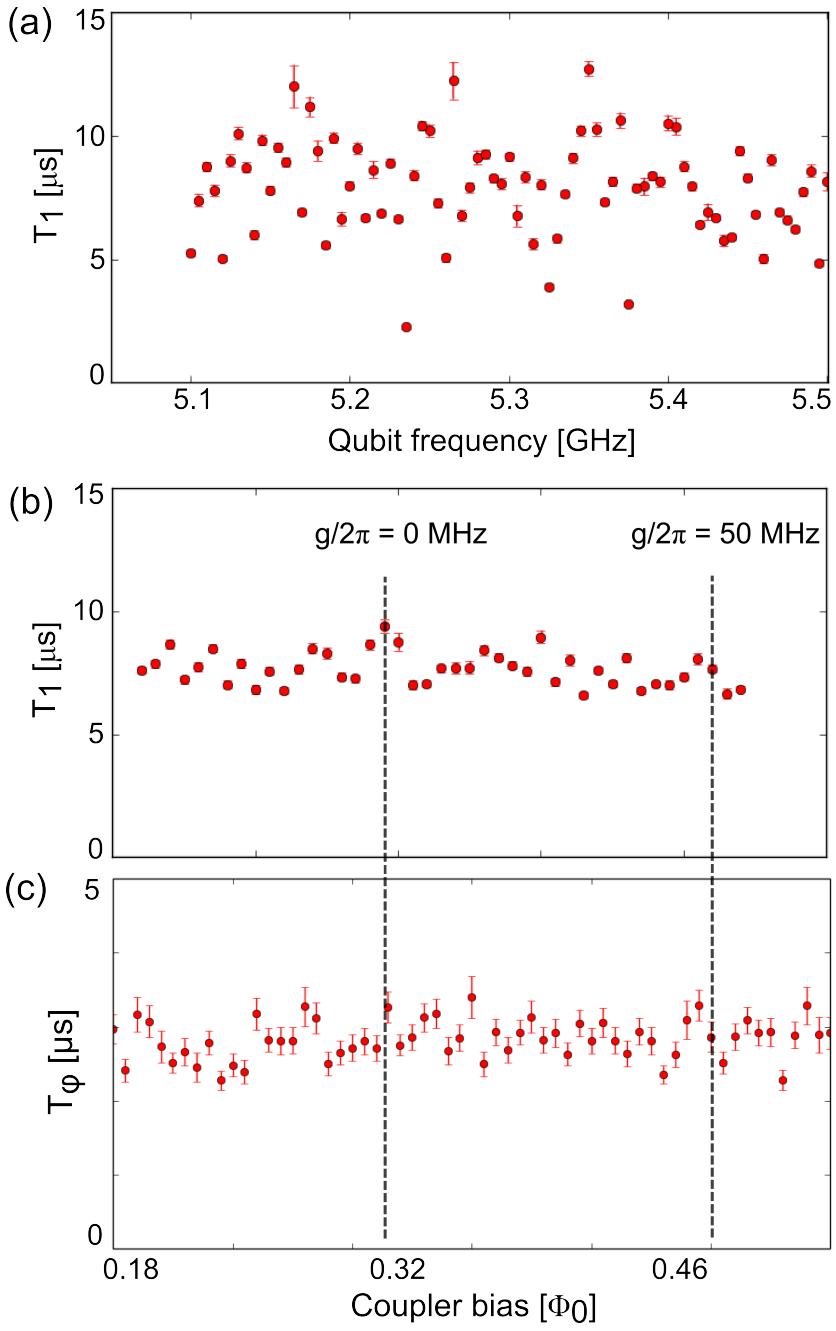

Figure A.2: (a) T_1 of Q_1 as a function of the qubit frequency, when $g = 0$. These results are comparable to that of the Xmon with similar capacitor geometry and growth conditions. (b) T_1 of Q_1 as a function of the coupler bias, when the qubit frequency is set to 5.3 GHz. We find no dependence of the T_1 on the coupling strength.

results demonstrate that our gmon design preserves the high coherence of the Xmon qubit.

A.3 Zero coupling

An important application of tunable coupling is to isolate individual qubits for local operations by turning off the coupling. We characterize the zero coupling of our architecture using a modified swap spectroscopy measurement. We bring the two qubits on resonance and vary the coupler flux bias. For each value of the coupling strength, we excite Q_1, wait a variable delay time and measure its excited state probability. As the results in Fig. A.3(a) show, over a wide range of biases, the two qubits can interact and swap an excitation. At a coupler bias of $\sim 0.32\Phi_0$, there is no excitation swapping between the two qubits, indicating that the coupling is turned off. Focusing on zero coupling, we examine the excited state probability P_1 of Q_1 over a extended delay time, with the results shown in Fig. A.3(b). We see no indication of swapping between the two qubits after $6\,\mu$s. This places an upper bound on residual coupling of 50 kHz, resulting in an on/off ratio > 1000.

A.4 CZ error budget

We perform two measurements to determine the sources of errors in our CZ gate. The dominant contribution to the 0.93% error comes from decoherence. We measure this

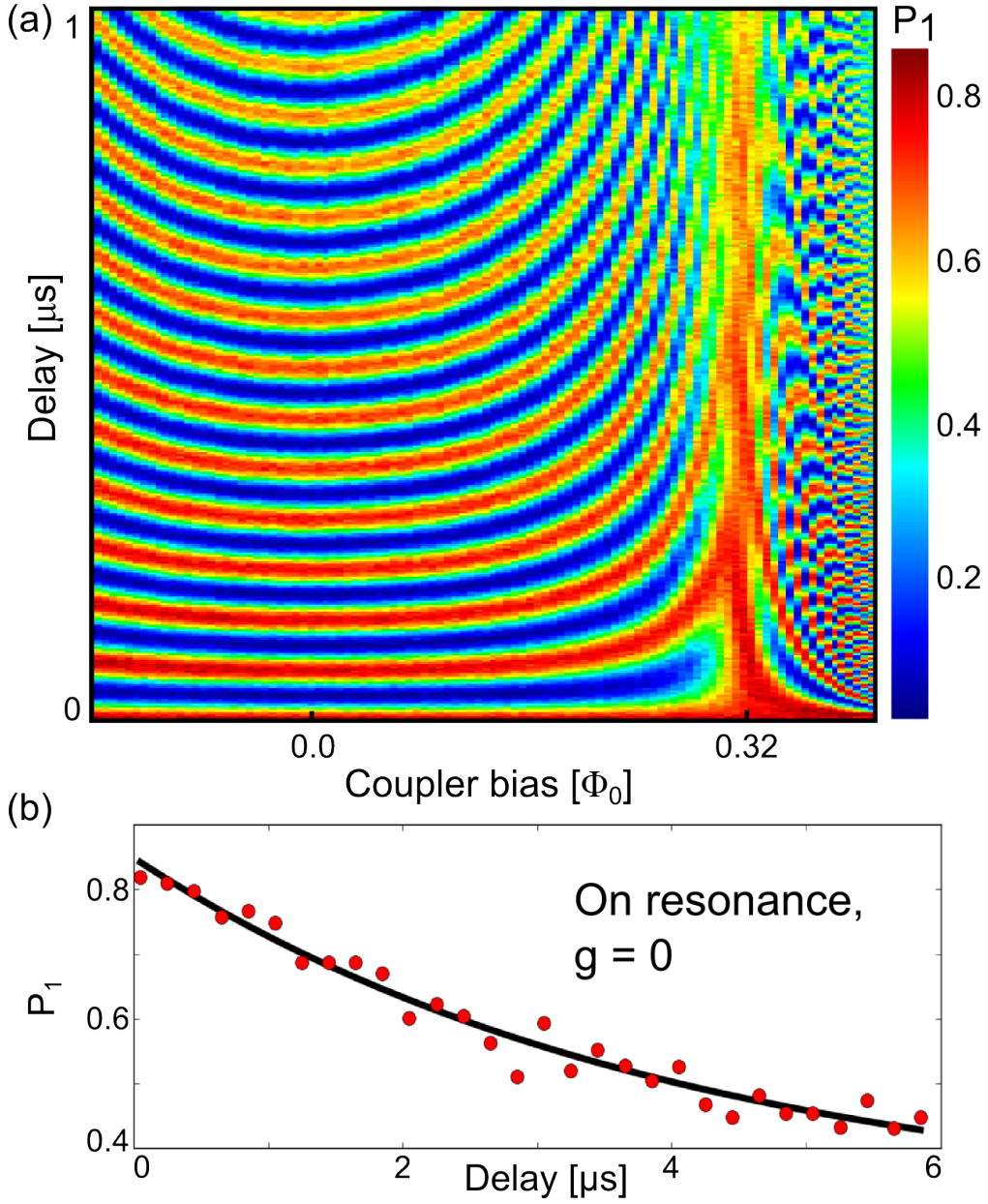

Figure A.3: (a) Swap spectroscopy for Q_1, as a function of the coupler flux bias, with the two qubits on resonance. For each value of the coupling strength, we excite Q_1, wait a variable delay time and measure the excited state probability P_1. We see no excitation swapping between the two qubits when coupler bias is $\sim 0.32\Phi_0$, indicating that the coupling is turned off. (b) We set the coupler bias to this value and examine the excited state probability P_1 of Q_1 over an extended delay time. We see no indication of swapping between the two qubits after 6 μs (placing an upper bound on residual coupling of 50 kHz.)

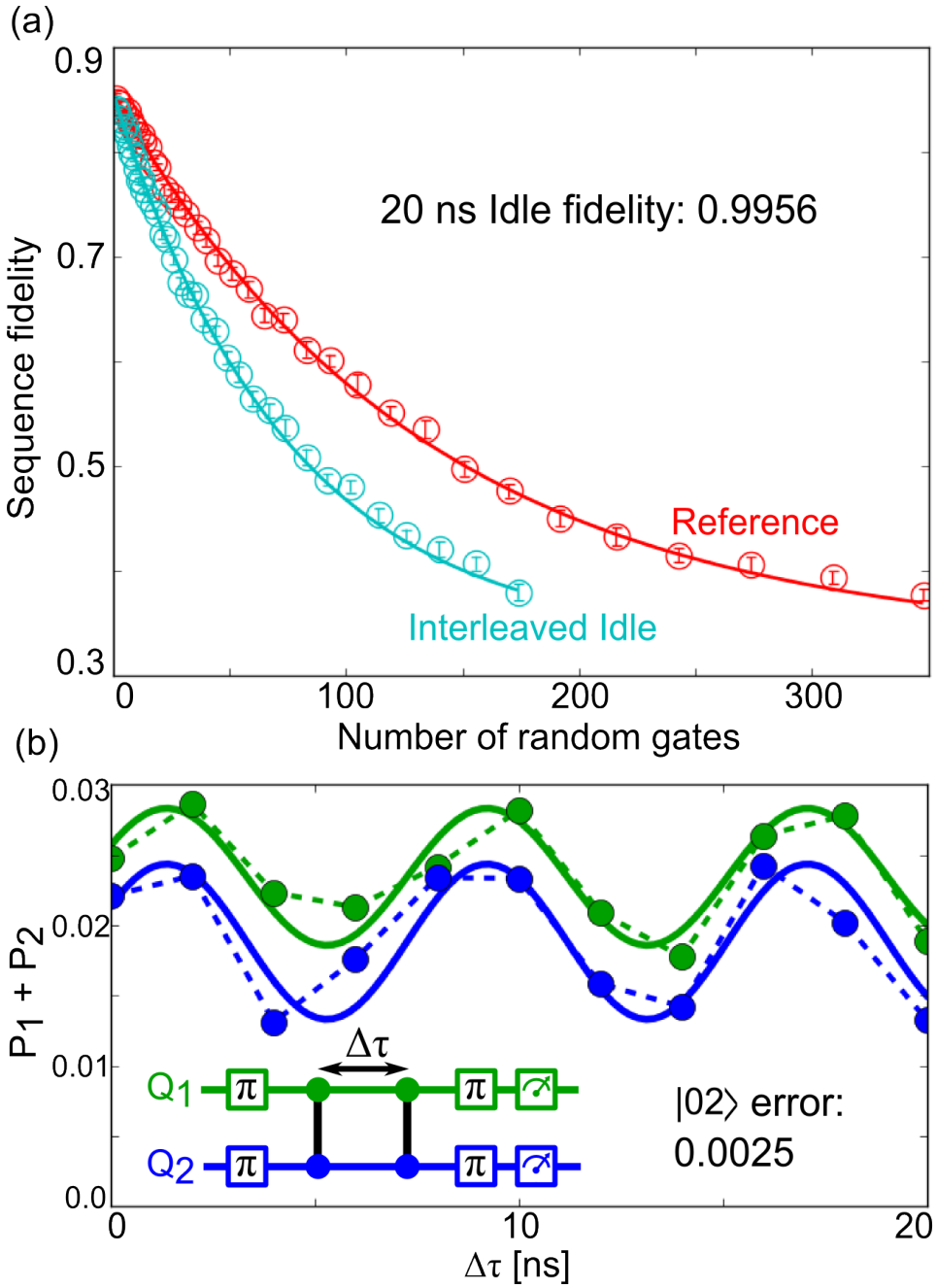

Figure A.4: (a) Interleaved randomized benchmarking on a 20 ns two-qubit idle gate ($g = 0$). We extract a fidelity of 99.56%, which suggests a decoherence error of 0.66% for the 30 ns CZ gate. (b) Inset: The pulse sequence for the Ramsey error filter technique. Main panel: The measured excited state probability $P_1 + P_2$ as a function of the delay between two CZ gates. We observe the expected sinusoidal oscillation with a peak-to-peak amplitude of 1%. The non-adiabatic error from $|02\rangle$ state leakage is 1/4 of the oscillation amplitude and is therefore $\sim 0.25\%$.

contribution by performing interleaved randomized benchmarking on a 20 ns two-qubit idle gate, with $g = 0$. We first measure a reference curve without the interleaved idle and plot the data in red in Fig.A.4(a). We then perform an interleaved randomized benchmarking sequence in which we insert an idle gate between each random Pauli gate, and overlay the data in blue. Comparing these two curves allows us to extract a fidelity of 99.56% for a 20 ns two-qubit idle gate. Scaling this error rate by a factor of 1.5 to account for the relative length of the CZ yields an error from decoherence of $\sim 0.66\%$.

The next largest contribution to errors are from non-adiabatic transitions from the $|11\rangle$ to $|02\rangle$ state. We directly measure this transition using a Ramsey error filter technique [120]; the pulse sequence is shown inset in Fig. A.4(b). We initialize the system in the $|11\rangle$ state and then apply two CZ gates separated by a variable delay time. Afer applying a π-pulse to each qubit, we measure the uncorrelated excited state probability for each qubit. The results are shown in Fig. A.4(b), where we see the expected oscillations that result from the interference between two CZ gates. The frequency of the oscillation is set by the detuning of the $|11\rangle$ and $|02\rangle$ states which was 130 MHz, corresponding to a period of 8 ns. The $|02\rangle$ state leakage error is given as 1/4 of the oscillation amplitude (peak-to-peak). For our 30 ns CZ gate, we measured a non-adiabatic error of $\sim 0.25\%$. This is suprisingly small considering such a short gate time, and can be exponentially surpressed with increasing gate length.

A.5 Transmon physics

The operation of the transmon has been previously described in detail [106]. Here, we give a simplified calculation in the phase basis that is useful to describe more complex transmon circuits, as for the gmon architecture.

Since the transmon produces qubit behavior from a weak non-linearity, we first review the physics of a linear inductor-capacitor (LC) oscillator. In terms of physical variables charge q and flux Φ, the oscillator Hamiltonian is given by

$$\hat{H}_o = \frac{\hat{q}^2}{2C} + \frac{\hat{\Phi}^2}{2L} \ . \tag{A.2}$$

Here the quantum operators of flux and charge obey the standard commutation relation $[\hat{\Phi}, \hat{q}] = i\hbar$. The oscillator frequency is the classical value $\omega = 1/\sqrt{LC}$, and eigenstates m have energy $E_m = \hbar\omega(m + 1/2)$. The ground state wavefunction is given by

$$\Psi_0(\Phi) \propto \exp[-(\omega C/2\hbar)\Phi^2] \ . \tag{A.3}$$

Note that the width of the wavefunction is set by the oscillator impedance $Z_o = 1/\omega C = \omega L = \sqrt{L/C}$. Varying this impedance changes the widths of the charge and flux wavefunctions, as illustrated in Table A.1. The impedance is also important since it is used to describe how strongly the oscillator couples to other modes. The flux and charge

operators are conveniently expressed in terms of the raising and lowering operators

$$\hat{\Phi} = (\hbar/2\omega C)^{1/2}(a^\dagger + a) \tag{A.4}$$

$$\hat{q} = \left(\hbar\omega C/2\right)^{1/2} i(a^\dagger - a) \ . \tag{A.5}$$

For a tunnel junction with shunting capacitor, the charge on the metal island takes on discrete values corresponding to the number of Cooper pairs n. The Hamiltonian for this system is given by

$$\hat{H}_t = 4E_c(\hat{n} - n_g)^2 - E_J \cos\hat{\delta} \ , \tag{A.6}$$

where $E_c = e^2/2C$ is the charging energy and $E_J = I_0\Phi_0/2\pi$ is the Josephson energy from the tunnel junction, with critical current I_0. The normalized coordinates are related to ordinary electrical variables by $\hat{q} = 2e\hat{n}$ and $\hat{\Phi} = (\Phi_0/2\pi)\hat{\delta}$, and thus their commutation relation is $[\hat{\delta}, \hat{n}] = i$. Here we have included a *continuous* charge bias n_g, produced for example by a small coupling capacitor with voltage bias. The Josephson term can be written as $\cos\hat{\delta} = [\exp(+i\hat{\delta}) + \exp(-i\hat{\delta})]/2$, corresponding to number displacement operators $\exp(\pm i\hat{\delta})$ that couple states that differ by one in the number of Cooper pairs.

C	Z_o	$\langle\hat{q}^2\rangle$	$\langle\hat{\Phi}^2\rangle$
small	large	small	large
large	small	large	small

Table A.1: Table of relative width of charge and flux wavefunctions as capacitance C (and impedance Z_o) are changed.

The form of the solution for this Hamiltonian depends on the ratio of these two energies. For small capacitance where $E_c \gg E_J$, the "Cooper-pair box" limit, the charging energy dominates, and the eigenstates are described by one or the superposition of two number states. The states sensitively depend on the gate charge n_g. This is death to qubit physics, since fluctuations of gate charge from the movement of trapped charge around the junction produces large qubit decoherence from dephasing.

We are interested in the large capacitance "transmon" limit, where $E_J \gg E_c$. Here, the dependence of qubit energy on the gate charge becomes exponentially small, so qubit decoherence from charge fluctuations essentially vanishes. To understand this, note that for large capacitance the phase fluctuations are small. The potential $\cos\hat{\delta}$ can then be expanded in powers of $\hat{\delta}$, with the lowest non-trivial term giving an inductive energy. First considering the case $n_g = 0$, one obtains a harmonic oscillator-like Hamiltonian

$$H_{to} = 4E_c\hat{n}^2 + (\Phi_0/2\pi)^2\hat{\delta}^2/2L_J \ , \tag{A.7}$$

where the Josephson inductance is $L_J = (\Phi_0/2\pi)^2/E_J = \Phi_0/2\pi I_0$. We can thus use harmonic oscillator solutions as the basis eigenstates for perturbation theory.

Note that formally the charge wavefunction is a delta-function comb with spacings $2e$ in charge, with amplitudes given by the harmonic oscillator solution. The charge comb corresponds to a phase wavefunction periodic in 2π. As the capacitance increases, the number of states in the charge wavefunction increases, so that the relative separation of the teeth in the charge comb become so closely spaced as to look like the normal

continuous solution for the harmonic oscillator. In phase, this implies the wavefunction is so localized in phase that the 2π periodicity does not matter.

The phase wavefunction has a width $\langle\hat{\delta}^2\rangle$ that can be computed using the exponential term in the wavefunction given by Eq. (A.3)

$$1 = \frac{\omega C}{\hbar}\Big(\frac{\Phi_0}{2\pi}\Big)^2\langle\hat{\delta}^2\rangle \ , \tag{A.8}$$

which gives

$$\langle\hat{\delta}^2\rangle = \sqrt{8E_c/E_J} \tag{A.9}$$

$$= Z_J/(R_K/8\pi) \ , \tag{A.10}$$

where in the last equation $R_K = h/e^2 = 25.8\,\mathrm{k\Omega}$ is the resistance quantum, and $R_K/8\pi = 1.026\,\mathrm{k\Omega}$. The phase basis works well when the mean quantum fluctuation of the phase is small, which corresponds to a small E_c/E_J ratio or a junction impedance $Z_J = \sqrt{L_J/C}$ much less than $1\,\mathrm{k\Omega}$.

The effect of the gate charge n_g in the Hamiltonian can be computed by noting that this offset in the operator $\hat{n}$ can be accounted for by the displacement operator $\exp(in_g\hat{\delta})$ applied to the solution of H_t with $n_g = 0$. This is equivalent to imposing periodic boundary conditions at the phase $\delta = \pm\pi$

$$\Psi(-\pi) = \Psi(\pi)\ e^{i2\pi n_g} \ . \tag{A.11}$$

We can estimate the effect of this boundary condition on the eigenstates by noting that it should be proportional to the probability of the wavefunction at $\delta = \pi$. Using the harmonic oscillator solution, the magnitude of the modulation of eigenstate energy from charge n_g should scale approximately as

$$\Delta E \propto |\Psi_0(\delta = \pi)|^2 \tag{A.12}$$

$$= \exp[-(\omega C/\hbar)(\Phi_0/2)^2] \tag{A.13}$$

$$= \exp[-(\pi^2/8)\sqrt{8E_J/E_c}] \ . \tag{A.14}$$

We may calculate the exponential factor precisely by including the non-linear junction energy. Using the WKB theory, with constants $2m = 1/4E_c$ and $\hbar = 1$ from Eq. (A.6) and its commutation relation, we find

$$|\Psi_0(\pi)|^2 = \exp[-2\int_0^\pi d\delta\sqrt{(1/4E_c)E_J(1-\cos\delta)}\,] \tag{A.15}$$

$$= \exp[-\sqrt{8E_J/E_c}] \ , \tag{A.16}$$

matching the result of Ref. [106]. A large E_J/E_c ratio gives exponentially low sensitivity to charge noise.

Note that the phase qubit has vanishing sensitivity to charge noise for two reasons. First, the ratio of E_J/E_c is even larger than for the transmon. Second, the latest versions of the device used a shunting inductor for current biasing. The continuous flow of charge across the junction then shunts any DC change in charge bias. This latter effect is the

purpose of the inductor shunt in the fluxonium device.

For completeness, we compute the change in the harmonic oscillator energy eigenvalues due to the cosine nonlinearity. Starting from

$$\cos\hat{\delta} \simeq 1 - \hat{\delta}^2/2 + \hat{\delta}^4/24 \ , \tag{A.17}$$

the correction to the energy from the fourth order term is

$$\Delta E_m = -E_J \langle m|\hat{\delta}^4|m\rangle/24 \tag{A.18}$$

$$= -\frac{E_J}{24}\Big(\frac{\hbar}{2\omega C}\Big)^2\Big(\frac{2\pi}{\Phi_0}\Big)^4 \langle m|(a^\dagger + a)^4|m\rangle \ . \tag{A.19}$$

The matrix element can be calculated by using the square $(a^\dagger + a)^2 = a^{\dagger 2} + a^2 + 2a^\dagger a + 1$, giving

$$\langle m|(a^\dagger + a)^4|m\rangle = \langle m|a^{\dagger 2}a^2 + a^2 a^{\dagger 2} + (2a^\dagger a + 1)^2|m\rangle \tag{A.20}$$

$$= m(m-1) + (m+1)(m+2) + (2m+1)^2 \tag{A.21}$$

$$= 6m^2 + 6m + 3 \tag{A.22}$$

where in the first equation we have only kept terms that leave $|m\rangle$ unchanged. The change in energy between adjacent states is

$$\Delta(E_m - E_{m-1}) = -mE_c \tag{A.23}$$

as expected. As the unperturbed oscillator frequency can be written as $\hbar\omega = \sqrt{8E_J E_c}$, the fractional change in qubit frequency is $\sqrt{E_c/8E_J}$.

A.6 Series Inductance

We next consider how this physics changes when including an inductance L in series with the Josephson junction. The total phase across the two elements is given by $\delta = \delta_L + \delta_J$. The conservation of current at the node between the two elements gives the constraint $I_L = I_0 \sin\delta_J$, which then can be used to relate the individual phase changes and their derivative

$$\delta_L/L = \sin\delta_J/L_{J0} \tag{A.24}$$

$$d\delta_L/L = d\delta_J \cos\delta_J/L_{J0}\ , \tag{A.25}$$

where we have defined $L_{J0} = \Phi_0/2\pi I_0 = (\Phi_0/2\pi)^2/E_J$ as the Josephson inductance at zero current.

The WKB theory gives a charge sensitivity that includes both Josephson and inductor

energies

$$
\begin{aligned}
&-\ln|\Psi_0(\pi)|^2 \\
=&\sqrt{\frac{1}{E_c}}\int_0^\pi d\delta\sqrt{E_J(1-\cos\delta_J)+(\delta_L\Phi_0/2\pi)^2/2L} && \text{(A.26)}\\
=&\sqrt{\frac{E_J}{E_c}}\int_0^\pi d\delta_J[1+(L/L_{J0})\cos\delta_J] \\
&\qquad\times\sqrt{1-\cos\delta_J+(L/2L_{J0})\sin^2\delta_J} && \text{(A.27)}\\
\simeq&\sqrt{8E_J/E_c}\,(1-0.166\,L/L_{J0})\ , && \text{(A.28)}
\end{aligned}
$$

where the integral was evaluated numerically. The linear expansion in Eq. (A.28) is quite good for $L/L_{J0} \leq 1$

The nonlinearity in the energy levels can be evaluated by noting that the quantum fluctuations of the phase is small, so that we can use the linear relation for phase change $\delta_L/L = \delta_J/L_{J0}$. The junction phase can then be found using an inductance divider relation

$$\delta_J = \frac{L_{J0}}{L+L_{J0}}\delta\ . \tag{A.29}$$

Following Eq. (A.19), the change in energy eigenvalues is proportional to $\langle\hat{\delta}_J^4\rangle = \langle\hat{\delta}^4\rangle/(1+$

$L/L_{J0})^4$, giving

$$\Delta(E_m - E_{m-1}) = -\frac{E_J}{24}\Big(\frac{\hbar}{2\omega C}\Big)^2\Big(\frac{2\pi}{\Phi_0}\Big)^4 \frac{12m}{(1+L/L_{J0})^4} \tag{A.30}$$

$$= -mE_c \frac{1}{\omega^2 L_{J0} C} \frac{1}{(1+L/L_{J0})^4} \tag{A.31}$$

$$= -mE_c \frac{1}{(1+L/L_{J0})^3} \ , \tag{A.32}$$

where for the last equation we have used the resonance condition $\omega^2 = 1/(L+L_{J0})C$. We see that the extra linear inductance lowers the nonlinearity coming from the junction.

Appendix B

Supplementary Information for Chapter 3

B.1 Qubit architecture

There are two fundamental requirements for implementing the quantum dynamics demonstrated in this work: a high level of individual control and long coherence times. In pursuit of these goals, we have designed three transmon qubits with tunable qubit-qubit coupling, tunable frequencies and individual microwave control [38]. Transmon qubits, the Xmon design in particular, have been shown to have long coherence times [17, 18, 106]. The qubits are arranged into a ring in order to explore the model outlined in the main text beyond the more technologically straight-forward two-qubit realization.

A circuit diagram and optical micrographs of our gmon qubits are shown in Fig. B.1.

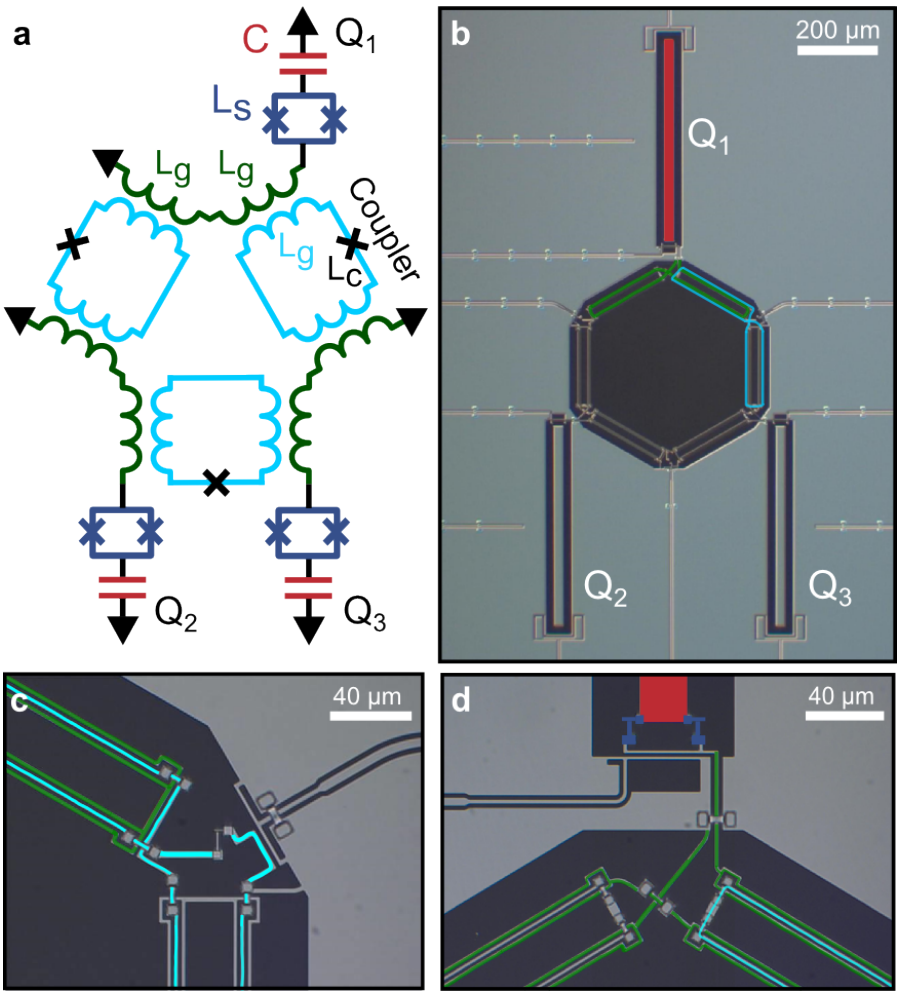

Figure B.1: **gmon architecture.** We have designed a modified version of an Xmon qubit with tunable inter-qubit coupling. Panel **a** shows the circuit diagram for the device. Each qubit is represented as a capacitor ($C = 75\,\mathrm{fF}$) in series with a DC SQUID ($L_S = 8.1\,\mathrm{nH}$) and two inductors ($L_g = 0.35\,\mathrm{nH}$). Each inductor is flux coupled to an RF SQUID ('coupler') through a mutual inductance ($M = 0.2\,\mathrm{nH}$). Applying a flux to the RF SQUID loop modulates the effective junction inductance ($L_C = 0.9\,\mathrm{nH}$) and consequently the inter-qubit coupling strength. The effective SQUID inductances are the values at zero external flux. **b,** Optical micrograph of the device. Grey regions correspond to aluminum; black regions are where the aluminum has been etched away to expose the underlying sapphire substrate to define the qubits and wiring. **c,d,** Optical micrographs showing the coupler and qubit flux biases. The qubit and coupler inductors L_g can be seen highlighted in green and cyan, respectively. All crossover connections are made using dielectric-free airbridges [39].

The individual qubits are composed of a capacitor (red), a DC SQUID (blue), and two inductors in series to ground (green). The capacitor and SQUID form the basis of the standard Xmon qubit with the added inductors each allowing for tunable coupling to a neighboring qubit.

Tunable coupling is achieved through a mutual inductance to a loop containing a Josephson junction (cyan). This loop mediates the interaction between pairs of qubits. An excitation in either qubit generates a current in this loop which then excites the neighboring qubit. The strength of the qubit-qubit interaction g is modulated by applying a flux to the coupler loop; this flux sets the effective junction inductance. If the junction

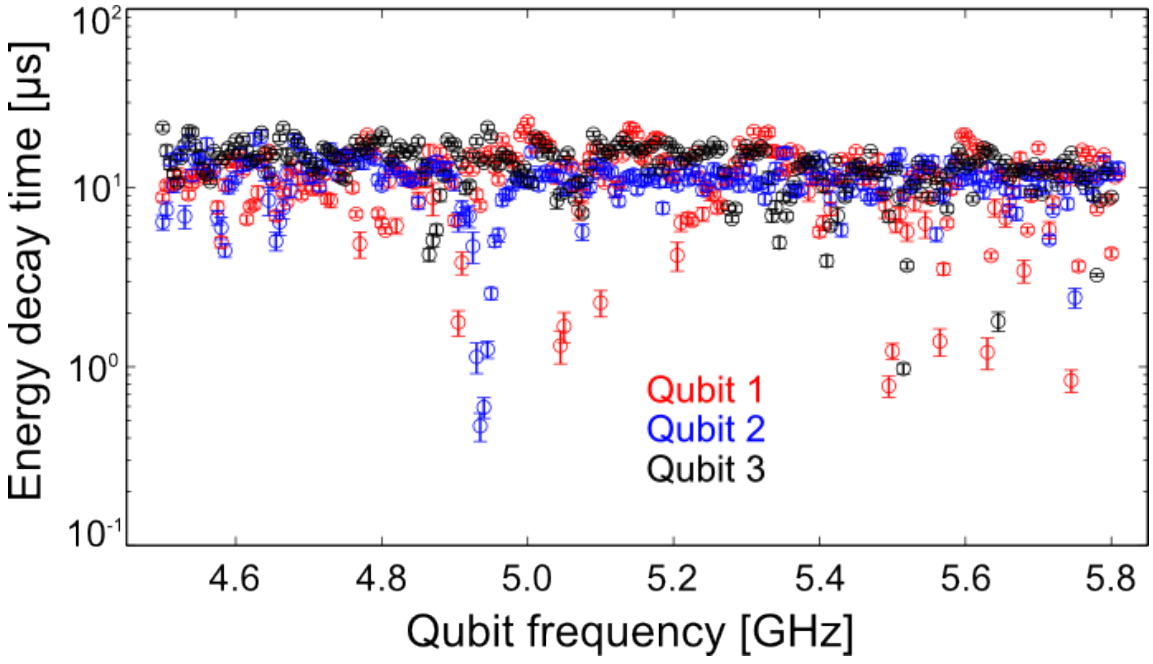

Figure B.2: **Energy decay time T_1.** The energy decay time of each qubit as a function of the qubit frequency. Each data point is measured by exciting the qubit, detuning it to the desired frequency, waiting a variable delay time, measuring the qubit excited state probability and fitting the decay curve to an exponential. The experimental results in this work were obtained near 5.7 GHz where the decay times ranged from 12 to 18 μs.

inductance is large, then a smaller current will flow through the coupler loop and the coupling will become weaker. For this device, the interaction strengths $g/2\pi$ were tunable from +5 MHz to -15 MHz; a value of -5 MHz was used for all of the experiments.

The energy decay times T_1 for all three qubits are shown in Fig. B.2 versus qubit frequency. During the thermalization experiments, the qubits were operated near 5.7 GHz where the decay times of the three qubits were between 12 and 18 μs. Each experimental sequence ran for at most 500 ns, excluding measurement. The time scales of the experiment were an order of magnitude below the energy decay times. The single-qubit dephasing times measured with Ramsey, however, ranged between 2 to 4 μs, closer to the relevant time scales of the experiment. In the single qubit experiments shown in Fig 2 of the main text, decoherence is indistinguishable from entanglement with the other qubits. Measurements of the full three-qubit density matrix, however, allow us to separate decoherence from entanglement through multi-qubit correlation functions [43].

B.2 Pulse sequence

In Fig. B.3 we show the pulse sequence and corresponding control waveforms used to implement the experiments in the main text. The pulse sequence can be broken up into three sections: state preparation, evolution and measurement. The initial states $|\theta_0, \phi_0\rangle$ were prepared in 40 ns using resonant microwave pulses, shown as a red oscillatory signal in the lower panel. The amplitude and length of the microwave pulse set the angle θ_0; the phase of the microwave pulse sets ϕ_0. Each time step in the evolution then consists

of two parts: a y-rotation and a symmetric three-qubit interaction. The y-rotation is achieved in 20 ns using a resonant microwave pulse shown in blue. The three-qubit interaction is performed by applying a square pulse to each coupling circuit, the duration of which sets κ. During the interaction, square pulses are used to maintain the qubits on resonance with one another as the coupler pulses cause the qubits to shift in frequency. We additionally calibrate for cross-talk between the six low-frequency control lines: three lines which tune the qubit frequencies and three which tune the coupling. The cross-talk matrix dV defined as $V_{\text{actual}} = (1 + dV)\, V_{\text{ideal}}$ was measured to be

$$dV = \begin{array}{c} \begin{array}{cccccc} \text{cp12} & \text{cp23} & \text{cp31} & \text{q1} & \text{q2} & \text{q3} \end{array} \\ \begin{pmatrix} 0.00 & 0.09 & 0.07 & -0.08 & -0.05 & 0.15 \\ 0.03 & 0.00 & 0.05 & 0.14 & 0.06 & -0.07 \\ 0.09 & 0.11 & 0.00 & -0.35 & 0.15 & -0.04 \\ 0.04 & 0.00 & -0.05 & 0.00 & 0.05 & -0.04 \\ -0.02 & 0.02 & 0.02 & 0.01 & 0.00 & 0.03 \\ 0.02 & 0.02 & -0.02 & -0.01 & 0.04 & 0.00 \end{pmatrix} \end{array}$$

After evolving the system forward N times, we reconstruct the density matrix of the qubits using state tomography. State tomography consists of single qubit rotations, shown in black, followed by measurements along the z-axis; this is then repeated for various rotation axes and angles. The rotations are chosen from a set of four rotations containing I, $X_{\pi/2}$, $Y_{\pi/2}$, and X_{π}. The measured z-projections are then used along with maximum likelihood estimates to construct a physical density matrix [138].

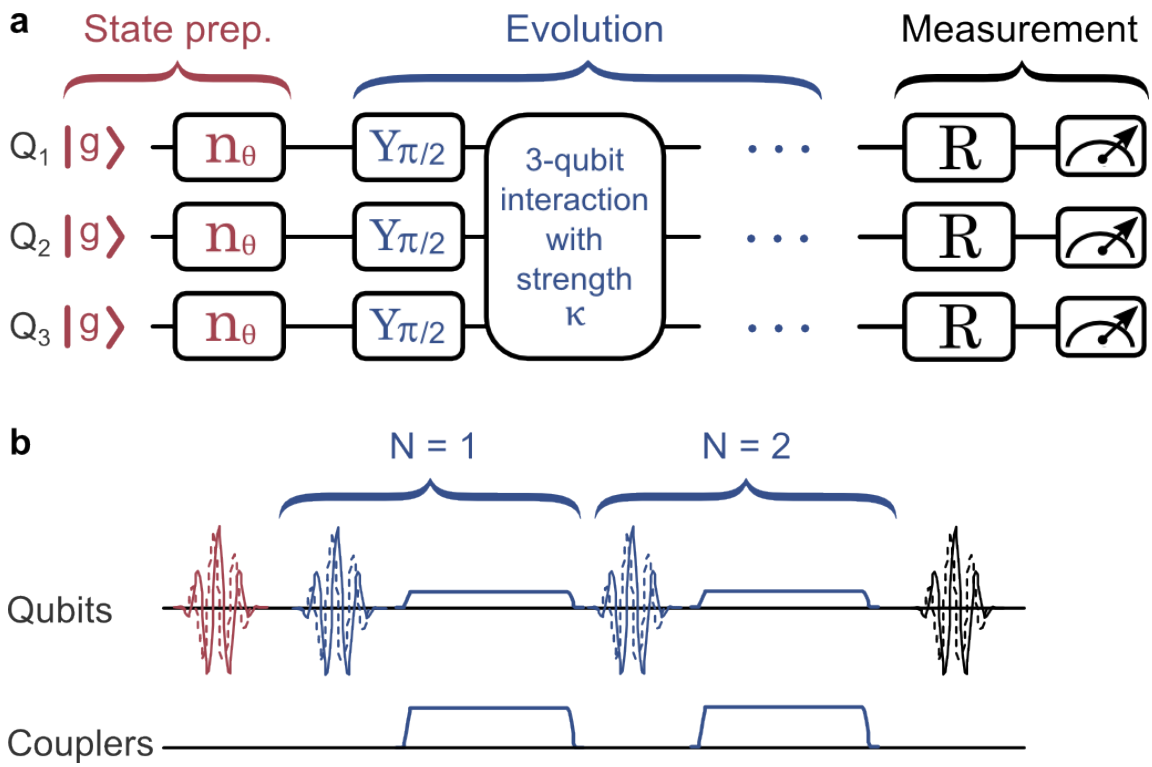

Figure B.3: **Pulse sequence and control waveforms. a,** Gate sequence used to study ergodic dynamics and thermalization. First, each qubit is prepared in the ground state by waiting several energy decay times. Next, we rotate each qubit into the state $|\theta_0, \phi_0\rangle$ through a rotation around the axis $n = -\sin(\phi_0)\,\hat{x} + \cos(\phi_0)\,\hat{y}$ by angle θ_0. This initial state is then evolved by N applications of a rotation around the y-axis by $\pi/2$ and a symmetric multi-qubit interaction. Following the evolution, the density matrix of either individual qubits or of the full system is determined using state tomography. State tomography consists of a rotation followed by a measurement along the z-axis. This is repeated for different rotation angles and axes to reconstruct the density matrix. **b.** The control waveforms used to implement the gate sequence are shown for $N = 2$. Oscillatory signals correspond to resonant microwave pulses used to rotate the single-qubit states. The amplitude and phase of the control waveform determine the rotation angle and axis respectively. Square pulses applied to the coupler and qubit SQUID loops are used to turn on the multi-qubit interaction and to maintain the qubits on resonance.

B.3 Simultaneous three-qubit interaction

The characterization procedure for the simultaneous three-qubit interaction is shown in Fig. B.4. This procedure is broken up into three steps. First, we calibrate the six square pulse amplitudes (three qubits, three couplers) to ensure that the interaction strengths are all equal and that the qubits are on resonance. Second, these pulses can cause the qubits to detune from the microwave source; measuring this detuning allows us to correct for the resulting phase accumulation. Third, if there is a relative phase between the control signals on different qubits, this also needs to be corrected for.

The first experiment, shown in panel (a), demonstrates that the interaction energies are symmetric and that the qubits are on resonance. We begin by putting one of the qubits into its excited state, turning on the interaction for a variable length of time, and then measuring all three qubit excited state probabilities P_e. This experiment is then repeated exciting a different qubit each time; all 9 curves are plotted as a function of interaction length. In order to isolate the effects of interaction, we measure P_e as a function of time, without interactions, and subtract the results. If the qubits are detuned or the interaction strengths differ from one another, then the curves will not lie on top of each other. Additionally, both error sources will prevent the probabilities from returning to zero periodically. The data suggests that errors in the coupling and detuning are small over relevant time scales.

Measurements of P_e alone do not provide information about the phase of the qubit. In panel (b), we rotate one qubit to the equator of the Bloch sphere, turn on the interaction

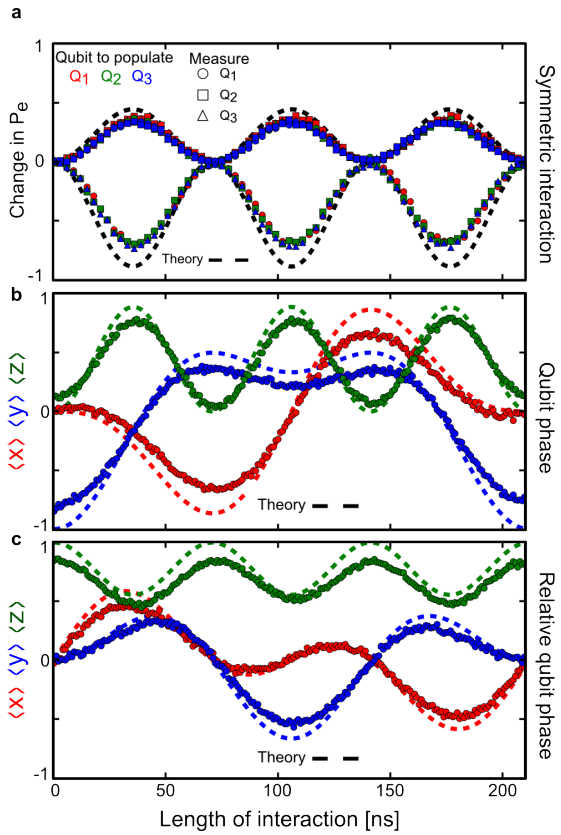

Figure B.4: **Characterizing the 3-qubit interaction. a,** Here we demonstrate that the inter-qubit interaction energies are all of equal strength and that the qubits are on resonance during the interaction. This is done by exciting a single qubit, turning on the interaction for a variable length of time (horizontal axis) and then measuring all three qubit excited state probabilities P_e. We plot the change in P_e relative to having waited the corresponding length of time. We then repeat the experiment exciting different qubits, resulting in a total of 9 curves. The symmetry of the curves and the periodically going to zero indicate that the gate is properly calibrated. **b,** Here we demonstrate that we have corrected for changes in the single qubit phase that result from the interaction gate. We rotate one qubit to the equator of the Bloch sphere, turn on the interaction for a variable length of time, and then perform state tomography on the qubit which we rotated. The agreement with theory indicates that the phase is being properly corrected for. **c,** The relative control phases of the different microwave signals also needs to be corrected for. Here we rotate one qubit to the equator of the Bloch sphere, turn on the interaction for a variable length of time, and then perform state tomography on a neighboring qubit. The agreement of the curves with theory indicates that we have properly calibrated for this phase difference.

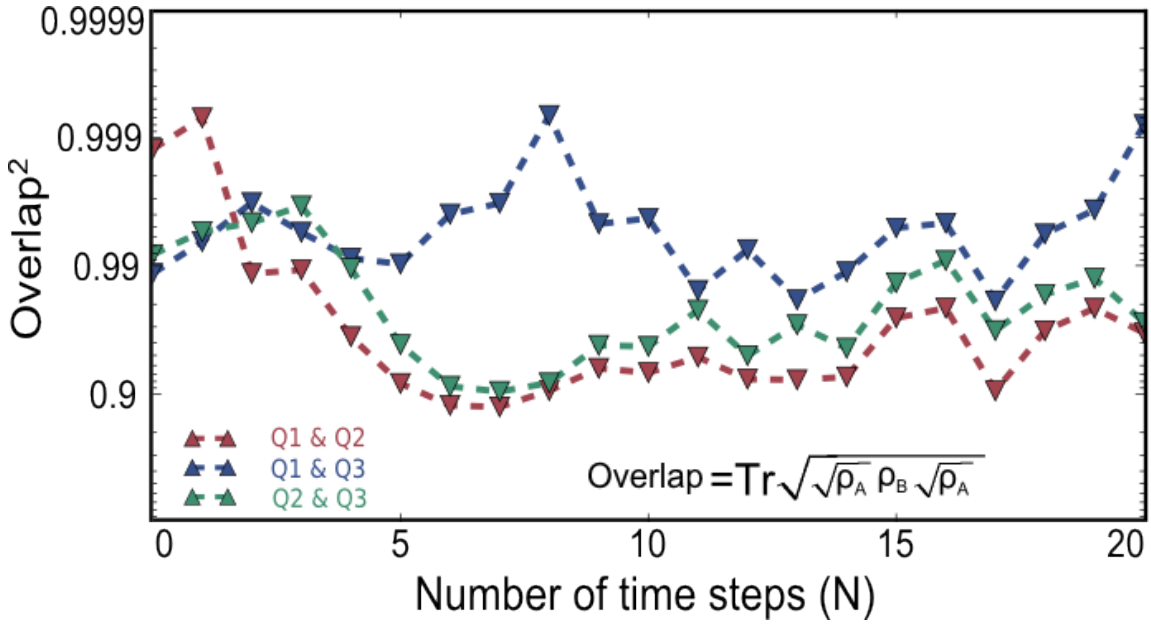

Figure B.5: **Symmetric evolution.** We measure the single qubit density matrices as a function of the number of time steps N for $\kappa = 2.5$. At each time, we compute the overlap of the individual single qubit density matrices and plot the results.

for a variable length of time, and then perform state tomography on the qubit which was rotated; we plot the expectation values of the single qubit Pauli operators. If the qubit is accumulating a phase during the interaction as a result of detuning from the microwave source, then $\langle x \rangle$ and $\langle y \rangle$ will rotate into one another. We determine the rate of phase accumulation by measuring $\langle y \rangle$ for a 210 ns interaction length as a function of the phase accumulation rate correction and look for a minimum, as $\langle y \rangle$ is ideally minimum for this choice of interaction length. Correcting for this results in tomography which agrees well with an ideal operation; deviations result primarily from measurement visibility.

In panel (c), we rotate one qubit to the equator of the Bloch sphere, turn on the interaction for a variable length of time, and then perform state tomography on a neighboring qubit. If the relative phase of the microwave control signals on the individual

qubits is non-zero, then the measured $\langle x \rangle$ and $\langle y \rangle$ values will rotate into one another. This may result from differences in electrical path lengths in the two control lines. We determine this phase by measuring $\langle y \rangle$ for a 105 ns interaction length as a function of the relative phase and look for a minimum. Correcting for this static phase difference results in tomography which agrees well with an ideal operation.

B.4 Qubit dynamics

This three-qubit interaction along with local rotations are used to generate the dynamics that were explored in this experiment. As both the initial state and the evolution operators are symmetric under exchange of qubits, we expect to observe nominally identical behavior. In order to verify this, we measure the reduced density matrix of the individual qubits and compute their overlap. The results are shown in Fig. B.5 for $\kappa = 2.5$ and an initial state along the z-axis. We find that the qubits remain symmetric over the length of the evolution.

The evolution of the qubits involves both a rotation and an interaction. In Fig. B.6 we explore the effect of these pulses on the entanglement entropy of the individual qubits. In panel (a) we plot the time-average entropy versus initial state without either the rotation or interaction; instead, we simply wait for the corresponding length of time. For initial states near the ground state, the entropy is close to zero and increases slightly while approaching the excited state as a result of energy relaxation. In panel (b) we plot the same quantity, however, now we apply only the rotations without the interactions. Here,

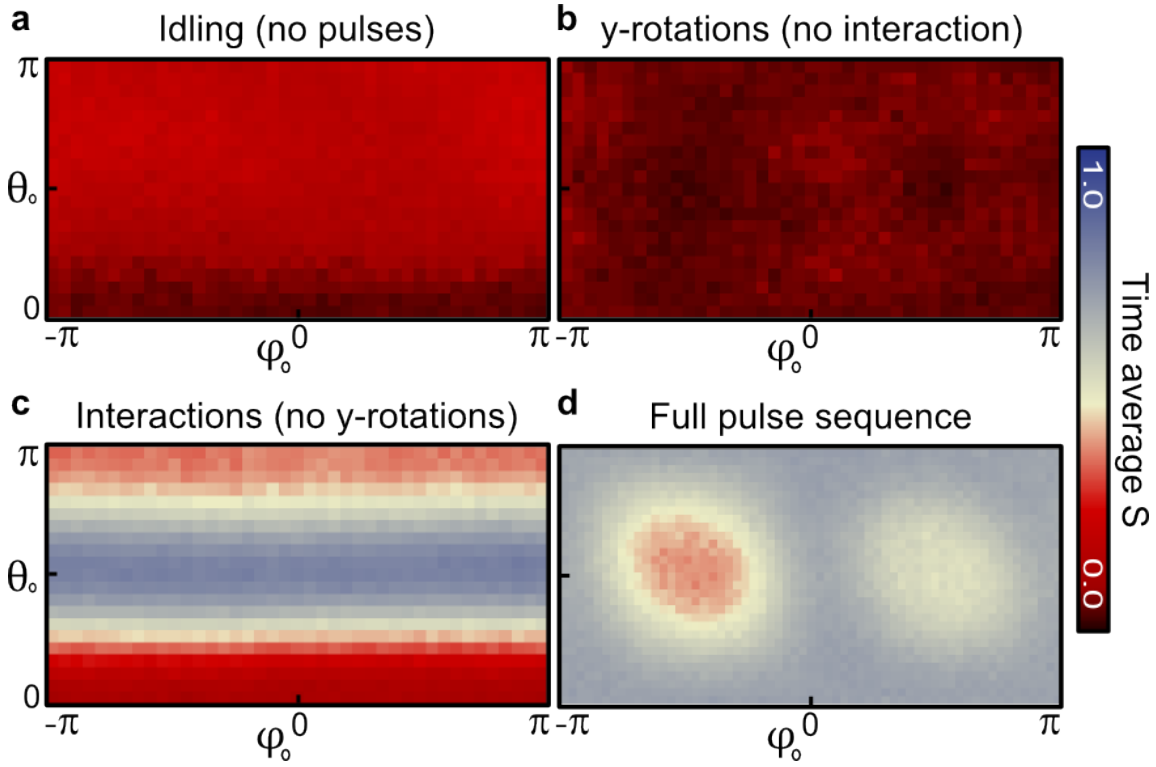

Figure B.6: **Dissecting the phase space dynamics**. In all four panels we plot the time-average entanglement entropy of a single qubit versus initial state for $N = 20$ and $\kappa = 0.5$. To better understand the results, we consider four different pulse sequences: no pulses (just waiting), only y-rotations (no interactions), only interactions (no rotations), and both interactions and rotations. **a,** Average entanglement entropy after waiting a length of time equivalent to the full pulse sequence. **b,** Here, we apply only the y-rotations and replace the interactions with a wait of equivalent length. **c,** Now we perform the opposite experiment, applying only the interactions and wait instead of rotating. **d,** We now apply the full pulse sequence.

the entropy is uniform over initial states as the rotations average the results over many states. In panel (c), we apply only the interaction without the rotations. We see that near the ground or excited states the entropy stays near-minimum as the qubits do not entangle here. For initial states closer to the equator, we see an entanglement entropy near a half. Putting the interaction and the rotation together we recover the results shown in the main text.

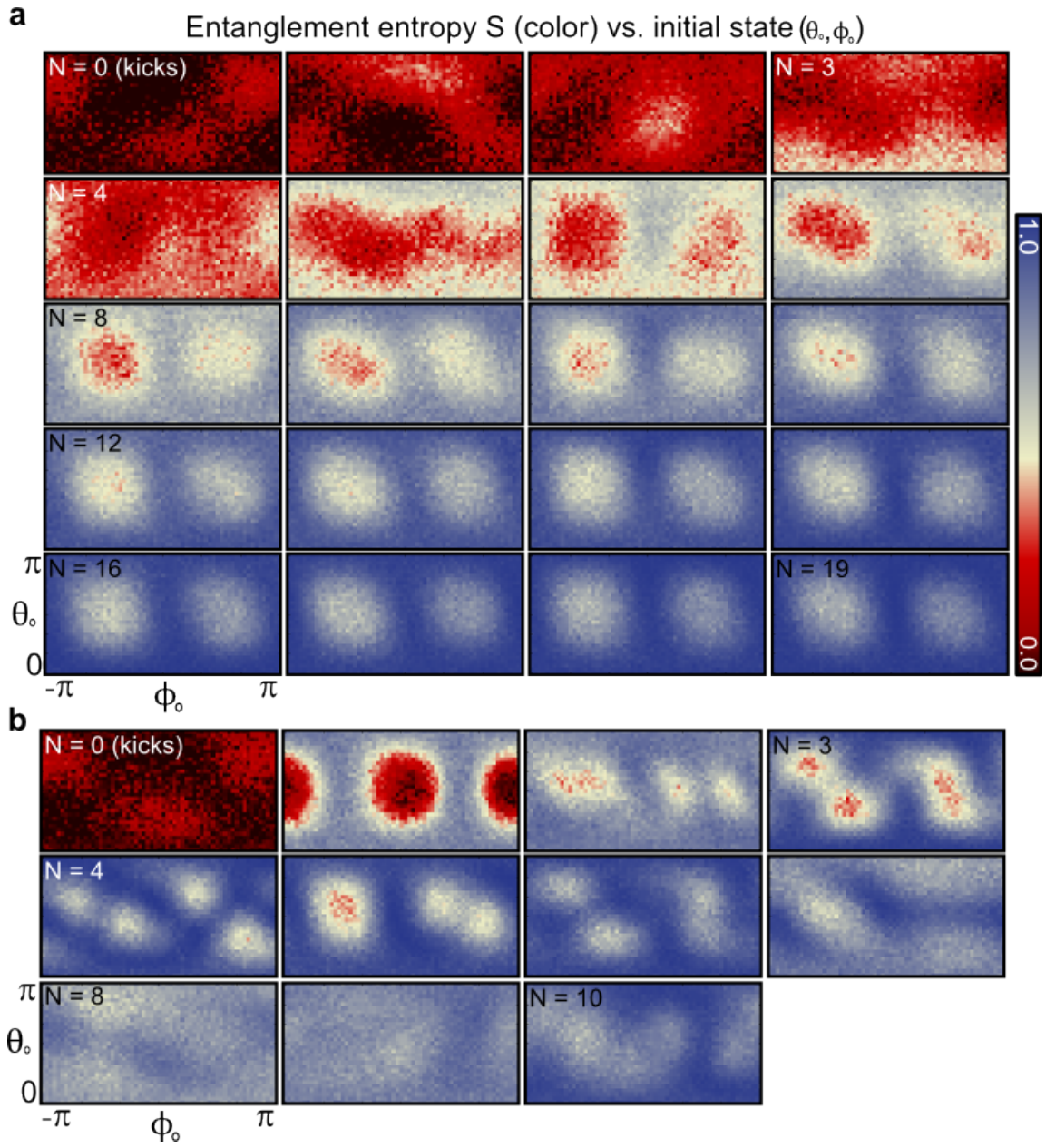

Figure B.7: **Snapshots of entanglement entropy. a,** Entanglement entropy of a single qubit as a function of intial state for $N = 0$ to 19 at $\kappa = 0.5$. **b,** We repeat the experiment for $N = 0$ to 10 at $\kappa = 2.5$.

In Fig. 2 of the main text, we show the entanglement entropy at single instances in time for N = 1,3,5 and 7 for both $\kappa = 0.5$ and $\kappa = 2.5$. In Fig. B.7, we show the data for all time steps from $N = 1$ to 20 for $\kappa = 0.5$ (a) and from $N = 1$ to 10 for $\kappa = 2.5$ (b).

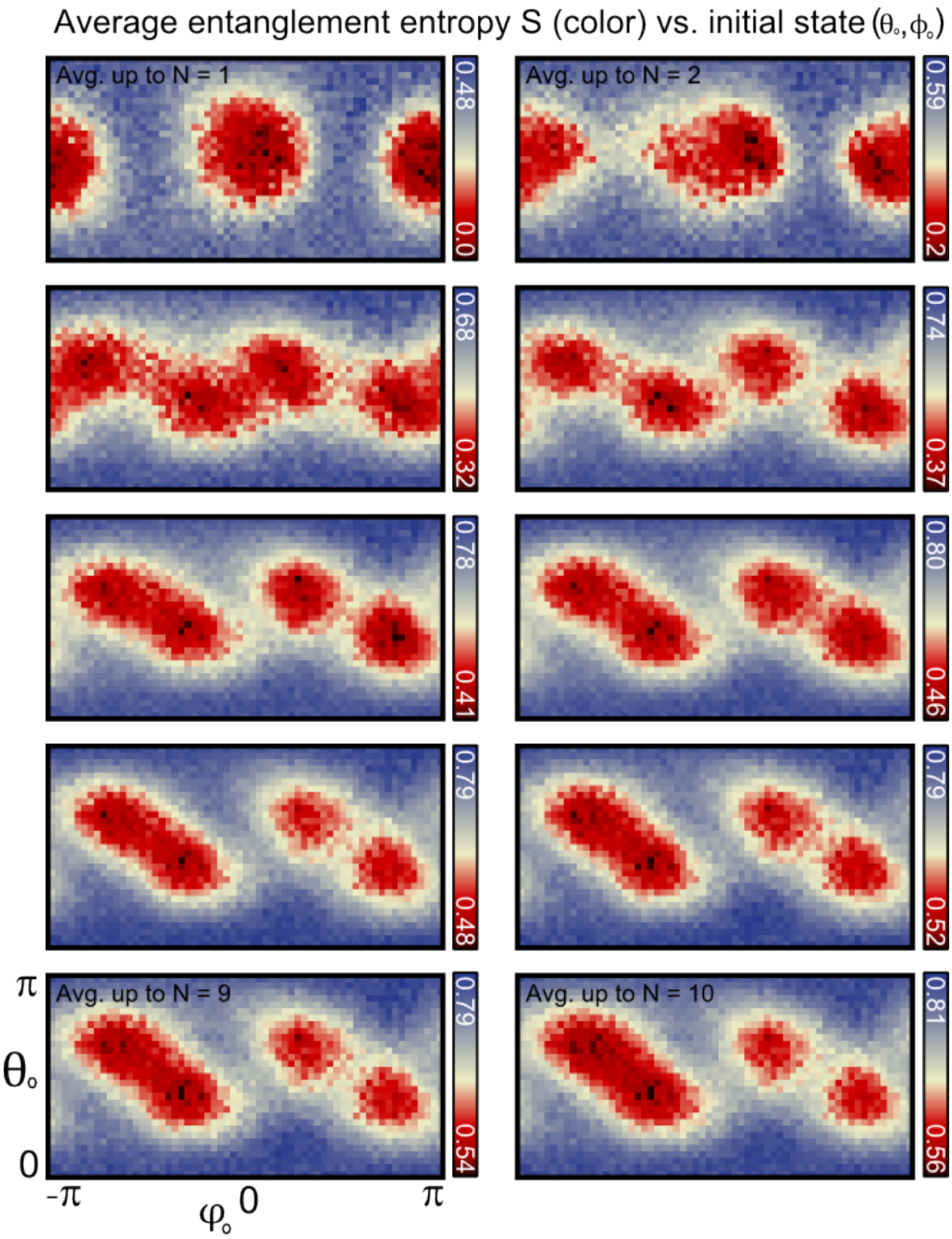

Figure B.8: **Entanglement entropy, convergence with number of averages.** Entanglement entropy of a single qubit as a function of intial state at $\kappa = 2.5$. In the different panels, we increase the number of time steps over which we average the entropy. We find that the entanglement entropy qualitatively converges to the long time behavior after merely four time steps.

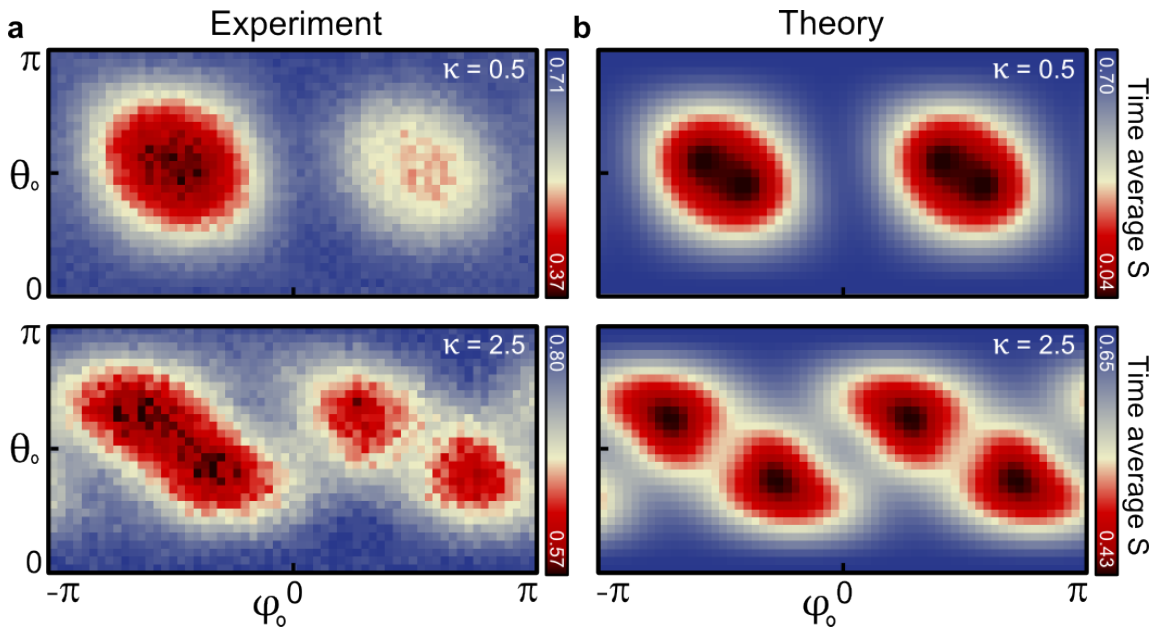

Figure B.9: **Entanglement entropy, comparison with theory. a,** The time-average entanglement entropy of a single qubit versus intial state for $\kappa = 0.5$ (top) and $\kappa = 2.5$ (bottom) **b,** For comparison, we numerically compute the expected behavior and plot the results.

In Fig. B.8, we vary the number of time steps over which we average the entanglement entropy. We find that the regions of high and low entropy qualitatively approach the long time results after just four steps. In Fig. B.9a, we show the entanglement entropy average over N, as shown in the main text. For comparison, we numerically compute the ideal behavior and show the results in Fig. B.9b. The ideal behavior has a left/right symmetry that is not present in the experimental data. This is likely the result of control errors arising from imperfect calibrations and modifications to the dynamics resulting from dispersive shifts from higher states of the transmon qubit.

In Fig. B.10 we consider the degree to which the model outlined in the main text describes the experimental results. Using the measured three-qubit density matrix ρ_{expmt},

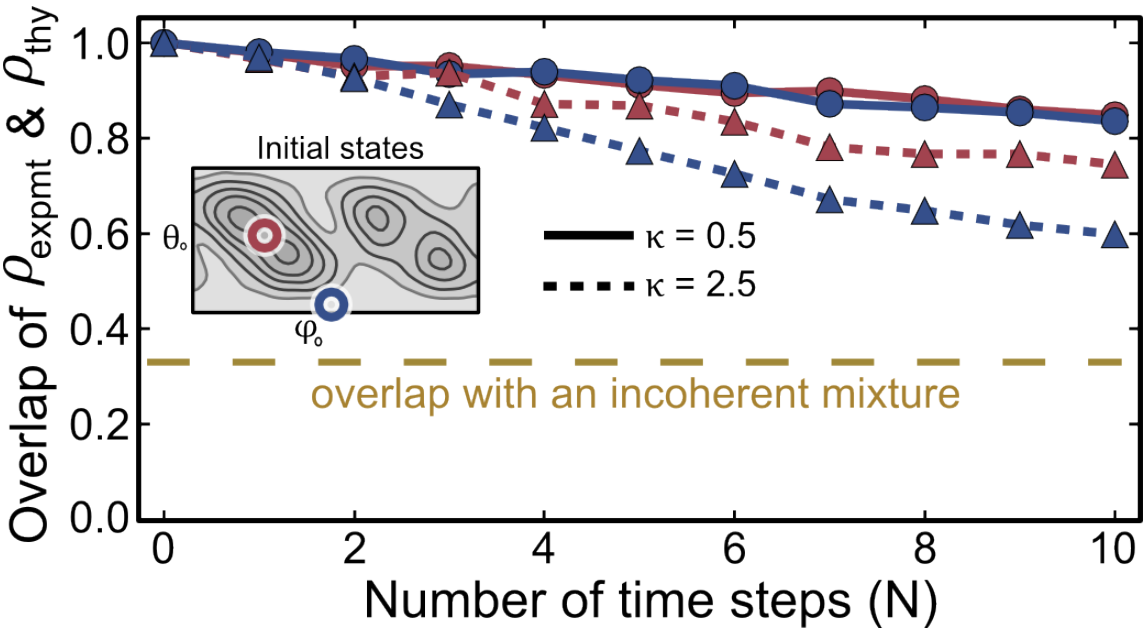

Figure B.10: **Comparison with theory.** We measure the three-qubit density matrix for two initial states, one where subsystems thermalized (blue) and one where subsystems did not thermalize (red). We plot the overlap of the experimental density matrix ρ_{expmt} and the theoretical density matrix ρ_{thy} calculated using the model presented in the main text.

we compute the overlap of ρ_{expmt} and the theoretically calculated density matrix ρ_{thy}. We plot the results as a function of time for two initial states, one where subsystems thermalized (blue) and one where subsystems did not thermalize (red), and for two values of interaction strength, $\kappa = 0.5$ and $\kappa = 2.5$.

In Fig. B.11 we show the Pauli representation of the three-qubit density matrix for $\kappa = 2.5$. Initially, when $N = 0$, all of the single qubit states are along the Z axis and the remaining peaks reflect the corresponding classical correlations. After just a few kicks, however, the correlations are dominated by peaks that are not reflective of the single-qubit orientations.

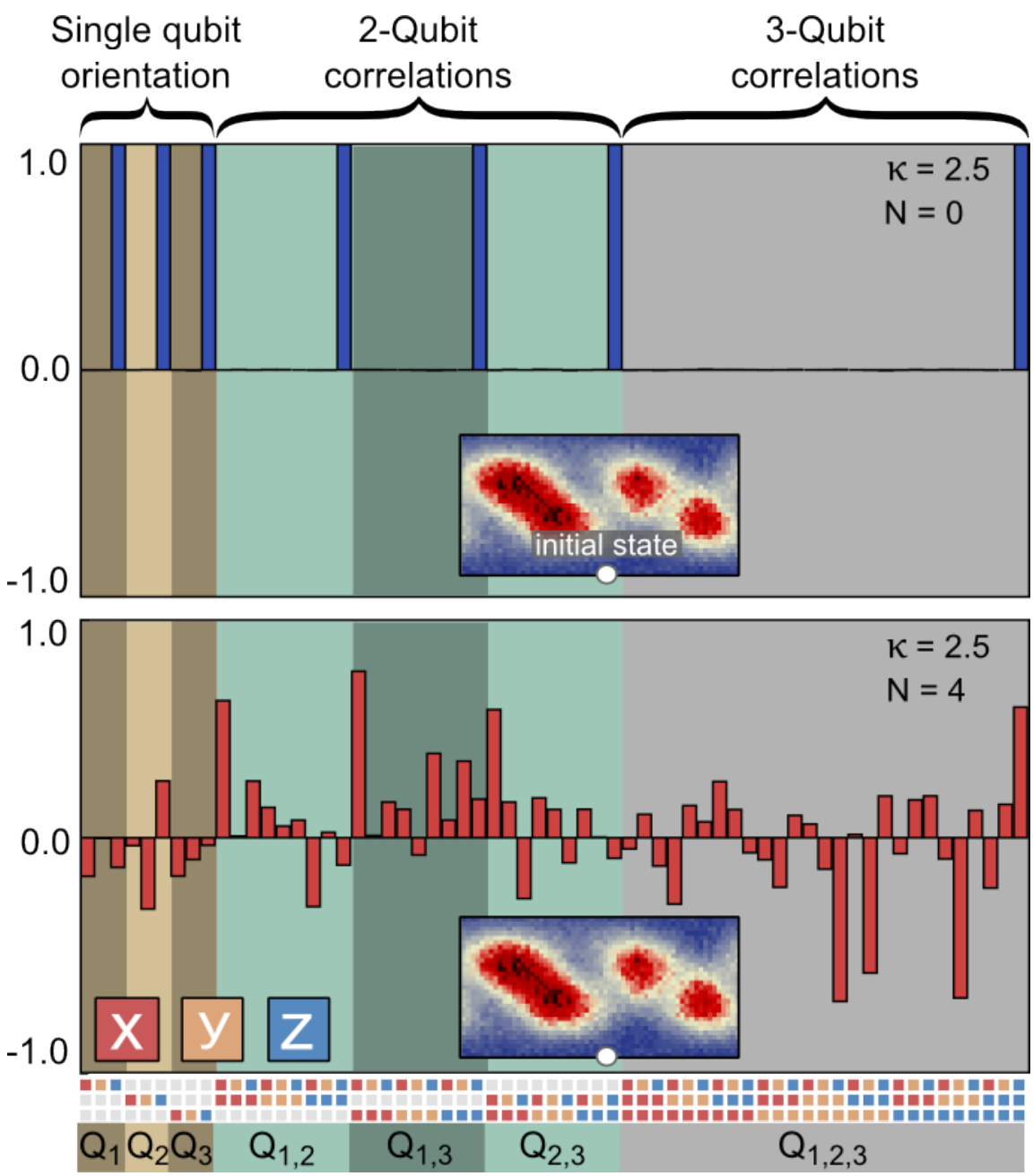

Figure B.11: **Pauli representation.** We represent the three-qubit density-matrix for an initial state shown inset and $\kappa = 2.5$. Each bar indicates the expectation value of one possible combination of Pauli operators on the three qubits, the corresponding operator is shown using colored squares. The increase in multi-qubit correlations in the lower panel is the result of two- and three-qubit entanglement.

B.5 Unitary dynamics vs. decoherence

In the main text we show that single-qubit subsystems approach maximal entropy (i.e thermalize, Fig. 2) as a result of entanglement (Fig. 3). Additionally, we show that this occurs for initial states where time-averages are equal to state-space averages (i.e the dynamics are ergodic, Fig. 4). In contrast, we find that where the dynamics are less ergodic that subsystems do not thermalize or entangle. However, we have yet to determine if the contrast between high and low entropy, entanglement, and ergodicity results from unitary dynamics or environmental decoherence.

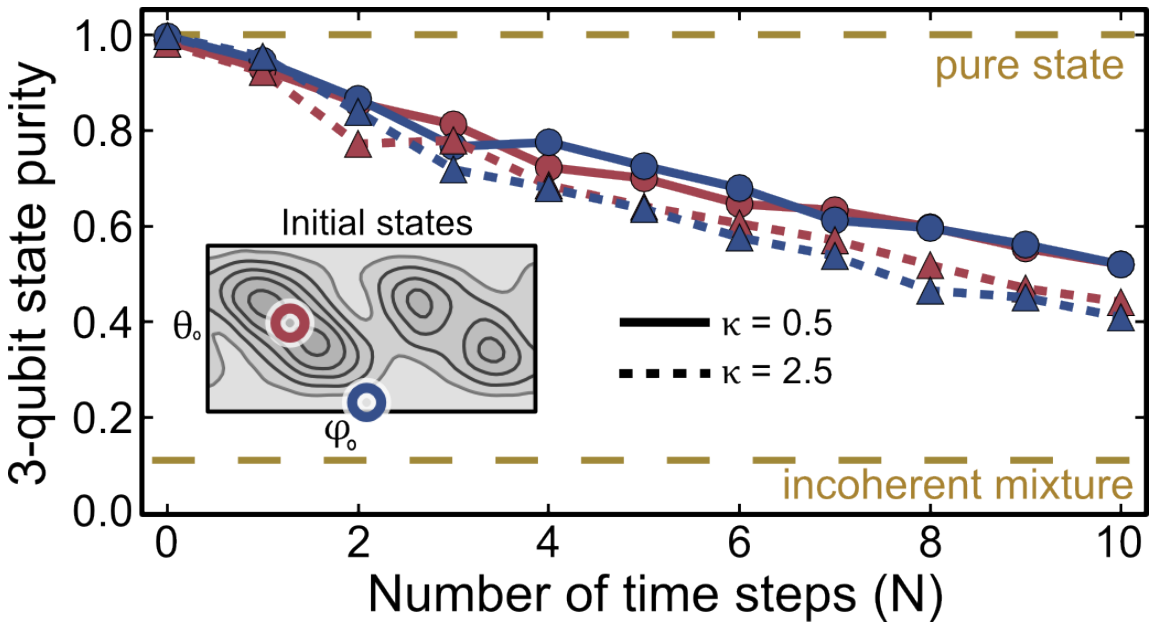

Figure B.12: **State purity as a measure of decoherence.** We measure the three-qubit density matrix for two initial states, one where subsystems thermalized (blue) and one where subsystems did not thermalize (red). We plot the state purity, a measure of decoherence, as a function of the number of time-steps. We find that the decoherence is independent of initial state for all times and for both values of interaction strength $\kappa = 0.5$ and $\kappa = 2.5$. This suggests that the contrast between high and low entropy, entanglement and ergodicity found in the main text is the result of coherent quantum dynamics.

In Fig. B.12 we show the state purity of the three-qubit density matrix ρ_{expmt} as a function of time. We plot the purity for both an initial state where subsystems thermalized (blue) and did not thermalize (red). The state-purity, a measure of decoherence, is given by $\text{Tr}\,\rho^2_{\text{expmt}}$ and is 1 for a pure state and $1/2^3$ for a three-qubit incoherent mixture. We find that the decoherence is independent of the initial state of the qubits. This result strongly suggests that the contrast in entropy, entanglement, and ergodicity is the result of coherent quantum dynamics.

B.6 Finite-size scaling

In statistical mechanics, fluctuations from equilibrium are expected to vanish with increasing system size. In our experiment, we average over these fluctuations in order to estimate the equilibrium value of entropy. In Fig. B.13, we numerically show that these fluctuations in entropy over time decrease as we consider larger systems. The points correspond to the standard deviation in entropy from N = 10 to 500 as a function of the number of spin-1/2 from 4 to 10. The solid line corresponds to the expected behavior from statistical mechanics where fluctuations decrease with the square root of system size. We find agreement between the fluctuations as computed from the quantum dynamics and the predictions from statistical mechanics.

A major achievement of statistical mechanics is the ability to predict the behavior of physical systems independent of their initial configuration. In our experiment, we show a clear difference in the entropy of initial quantum states whose classical limits

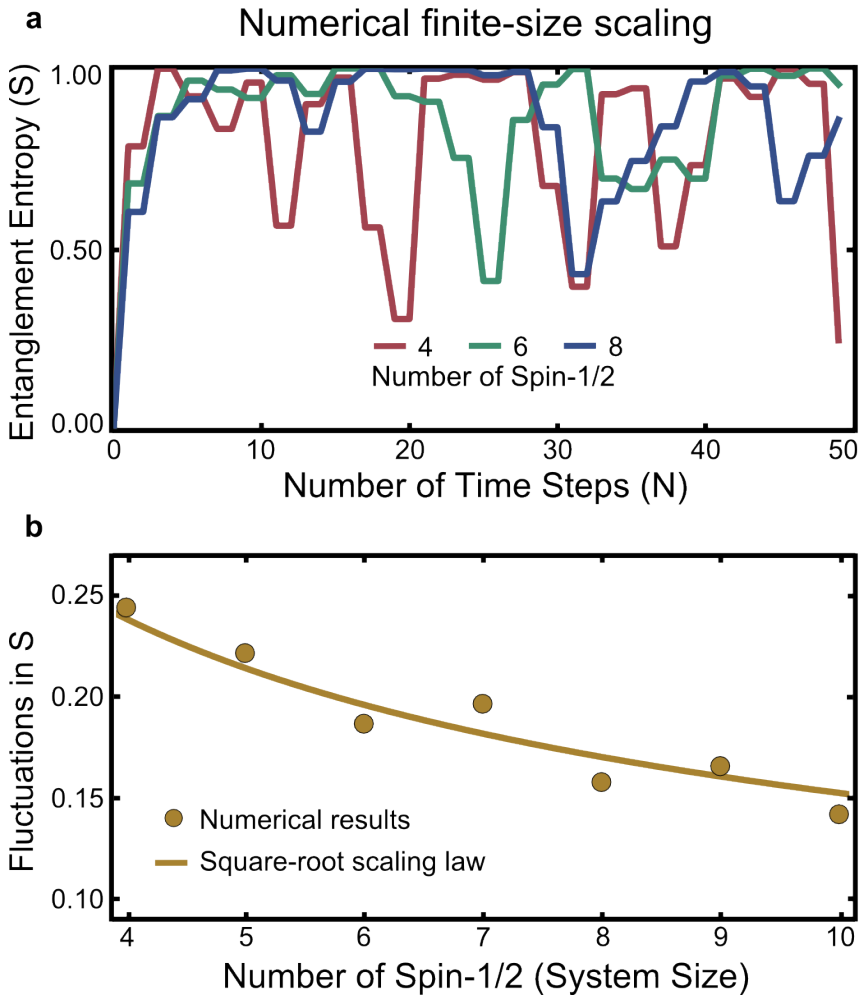

Figure B.13: **Decreasing fluctuations with system size. a,** We numerically compute the entanglement entropy S versus the number of time steps N for increasing number of qubits. In all cases, the entropy approaches 1.0 after a few steps. However, there are significant fluctuations from this value over time due to the small size of the system. **b,** In the lower panel, we numerically compute the standard deviation in entropy from N = 10 to 500 as a function of the number of qubits and show that fluctuations in entropy decrease with increasing system size. For comparison, we overlay a curve with the square-root of system-size behavior typically found in statistical mechanics.

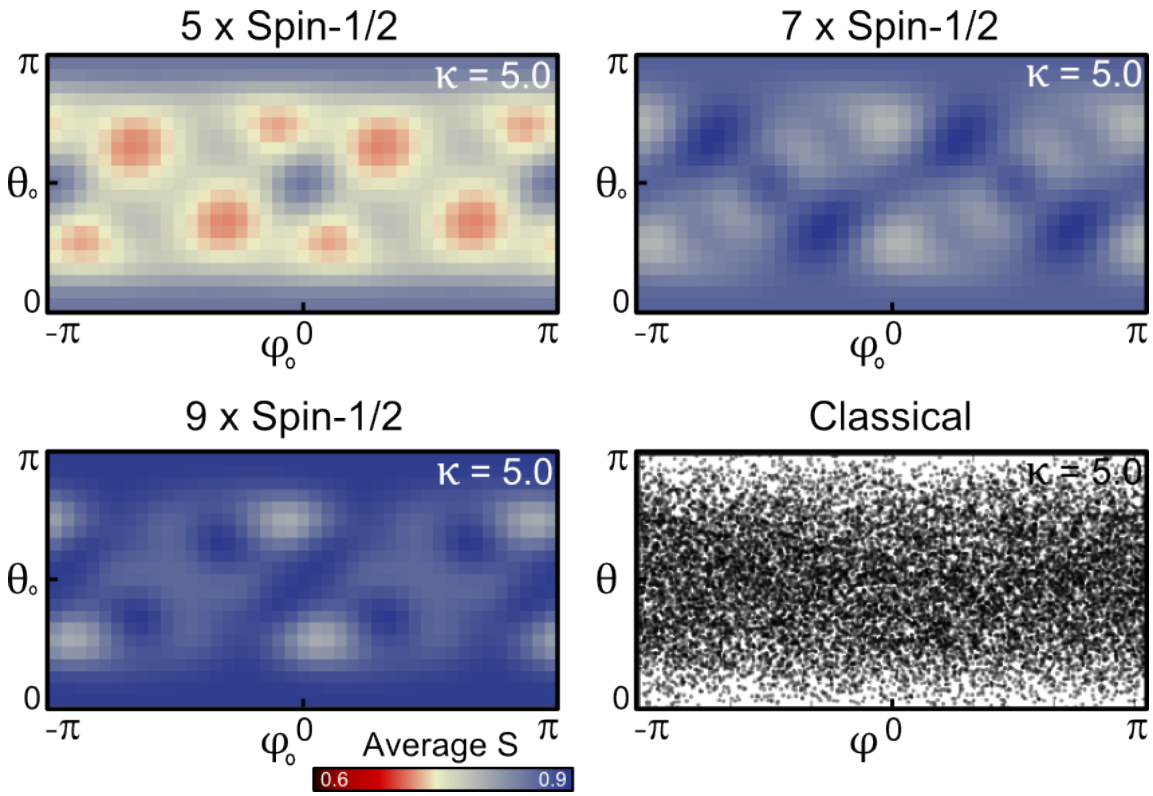

Figure B.14: **Thermalization for all initial states.** We numerically compute the time-average entanglement entropy S as a function of initial state for an interaction energy $\kappa = 5.0$. The value of κ is chosen so that the classical phase space is no longer mixed but completely chaotic. In the first three panels we observe that the time-average entropy increases as a function of the number of spins, for all initial states. This suggests that at strong interaction all initial states thermalize in the limit of large systems. In the last panel (lower right), we show the classical phase space dynamics for comparison.

are either chaotic or stable. If the system were thermal for all initial states, then we would not expect this state-dependent behavior. In Fig. B.14, we consider larger values of interaction strength where the classical phase space is completely chaotic and compute the quantum evolution.

When the classical phase space is completely chaotic, we find the the entropy increases with system size independent of the initial state. This further supports the conclusion in the matin text that the observations correspond to a thermalization process.

Appendix C

Supplementary Information for Chapter 4

C.1 The gmon qubits

C.1.1 1.1. The gmon coupling architecture

In this work we implemented an adjustable inductive coupling between two qubits. Adjustable coupling has typically been difficult with superconducting qubits, as fixed capacitive coupling may only be modified by detuning, so it has the problems of limited on/off range and crosstalk. Here we use a novel qubit design called the gmon, which allows a continuous variation of the inter-qubit coupling strength g over nanosecond time scales without any degradation in the coherence of the constituent Xmon qubits [58, 38]. The adjustable inductive coupling between the transmons allows $g/2\pi$ to be varied between

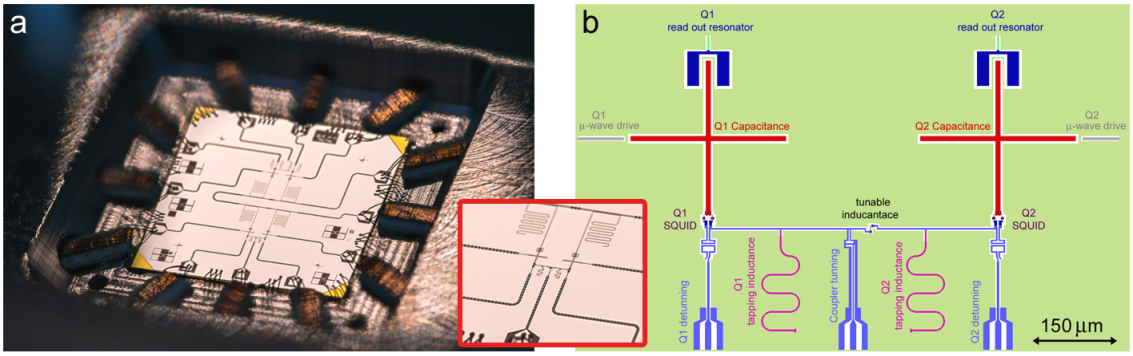

Figure C.1: **Device architecture. (a)** Optical image of the device showing two coupled gmon transmons on the top half of the chip and the two coupled gmons used in this work on the lower half (zoomed-in view in inset). **(b)** The layout of the two-qubit gmon system. We supply bias currents using the lower blue lines to tune the inductance of the coupler junction (middle) and the qubit frequencies (left, right). We apply microwave pulses to each qubit via the gray trace. We read out the state of the qubits dispersively via readout resonators: each qubit is capacitively coupled to a resonator (green lines; meandered lines in inset of (a)).

-5 MHz and 55 MHz, including zero, without changing the bare qubit frequencies. The device was fabricated using standard optical and e-beam lithography techniques, discussed in recent works of our group such as [18]. The qubit frequencies are tunable, but mainly flux biased to around 6 GHz. The energy relaxation time, T_1, is $\sim 10\mu s$, and the de-coherence time, T_2 is $\sim 5\mu s$. The experiment was performed at the base temperature of a dilution fridge ($\sim$20 mK).

C.1.2 Basic design principle of the gmon

As shown in Fig. S1, the gmon design is based on the Xmon qubit design. One important feature of the Xmon design [17] is the single-ended ground in contrast to differential or floating grounds. In the absence of adjustable coupling, the SQUID loops (Fig. S1(b)) would be directly connected to the ground plane. This design feature gives

us the ability to capacitively couple qubits with elements such as the drive lines, the readout resonators, and nearby qubits. In the gmon architecture, instead of immediately terminating the qubit SQUID to ground, we add a linear inductor (the meandering CPW element colored in purple and labeled "tapping inductance") between the SQUID and ground(CPW stands for coplanar waveguides). This creates a node (where the purple CPW meets the horizontal blue CPW) that allows us to couple the two qubits. The two qubits then can be connected with a CPW line. This connecting line is interrupted with a Josephson junction, which acts as a tunable inductor that can be used to tune the inter-qubit coupling strength g, hence the name gmon.

The basic operation of the gmon can be understood from a simple linear circuit model. An excitation created in Q1 will mostly flow to ground through its tapping inductance, but a small fraction will flow to the tapping inductance of Q2, generating a flux in Q2. The mutual inductance resulting from the flux in Q2 due to an excitation current in Q1 can be calculated from simple current division, and the coupling strength is proportional to this mutual inductance to high accuracy [58, 38]. The current division ratio, which sets the coupling strength g, can be varied by changing the superconducting phase difference across the tunable inductance. This is done by flux biasing its junction, using the current line labeled "coupler tuning" in panel (b).

An important advantage of this architecture is that it prevents crosstalk, a serious hurdle for many other experimental works. Coupling the qubits at the nodes between the SQUID and the tapping inductance allows a DC current to set the coupling strength.

Because of the open loop of each qubit (due to capacitance) this DC current cannot flow to the SQUID and change the qubit frequencies. Thus, the two capacitors act as DC blocks. This key ingredient of the gmon design minimizes the crosstalk between the qubits and the coupler.

C.1.3 1.3. Coherence of the gmon

One major concern of the coupler circuit is degradation of the qubit coherence. The gmon architecture required adding CPW lines to connect qubits, ground plane cross-overs which involve dielectrics, and a tunable inductance. If the capacitive loss due to these elements are not properly considered, the coherence of the system could be substantially degraded. With the gmon design, the fraction of the qubit energy stored in these coupling elements scales as the square of the ratio of the tapping inductance to the qubit SQUID inductance, which is 1/2000. Therefore these elements do not affect the qubit coherence [38]. Furthermore, to avoid inductive loss, we used a relatively small mutual coupling of around 1 pH to the coupler tuning line. This coupling places an upper bound of 200 μs on the energy relaxation time T_1. The average measured T_1 for our device was around 10 μs, independent of the coupling strength. This is comparable to the performance of Xmon qubits with the same geometry and material. As demonstrated with Xmon qubits [18], the coherence can be improved by widening the capacitor and using MBE-grown aluminum films.

C.2 Mapping the Single-Qubit Hamiltonian to the Haldane Model and Adiabatic Measurement of the Chern number

C.2.1 Haldane model

To show that the quantum Hall effect could be achieved without a global magnetic field, Haldane introduced a non-interacting Hamiltonian[68], which served as the cornerstone of future topological band studies. He introduced a massive Dirac Hamiltonian with different mass terms at the two non-equivalent corners of the Brillouin zone $\mathbf{K}, \mathbf{K}'$. Near these points the Hamiltonian is given by

$$\mathcal{H}_G^{\pm}(k_x^{\pm}, k_y^{\pm}) = \hbar v_F(k_x^{\pm}\sigma^x \pm k_y^{\pm}\sigma^y) + (m_0 \mp m_t)\sigma^z, \tag{C.1}$$

where v_F is Fermi velocity, and $k_x^+(k_x^-), k_y^+(k_y^-)$ are measured from two non-equivalent corners of the Brillion zone $\mathbf{K}(\mathbf{K}')$. m_0 is the mass associated with inversion symmetry breaking, and m_t corresponds to a second-neighbor hopping in a local magnetic field. The key prediction of the Haldane model is that if $m_0/m_t > 1$ the system is in a trivial insulating phase, and otherwise in a topological phase, where edge states and quantized conductance appear.

Using a confocal mapping, discussed below, one can recast Eq. (C.1) into the single qubit Hamiltonian of the main text (eqn. (3)). For convenience we re-parameterize that equation in terms of a field H_0 along the z-axis, and a radial field H_r with orientation

given by θ, ϕ, such that $\mathbf{H} = (H_r \sin\theta\cos\phi, H_r \sin\theta \sin\phi, H_0 - H_r \cos\theta)$. Then, for θ values close to 0 and π the single qubit Hamiltonian becomes

$$\mathcal{H}_S^{\pm}(H_0, H_r, \theta, \phi) = -\frac{\hbar}{2}(H_r(\sin(\theta)\cos(\phi)\sigma^x + \sin(\theta)\sin(\phi)\sigma^y) + (H_0 \pm H_r)\sigma^z). \quad \text{(C.2)}$$

By comparing $H_S^+(H_S^-)$ to $H_G^+(H_G^-)$, it becomes evident that H_0/H_r in the qubit system plays the same role as m_0/m_t in the Haldane model. The fact that the topological phase transition occurs at H_0/H_r=1 is consistent with the Haldane model, where the transition takes place at m_0/m_t=1. Similar to the Haldane model, where k_x and k_y span a manifold of states in the Brillouin zone, θ and ϕ span a manifold in the parameter space of the qubit system. With this mapping, the two distinct phases observed in Fig. 3(a) of the main text correspond to the topological and trivial phases in the Haldane model.

C.2.2 Adiabatic measurement, confocal mapping, and direct measurement of the Chern number

To visualize how the qubit and Haldane model are topologically related, we now explicitly construct a mapping between the single qubit parameter space and momentum space in the Haldane model. We use this to map the qubit Bloch vector measured by adiabatic state preparation to the first Brillouin zone of graphene and then compute its Chern number, thus completing the analogy with the Haldane model. By using a confocal mapping, the parameter space points can be mapped to the hexagonal Brillouin zone of

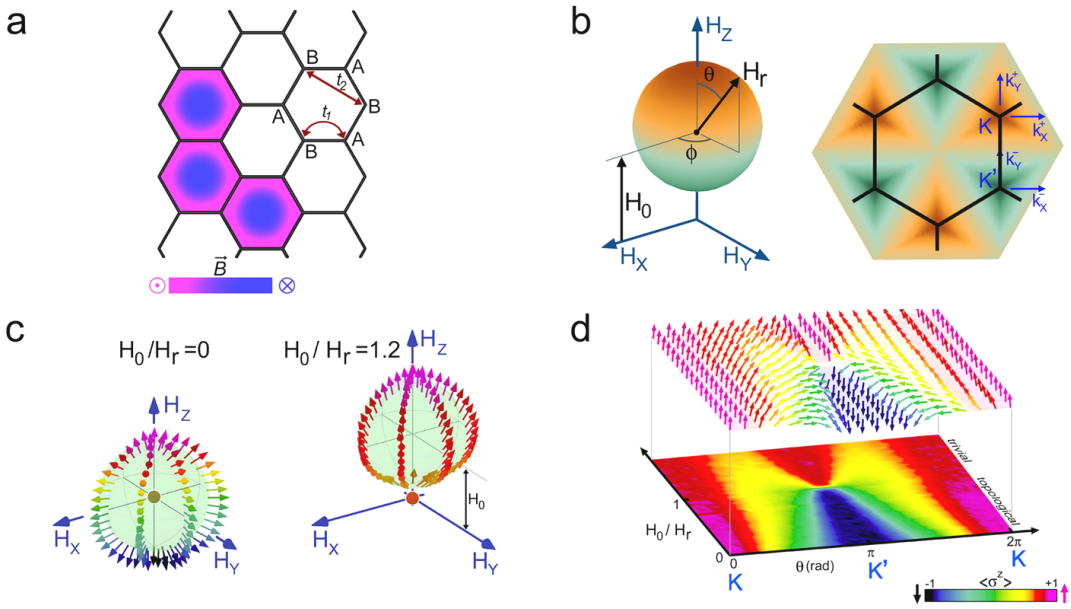

Figure C.2: **Experimental visualization of the topological phases and their evolution across the transition. (a)** In the Haldane model of graphene, in addition to the nearest neighbor hopping (t_1), a second neighbor hopping (t_2) is also considered with a variable phase ϕ controlled by the locally-varying flux through the plaquette, as well as a sublattice "mass" m_0 corresponding to a difference in chemical potentials between the sublattices. This system is topologically trivial if $|m_0| > |m_t = 3\sqrt{3}t_2 \sin\phi|$ and non-trivial otherwise. **(b)** A color-assisted representation of the mapping from a sphere parameterized by H_0, H_r, θ, ϕ to the hexagonal Brillouin zone of graphene. **b.** With adiabatic state preparation, the state of the qubit was prepared and measured over a grid on the surface of the parameter space spheres. Selected adiabatic Bloch sphere vectors are shown for $H_0/H_r = 0$ and 1.2. **(d)** With adiabatic state preparation, the state of the qubit was prepared and measured along the $\phi = 0$ meridian for various H_0/H_r values. The Bloch sphere states are presented with arrows whose colors indicate their $\langle\sigma^z\rangle$ values. The topological and trivial phase each has its own signature textures. By following the orientation of the state-vector along any path starting from **K** to **K′** and back to **K** one can see that in the topological case the state-vector fully winds around; however, for the trivial phase it only tilts away from the north pole of the Bloch sphere and comes back without winding around.

the honeycomb lattice of graphene (from H-space to k-space). The mapping places the points on the northern part of the spherical manifold of radius unity around the $\mathbf{K}$ point of the Brillouin zone and the southern hemisphere points around the $\mathbf{K}'$ point. For the northern hemisphere

$$\begin{aligned} \rho &= r(\phi) \tan \frac{\theta}{2} \\ \varphi &= \phi \end{aligned} \tag{C.3}$$

where θ and ϕ are the spherical coordinates of the northern hemisphere of the sphere in the parameter space, ρ and φ are the polar coordinates of the mapped circle, and r is given by

$$\begin{aligned} r(\phi) &= \frac{b \sin(\pi/6)}{\sin(5\pi/6 - \phi)} \text{for } 0 \leq \phi < 2\pi/3 \\ &= \frac{b \sin(\pi/6)}{\cos \phi} \text{ for } 2\pi/3 \leq \phi < 4\pi/3 \\ &= \frac{b \sin(\pi/6)}{\sin(\phi - 7\pi/6)} \text{ for } 4\pi/3 \leq \phi < 2\pi, \end{aligned} \tag{C.4}$$

where $b = |\mathbf{K} - \mathbf{K}'|$. The mapping of the southern hemisphere takes a similar form. This mapping is illustrated in Fig. S2(b), and covers only one third of the first Brillouin zone (FBZ). To cover the entire FBZ, the mapping was repeated three times. As the colors in Fig. S2(b) show, the north pole in the parameter space maps to three equivalent $\mathbf{K}$ points at the corners of FBZ and the south pole to the three $\mathbf{K}'$ points. With the mapping principle explained, now we can "move" the ground states that are measured adiabatically on the spherical surfaces in the parameter space and place them in the FBZ of the honeycomb lattice. Fig. S2(c) and (d) show the results for $H_0/H_r = 1.2$, and 0,

corresponding to trivial and topological phases, respectively.

Knowing the ground state of the system for each k_x and k_y point in the FBZ, $\mathcal{C}\hbar$ can be calculated directly from

$$\mathcal{C}\hbar = \frac{1}{4\pi}\int_{B.Z} \boldsymbol{\sigma}(\mathbf{k}) \cdot \left[\frac{\partial \boldsymbol{\sigma}(\mathbf{k})}{\partial k_x} \times \frac{\partial \boldsymbol{\sigma}(\mathbf{k})}{\partial k_y}\right] d^2\mathbf{k}. \tag{C.5}$$

Using this relation $\mathcal{C}\hbar$ numbers shown in Fig. 3(d) of the main text as well as the ones on panels (c) and (d) of Fig. S2 are calculated. While without any mapping, $\mathcal{C}\hbar$ could be calculated by modifying (C.5) to make it appropriate for spherical coordinates, mapping from the sphere to a 2D plane allowed us to use (C.5) directly. It is interesting to note that due to the topological nature of the phases, the details of the mapping do not matter, and other mappings could have worked as well.

C.2.3 Discussion

We note that the Haldane model consists of a half filled lattice of non-interacting spins, while we constructed a manifold of ground states by measuring the qubit over a closed surface. This difference is resolved by considering a mapping of the ground state manifold to the valence band of graphene, while the excited state manifold maps to the conduction band. Therefore, by probing the entire parameter manifold of the qubit ground state, we are probing the entire valence band. This distinction is why $\mathcal{C}\hbar$ of the electronic system can be measured with a single measurement, since all of the electronic states at different momenta are filled and hence probed simultaneously. On the other hand, the qubit can be measured only at a single point of the qubit system's parameter space at a given time,

which is why all the parameter angles must be probed separately and integrated to give $\mathcal{C}\hbar$.

C.3 Loci of Monopole Singularities for the Two-Qubit System

We have used the electromangetic analogy extensively in the main text to plot the (theoretical) locations of the magnetic monopoles in parameter space; we now show how one can identify their locations. We begin by pointing out that the magnetic monopole density can also be written as $\rho_m = \frac{1}{2\pi}\nabla \cdot (\nabla \times \mathbf{A})$, a seeming contradiction given that the divergence of a curl is known to be zero! The resolution to this seeming contradiction is that $\nabla \cdot (\nabla \times \mathbf{A})$ is indeed zero whenever the function $\mathbf{A}$ is smooth. However, near ground state degeneracies one cannot pick a smooth choice of gauge (even locally), since the ground state undergoes a sharp change. Therefore ρ_m is allowed to be non-zero if and only if the ground state is degenerate. Thus, one can reduce the problem of finding the magnetic charge density to the simpler one of locating the ground state degeneracies.

For general two qubit Hamiltonians, degeneracies can be readily located numerically using conventional techniques to minimize the ground state energy gap. However, for the specific case of our cylindrically symmetric two-qubit Hamiltonian, we can solve the problem analytically. As a reminder, the Hamiltonian of interest is

$$\mathcal{H} = -\frac{1}{2}\left[H_r \hat{n}(\theta,\phi)\cdot(\boldsymbol{\sigma_1}+\boldsymbol{\sigma_2}) + H_0\sigma_1^z + g(\sigma_1^x\sigma_2^x + \sigma_1^y\sigma_2^y)\right] \ . \tag{C.6}$$

This Hamiltonian has $U(1)$ invariance, meaning that the Hamiltonian at $\phi = 0$ can be mapped to arbitrary ϕ using

$$\mathcal{H}(\theta, \phi) = e^{i\phi\sigma^z_{\rm tot}/2} H(\theta, 0) e^{-i\phi\sigma^z_{\rm tot}/2} \ , \tag{C.7}$$

where $\sigma^z_{\rm tot} = \sigma^z_1 + \sigma^z_2$. While this invariance is computationally useful, it does not lead to any additional conservation laws, so on general grounds one does not expect to find degeneracies of our Hamiltonian (a 4×4 matrix) in the absence of symmetry. However, at $\theta = 0$ and π, the $U(1)$ invariance becomes a $U(1)$ symmetry, $\sigma^z_{\rm tot}$ is a conserved quantity, and this enables ground state degeneracies.

The values $\theta = 0$ and π lie along the z-axis, so we reparameterize the Hamiltonian along this axis as

$$\mathcal{H} = -\frac{1}{2}\left[H_z(\sigma^z_1 + \sigma^z_2) + H_0\sigma^z_1 + g(\sigma^x_1\sigma^x_2 + \sigma^y_1\sigma^y_2)\right] \ . \tag{C.8}$$

Since total spin along the z axis is now conserved, there are two obvious eigenstates: with energies $E_{\uparrow\uparrow/\downarrow\downarrow} = \pm(H_z + H_0/2)$. Within the $s^z_{\rm tot} = 0$ sector, the Hamiltonian reduces to

$$\mathcal{H}_{\uparrow\downarrow} = -\frac{1}{2}\begin{pmatrix} H_0 & 2g \\ 2g & -H_0 \end{pmatrix} \ , \tag{C.9}$$

which has eigenenergies $E_{\uparrow\downarrow} = \pm\sqrt{H_0^2/4 + g^2}$.

The ground state energy levels of these two sectors are degenerate when $|H_z + H_0/2| = \sqrt{H_0^2/4 + g^2}$, from which we find

$$H_z^{\rm deg} = \frac{-H_0 \pm \sqrt{H_0^2 + 4g^2}}{2} \ . \tag{C.10}$$

Having located these degeneracies, we can identify their magnetic monopole charges as $Q_m = 1$ based on the jump $\mathcal{C}\hbar$ that we find (experimentally and theoretically) at the

topological transitions.

This $U(1)$ symmetry at the poles was useful for our analysis, but it is not likely to exist for more complicated cases in which the Hamiltonians are not quite so exquisitely tunable. Therefore, by our above logic, we might argue that the degeneracies should go away if there are no longer any symmetries protecting them. However, our topological properties are robust against any perturbation, so despite the loss of symmetry, the degeneracies may drift around, but they do not disappear! This is a situation in which the degeneracies are protected not by a global symmetry, but rather by an emergent topological protection [111]. Breaking the $U(1)$ invariance of the model – for example by adding a σ_1^x term to the Hamiltonian – would disrupt the measurement. In our case, such a symmetry-breaking term does not present any fundamental challenges. It would simply add ϕ dependence to the Berry curvature, now requiring data to be taken for ramps of θ at multiple values of ϕ to allow integration over this direction as well. While it is certainly more time consuming to take this extra data, fundamentally it is no more difficult.

C.4 Hitchhiker's Guide to the Chern number and Berry Curvature

In the main paper, we defined $\mathcal{C}\hbar$ in terms of something called the "Berry curvature," which may have seemed mysterious. Here, we introduce the concept of Berry curvature

in the context of the more familiar Berry phase studied in adiabatic quantum mechanics. This will allow us to understand both the geometric and "electromagnetic" interpretations of Berry physics in an intuitive but quantitative way, which will in turn lead to the topological interpretation used in the main paper of $\mathcal{C}\hbar$ as a count of the number of degeneracies enclosed by a ground state manifold. We note that our pedagogical treatment of degeneracies as sources of a curvature field largely follows the original exposition of the Berry phase and curvature by M. V. Berry [22].

C.4.1 Berry connection, phase, curvature and all that

Berry connection and phase

Suppose we have a Hamiltonian that depends on a set of external parameters, which we describe by the parameter space vector $\mathbf{R}$, with corresponding ground states $|\psi_0(\mathbf{R})\rangle$; i.e., $\mathcal{H}(\mathbf{R})|\psi_0(\mathbf{R})\rangle = E_0|\psi_0(\mathbf{R})\rangle$. An example would be the three-dimensional (3D) parameter space associated with a single-qubit Hamiltonian in a rotating frame, $\mathcal{H}(\mathbf{R}) = -\frac{\hbar}{2}(H_X\sigma^x + H_Y\sigma^y + H_Z\sigma^z)$, with $\mathbf{R} = (H_X, H_Y, H_Z)$. Alternatively, if we take the rotating field in spherical coordinates, the natural parameters are magnitude $H_r \equiv |\mathbf{H_r}|$ and angles θ and ϕ (as in the main text). The Berry connection (from which the Berry curvature is defined) associated with the ground state manifold is then

$$\mathbf{A} = i\,\langle\psi_0|\nabla_{\mathbf{R}}|\psi_0\rangle\,, \tag{C.11}$$

which when integrated around a closed path C in parameter space yields the celebrated geometric Berry phase associated with that path [22, 62]

$$\gamma(C) = \oint_C \mathbf{A} \cdot d\mathbf{R}. \tag{C.12}$$

This fact can be derived from the Schrödinger evolution of a quantum state as C is traversed in parameter space in the adiabatic limit, and is independent of whatever dynamical phase is accumulated throughout the closed trajectory. However, it is not necessary to understand the phenomena of Berry phase from the perspective of the time-evolution of adiabatic systems – one can simply view it as a consequence of the geometry of an eigenstate manifold, which will soon become apparent in our discussion.

Geometric interpretation of Berry connection

The Berry connection $\mathbf{A}$ is an interesting construct because the meaning of the expression $\nabla_{\mathbf{R}}|\psi_0\rangle$ is ambiguous when only $\mathcal{H}(\mathbf{R})$ is given: unlike the coordinates $\mathbf{X}$ of real space, where a state $|\psi\rangle$ can be expanded as a wavefunction of spatial coordinates and $\nabla_{\mathbf{X}}$ is a natural operator on these wavefunctions, here it is instead the Hamiltonian itself that is a function of the parameter space coordinates $\mathbf{R}$. A manifold of ground states can be associated with a manifold in parameter space via the defining eigenvalue condition $\mathcal{H}(\mathbf{R})|\psi_0(\mathbf{R})\rangle = E_0(\mathbf{R})|\psi_0(\mathbf{R})\rangle$; however, although the states $|\psi_0(\mathbf{R})\rangle$ all live in the same Hilbert space, this eigenvalue condition does not tell us the phase of $|\psi_0(\mathbf{R})\rangle$ at different $\mathbf{R}$. In other words, we must specify what is essentially a choice of gauge when it comes to relative phase relations, and since this choice can be made arbitrarily, we cannot expect it

to have any intrinsic physical meaning. Once a choice is made for these phases however, the name "connection" for $\mathbf{A}$ signifies that $\mathbf{A}$ encodes a way to equate (or "connect") ground state vectors at two nearby points $\mathbf{R}$ and $\mathbf{R}+d\mathbf{R}$ in parameter space, analogous to the differential geometric notion of parallel transport of tangent vectors along a manifold [1].

Berry connection as a vector potential: deriving an observable field

In light of its dependence on $\nabla_{\mathbf{R}}$, $\mathbf{A}$ is therefore *gauge-dependent*. The remarkable fact however, as realized by Berry, is that its integral around a loop is actually gauge-*independent* (modulo 2π), and can therefore be measured. This is easily seen: suppose we change our definition of $|\psi_0(\mathbf{R})\rangle$ by an arbitrary local phase factor, $|\psi_0(\mathbf{R})\rangle \to e^{i\Gamma(\mathbf{R})}|\psi_0(\mathbf{R})\rangle$. Then by equation (C.11), $\mathbf{A}(\mathbf{R})$ is modified by the addition of the term $-\nabla_{\mathbf{R}}\Gamma(\mathbf{R})$, which integrates to zero around a closed path. The observant reader will notice that this takes the same form as the change of the magnetic vector potential under a gauge transformation. Recalling that the magnetic field is a gauge-invariant (i.e., directly measurable) quantity derivable from the magnetic vector potential, this motivates us to follow our experience with classical electromagnetism and define the analogue of the magnetic field, $\mathbf{B} \equiv \nabla \times \mathbf{A}$. This will allow us to rewrite the integral (C.12) defining the Berry phase in terms of an *observable* integrand $\mathbf{B}$. We will see that this "Berry field" has the interpretation of intrinsic curvature of the ground state manifold. In addition,

[1] In the language of geometry, A_μ intuitively gives (up to a factor of i) the component of $|\psi_0\rangle$ that one must subtract from $\partial_\mu|\psi_0\rangle$ in order to turn the derivative $\partial_\mu|\psi_0\rangle$ into a "covariant" derivative $D_\mu|\psi_0\rangle$ with the property that $|D_\mu\psi_0\rangle$ is orthogonal to $|\psi_0\rangle$, which defines what it means to keep a quantum state "parallel" as $\mathbf{R}$ is moved from $\mathbf{R}$ to $\mathbf{R}+d\mathbf{R}$.

this endeavor will expose some interesting physics, including the main topic of our work: topological transitions (jumps in $\mathcal{C}\hbar$) associated with degeneracy points.

Continuing the analogy, where for simplicity we consider a 3D parameter space, we obtain the Berry field from the Berry connection:

$$\mathbf{B}(\mathbf{R}) \equiv \nabla_{\mathbf{R}} \times \mathbf{A}(\mathbf{R}). \tag{C.13}$$

The Berry curvature field $\mathbf{B}$ is the vector form of what is known as the Berry curvature tensor, defined for general dimensionality and coordinate parametrizations by the antisymmetric tensor $\mathcal{B} \equiv \partial_\mu A_\nu - \partial_\nu A_\mu$ generalizing the curl:

$$\mathcal{B} = \begin{pmatrix} \mathcal{B}_{xx} & \mathcal{B}_{xy} & \mathcal{B}_{xz} \\ \mathcal{B}_{yx} & \mathcal{B}_{yy} & \mathcal{B}_{yz} \\ \mathcal{B}_{zx} & \mathcal{B}_{zy} & \mathcal{B}_{zz} \end{pmatrix} = \begin{pmatrix} 0 & B_z & -B_y \\ -B_z & 0 & B_x \\ B_y & -B_x & 0 \end{pmatrix} ; \tag{C.14}$$

that is, $\mathbf{B} = (B_x, B_y, B_z) = (\mathcal{B}_{yz}, \mathcal{B}_{zx}, \mathcal{B}_{xy})$. In our case, for short we will simply call $\mathbf{B}$ the Berry curvature.

Geometric interpretation of the Berry curvature field

The Berry phase associated with a closed path can now be calculated from (C.12) using Stokes' theorem by integrating the Berry curvature over a bounding surface,

$$\gamma(C) = \iint_{\mathcal{S}} \mathbf{B}(\mathbf{R}) \cdot d\mathbf{S}, \tag{C.15}$$

where $\mathcal{S}$ is a surface manifold in parameter space whose boundary is C. This is the direct analogue of a charged particle acquiring an Aharanov-Bohm phase when its path encloses a magnetic flux. However, the Berry curvature is a local geometric property, and for 2D manifolds can be physically measured through equation (2) of the main text. Intuitively,

the Berry curvature at $\mathbf{R}$ is equal to the ratio of the geometric phase accumulated over a loop surrounding $\mathbf{R}$ to the parameter space area enclosed by that loop, in the limit that the size of the loop goes to zero; in other words, it locally measures the noncommutativity of parallel transport, which manifests itself as a local "twisting and turning" of the state vector in parameter space via the accumulation of Berry phase. This is analagous to the fact that carrying a tangent vector on a geodesic triangle on the surface of a sphere causes the tangent vector to change direction when the triangular path returns to its starting point, even though locally the vector is always transported in a parallel fashion. The analogue of the Lorentz force [equation (2) of the main text] for the "magnetic field" $\mathbf{B}$ is related to this geometry-induced "deflection."

From local to global properties: the Chern number $\mathcal{C}\hbar$

One of the main points of this work is that through the analogy to electromagnetism, we can understand how to relate these geometric properties to topological properties of the ground state manifold as a whole. The natural question is then what generates the field $\mathbf{B}$? is it the current of "charged particles," or an analogue to the magnetic monopole? Consideration of this question leads us to a Gauss's law interpretation of $\mathcal{C}\hbar$, whose definition we repeat here [equation (1) of the main text]:

$$\mathcal{C}\hbar(\{|\psi_0\rangle\}) \equiv \frac{1}{2\pi}\oint_{\mathcal{S}} \mathbf{B}\cdot d\mathbf{S}. \tag{C.16}$$

Note that this form of the Gauss's law in which the Berry curvature is treated as a 3-vector is only valid in a three-dimensional parameter space. Generalization of this logic

to higher-dimensional manifolds remains work in progress. The above equation shows an integral of $\mathbf{B}$ over a closed (meaning no boundary curve C) ground state manifold in parameter space, and gives *nonlocal* information about this manifold in the form of a discrete integer through the Chern theorem [20]. To deduce the quantization of $\mathcal{C}\hbar$, we will use an argument similar to Dirac's argument [50] showing that the magnetic monopole charge is quantized. After that, we will explicitly relate this quantized value to the number of enclosed "magnetic monopoles" in parameter space. As usual, we restrict ourselves to 2D surfaces in a 3D parameter space.

The astute reader may wonder, given the definition of $\mathbf{B} = \nabla \times \mathbf{A}$, why $\mathcal{C}\hbar$ is not simply zero – after all, a simple application of Stokes' theorem shows that the integral of the curl of a function over any closed surface must vanish: imagine forming an arbitrary closed path C on the surface manifold $\mathcal{S}$, and let $\mathcal{S}_1$ and $\mathcal{S}_2$ be the two surfaces into which C divides $\mathcal{S}$. Taking into account the relative orientation of the two surfaces we then have

$$\mathcal{C}\hbar = \frac{1}{2\pi}\left(\int_{\mathcal{S}_1} \mathbf{B}\cdot d\mathbf{S} - \int_{\mathcal{S}_2} \mathbf{B}\cdot d\mathbf{S}\right). \tag{C.17}$$

A naive application of Stokes' theorem would say that each term is equal to the line integral of $\mathbf{A}$ around the same path, but with opposite signs, leading to $\mathcal{C}\hbar = 0$. However, this assumes that a single Berry connection (i.e., vector potential) can be defined over the entire manifold with some sufficient smoothness condition. Since Stokes' theorem can be intuitively understood by dividing the surface of integration into infinitely many infinitesimal circulation integrals of $\mathbf{A}$ and noting that neighboring circulations cancel

everywhere except along the surface boundary C, if there is a singularity in $\mathbf{A}$ then Stokes' theorem will break down. It then becomes a topological constraint on any vector potential covering $\mathcal{S}$ that there must be a singularity in $\mathbf{A}$ somewhere on the surface, which allows for the possibility of non-zero $\mathcal{C}\hbar$. The interesting fact is that the location of this singularity depends on the choice of vector potential (i.e., is gauge-dependent), but its existence does not depend on the choice of gauge. We note that a similar argument with what is now known as the Aharanov-Bohm phase associated with a physical magnetic field leads to Dirac's quantization condition for real magnetic monopoles [50].

However, there is still a constraint on the possible values of $\mathcal{C}\hbar$. Looking again at equation (C.17), since the geometric phase (C.12) accumulated by traversing C is physically observable (modulo 2π), using Stokes' theorem for each surface with its own vector potential it must be the case that the flux of $\mathbf{B}$ through $\mathcal{S}_1$ differs from the flux of $\mathbf{B}$ through $\mathcal{S}_2$ by a factor of $2\pi N$, where $N = \mathcal{C}\hbar$ is an integer.

$\mathcal{C}\hbar$, which is a property of the entire ground state manifold and cannot be probed locally, is therefore an example of a discrete topological invariant. In particular, $\mathcal{C}\hbar$ is robust to perturbations to the parameter space manifold, and it is reasonable to expect that it can only undergo transitions between different quantized values when there is singular behavior on the surface $\mathcal{S}$. In the next section, we will see that in our experiment, these singularities are precisely the locations of ground state degeneracy in the Hamiltonian, and will show that when the degeneracies considered are two-fold, N is in fact precisely equal to the number of two-fold degeneracies enclosed by the surface.

C.4.2 Topological interpretation of $\mathcal{C}\hbar$ in terms of enclosed degeneracies

What determines this mysterious integer N, and how can we observe it? The concept of $\mathcal{C}\hbar$ as a topological invariant is reminiscent of the Gauss-Bonnet theorem from differential geometry, which relates the integral of the Gaussian curvature over a closed surface to its topological genus. In the case of the Gauss-Bonnet theorem, the topological genus is equal to the number of "holes" it has, for example, 0 for a sphere and 1 for a torus (a "donut"). Just as the number of "holes" of a torus cannot be determined by local probing, $\mathcal{C}\hbar$ is a global, "topological" property of a ground state manifold. To understand what determines topological transitions between its different integral values, we must consider that there are other energy levels above the ground state energy level E_0, and include the possibility of degeneracies where for example $E_0(\mathbf{R}) = E_1(\mathbf{R})$. In 4.2.1 we will see that degeneracies behave analogously to magnetic monopoles as the "sources" for $\mathbf{B}$ and, through the familiar Gauss's law, see in 4.2.2 that for well-behaved two-fold degeneracies $\mathcal{C}\hbar$ simply counts the number of degeneracies enclosed by the manifold.

Degeneracy as a source of Berry curvature

In this work, measurements are made of the ground state manifold $|\psi_0(\mathbf{R})\rangle$, but states of higher energy must be considered to understand the important role of degeneracy points in topological transitions. Namely, let $|\psi_n(\mathbf{R})\rangle$ denote the eigenstate corresponding to the n^{th} energy level. To relate Berry curvature to degeneracy, we first use the fact that

the curl of a gradient is zero along with the definitions of $\mathbf{A}$ and $\mathbf{B}$ [equations (C.11) and (C.13)] to write $\mathbf{B} = i\left[\nabla_{\mathbf{R}}\langle\psi_0|\right] \times \left[\nabla_{\mathbf{R}}|\psi_0\rangle\right]$. We can then use the common trick of inserting the identity, expanded in terms of the energy eigenstates $|\psi_n(\mathbf{R})\rangle$, in between the bra and the ket: $\mathbf{B}(\mathbf{R}) = i\sum_{n\neq 0}\left[\nabla_{\mathbf{R}}\langle\psi_0|\right]|\psi_n\rangle \times \langle\psi_n|\left[\nabla_{\mathbf{R}}|\psi_0\rangle\right]$, where we have excluded the $n = 0$ term because it vanishes (this is easily seen as a consequence of normalization, $\langle\psi_0|\psi_0\rangle = 1$). We can replace $\langle\psi_n|\left[\nabla_{\mathbf{R}}|\psi_0\rangle\right]$ with the equivalent expression $\langle\psi_n|\left[\nabla_{\mathbf{R}}\mathcal{H}\right]|\psi_0\rangle/(E_0 - E_n)$ for $n \neq 0$ (this is a straightforward consequence of differentiating the defining eigenvalue equation $\mathcal{H}(\mathbf{R})|\psi_n(\mathbf{R})\rangle = E_n(\mathbf{R})|\psi_n(\mathbf{R})\rangle$ with respect to $\mathbf{R}$ and rearranging terms), arriving at the equation

$$\mathbf{B}(\mathbf{R}) = i\sum_{n\neq 0}\frac{\langle\psi_0|\left[\nabla_{\mathbf{R}}\mathcal{H}\right]|\psi_n\rangle \times \langle\psi_n|\left[\nabla_{\mathbf{R}}\mathcal{H}\right]|\psi_0\rangle}{(E_n - E_0)^2}. \tag{C.18}$$

From this, we can see that degeneracies (where $E_n = E_0$) can act as sources for the Berry curvature field $\mathbf{B}$. This also explicitly shows that $\mathbf{B}$ can be written without using phase-ambiguous derivatives $\nabla_{\mathbf{R}}|\psi_0\rangle$ of kets with respect to $\mathbf{R}$ [as in the definition of $\mathbf{A}(\mathbf{R})$], but instead in terms of more natural derivatives $\nabla_{\mathbf{R}}\mathcal{H}$ of $\mathcal{H}$ with respect to $\mathbf{R}$, meaning that it does not matter what phase we assign to eigenstates corresponding to different $\mathbf{R}$. Furthermore, we see that under certain assumptions about the behavior of $\mathcal{H}$ and E_n near degeneracy, the singularities in Berry curvature are precisely the points of degeneracy. We also note that equation (C.18) relates the Berry curvature to the generalized force operator $-\nabla_{\mathbf{R}}\mathcal{H}$, which connects this discussion to formula (2) of the main text for the Lorentz force. A derivation of this force in terms of $\mathcal{B}_{\mu\nu}$ using perturbation theory can be found in [63].

Sources of degeneracy as magnetic monopoles

Finally, we make the analogy between degeneracies and magnetic monopoles concrete. If we consider a closed 2D surface manifold $\mathcal{S}$ which bounds a 3D manifold in parameter space that possibly contains two-fold degeneracies, we can straightforwardly derive the interpretation of $\mathcal{C}\hbar$ as the number of source "magnetic monopole" singularities enclosed by the ground state manifold. Note that we can assume in a 3D space that degeneracies will occur at isolated points. This is an instance of a general result, originally shown by VonNeumann1929, stating that unless there is some special kind of symmetry in the Hamiltonian, three parameters must be tuned in order to reach a degeneracy, and are therefore the magnetic monopoles that we seek. When only two energy levels E_0 and E_1 are involved in a two-fold degeneracy, we only need to consider one term from the sum (C.18) and can restrict ourselves to the relevant two-level subspace. It can be shown that $\mathcal{C}\hbar$ is invariant under manifold perturbations as long as those perturbations don't cause a degeneracy to cross $\mathcal{S}$, so to extract the contribution to $\mathcal{C}\hbar$ from a single enclosed degeneracy at $\mathbf{R}_0$ we are free to shrink the manifold down to a small sphere centered around $\mathbf{R}_0$ [so that only the $(E_1 - E_0)^2$ term contributes] and shift the origin of our coordinates to $\mathbf{R}_0$. With an appropriate rescaling of parameter space coordinates, following [22] we can then write a general hermitian two-level Hamiltonian as

$$\mathcal{H} = \begin{pmatrix} Z & X - iY \\ X + iY & -Z \end{pmatrix}, \tag{C.19}$$

where X, Y, and Z are the rescaled coordinates in the Pauli basis, i.e., $\mathbf{R} = (X, Y, Z)$ (the exact nature of this scaling is unimportant). In terms of this parametrization the

energies are $E_{1/0} = \pm\sqrt{X^2 + Y^2 + Z^2} = \pm R$, so that the degeneracy is at the origin. We can immediately suspect that this leads to a monopole distribution for $\mathbf{B}$ because $1/(E_1 - E_0)^2 \propto 1/R^2$. The precise calculation is dealt with in Berry's original paper [22] using basic Pauli matrix algebra, resulting in the ground state Berry curvature field for a two-fold degeneracy at the origin,

$$\mathbf{B} = -\frac{\mathbf{R}}{2R^3}. \tag{C.20}$$

We note that this is the same answer obtained for the Berry field for the specific case of a spin-$\frac{1}{2}$ particle subjected to a physical magnetic field [62, 164]. This is (up to a sign) the same expression for the magnetic field generated by a magnetic monopole of magnetic charge 1/2, and therefore by Gauss's law leads to a contribution to $\mathcal{C}\hbar$ of $(4\pi)/(2\pi) \times 1/2 = 1$, as we claimed. Gauss's law then immediately yields for our experiment

$$\mathcal{C}\hbar = Q_{\mathrm{m}}^{\mathrm{enc}}. \tag{C.21}$$

C.4.3 Choice of coordinate system

Here we clarify the choice of coordinate system used throughout the main work. There is some ambiguity in how we define the Berry connection in spherical coordinates. One way is to close our eyes and pretend that we don't know that θ and ϕ are spherical angles, instead simply treating them as Euclidean parameters. We will call this the "Cartesian"

choice, which gives for example the ϕ-component

$$A_\phi^C = i \langle \psi_0 | \partial_\phi | \psi_0 \rangle \, . \tag{C.22}$$

Alternatively, we could explicitly take into account the non-Euclidean metric associated with spherical coordinates, using $\nabla f = \frac{\partial f}{\partial r}\hat{r} + \frac{1}{r}\frac{\partial f}{\partial \theta}\hat{\theta} + \frac{1}{r\sin\theta}\frac{\partial f}{\partial \phi}\hat{\phi}$ [86] to yield the "spherical" definition

$$A_\phi^S = i\frac{1}{r\sin\theta} \langle \psi_0 | \partial_\phi | \psi_0 \rangle = \frac{A_\phi^C}{r\sin\theta} \, . \tag{C.23}$$

This difference may have confused the reader. Below, we will show that either method works, and both of them can be used to arrive at Eq. (4) of the main text.

Cartesian coordinates

This is arguably the simpler method, though it is a bit harder to justify. As above, for the ground state manifold we define for ϕ or θ

$$A_{\phi/\theta}^C \equiv i \left\langle \psi_0 \middle| \partial_{\phi/\theta} \middle| \psi_0 \right\rangle . \tag{C.24}$$

Since we are integrating over a spherical surface (r fixed), we will not need to take any derivatives with respect to r. In these pseudo-Cartesian coordinates then, the non-trivial component of the Berry curvature is

$$B_{\theta\phi}^C \equiv \partial_\theta A_\phi^C - \partial_\phi A_\theta^C \, . \tag{C.25}$$

We can then perform the surface integral by noting that, in Cartesian coordinates, the surface element is just $dS = d\theta d\phi$, so that for a spherical manifold

$$\mathcal{C}\hbar = \frac{1}{2\pi}\int \mathbf{B}\cdot d\mathbf{S} = \frac{1}{2\pi}\int_0^{2\pi} d\phi \int_0^{\pi} d\theta B_{\theta\phi}^C \, , \tag{C.26}$$

which is the expression we expected.

Spherical coordinates

If we take the spherical version of the gradient, then the ϕ and θ components are

$$A^S_\phi = i\frac{1}{r\sin\theta}\langle\psi_0|\partial_\phi|\psi_0\rangle = \frac{A^C_\phi}{r\sin\theta} \ ,$$
$$A^S_\theta = i\frac{1}{r}\langle\psi_0|\partial_\theta|\psi_0\rangle = \frac{A^C_\theta}{r} \ . \tag{C.27}$$

The Berry curvature vector is given by $\mathbf{B}^S = \nabla \times \mathbf{A}^S$, which in general is a complicated expression. However, for our spherical surface of integration, the Chern integral is given by

$$\mathcal{C}\hbar = \frac{1}{2\pi}\int \mathbf{B}\cdot d\mathbf{S} = \frac{1}{2\pi}\int B^S_r dS_r \ , \tag{C.28}$$

since the surface element is strictly radial:

$$d\mathbf{S} = \hat{r}dS_r = \hat{r}(r^2\sin\theta d\theta d\phi) \ , \tag{C.29}$$

where we have used the standard form of a spherical surface element. Taking the curl in spherical coordinates, the radial component of $\mathbf{B}^S$ is

$$B^S_r = \frac{1}{r\sin\theta}\left[\partial_\theta(\sin\theta A^S_\phi) - \partial_\phi A^S_\theta\right] = \frac{1}{r^2\sin\theta}\left[\partial_\theta A^C_\phi - \partial_\phi A^C_\theta\right] = \frac{B^C_{\theta\phi}}{r^2\sin\theta} \ . \tag{C.30}$$

Plugging Eqs. (C.29) and (C.30) into (C.28), we again get the Cartesian expression for $\mathcal{C}\hbar$ (C.26).

Finally, we note that for our case, the Hamiltonian is cylindrically invariant: we can

get the Hamiltonian at arbitrary ϕ from the Hamiltonian at $\phi = 0$ by just rotating the spins by an angle ϕ around the z-axis. Accordingly, the Berry curvature must be cylindrically symmetric, meaning that $B_{\theta\phi}(\theta, \phi) = B_{\theta\phi}(\theta)$ is independent of ϕ. Therefore, if we plug into the expression for the Chern number, we find

$$\mathcal{C}\hbar = \underbrace{\frac{1}{2\pi}\int_0^{2\pi} d\phi}_{=1} \int_0^{\pi} d\theta B_{\theta\phi}(\theta) = \int_0^{\pi} B_{\theta\phi}(\theta) d\theta \ . \tag{C.31}$$

We now show how the equation (4) of the main text was derived. Starting with the Hamiltonian of a single qubit or equivalently spin-1/2 particle in a magnetic field:

$$\mathcal{H}_S = -\frac{\hbar}{2}(H_X\sigma^x + H_Y\sigma^y + H_Z\sigma^z), \tag{C.32}$$

and re-parameterizing it for spherical coordinates, it becomes

$$\mathcal{H}_S(H_r, \theta, \phi) = -\frac{\hbar}{2}H_r(\sin\theta\cos\phi\,\sigma^x + \sin\theta\sin\phi\,\sigma^y + \cos\theta\,\sigma^z). \tag{C.33}$$

Therefore,

$$F_\phi = -\langle\partial_\phi\mathcal{H}(\phi = 0)\rangle = \frac{\hbar}{2}H_r\sin\theta\,\langle\sigma^y\rangle. \tag{C.34}$$

Using equation (2) of the main text,

$$\hbar B_{\theta\phi}d\theta = \frac{\hbar}{2}H_r\sin\theta\,\langle\sigma^y\rangle dt, \tag{C.35}$$

which is used in the main text in computing $\mathcal{C}\hbar$ from the measured values of H_r and $\langle\sigma^y\rangle$.

C.5 Mapping the Two-Qubit Hamiltonian to Electronic Band Structure

As in the main text, we consider the two-qubit Hamiltonian

$$\mathcal{H} = -\frac{\hbar}{2}\Big[H_0\sigma_1^z + H_r\hat{n}(\theta,\phi)\cdot(\boldsymbol{\sigma_1}+\boldsymbol{\sigma_2}) - g(\sigma_1^x\sigma_2^x + \sigma_1^y\sigma_2^y)\Big] \tag{C.36}$$

for fixed H_0, H_r, and g. For this section we assume $\hbar = 1$. At a given value of θ and ϕ, this Hamiltonian is a 4×4 matrix; a general N-qubit Hamiltonian would similarly be $2^N \times 2^N$. To help understand the topology of this Hamiltonian, we wish to map it to a more conventional electronic Hamiltonian, as we did in mapping the single qubit to the Haldane model of graphene. In this supplement, we show that (C.36) can be mapped to either a four-band model of non-interacting electrons in the spirit of the Haldane mapping or a four-band interacting electron model with interactions that are short-range in momentum space. Finally, we comment on the extension of these mappings to higher numbers of qubits.

For both non-interacting and interacting electron mapping, we again utilize the idea that a given angle (θ,ϕ) of the rotating field H_r corresponds to a point in momentum space (see the single qubit Haldane supplement): $\mathbf{k} = (k_x, k_y) \leftrightarrow (\theta,\phi)$. Then the simple idea which worked for mapping the single qubit to the Haldane model is to "fermionize" the spin:

$$\sigma_j^\alpha \to \sum_{ss'} c_{js}^\dagger \sigma_{ss'}^\alpha c_{js'} \ , \tag{C.37}$$

where $\alpha = x, y, z$, $j = 1, 2$ specifies the qubit, and $s, s' = \{\uparrow,\downarrow\}$ iterate through the

spin states. For example, this mapping gives $\sigma_1^x \rightarrow c_{1\uparrow}^\dagger c_{1\downarrow} + c_{1\downarrow}^\dagger c_{1\uparrow}$. Performing these replacements we get

$$\begin{aligned}
\mathcal{H}(\mathbf{k}) &= (H_r \cos\theta_{\mathbf{k}} + H_0)[\underbrace{(c_{1\uparrow}^{\mathbf{k}})^\dagger c_{1\uparrow}^{\mathbf{k}} - (c_{1\downarrow}^{\mathbf{k}})^\dagger c_{1\downarrow}^{\mathbf{k}}}_{\sigma_1^z}] + H_r \cos\theta_{\mathbf{k}}[\underbrace{(c_{2\uparrow}^{\mathbf{k}})^\dagger c_{2\uparrow}^{\mathbf{k}} - (c_{2\downarrow}^{\mathbf{k}})^\dagger c_{2\downarrow}^{\mathbf{k}}}_{\sigma_2^z}] + \\
&\quad H_r \sin\theta_{\mathbf{k}} \cos\phi_{\mathbf{k}}[\underbrace{(c_{1\uparrow}^{\mathbf{k}})^\dagger c_{1\downarrow}^{\mathbf{k}} + (c_{1\downarrow}^{\mathbf{k}})^\dagger c_{1\uparrow}^{\mathbf{k}}}_{\sigma_1^x} + (1 \rightarrow 2)] + \\
&\quad H_r \sin\theta_{\mathbf{k}} \sin\phi_{\mathbf{k}}[\underbrace{-i(c_{1\uparrow}^{\mathbf{k}})^\dagger c_{1\downarrow}^{\mathbf{k}} + i(c_{1\downarrow}^{\mathbf{k}})^\dagger c_{1\uparrow}^{\mathbf{k}}}_{\sigma_1^y} + (1 \rightarrow 2)] + \\
&\quad \frac{g}{2}[(c_{1\uparrow}^{\mathbf{k}})^\dagger c_{1\downarrow}^{\mathbf{k}} (c_{2\downarrow}^{\mathbf{k}})^\dagger c_{2\uparrow}^{\mathbf{k}} + (\uparrow \leftrightarrow \downarrow)] \; . \qquad \text{(C.38)}
\end{aligned}$$

The last term of this Hamiltonian contains a four-fermion operator, so this is an interacting fermionic Hamiltonian with four flavors of fermion $(c_{1\uparrow}, c_{1\downarrow}, c_{2\uparrow}, c_{2\downarrow})$. To maintain one spin per qubit, we want the many-body ground state at half-filling and without double occupancy on "site" $j = 1, 2$. However, the interaction remains short-range in momentum space, meaning the electronic Hamiltonian is still separable into momentum sectors: $H = \sum_{\mathbf{k}} H_{\mathbf{k}}$. Such models are similar to the mean-field BCS Hamiltonian [84], in this case with the additional wrinkle of being local in momentum space. momentum space.

While this first mapping is true to the interacting nature of the qubit, it gives little physical insight into the topological transition. To try to understand this better, we now discuss how the same system can be mapped to a four-band Haldane-like model of non-interacting electrons. Unlike the interacting case, we present a microsopic model that will realize this topology. The model is shown schematically in Fig. C.3a . The basic idea is to consider electrons hopping on stacked triangular lattices with a single internal

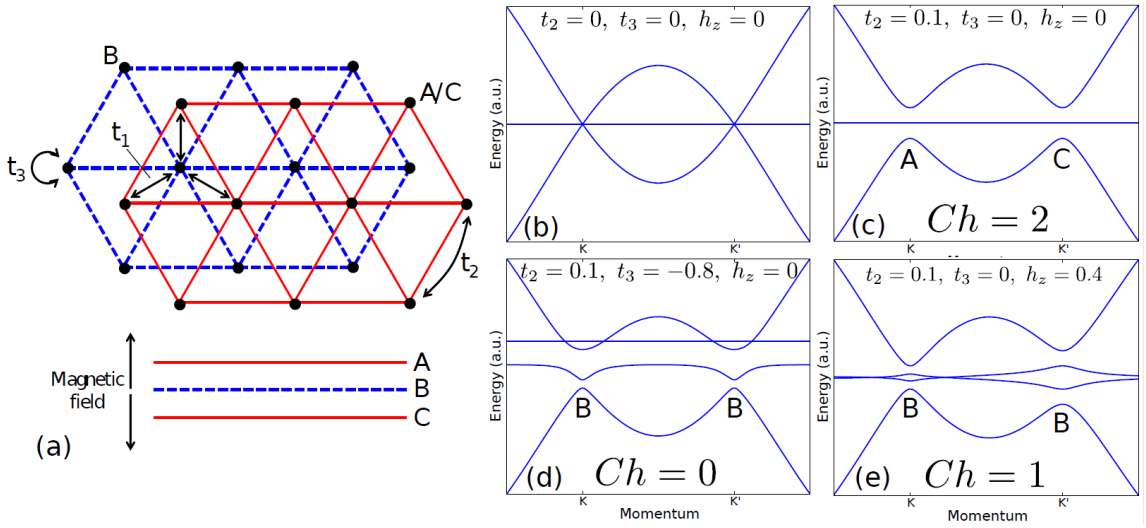

Figure C.3: Illustration of the four-band non-interacting lattice model to which we map our two-qubit model. **(a)** The model consists of three stacked triangular lattices (A, B, and C), the middle of which (B) contains two spin/orbital states. In addition to nearest neighbor hopping (t_1) and on-site hybridization the B sublattice (t_2), electrons on the A and C sublattices experience magnetic field that adds phase to the hopping ($t_2 e^{i\varphi}$). Finally, an effective Zeeman field splits the spin/orbital states on all sublattices. **(b)** to **(e)** Energy dispersions for this model along a cut containing the K and K' corners of the first Brillouin zone. We fix energy by setting $t_1 = 1$. At the K and K' points, the sublattices decouple; we label the sublattice that is occupied in the ground state at these points. $\mathcal{C}h$ then counts the number of times the wavefunction "twists" between the sublattices.

degree of freedom (spin/orbital/etc.) that can take one of two values, which we denote $\uparrow$ and $\downarrow$. The middle layer of the stack, which we call B, supports both $\uparrow$ and $\downarrow$ states, while the upper (lower) layer supports only $\uparrow$ ($\downarrow$). This could be realized, for example, by a lattice where the middle layer has two orbital states (e.g. p_x and p_y orbitals), while the outer layers have only one orbital state (e.g. s orbitals). We assume there is a magnetic field gradient as in Fig. C.3a, which gives zero field layer B and yields opposite magnetic field at A and C. We then consider four quadratic terms in the Hamiltonian:

1. Nearest neighbor hopping t_1, which connects the B sublattice to the A and C sublattices. The matrix element is assumed to be equal for spin up hopping to either up or down, which make senses for orbital degrees of freedom or if $\uparrow$ and $\downarrow$ represent real spins, but with different quantization axes on A/C than on B.

2. Second neighbor hopping on the A and C sublattices, which picks up a phase due to the magnetic flux. For simplicity, we consider a flux of $\Phi = 3\Phi_0/4 = -\Phi_0/4$ per plaquette, where $\Phi_0 = h/e$ is the quantum of flux; this gives phase $\varphi = \pi/2$ on the hopping, removing a diagonal shift in the energy bands of the A and C sublattices (see [68]).

3. On-site hybridization t_3 between the effective spin states on the B sublattice.

4. An effective Zeeman shift $h_z s^z$, where s^z is the internal spin/orbital degree of freedom.

Let us examine these terms in the language of the Haldane Hamiltonian. First note

that the A and B (or equivalently C and B) sublattices have the exact structure as the sublattices of monolayer graphene. Therefore, the first Brillouin zone of this non-interacting electron model is equivalent to that of graphene, and we can naturally expand the Hamiltonian in small deviations of the momenta around the non-identical zone corners K and K' (see [cite Haldane supplement]). There are four states in each unit cell: $B\uparrow$, $B\downarrow$, $A\uparrow$, and $C\downarrow$. The nearest neighbor hopping t_1 is the only term that connects the sublattices, so it is responsible for producing a graphene-like dispersion relation. However, to get the Chern number of 2, this is slightly different from the Haldane model of graphene. To see this, consider quantizing the spins along the x-axis. It is easy to see that the state $|\uparrow_x\rangle = \frac{1}{\sqrt{2}}(|\uparrow_z\rangle + |\downarrow_z\rangle$ hops freely and will give the dispersion of a graphene lattice with hopping amplitude $2t_1$. However, a state with spin $|\downarrow_x\rangle = \frac{1}{\sqrt{2}}(|\uparrow_z\rangle - |\downarrow_z\rangle$ is annihilated by this hopping term, so in addition to the graphene dispersion, there are two flat bands at energy zero if only the t_1 term is considered (see Fig. C.3(b)).

The remaining terms then determine the topology by breaking the degeneracies at momenta K and K'. For instance, the $t_2 e^{i\varphi}$ hopping only occurs on the A and C sublattices, so at the K and K' points (where the t_1 hopping vanishes), the electrons only live on the A or the C sublattice. As the momentum is varied from K ($\theta = 0$) to K' ($\theta = \pi$), the electronic ground state winds from sublattice A to C, which results in $\mathcal{C}\hbar = 2$ (see Fig. C.3(c)). This is precisely the action of the probe field, so we see that $t_2 \sim H_r$. Similarly, the t_3 term hybridizes the orbitals on the B lattice, causing the energy of the symmetric state on the B lattice to go down. For strong enough t_3, this can push the

energy of the symmetric state on B lattice below the A and C energies throughout the Brillouin zone, resulting in Chern number zero (i.e., no wrapping of wave function, see Fig. C.3(d)). This is the same role as the qubit interactions, so not surprisingly $t_3 \sim g$. Finally, if we again consider $t_3 = 0$, then a large positive Zeeman field h_z will push the energy of the spin down state below that of the spin up. In the presence of t_2 hopping, this gives a ground state winding from the A sublattice to the B sublattice as momentum goes from K to K' (Fig. C.3(e)), yielding Chern number one. Not surprisingly, this gives that $h_z \sim H_0$.

More explicitly, the Hamiltonian described above can be written

$$\begin{aligned}\mathcal{H} &= \sum_{\mathbf{r}} \Big[-t_1 \sum_j (c^\dagger_{\mathbf{r}\uparrow} + c^\dagger_{\mathbf{r}\uparrow})(c_{\mathbf{r}+\mathbf{a_j}\downarrow} + c^\dagger_{\mathbf{r}+\mathbf{a_j}\downarrow}) - t_2 \sum_j (\overbrace{e^{i\varphi} c^\dagger_{\mathbf{r}\uparrow} c_{\mathbf{r}+\mathbf{b_j}\uparrow}}^{\text{A sublattice}} + \overbrace{e^{-i\varphi} c^\dagger_{\mathbf{r}\downarrow} c_{\mathbf{r}+\mathbf{b_j}\downarrow}}^{\text{C sublattice}}) + \\ &\quad \frac{t_3}{2}(c^\dagger_{\mathbf{r}+\mathbf{a_1}\uparrow} c_{\mathbf{r}+\mathbf{a_1}\downarrow} + (\uparrow \leftrightarrow \downarrow)) - \frac{h_z}{2}(c^\dagger_{\mathbf{r}\uparrow} c_{\mathbf{r}\uparrow} + c^\dagger_{\mathbf{r}+\mathbf{a_1}\uparrow} c_{\mathbf{r}+\mathbf{a_1}\uparrow} - (\uparrow \to \downarrow))\Big] + h.c.\,, \end{aligned} \quad \text{(C.39)}$$

where $\mathbf{r}$ are the sites on the A/C sublattice, $\mathbf{a_j}$ are the nearest neighbor displacements, and (following Haldane's convention), $\mathbf{b_j}$ are the next-nearest-neighbor displacements along directions with positive hopping phase on the A sublattice. Diagonalizing with phase $\varphi = \pi/2$, this gives Bloch Hamiltonian

$$\mathcal{H}_{\mathbf{k}} = \begin{pmatrix} -2t_2 \sum_j \sin(\mathbf{k}\cdot\mathbf{b_j}) - h_z & -2t_1 \sum_j \cos(\mathbf{k}\cdot\mathbf{a_j}) & -2t_1 \sum_j \cos(\mathbf{k}\cdot\mathbf{a_j}) & 0 \\ -2t_1 \sum_j \cos(\mathbf{k}\cdot\mathbf{a_j}) & -h_z & t_3 & -2t_1 \sum_j \cos(\mathbf{k}\cdot\mathbf{a_j}) \\ -2t_1 \sum_j \cos(\mathbf{k}\cdot\mathbf{a_j}) & t_3 & h_z & -2t_1 \sum_j \cos(\mathbf{k}\cdot\mathbf{a_j}) \\ 0 & -2t_1 \sum_j \cos(\mathbf{k}\cdot\mathbf{a_j}) & -2t_1 \sum_j \cos(\mathbf{k}\cdot\mathbf{a_j}) & 2t_2 \sum_j \sin(\mathbf{k}\cdot\mathbf{b_j}) + h_z \end{pmatrix}, \quad \text{(C.40)}$$

where the columns denote A↑, B↑, B↓, and C↓ in that order. For comparison, the

two-qubit Hamiltonian in the basis $\uparrow\uparrow$, $\uparrow\downarrow$, $\downarrow\uparrow$, $\downarrow\downarrow$

$$\mathcal{H}_{2Q} = \frac{1}{2}\begin{pmatrix} -2H_r\cos\theta - H_0 & -2H_r\sin\theta & -2H_r\sin\theta & 0 \\ -2H_r\sin\theta & -H_0 & -2g & -2H_r\sin\theta \\ -2H_r\sin\theta & -2g & H_0 & -2H_r\sin\theta \\ 0 & -2H_r\sin\theta & -2H_r\sin\theta & 2H_r + H_0 \end{pmatrix} . \tag{C.41}$$

By inspecting these two Hamiltonians, we see that they map to each other under the identification

$$\mathbf{k} \leftrightarrow (\theta, \phi) \ , \ 3t_2\sqrt{3} = H_r \ , \ -t_3 = g \ , \ 2h_z = H_0 \ , \tag{C.42}$$

where we used the fact that $\sum_j \sin(\mathbf{k}\cdot\mathbf{b_j}) = \pm 3\sqrt{3}/2$ at the corners of the first Brillouin zone. Therefore, the topology of the ground band of this four-band electronic model is equivalent to that of the two-qubit system that we experimentally investigate.

It is clear from the above discussion that a system of L qubits with 2^L eigen states would map to a non-interacting model with 2^L bands. While 2 or 4 band models are not so crazy, an eight band model with only a singled filled band – as would be needed for $L = 3$ qubits – is starting to get physically less realistic. Clearly the scaling of the number of bands with the number of qubits is such that these non-interacting Haldane-like models will become exponentially more difficult to engineer as the system becomes larger. Working instead with the interacting model helps quite a bit; simple counting requires only $2L$ flavors of fermion (spin up and down for each qubit) at half-filling and with no double-occupancy. However, this model has no obvious microscopic interpretation, so for the time being we consider it less physical. Therefore, we conclude that as the qubit number is increased (and restricted to the above mapping methods), it becomes

increasingly unworkable to think of the system in terms of electrons on a lattice. For large spin lattices, we really should think of our measurement as simply probing the topology of the spin manifold, a problem which is interesting in and of itself. It is also worth pointing out that the two mapping we have described about only work for our choice of parameter manifolds, namely fixed external field strength with a rotating angle applied equally to each qubit. By using different choices of manifold, even within the same two-qubit system, we can engineer different effective condensed matter models, demonstrating the flexibility of these two-qubit systems.

C.6 Experimental protocols, calibration, and analysis

Here we provide the outline of the experiment and its basic protocols. The first step is the calibration of the pulses so we know $H_X/2\pi$ and $H_Z/2\pi$ with good accuracy. An important aspect of calibration is also finding the compensating pulse such that when we only $H_X/2\pi$, the state of the qubit remains in the YZ plane. The details of these steps are explained in Fig. S5. Next, one needs to find a proper ramp speeds to be sure the higher order errors in equation 2 of main text remain small; another words, how much non-adiabatic a ramp can be and still yield a good result. This is shown in figure S6, where we explored the three parameters that set the non-adiabaticity of a ramp: $H_X/2\pi$, $H_Z/2\pi$, and T_f. After finding that one needs to set all the ramps such

that the adiabaticity measure A remains acceptable. After finding proper ramp speeds and calibrations, one can do the single qubit experiment, which involves applying $H_X/2\pi$ with sine envelope and $H_Z/2\pi$ with a cosine profile, as discussed in Fig. S4. The two qubit experiment requires additional calibrations to what is mentioned in here and is discussed in [38]. In Fig. S9, we provide further analysis of the 2-qubit data to gain a better understanding of the topological phases.

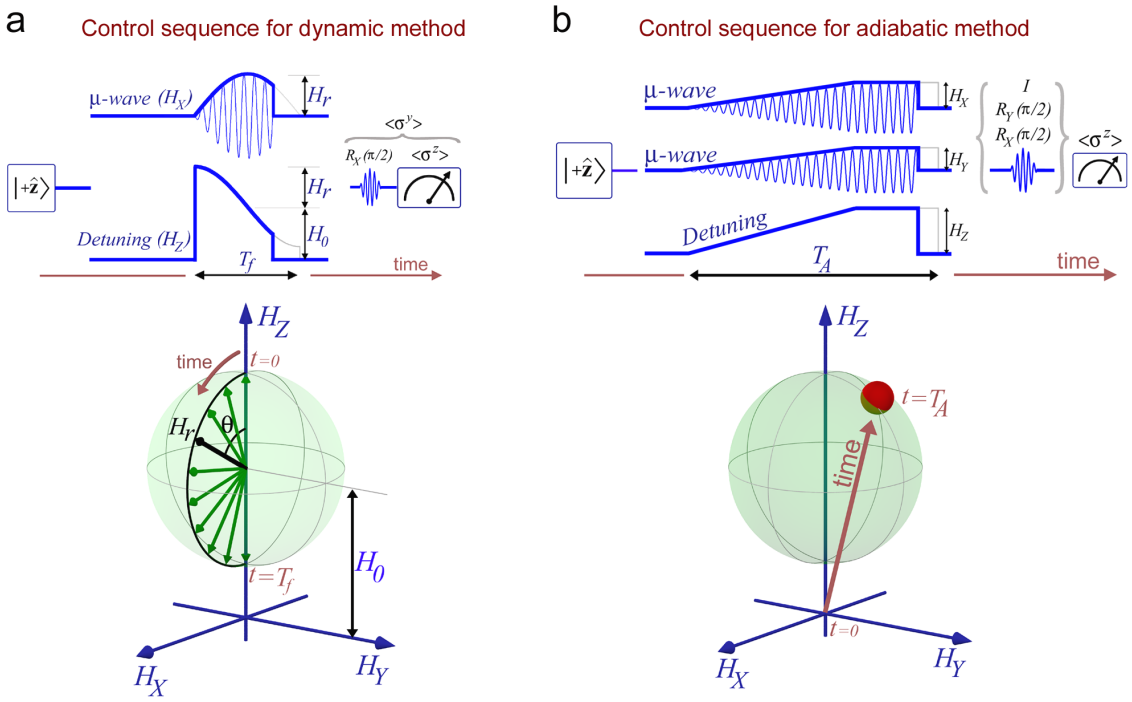

Figure C.4: **Control sequence used for the single qubit experiments. (a)** The pulse sequence used to obtain the phase diagram shown in Fig. 3(a) of the main text. Every control sequence began with preparing the qubit in its ground state, which was achieved by waiting for times much longer than the qubit relaxation time (a few tens of microseconds). In the phase diagram measurements, $\langle\sigma^y\rangle$ was measured at 50 time steps during the ramps, where the first data point was measured at $t = 0$ and the last one at $t = T_f = 1000$ ns. To measure each data point the sequence was repeated 300 times. This 50-point $\langle\sigma^y\rangle$ profile as a function of time from 0 to T_f was then multiplied by a sine profile (see equation (4) in the main text) and integrated to give $\mathcal{C}\hbar$. $\langle\sigma^y\rangle$ was measured by inserting a $R_X(\pi/2)$ pulse before the $\langle\sigma^z\rangle$ measurement. The microwave pulse with a sine profile and detuning pulse with a cosine profile constitute a semi-circular ramp in the parameter space, and given the symmetry of the single-qubit Hamiltonian, this is sufficient to calculate the curvature over the entire spherical manifold. **(b)** Control sequence for adiabatic state preparation and measurement. In contrast to the dynamic method (equation (4) of the main text), in the adiabatic state preparation process, the qubit needs to remain close to the instantaneous eigenstate of the system during the ramp. To evolve to the ground state of the Hamiltonian with parameters (H_X, H_Y, H_Z), we start from the origin of parameter space, where all pulses are zero, and gradually turn (H_X, H_Y, H_Z) to their final values in 500 ns. The pulses then remain at their target values for 500 ns (hence $T_A = 1000\,ns$). Over this fixed pulse regions at 100 points (distributed uniformly from 500 ns to 1000 ns) the state of the qubit was measured with tomography and the results are averaged to present a single Bloch vector data corresponding to given (H_X, H_Y, H_Z) values. To visualize the ground states over the entire spherical manifold $\mathcal{S}$, the process was repeated for different values of (H_X, H_Y, H_Z) to form a grid over this parameter space sphere.

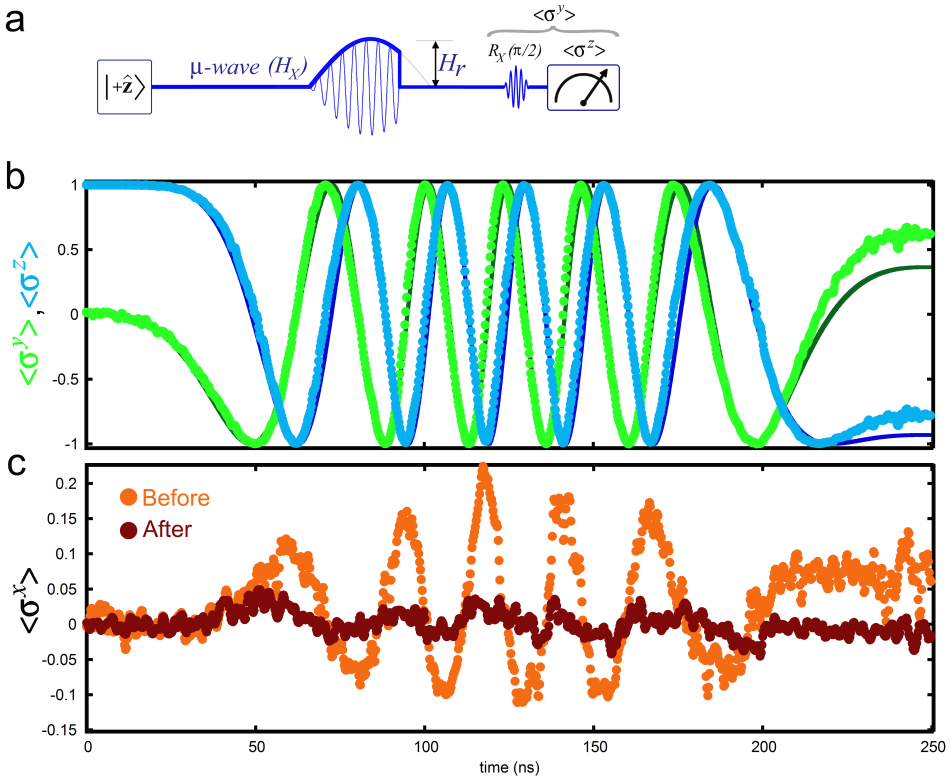

Figure C.5: **Pulse Calibration.** Single qubit microwave and detuning pulses were calibrated separately before applying them simultaneously to the qubits. **(a)** To calibrate the microwave pulse, the qubit was prepared in its groundstate $|+\hat{z}\rangle$ and a microwave pulse with a sine envelope of amplitude H_r was applied to the qubit. The state of the qubit (the Bloch vector) was measured at each point in time by interrupting the ramp and performing full state tomography. As shown in panel **(a)**, for instance, to measure $\langle\sigma^y\rangle$, a rotation of $\pi/2$ around the X axis was performed before the $\langle\sigma^z\rangle$ measurement. This pulse results in a cyclic motion of the Bloch vector in the Y-Z plane, with a non-zero out of plane component. The out of plane component is mainly due to leakage to other states due to finite inharmonicity of the qubit system. Therefore, the measured out of plane component ($\langle\sigma^x\rangle$, orange points in panel **(c)**) needs to be calibrated, which was done by adding a compensating microwave pulse on the Y-axis, with a variable amplitude during the pulse sequence such that it keeps $\langle\sigma^x\rangle$ close to zero. A typical result before and after calibration is shown in **(c)**. Fitting the $\langle\sigma^z\rangle$ and $\langle\sigma^y\rangle$ with a single fitting parameter can be done using the Schrödinger equation. The resulting value in this case is $H_r/2\pi = 44.5$ MHz. The dark blue and green solid lines are the result of the fitting. During the calibration since full state tomography was performed, we normalized the measured values of $\langle\sigma^x\rangle$, $\langle\sigma^y\rangle$, $\langle\sigma^z\rangle$ such that $\langle\sigma^x\rangle^2 + \langle\sigma^y\rangle^2 + \langle\sigma^z\rangle^2 = 1$. The detuning pulse was applied and measured similarly. This was done by bringing the qubit to the equator of the Bloch sphere with a $\pi/2$-pulse first, and then applying the detuning in the absence of microwave pulse, and fitting the result with the Schrödinger equation. There was no compensation pulse to be considered in this case.

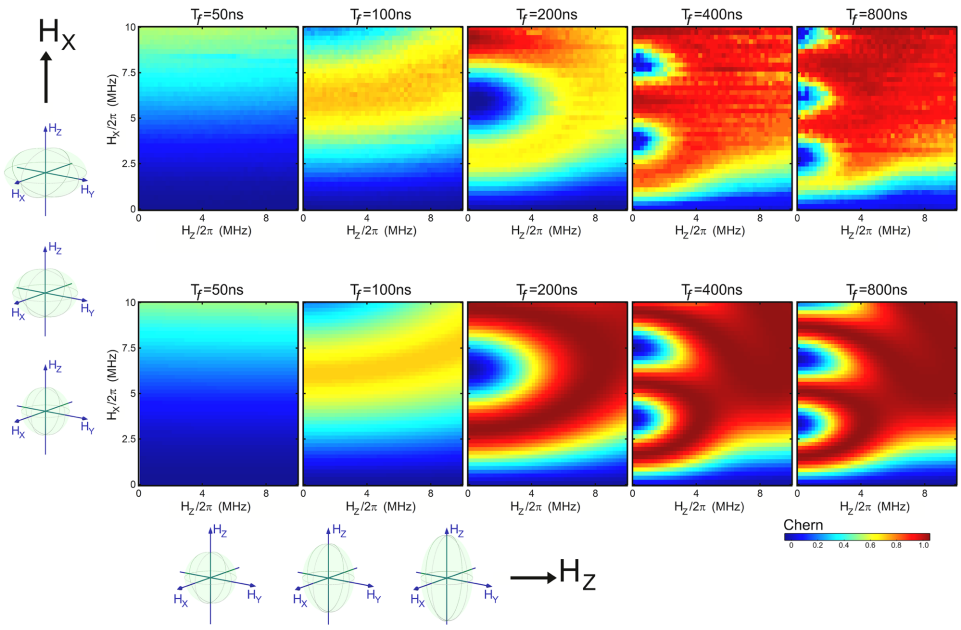

Figure C.6: **Adiabaticity required to measure $\mathcal{C}\hbar$.** Although equation (2) of the main text does not require adiabaticity, it does require the ramp in parameter space to be done slowly, such that $O(v_\theta^2)$ remains negligible. One needs to operate with ramp velocities for which deviation from adiabaticity varies linearly with the ramp speed. Slower ramps are more adiabatic and hence better in this regard, but they have a small deviation from adiabaticity, which would be hard to measure experimentally. On the other hand, ramps that are too fast also contain non-adiabatic errors that are not linearly proportional to ramp speed, and hence should be avoided. In this figure, the top row shows the experimental results of measuring $\mathcal{C}\hbar$ by making various elliptical ramps and traversing them with different velocities. A microwave pulse of $X(t) = H_X \sin(\pi t/T_f)$ and detuning of $Z(t) = H_Z \cos(\pi t/T_f)$ are used, with $H_X/2\pi$ and $H_Z/2\pi$ varied from 0 to 10 MHz. Five different speeds are used, which are set by T_f, where T_f is the time it takes to ramp from the north pole of the manifold to its south pole. The lower row shows the numerical results using the same ramps, obtained from the time dependent Schrödinger equation. In this example, we seek to measure $\mathcal{C}\hbar$ over a manifold of ground states that encloses the origin of the parameter space. The theoretical value of $\mathcal{C}\hbar$ in this case is 1 [62]. From left to right, as T_f becomes longer, the ramps are more adiabatic and the measured value for $\mathcal{C}\hbar$ approaches one. In each panel, moving from lower left to upper right, adiabaticity increases, since $A = T_f H_r/2\pi = T_f\sqrt{{H_X}^2 + {H_Z}^2}/2\pi$. For $T_f = 400$ ns or longer, a good estimate of $\mathcal{C}\hbar$ can be achieved, as almost the entire plot is red, regardless of the shape of the manifold. The method yields a good estimate of $\mathcal{C}\hbar$ for $A > 1.5$. To provide a visual guide, the deformation of the spherical manifolds to ellipsoids, by keeping H_X fixed and increasing H_Z (horizontal axis below figure), and by keeping H_Z fixed and increasing H_X (vertical axis left of figure) are shown.

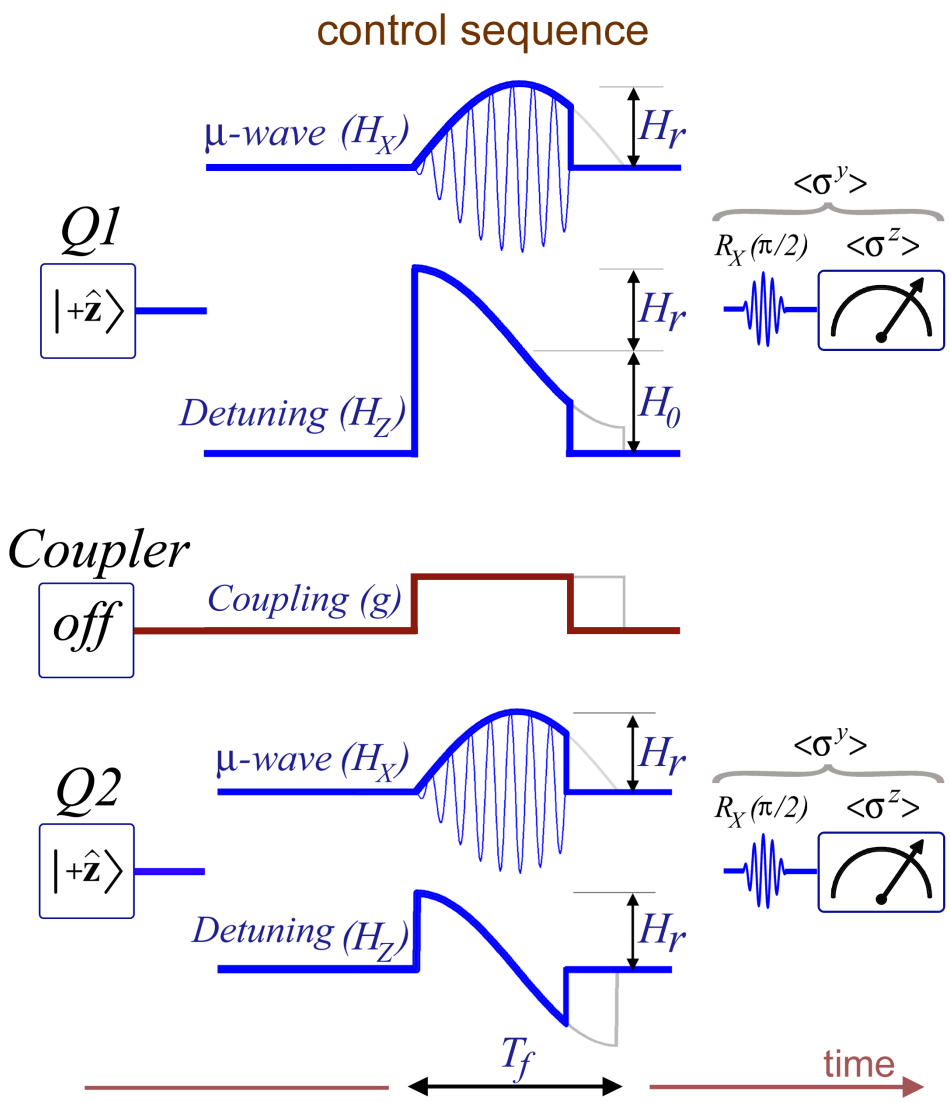

Figure C.7: **Control sequence used for the 2-qubit experiments. (a)** The pulse sequence used on individual qubits and the coupler elements are shown. The microwave pulse applied to each qubit had a sine envelope. The detuning of Q2 has a cosine profile, and the detuning of Q1 has a cosine profile plus an offset defining H_0. With a rectangular pulse, the coupling between the two qubits is turned on during the active part of other pulses. The synchronization of the pulses as well as finding the flux value corresponding to $g = 0$ were done [38] prior to running the sequence. In addition, a calibration matrix to take various types of crosstalk into account was measured and implemented. This included both microwave and flux-biasing crosstalk [38]. Using equation (4) of the main text, the $\mathcal{C}\hbar$ for 2-qubit manifolds is the summation of individual ones. Therefore, each pulse sequence was run twice, once to measure $\langle\sigma_1^y\rangle$ and again to measure $\langle\sigma_2^y\rangle$ and the results were added to give the phase diagram plots shown in the Fig. 4 of the main text.

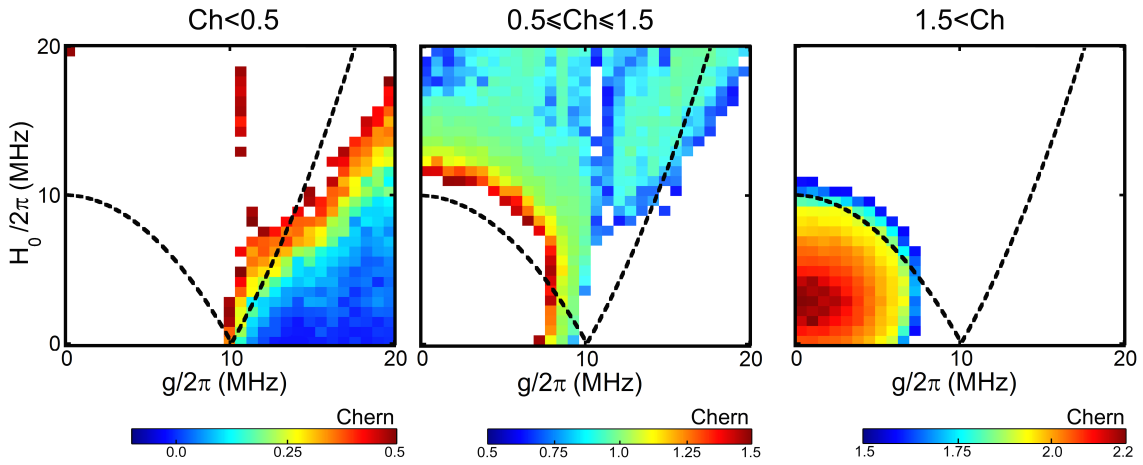

Figure C.8: **"Decomposition" of the topological phase diagram obtained with 2 qubits.** To demonstrate the fluctuation at each $\mathcal{C}\hbar$ plateau and avoid obscuring it with the color map, here we replot the topological phase diagram shown in Fig. 4(c) of the main text ($H_r/2\pi = 10\,MHz$). Each panel shows the data in a given interval of $\mathcal{C}\hbar$ values. The same order of color tones is used in each panel, but the limits of the color scale for each panel is different. The black dashed lies are the fit using the analytical solution based on finding the loci of the monopoles(degeneracies of the Hamiltonian in this case). The deviations from the expected values have several sources: the crosstalk between the two qubits is likely the primary source, as the individual qubits were calibrated accurately. While the pulse length T_f was kept an order of magnitude smaller than the decoherence time in the system, decoherence and measurement errors also contribute to the error. Understanding these error mechanism is currently under way. The sharpness of the transition from one $\mathcal{C}\hbar$ plateau to another is mainly related to the speed of the ramps. Slower ramping in parameter space (longer T_f) would result is sharper transitions. In order to successfully use slower ramps longer coherence times are required, which based on our current understanding of decoherence mechanisms gathered from this first generation of gmon devices, is achievable and will be implemented in the next generation of this experiment.

Appendix D

Supplementary Information for Chapter 5

D.1 Device: the superconducting qubits with gmon architecture

In this section, we briefly discuss the working principle of the coupled superconducting qubits used in this work. For a detailed discussion, please see references [58, 38].

Our superconducting qubits are non-linear LC resonators composed of a capacitor C, a DC SQUID with total inductance of L_q, and an inductor L_0 in series with L_q to ground. The capacitance and SQUID form the basis of the standard Xmon qubit [17] with the added inductor allowing for tunable coupling to a neighboring qubit. A circuit diagram of two coupled qubits is shown schematically in Fig. F.1**(a)**. We couple qubits with an

inductive coupler loop, which allows changing the strength of the qubit-qubit interaction g, hence the name "gmon" [58, 38].

The adjustable coupling in gmon qubits can be intuitively understood by comparing them with conventional variometers. Variometers are transformers capable of varying the mutual inductance between their primary and secondary solenoid coils by changing the angle between the axis of these two coaxial inductors. In the gmon architecture, the same functionality is achieved by the coupler loop. An excitation in either qubit generates a current in this loop which then excites the neighboring qubit. Changing the magnetic flux through the coupler loop is analogous to rotating the axis of the solenoids in a variometer, and allows tuning the coupling between the two qubit loops. This is because the magnetic flux sets the effective junction impedance of L_{CP}. If the inductance is large, then a smaller current will flow through the coupler loop and the coupling become weaker. This qubit design enables us to continuously vary the coupling strength g over nanosecond timescales without any degradation in the coherence of the qubits [58, 38]. As shown in Fig. F.1**(b)**, $g/2\pi$ can take any value between -55 MHz and $+5$ MHz, including zero.

In this work, we placed three qubits in a triangular loop and implemented an adjustable coupling between every pair of qubits (see Fig. F.1**(c)**). Synthesizing gauge fields requires periodically modulating the flux into the three coupling loops, with various frequencies on the order of tens of MHz. This requirement leads to an arbitrary pulse sequence (see Fig. 2 of the main text) that need careful calibration to allow observation

of the patterns such as those shown in Fig.2 of the main text.

The device was fabricated using standard optical and e-beam lithography techniques, discussed in [17] and is benefited from the low-loss crossovers discussed in [39]. The qubit frequencies are tunable, but mainly flux biased to around 6 GHz, with non-linearities close to 210 MHz. The energy relaxation time, T_1, is $\sim 10\mu s$, and the de-coherence time, T_2 is $\sim 2\mu s$. The experiment was performed at the base temperature of a dilution refrigerator ($\sim$20 mK).

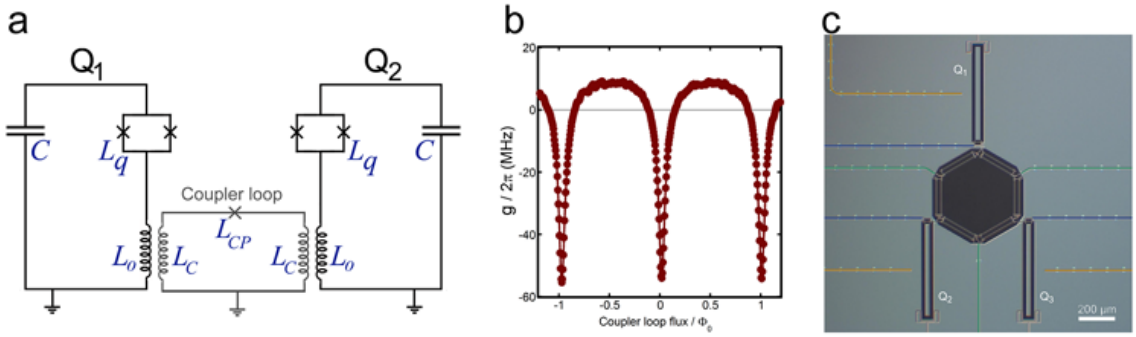

Figure D.1: **Device architecture. (a)** The circuit diagram of two superconducting qubits connected with an adjustable coupler. Each qubit is a non-linear LC resonator, and the two qubits are inductively coupled to a coupler loop through the mutual inductance between their L_0 and the loop's L_C. The coupler loop has a single Josephson junction with inductance L_{CP}, which can be tuned by applying magnetic flux into the coupler loop, allowing variable coupling strength between the two qubits g. **(b)** The measured value of g as a function of flux into the coupler loop. **(c.)** An optical micrograph of the three qubit device used in this work with coupling between each pair of them. Gray regions correspond to aluminum; black regions are where the aluminum has been etched away to expose the underlying sapphire substrate to define the qubits and wiring. Microwave drive lines which are used to excite qubits are shown in light brown. The flux bias lines, which are used to bring qubit on and off resonance, are highlighted with blue, and the lines used to adjust flux into coupling loops are highlighted with green.

D.2 Method: synthesizing gauge fields with AC modulation of inter-qubit couplings

In this section, we discuss the theory implemented for realizing complex hopping terms in our superconducting qubit system and present the logic behind the equations used in the main text. For a detailed discussions, please see references [90, 91]. Also, we provide the rationale for the current operator defined and show intuitively why this quantity provide a measure of chirality.

For quantum particles hopping on a lattice, an external gauge field $\mathbf{A}$ causes the tunneling terms between nearby sites to become complex, with the Peierls tunneling phase accumulated when tunneling between sites j and k given by $\varphi_{jk} \equiv e\int_{r_j}^{k} \mathbf{A}\cdot d\mathbf{r}$. This modifies the tunneling term $g_{jk}\left(a_j^\dagger a_k + a_k^\dagger a_j\right) \rightarrow g_{jk}\left(a_j^\dagger a_k e^{i\phi_{jk}} + a_k^\dagger a_j e^{-i\phi_{jk}}\right)$, and breaks time reversal symmetry, as the time reversal symmetry operator T is antiunitary and enacts charge conjugation. The complex phase in H between any two sites can be eliminated through a local unitary transformation $|\psi\rangle \rightarrow e^{i(\alpha n_j + \beta n_k)}|\psi\rangle$ (equivalent to shifting $\mathbf{A}$ by the gradient of a scalar function), but the sum of the phases φ_{jk} along any closed loop is a gauge invariant quantity that is invariant under any local unitary transformations. So long as this phase is nonzero modulo 2π, the effective magnetic flux Φ_B through the loop is nonzero, with real physical consequences for the system's time evolution.

To engineer these phases in a qubit array, it is sufficient to consider a pair of qubits

coupled by a real, time dependent exchange coupling $g(t)$. We let the energy of qubit 1 be equal to ω and the energy of qubit 2 be equal to $\omega + \Delta$. Our two-qubit Hamiltonian becomes

$$H = \omega n_1 + (\omega + \Delta) n_2 + g(t) \left(a_1^\dagger a_2 + a_2^\dagger a_1 \right). \tag{D.1}$$

If we assume that $|g(t)| \ll \Delta$ and initialize the system with a single photon in one of the two qubits, then the photon will remain at that qubit indefinitely, as the two qubits are far off-resonant from each other. To exchange photons between the qubits, we must oscillate $g(t)$, i.e.

$$g(t) = 2g \cos(\Delta t + \varphi), \tag{D.2}$$

$$H = \omega n_1 + (\omega + \Delta) n_2 + g \left(e^{i\Delta t + i\varphi} + e^{-i\Delta t - i\varphi} \right) \left(a_1^\dagger a_2 + a_2^\dagger a_1 \right).$$

We now move to the rotating frame via the unitary transformation $|\psi\rangle \to e^{i\Delta n_2 t} |\psi\rangle$. Incorporating this transformation into the time dependent Schrodinger equation $i\partial_t |\psi\rangle = H(t) |\psi\rangle$ we get

$$H = \omega (n_1 + n_2) + g \left(e^{i\Delta t + i\varphi} + e^{-i\Delta t - i\varphi} \right) \left(a_1^\dagger a_2 e^{-i\Delta t} + a_2^\dagger a_1 e^{i\Delta t} \right). \tag{D.3}$$

Expanding the tunnel coupling leaves a pair of terms which are time-independent and a pair terms which rapidly oscillate at $\pm 2\Delta t$, which we can ignore in the rotating wave

approximation, valid if we assume $|g| \ll \Delta$. We are thus left with a final Hamiltonian which is time independent but complex,

$$H = \omega (n_1 + n_2) + g \left(a_1^\dagger a_2 e^{-i\varphi} + a_2^\dagger a_1 e^{i\varphi} \right). \tag{D.4}$$

Thus, just as charge conservation leads to nontrivial phases for electrons moving in a real magnetic field, energy conservation leads to nontrivial phases for tunneling photons, since the photon must accumulate the phase of the drive field when it gains or loses energy to tunnel between qubits. Since this example only considers two sites, we can eliminate this phase through a unitary transformation (equivalent to choosing a different origin of time $t = 0$), but when we consider a closed loop of three or more qubits with drive fields that differ in phase by values other than 0 or π, we can no longer regain time reversal symmetry by choosing an appropriate origin for time so that $H(t) = H(-t)$, and are thus left with a nontrivial artificial magnetic flux in our rotating frame Hamiltonian.

To define a current operator, we consider the continuity equation for each site j, $\partial_t n_j = I_{in} - I_{out}$. Since $\partial_t n_j = -i [H, n_j]$, we have three equations for qubits 1,2,3:

$$\partial_t n_j = -i [H, n_j] = -i \left(a_j a_{j-1}^\dagger e^{-i\varphi_{jj-1}} - a_j^\dagger a_{j+1} e^{-i\varphi_{jj+1}} \right) \equiv (-I_{jj-1} + I_{jj+1}). \tag{D.5}$$

From these equations, we readily define the current I_{jk} between qubits j and k to be:

$$I_{jk} = i \left(a_j^\dagger a_k e^{i\varphi_{jk}} - a_j a_k^\dagger e^{-i\varphi_{jk}} \right). \tag{D.6}$$

Since our Hamiltonian is uniform and has magnetic translational symmetry, to measure the current in any eigenstate it is sufficient to measure the current through a single link.

D.3 Supplementary data

In this section, we provide additional experimental data to better explain the method we used for realizing complex hopping, and to provide a deeper insight into the physics of the excitation circulation among the three qubits. At the end we outline the next stages of this project and provide a road-map for realization of FQH states with superconducting qubits.

D.3.1 Parametric modulation of hopping.

The basic idea of parametric modulation of the hopping term can be implemented in a superconducting qubit platform, where qubits play the role of the lattice sites and modulating the strength of the inter-qubit couplings g sets the microwave photon hopping rate (Fig. S2). Hopping also depends on the on-site energies ω, and Fig. S2 demonstrates its interplay with g. In a system of two coupled qubits Q_1 and Q_2, at $t = 0$ we excite Q_1 and measure its photon occupation probability,P_{Q_1}, as a function of time t and on-site energy differences $\omega_1 - \omega_2$. For a constant g, when on-site energy differences are larger than g, the hopping is impeded (away from the center in panel **(a)**). However, if g is modulated with the frequency of the on-site energy difference of the sites that it connects, then photon hopping would be restored (panel **(b)**). In spite of the astonishing similarity of the two data sets, the hopping in **(b)** is not generally equivalent to **(a)**, and has the major advantage that its control sequence can be utilized for synthesizing

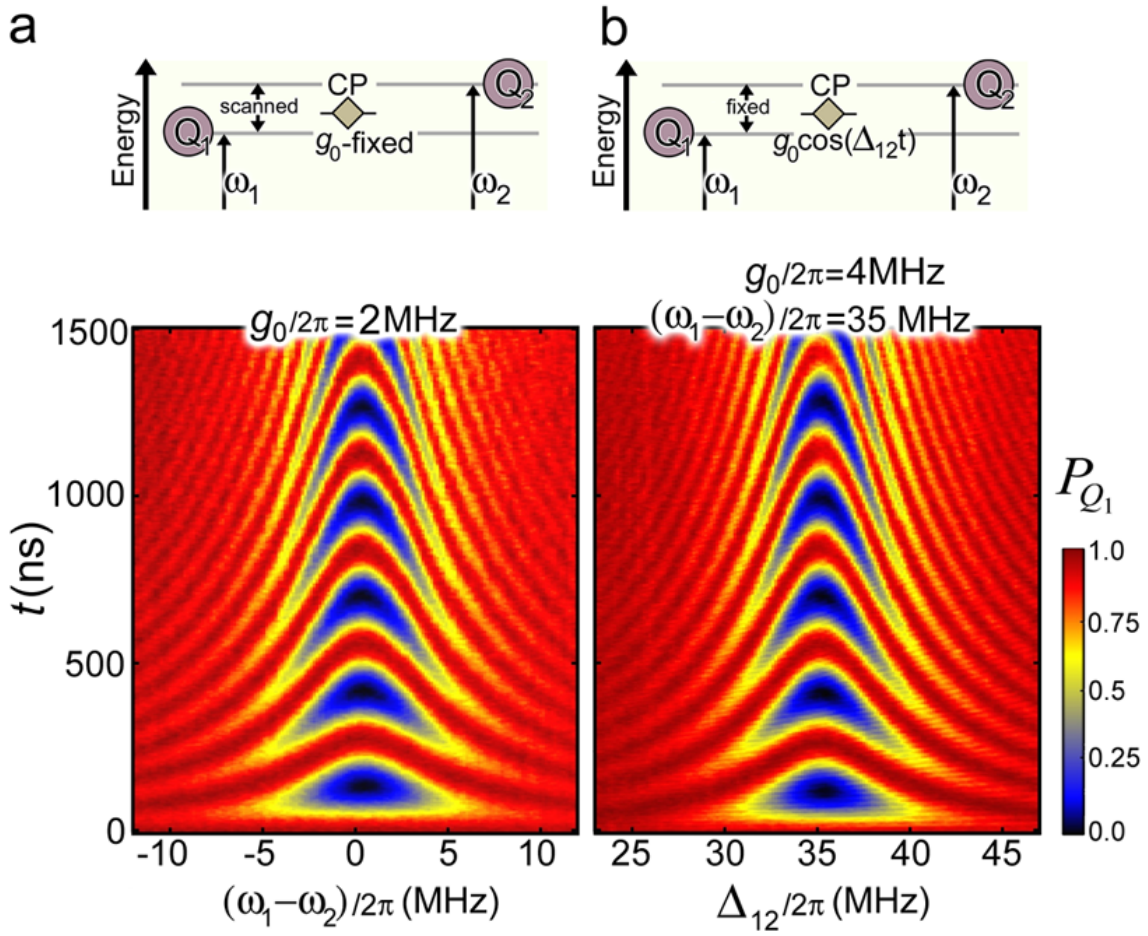

Figure D.2: **On and off resonance tunneling.** Two qubits Q_1 and Q_2 with $|0\rangle \rightarrow |1\rangle$ transitions of ω_1 and ω_2, respectively, are connected via a coupler of strength g. At $t = 0$, Q_1 is excited and its photon occupation probability, P_{Q_1}, is measured as a function of time. **(a) Fixed coupling**. The frequency difference of the two qubits $(\omega_1 - \omega_2)/2\pi$ is varied, while coupling is fixed at $g_0/2\pi = 2\,\text{MHz}$. **(b) Periodically modulating coupling**. Q_1 and Q_2 are set to a fixed detuning $(\omega_1 - \omega_2)/2\pi = 35\,\text{MHz}$ and the coupling frequency Δ_{12} is varied while its amplitude is fixed to $g_0/2\pi = 4\,\text{MHz}$. The measured chevron patterns are nominally identical.

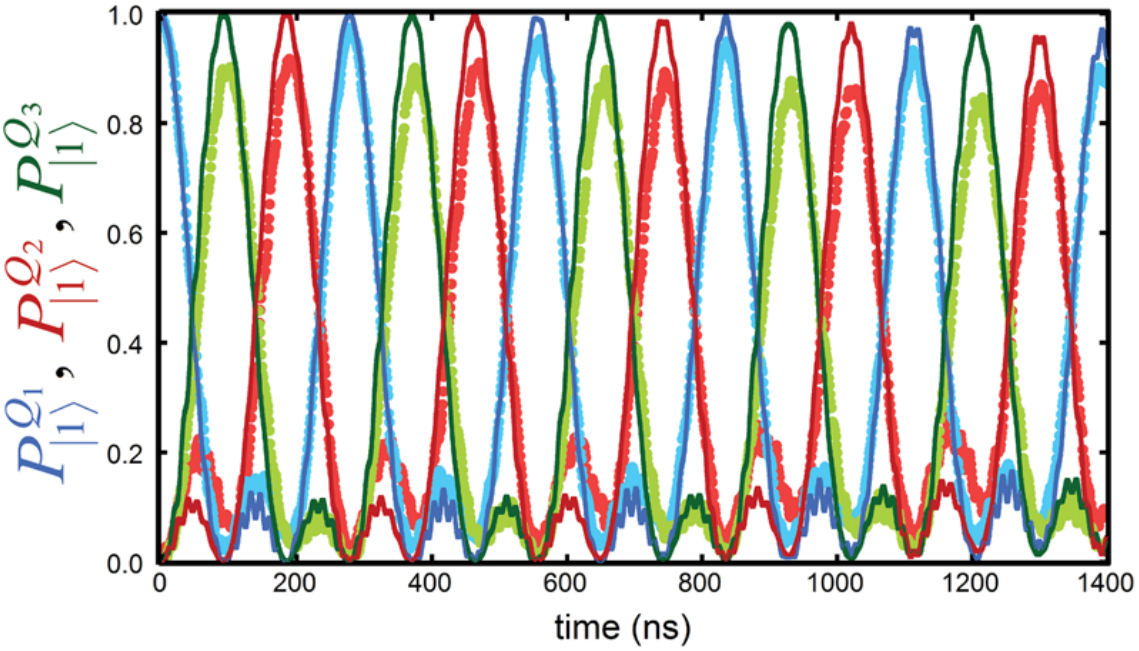

Figure D.3: **Numerical computation of the circulation patterns**. Using Eqn. (2) of the main text, the measured evolution of $|100\rangle$ is fitted with a single fitting parameter $g_0/2\pi = 4.1$MHz. The experimentally measured data points are shown in brighter colors and the fittings are presented with solid, thin darker lines. The fitting does not consider any decaying or decoherence mechanism. For the experiment, we use $\omega_1 = 5.8\,\text{GHz}$, $\omega_2 = 5.8\,\text{GHz}$, $\omega_3 = 5.835\,\text{GHz}$, $\Delta_{12} = 0$, $\Delta_{23} = 35\,\text{MHz}$, $\Delta_{31} = 35\,\text{MHz}$, $\varphi_{12} = 0$, $\varphi_{23} = 0$, and φ_{31} was used to set Φ_B.

magnetic fields. The key idea is that in **(b)** the photon's wavefunction can pick up the phase of the modulation during hopping. This phase is analogous to the Peierls phase $e \oint_{r_i}^{r_j} \mathbf{A}\cdot d\mathbf{r}$ accumulated by a particle of charge e tunneling in an external magnetic vector potential $\mathbf{A}$.

D.3.2 Decoherence effects.

Given the small size of our system, one can numerically generate the measured circulation patterns and fit the data. We adopted the time dependent Hamiltonian given in Eq.

(1) of the main text and used only one fitting parameter, which is $g_0/2\pi = 4.1$MHz. Our fit shows a remarkably good agreement with data. The fast ripples, seen close to zero excitation in the data, are also observed in the fits, indicating that they originate from unitary, counter-rotating corrections to the rotating frame Hamiltonian and not incoherent processes or experimental errors. Remarkably, the effect of the two dominant error channels (T_1 photon losses and T_2 dephasing) is negligible over the window of time plotted. For photon losses, this is simply because the average lifetime $T_1 \sim 10\mu s$ is much larger than the duration of the experiment, so photon losses are rare. The absence of phase noise in the plot, however, is a more subtle point, and stems from the basic fact that a single number T_2 does not capture all of the physics of dephasing processes. Unlike photon losses (which have a noise power spectrum that is approximately flat in our regime of operation), phase noise is generated by random $1/f$ and telegraph fluctuators, which have a power spectrum that is peaked at $\omega = 0$ and decays to zero as ω becomes large. This low-frequency peak has dramatic consequences for free Ramsey decay (where there is no Hamiltonian that anticommutes with the fluctuating $\delta(t)\sigma^z$ term responsible for phase noise), but in our case the presence of a nontrivial, continuously applied Hamiltonian $H(t)$ means that to change the quantum state, the phase noise must induce transitions between states of different energy under $H(t)$, at a finite energy cost [126]. This finite energy cost eliminates the low frequency divergence in the noise power spectrum $S(\omega)$ and dramatically suppresses phase noise, leading to our circulation pattern best fit by assuming a white noise $T_2 \simeq 2T_1$, the standard limit from photon losses. We note that

this replicates the result of Averin *et al.* [14], who demonstrated phase noise suppression by applying sequential SWAP operations in a ring of qubits; our continuous Hamiltonian can be thought of as a passive, analog equivalent to their gate-based method when viewed through the lens of quantum error suppression.

D.3.3 Chirality.

The energy spectra provide a holistic picture that allows exploring quantum correlations in various eigenstates of the system. In particular, measuring the chirality of can provide insight into how states on different energy manifolds respond to gauge fields. The chirality operators is defined as

$$\hat{\chi} = \overrightarrow{\sigma}_{Q_1}.(\overrightarrow{\sigma}_{Q_2} \times \overrightarrow{\sigma}_{Q_3}), \tag{D.7}$$

where $\overrightarrow{\sigma} = (\sigma^X, \sigma^Y, \sigma^Z)$. Chirality is computed using the measured density matrices $(tr(\hat{\rho}\hat{\chi}))$, and is presented in Fig. S5**(b)**. On the ground and first-excited manifolds, any non-zero value of Φ_B breaks TRS and leads to chiral states, with the chirality. Close to $\Phi_B = 0$, The highest excited manifold, shows a weaker dependance on Φ_B.

D.3.4 A single photon circulator.

From the quantum technology perspective, the setup presented here is a single photon circulator device and is interesting by itself. However, the excitation circulation in this device is distinct from circulations seen in classical non-reciprocal three port devices [52, 53, 51, 95]. To gain deeper insight into the underlying circulation mechanism,

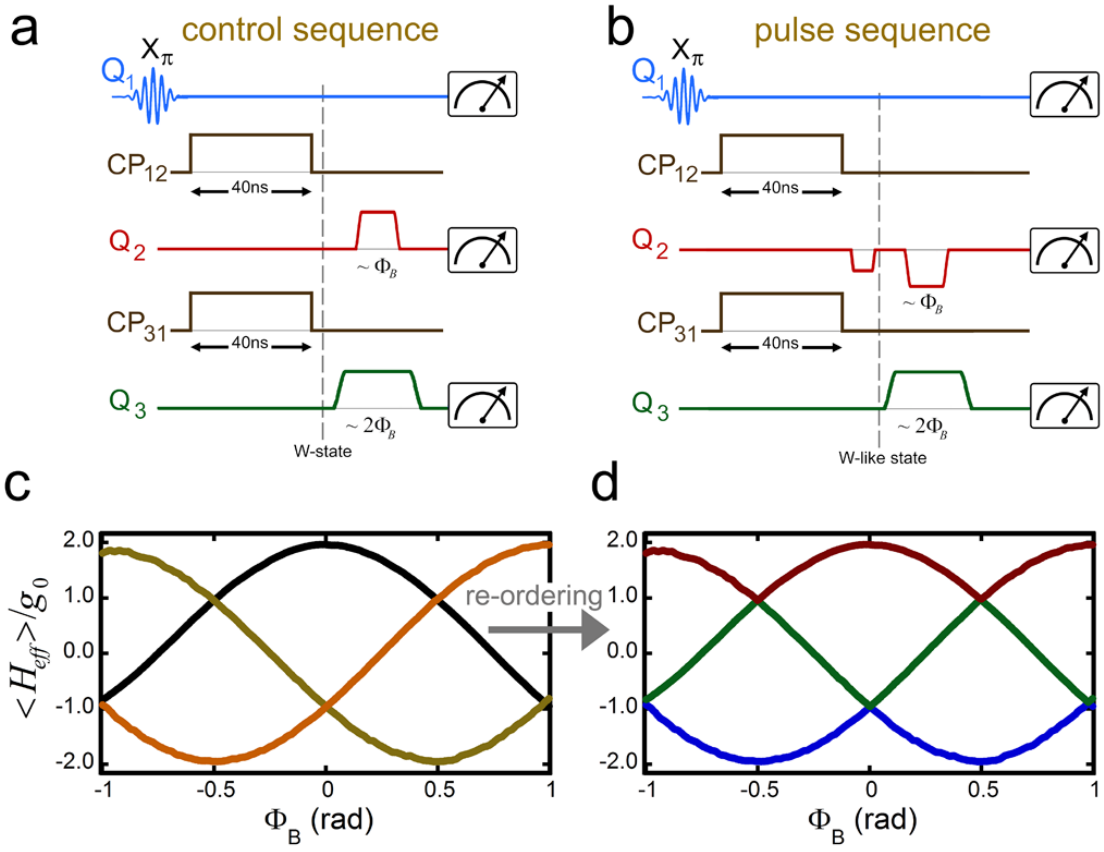

Figure D.4: **Generating the full spectrum of eigen-energies**. The pulse sequence used for generating all energy eigenstates of the system. **(a)** By exciting one qubit and setting its coupling to other qubits to the fixed value of $g_0/2\pi = 4\,\mathrm{MHz}$ for 40ns, a W-state of the three qubits is generated. After that, individual qubits are rotated to produce the desired phases for creating the eigen-states of the problem according to the lemma. **(b)** W-like states are created, by a protocol similar to **(a)**. Next, proper phases were given to each qubit to create all the states on the energy manifold. A similar protocol (not shown) to **(a)** and **(b)** was used to create eigen-states on the third manifold. **(c)** After creating the eigen-energies of the system, the full density matrix of the system was measured, and the expectation values of energy for all eigen-energies extracted. **(d)** The three protocols are insensitive to degeneracies and only provide the eigen-states that are connected to each other through infinitesimal change of Φ_B. From panel **(c)** the degeneracies of the Hamiltonian become visible; here, we rearrange the measured values shown in **(c)** and re-plot them.

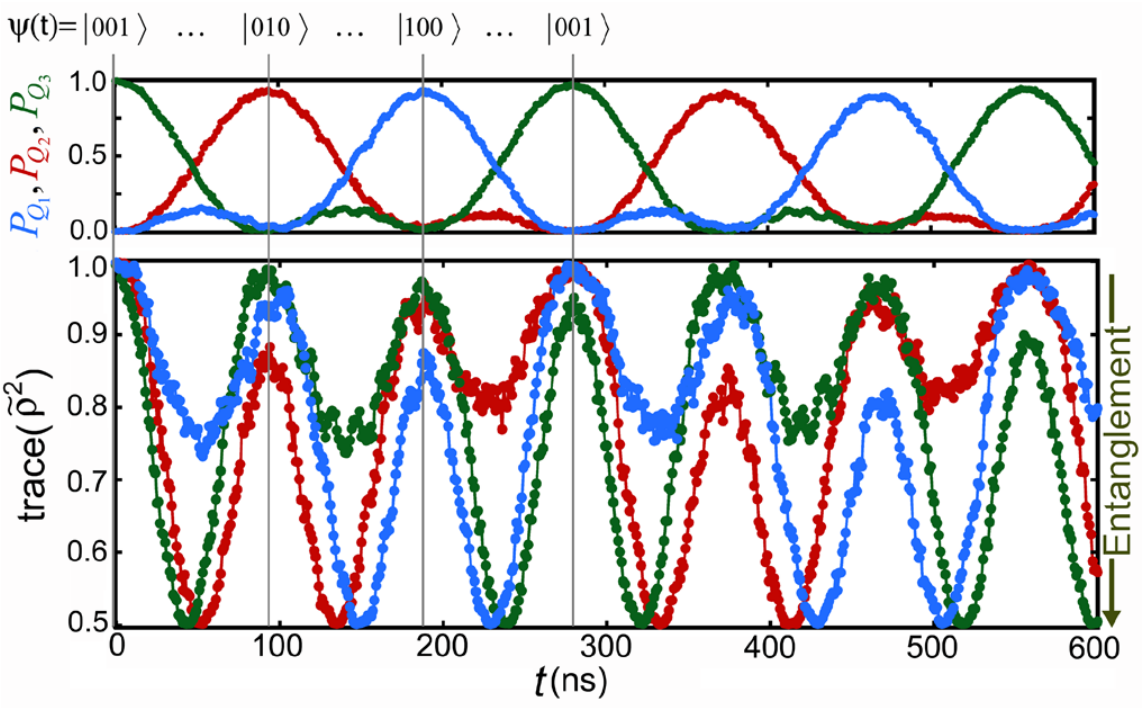

Figure D.5: **Entanglement Dynamics during circulation**. The top panel shows the photon occupation probability of each qubit P_{Q_j} as a function of time. Data is similar to Fig. 2**(c)** of the main text and presented here for the ease of comparison with the entanglement measurements. At time $t = 0$, the system is prepared in the $|001\rangle$ state, which has zero entanglement between the qubits. At later times $\langle\sigma^X\rangle$, $\langle\sigma^Y\rangle$, and $\langle\sigma^Z\rangle$ of each qubit are measured. From the expectation values of these Pauli operators, the reduced density matrix of each qubit $\tilde{\rho}$ was constructed and the entanglement of each qubit with the others computed and presented in the lower panel.

we investigate the role of quantum correlations during the photon circulation. The inherent quantum nature of the circulation observed here manifests itself in the generation of entanglement among the qubits during the evolution. In Fig. S6, we measure the reduced density matrix $\tilde{\rho}$ of each qubit for the single-photon circulation protocol. When a qubit is not entangled with other qubits, its $tr(\tilde{\rho}^2)$ is maximized to one, and when it is fully entangled with other qubits, its $tr(\tilde{\rho}^2)$ is minimized to 0.5. Comparing the top and lower panels provides insight into how the excited state circulates among the qubits. If an excitation moves from Q_j to Q_k, then these two qubits become entangled. This can be seen from comparing minima in the lower panel with maxima in the top panel and their successional appearances. When the excitation reaches the second qubit, all qubits become disentangled (gray vertical lines). During the passage of excitation between two qubits, the third qubit also becomes partially entangled with them. Therefore, as the excitation circulates, entanglement among the three qubits is periodically generated and annihilated. A time-resolved measurement of the the full density matrix of the system during the circulation is also presented.

Appendix E

Supplementary Information for Chapter 6

E.1 Device: the superconducting qubits with gmon architecture

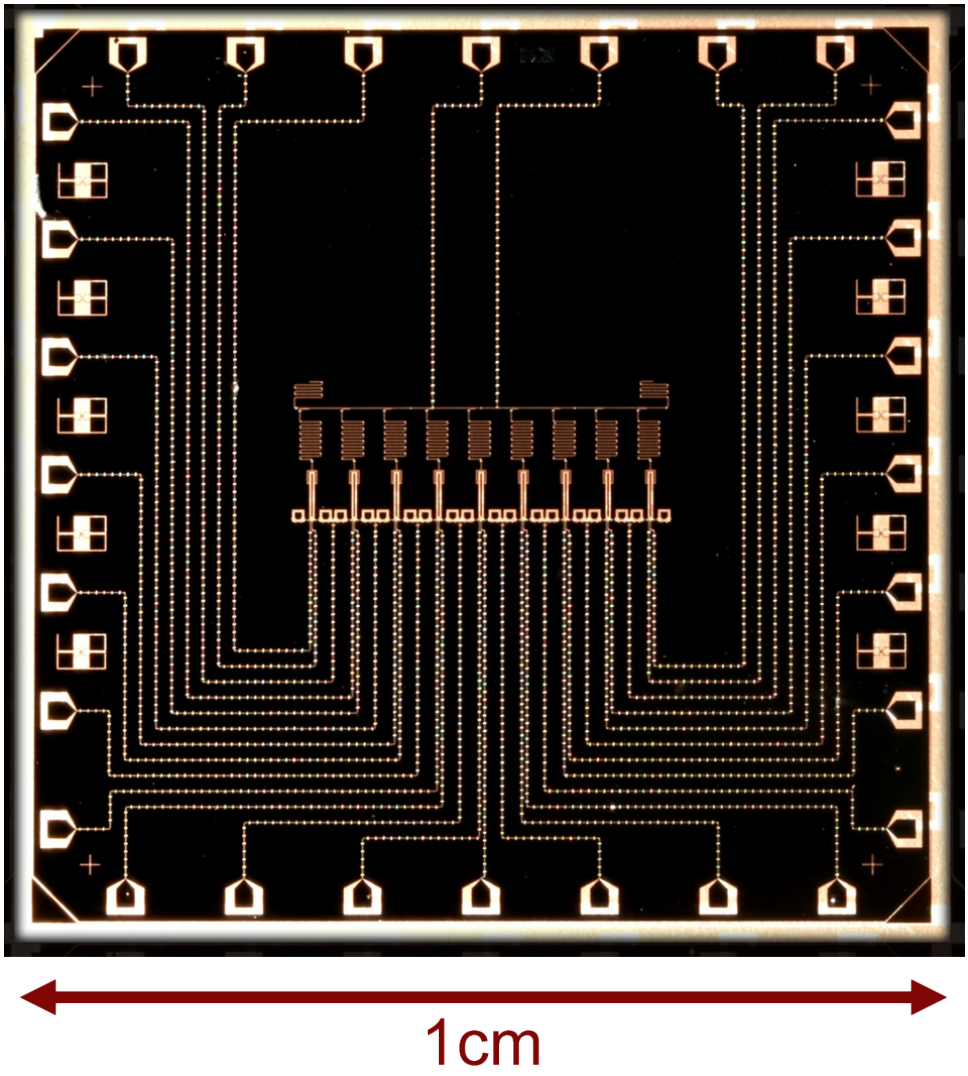

Figure E.1: An optical micrograph of the device used in this work. The chip consist of 9 qubits in a 1D chain with adjustable coupling between every pair of qubits. The qubits appear as small vertical rectangles in the middle of the chip. The couplers are the two square loops that are between the qubits. The wiring lines that are routed to the perimeter of the chip are used to control the qubits and the interaction between them. The meandering lines above the qubits are the readout resonators.

E.2 Spectroscopy based on fundamental postulate of quantum mechanics

According to the time-independent Schrödinger equation, the time evolution of the state of the system $|\psi(t)\rangle$ is given

$$|\psi(t)\rangle = \sum_{\alpha} C_{\alpha} e^{-iE_{\alpha}t} |\phi_{\alpha}\rangle, \tag{E.1}$$

where $C_{\alpha} = \langle\phi_{\alpha}|\psi_0\rangle$, and $|\psi_0\rangle$ is the initial state. On the other hand, an observable in the energy basis can be written as

$$\hat{O} = \sum_{\alpha,\alpha'} O_{\alpha',\alpha} |\phi_{\alpha'}\rangle\langle\phi_{\alpha}|, \tag{E.2}$$

where $O_{\alpha',\alpha} = \langle\phi_{\alpha'}|\hat{O}|\phi_{\alpha}\rangle$ and accordingly its expectation value is:

$$O(t) = \langle\psi(t)|\hat{O}|\psi(t)\rangle = \sum_{\alpha,\alpha'} O_{\alpha',\alpha} C_{\alpha} C^{*}_{\alpha'} e^{-i(E_{\alpha}-E_{\alpha'})t}. \tag{E.3}$$

For our spectroscopy purpose, we are interested in energies E_{α} and not energy differences $E_{\alpha} - E_{\alpha'}$. The above relation suggests that when measuring any observable one will generally end up with energy differences. It is not obvious *a priori* how to avoid energy differences. However, proper choices of observables and initial states can help to overcome this issue, enabling extraction of eigen-energies. A key observation here is that one should somehow fix $E_{\alpha'}$ to a specific energy, i.e., *a reference energy*. See the schematic in Fig. S2.

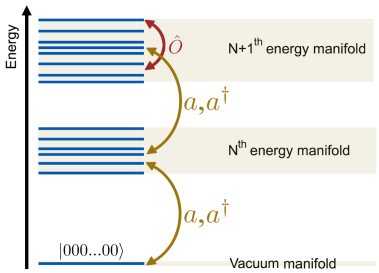

Initial states \ operators	$\langle a_1^\dagger a_1 \rangle$	$\langle a_1 \rangle$
$\lvert\psi_0\rangle = \lvert 10\rangle$	$\frac{1}{2}\left[1+\cos((E_+ - E_-)t)\right]$ ✗	0 ✗
$\lvert\psi_0\rangle = \frac{\lvert 00\rangle + \lvert 10\rangle}{\sqrt{2}}$	$\frac{1}{4}\left[3+\cos((E_+ - E_-)t)\right]$ ✗	$\frac{1}{4}\left(e^{-iE_+t} + e^{-iE_-t}\right)$ ✓

Figure E.2: **(a)** The schematic shows that generally operators, such as $\hat{O}$ connect different levels, and hence in their observables one would see the energy differences of the levels. The raising $a^\dagger$ and lowering a operators connect states in different manifolds. It is a fortunate coincidence that there is a manifold with only one state in it, the vacuum manifold, which can act as a energy reference. The initial states that are superposition of vacuum state and some other state are necessary for having a functional protocal. **(b)** We show expectation values of different operators for two different initial states, associated with the example that we used. Note that both proper initial states and choice of operators are needed to have a useful protocol.

E.2.1 Energy differences vs. absolute energies

We illustrate the method by considering first a simple example of two coupled harmonic oscillators described by the tight-binding Hamiltonian

$$H_{\text{dimer}} = \omega(a_1^\dagger a_1 + a_2^\dagger a_2) - J(a_1^\dagger a_2 + H.c.), \tag{E.4}$$

where ω is the frequency of the oscillators, J is the hopping rate, a_1 and a_2 are bosonic annihilation operators acting on the first and the second oscillators, respectively. The single-photon eigenstates are $|\phi_\pm\rangle = (|10\rangle \pm |01\rangle)/\sqrt{2}$ with the eigen-energies $E_\pm = \omega \pm J$, where $|10\rangle = a_1^\dagger|00\rangle$, $|01\rangle = a_2^\dagger|00\rangle$ and $|00\rangle$ is the vacuum. Different choices of initial states and observables are shown in Fig. E.2 (right panel). One quickly realizes that $a^\dagger a$ would have energy differences and not suitable; but a might, if the proper initial state is chosen. A proper initial state would be the superposition of the relevant number state

(here the $|10\rangle$ state) that has one particle and the vacuum $|00\rangle$. The vacuum here serves as the appropriate reference state and has energy $E_{\alpha'} = 0$. Since a is non-Hermitian an hence not an observable, a cannot be measured directly. However, it can be easily inferred from its Hermitian "quadratures" σ^X and σ^Y as $\langle a\rangle = \langle\sigma^X\rangle + i\langle\sigma^Y\rangle$, where $\sigma^X = |1\rangle\langle 0| + |0\rangle\langle 1|$ and $\sigma^Y = i|1\rangle\langle 0| - i|0\rangle\langle 1|$ are Hermitian and hence observable.

E.2.2 Single-particle spectroscopy: generalization

Now let us consider a general particle-conserving interacting Hamiltonian H in a lattice and assume first that there is only one particle in the system. As before, we choose an initial state as a product state of the form

$$|\psi_0\rangle_n = |0\rangle_1|0\rangle_2...\left(\frac{|0\rangle_n + |1\rangle_n}{\sqrt{2}}\right)...|0\rangle_{N-1}|0\rangle_N = \frac{1}{\sqrt{2}}\left(|\text{Vac}\rangle + |\mathbf{1}_n\rangle\right), \tag{E.5}$$

where N is the number of sites, $n \in \{1, 2, .., N\}$, $|\text{Vac}\rangle \equiv |0\rangle_1|0\rangle_2...|0\rangle_N$ is the vacuum state and $|1_n\rangle = |0\rangle_1|0\rangle_2...|1\rangle_n...|0\rangle_N$ is a one-photon Fock state. The state at time t is

$$|\psi(t)\rangle_n = \frac{1}{\sqrt{2}}\left(|\text{Vac}\rangle + \sum_\alpha C_{\alpha,n}e^{-iE_\alpha^{(1)}t}|\phi_\alpha^{(1)}\rangle\right), \tag{E.6}$$

where $\alpha \in \{1, 2, .., N\}$, $C_{\alpha,n} = \langle\phi_\alpha^{(1)}|\mathbf{1}_n\rangle$ and $|\phi_\alpha^{(1)}\rangle$ is the one-photon eigenstate with the eigen-energy $E_\alpha^{(1)}$. The expectation value of $\chi_1(n) \equiv \langle\sigma_n^X\rangle + i\langle\sigma_n^Y\rangle$ takes the form

$$\chi_1(n) = \frac{1}{2}\sum_\alpha |C_{\alpha,n}|^2 e^{-iE_\alpha^{(1)}t}. \tag{E.7}$$

Non-vanishing peak amplitudes $|C_{\alpha,n}|^2 > 0$ can be assured by varying the initial state, i.e. varying n, to span the space of the single-photon manifold.

E.2.3 Two-particle spectroscopy: generalization

The initial states are product states of the form

$$|\psi_0\rangle_{n,m} = |0\rangle_1|0\rangle_2...\left(\frac{|0\rangle_n + |1\rangle_n}{\sqrt{2}}\right)...\left(\frac{|0\rangle_m + |1\rangle_m}{\sqrt{2}}\right)...|0\rangle_{N-1}|0\rangle_N = \frac{1}{2}\left(|\text{Vac}\rangle + |\mathbf{1}_n, \mathbf{1}_m\rangle\right) + \frac{1}{2}\left(|\mathbf{1}_n\rangle + |\mathbf{1}_n\right. \tag{E.8}$$

where $n \neq m$, and $m, n \in \{1, 2, .., N\}$ and $|\mathbf{1}_n, \mathbf{1}_m\rangle = |0\rangle_1|0\rangle_2...|1\rangle_n...|1\rangle_m...|0\rangle_N$ are the two-photon Fock states. The state at time t is

$$|\psi(t)\rangle_{n,m} = \frac{1}{2}\left(|\text{Vac}\rangle + \sum_\beta C_{\beta,(n,m)} e^{-iE_\beta^{(2)}t}|\phi_\beta^{(2)}\rangle\right) + \frac{1}{2}\left(\sum_\alpha (C_{\alpha,n} + C_{\alpha,m}) e^{-iE_\alpha^{(1)}t}|\phi_\alpha^{(1)}\rangle\right), \tag{E.9}$$

where $\beta \in \{1, 2, .., \frac{1}{2}N(N+1)\}$, $|\phi_\beta^{(2)}\rangle$ is an energy eigenstate in the two-photon manifold with the corresponding energy $E_\beta^{(2)}$ and $C_{\beta,(n,m)} = \langle\phi_\beta^{(2)}|\mathbf{1}_n, \mathbf{1}_m\rangle$. A generalized two-photon lowering operator can be constructed as

$$\chi_2(n,m) \equiv \langle\sigma_n^X \sigma_m^X\rangle - \langle\sigma_n^Y \sigma_m^Y\rangle + i\langle\sigma_n^X \sigma_m^Y\rangle + i\langle\sigma_n^Y \sigma_m^X\rangle. \tag{E.10}$$

This operator measures the phase difference between the vacuum and the two-photon state, while projecting out the one-photon component to avoid measuring the energy

differences $E_\beta^{(2)} - E_\alpha^{(1)}$. Its expectation value takes the form

$$\chi_2(n,m) = \frac{1}{4}\sum_\beta |C_{\beta,(n,m)}|^2 e^{-iE_\beta^{(2)}t}. \tag{E.11}$$

One might observe that with our choice of initial states, we do not directly cover all the space in the two-photon subspace since we did not include double-occupancy states such as $|\mathbf{2}_n\rangle \equiv |0\rangle_1|0\rangle_2...|2\rangle_n...|0\rangle_N$. However, in the soft-core limit $U/J = 3.5$ where we operate, all 45 two-photon eigenstates $|\phi_\beta^{(2)}\rangle$ have appreciable overlap with our choice of initial states. Therefore, their energies can be measured as shown in the main text. As one get to the hardcore limit with $U/J \to \infty$, mainly 36 out of 45 eigen-energies will be picked up by $\chi_2(n,m)$, which again are all the physically relevant ones to probe the physics of the system in this regime.

E.2.4 Computation of the Participation Ratio

Here, we discuss in details how the participation ratios in the two-photon manifold are measured and computed. In the Bose-Hubbard Hamiltonian

$$H_{BH} = \sum_{n=1}^{9}\mu_n a_n^\dagger a_n + \frac{U}{2}\sum_{n=1}^{9} a_n^\dagger a_n(a_n^\dagger a_n - 1) + J\sum_{n=1}^{8} a_{n+1}^\dagger a_n + a_n^\dagger a_{n+1}, \tag{E.12}$$

we set $J/2\pi = 50\,\mathrm{MHz}$. By design of the chip, U is fixed $U/2\pi = 175\,\mathrm{MHz}$. We realize a quasi-periodic potential by setting $\mu_n = \Delta\cos(2\pi n b)$, where $b = (\sqrt{5}-1)/2$. We vary Δ from 0 to $\Delta/2\pi = 300\,\mathrm{MHz}$. Choosing the inverse of the so-called golden

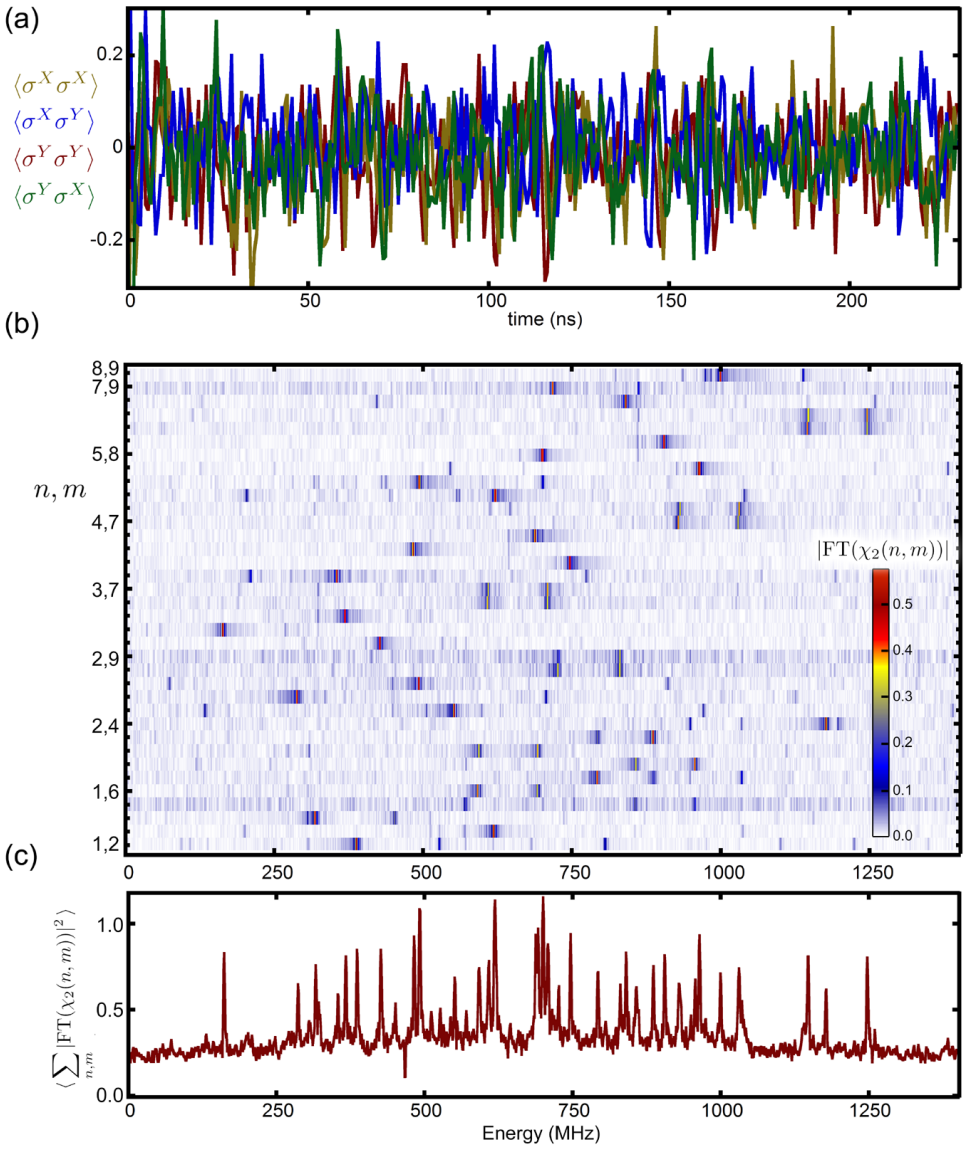

Figure E.3: **Spectroscopy of energy levels in the two-photon manifold** The protocol for taking data in the two-photon manifold is very similar to the method illustrated in Fig. (1) of the main text. **(a)** A typical time-domain measurement of the two-point correlations that are needed for constructing $\chi_2(n,m)$. For this data set $n = 5$ and $m = 7$. Similar measurements are done for every $m, n \in \{1, 2, .., N\}$ with $n \neq m$. **(b)** The magnitude of the Fourier transform of $\chi_2(n,m)$ for all m and n choices with $m, n \in \{1, 2, .., N\}$ and $n \neq m$. **(c)** Average of Fourier transforms presented in **(b)**.

ratio for b stems from the fact that this irrational number is considered to be "very" irrational number, meaning that approximating it in terms of ratio of integers involves large numbers. Nevertheless, in setting the parameters in the lab, there is no meaningful distinction between rational and irrational numbers. We chose this number just to reduce the chance of commensurability with the lattice, which could have been the case if we chose a number close to 0.5 or 0.33.

Initial states are made by placing two qubits (Qn and Qm) in the superposition of the $|0\rangle$ and $|1\rangle$ state. We measure two-point correlations and construct $\chi_2(n,m) \equiv \langle\sigma_n^X\sigma_m^X\rangle - \langle\sigma_n^Y\sigma_m^Y\rangle + i\langle\sigma_n^X\sigma_m^Y\rangle + i\langle\sigma_n^Y\sigma_m^X\rangle$. We consider all pairs of qubits for the initial states $n, m \in \{1, 2, ..., 9\}$. In the two-photon energy manifold, there are 36 single (e.g. $|\mathbf{1}_3, \mathbf{1}_7\rangle = |001000100\rangle$) and 9 double occupancy states (e.g. $|\mathbf{2}_5\rangle = |000020000\rangle$), which gives $\binom{9}{2} + \binom{9}{1} = 45$ energy levels. In the two-photon energy manifold of Egn. (2), we create all 36 single-occupation initial states:

$$|\psi_0\rangle_{n,m} \equiv |0\rangle_1|0\rangle_2...\left(\frac{|0\rangle_n + |1\rangle_n}{\sqrt{2}}\right)...\left(\frac{|0\rangle_m + |1\rangle_m}{\sqrt{2}}\right)...|0\rangle_{N-1}|0\rangle_N \tag{E.13}$$

In the average of the magnitude of FT of data (summed over all these 36 initial states), we identify 45 peaks. This constitute $\{E_\alpha\}$, a set of 45 eigen-energies of the Hamiltonian. Note that the number of initial states that one can begin with is technically infinitely many. Using more initial states only adds to the confidence for the detected peaks. Since all the eigen-energies of the Hamiltonian has been identified, by choosing one of the initial states, (e.g. $|001000100\rangle$), we can see how extended it is in the energy landscape. This

is done by considering the FT of the data and reading the magnitude of FT for all E_α values. Therefore in the expansion

$$|\psi_0\rangle_{n,m} = \sum_\alpha C_{\alpha,(n,m)} |\phi_\alpha\rangle \tag{E.14}$$

we now know $\{P_{\alpha,(n,m)}\} = \{|C_{\alpha,(n,m)}|^2\}$. Next, we want to extract the expansion of Fock states $|1_n\rangle$ from the expansions of our initial states that involved two photons. This is simply done by adding probabilities of the initial states which share one of the excited qubits $P_{\alpha,n} = \sum_m P_{\alpha,(n,m)}$. Now we can compute

$$PR_{\text{Energy}}(n) \equiv \frac{1}{\sum\limits_\alpha P_{\alpha,n}^2}, \tag{E.15}$$

which is a measure of the spread of a real-space localized state in energy landscape. Note that since $\sum\limits_\alpha P_{\alpha,n} = 1$, the PR_{Energy} is the simplest non-trivial moment of the probability distribution, which tells us about the spread of wavefunctions. The expansion of energy eigenstate in real space $|\phi_\alpha\rangle = \sum_n C_{\alpha,n} |\mathbf{1}_n\rangle$ is readily done by summing over n

$$PR_{\text{space}}(\alpha) \equiv \frac{1}{\sum\limits_n P_{\alpha,n}^2}. \tag{E.16}$$

E.2.5 Resolving the spectrum for large Hilbert-spaces

In this section, we address the main technical challenge that arises when dealing with a large many-body system. What sets the limit on how small and large energy differences we can resolve?

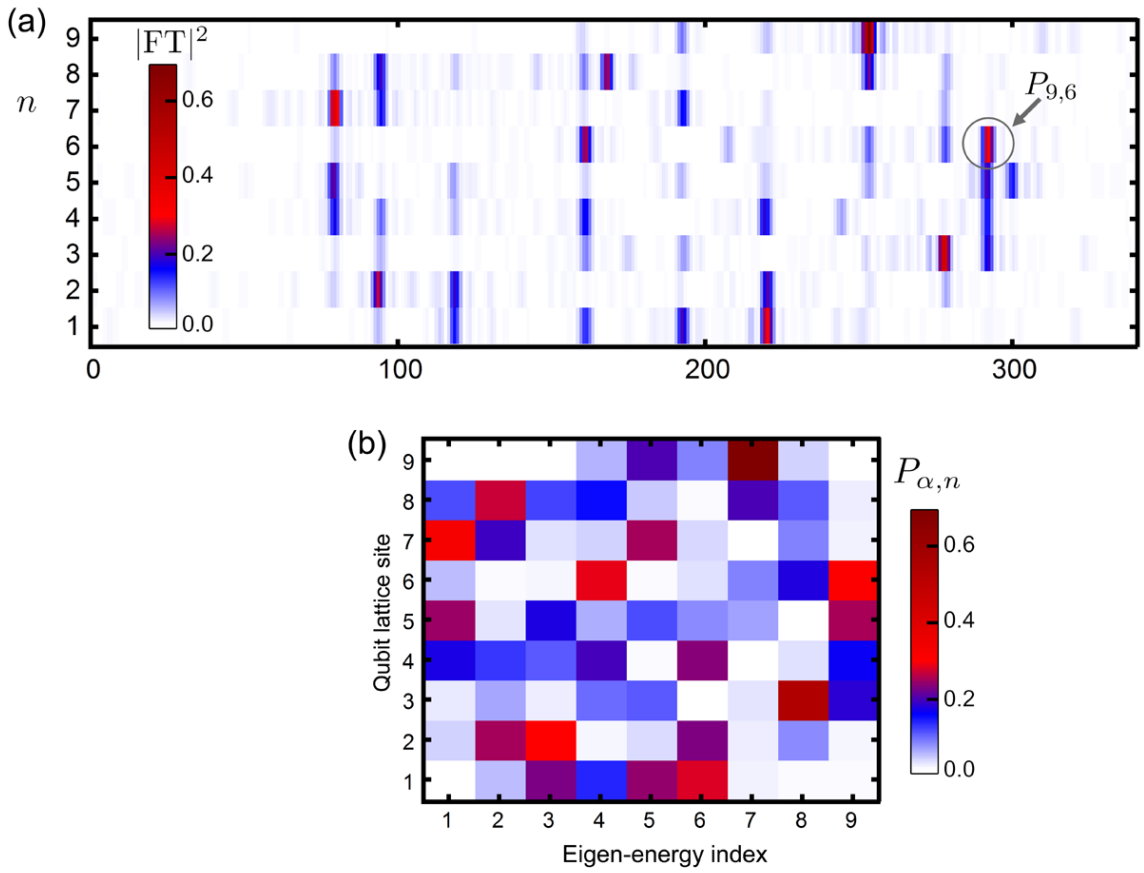

Figure E.4: **Computation of the Participation Ratio in the single-photon manifold. (a)** This is the same plot as Fig.1 (c) of the main text and for the ease of comparison is represented in here. **(b)** After identification of the peaks, we ask what is the magnitude of FT (false color) at each site (vertical axis) for a given eigen-energy (horizontal axis). We normalize the amplitudes such that $\sum_n P_{\alpha,n} = 1$ and $\sum_\alpha P_{\alpha,n} = 1$.

In the current work the main limitation comes from the data collecting rate. Each panel in the two-photon manifold (Fig 3,4, and 5), where we change Δ in about 20 steps, took about 2 days to be collected. Recall that we generated all single-occupancy two-photon states for every realization of the Hamiltonian. This is not a fundamental limit and one can take data for longer time, but we impose this limit ourselves. Instead of taking data with this rate for a longer time, we are addressing the core of this issue and working on improving our data taking rate. There are indications that with fast resetting techniques and better data streaming, we can improve the data taking rate by two orders of magnitude. These ideas will be tested and implemented in the future generations of our devices. These methods would help to push the limitations for implementation of our spectroscopy method to be limited only by the coherent time of the system.

When the system size N is increased, missing some energy peaks in the measurement will eventually become unavoidable because the resolution in the energy Fourier spectrum is fixed by the coherence time of the system. Here, we analyze what happen to level statistics when some levels are missing. To study the deviation from the ideal level spacing distributions, we use the Kullback-Leibler divergence and estimate the efficiency of our method

$$D_{KL}(P\|Q) = \sum_l P(r_l) \log\left(\frac{P(r_l)}{Q(r_l)}\right). \tag{E.17}$$

The KL divergence is close to zero when the two distributions P and Q are close. In Fig. S5(a) we show the number of missing levels for different parameter regimes and a

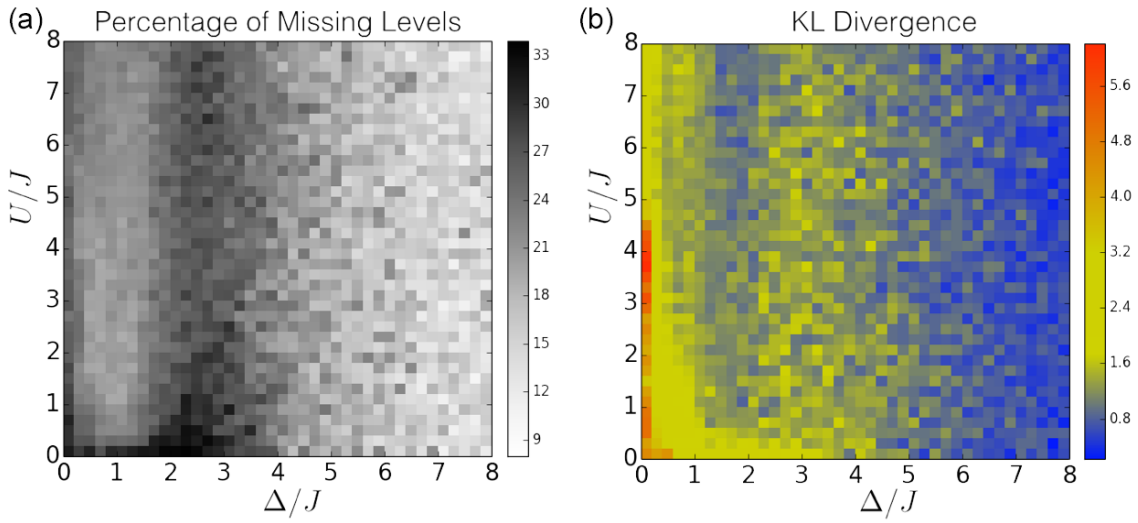

Figure E.5: **The effect of missing levels in level statistics** We numerically simulate a system of two interacting particles in a lattice with $N = 18$ sites and $J/2\pi = 50MHz$. **(a)** For a fixed resolution of $1MHz$, we calculate the percentage of missing levels for different parameter regimes. **(b)** To determine the effect of missing levels on the statistics we use the Kullback-Leibler (KL) divergence between the measured distribution (which had missing levels) to the distribution without missing levels.

fixed resolution of $1MHz$. Even for a finite size $N = 18$, it is interesting that one misses more levels close to the critical point of the AA model $\Delta \approx 2J$. This is expected because close to the critical point, some levels cluster and the statistics is neither Poisson nor GOE. Therefore, for a finite resolution of the Fourier spectrum, there would be more missing levels. Fig. S5(b) shows a second step to test the efficiency of our method. We calculate numerically the KL divergence for a fixed resolution which leads to different number of missing levels for different parameters.

E.3 Two-point quantum correlations

Here we discuss the details of the two-point correlation measurements (Fig. (5) of the main text) and also provide the numerical simulations. In the Bose-Hubbard Hamiltonian

$$H_{BH} = \sum_{n=1}^{9} \mu_n a_n^\dagger a_n + \frac{U}{2} \sum_{n=1}^{9} a_n^\dagger a_n (a_n^\dagger a_n - 1) + J \sum_{n=1}^{8} a_{n+1}^\dagger a_n + a_n^\dagger a_{n+1}, \tag{E.18}$$

we set $J/2\pi = 50\,\mathrm{MHz}$. By design of the chip, U is fixed $U/2\pi = 175\,\mathrm{MHz}$. We realize a quasi-periodic potential by setting $\mu_n = \Delta \cos(2\pi n b)$, where $b = (\sqrt{5}-1)/2$, and vary Δ.

In the data presented in Fig. (5) of the main text, The initial states are made by placing two qubits (Qn and Qm) in the superposition of the $|0\rangle$ and $|1\rangle$ states. We measure $\mathcal{S}_{m,n} = |\langle \sigma_m^1 \sigma_n^2 \rangle - \langle \sigma_m^1 \rangle \langle \sigma_n^2 \rangle|$, where $\sigma^1, \sigma^2 \in \{\sigma^X, \sigma^Y\}$ and $m, n \in \{1, 2, ..., 9\}$, for all m and n combinations and choices of Pauli operators. The number of pairs of qubits that one can pick for exciting initially and measuring the two-point correlation is $\binom{9}{2} = 36$. The total number of choices for Pauli operators is 4 (XX, YY, XY, YX), which means that $36 \times 4 = 144$ distinct $\mathcal{S}_{m,n}$ are measured. Next, we average $\mathcal{S}_{m,n}$ over time, from 0 to 250 ns, and over the 4 choices of the Pauli operators, and over all qubit pair combinations with the same $|m-n|$. This gives $\tilde{\mathcal{S}}_{m,n}$ for a given realization of Hamiltonian (a given Δ/J) as a function of $|m-n|$.

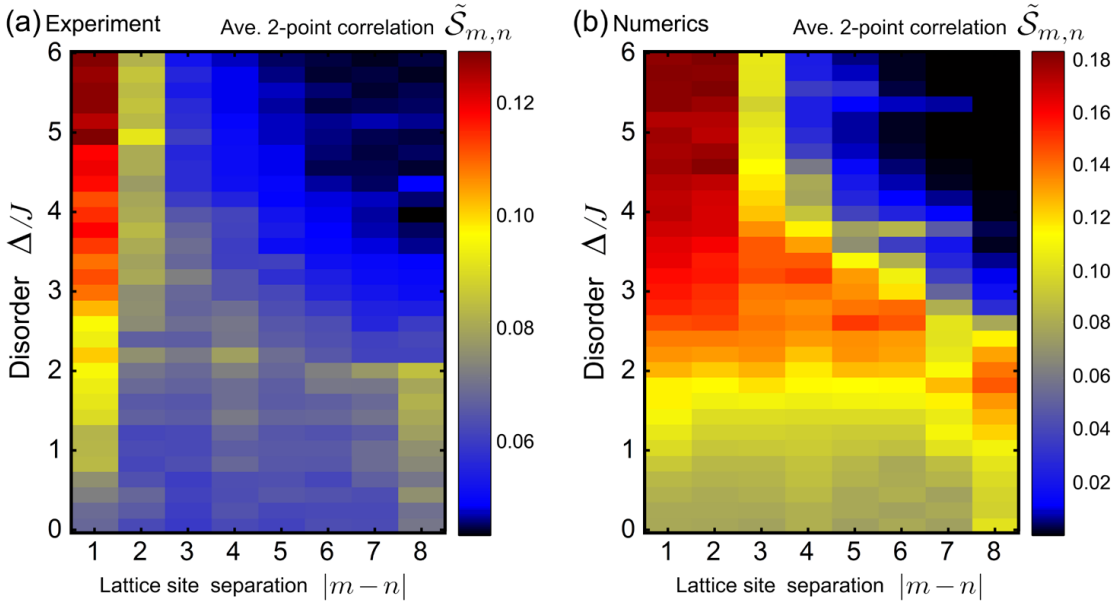

Figure E.6: **Numerical calculation of the quantum correlations** We consider $J/2\pi = 50MHz$, which fixes the interaction $U/J = 3.5$. The time-averaged(from 0 to 250 ns) correlation $\mathcal{S}_{m,n} = |\langle\sigma_m^1\sigma_n^2\rangle - \langle\sigma_m^1\rangle\langle\sigma_n^2\rangle|$ for $b = (\sqrt{5}-1)/2$ and a system size $N = 9$ is **(a)** experimentally measured (same as Fig. 5 in the manuscript), and **(b)** numerically computed.

E.4 Aubry-Andre model

In the absence of interactions (or at single-particle level), the Eqn. 3 of the main text is the celebrated Aubry-Andre (AA) model[83, 129]. We compare this model with the well-studied Anderson model. In 1D or 2D Anderson model, any amount of disorder would localize the entire system and there is no phase transition, or transition is at zero disorder. However, in the 3D Anderson model there is a localization-delocalization transition, where a mobility edge appears [4]. Similar to the 3D Anderson model, the 1D AA model exhibits a localization-delocalization transition. In the AA model, when $\Delta = 2J$, all the eigenstates are fully localized (delocalized) for $\Delta > 2J$ ($\Delta < 2J$) and the localization length is independent of the energy and is solely determined by the ratio between Δ and J [129]. Therefore, the AA model does not exhibit mobility edge [113]. The main difference between the 3D Anderson model and the AA model is that in the AA model, the delocalized phase is characterized by ballistic transport, i.e., scattering events are rare[83]. This implies a ballistic spreading of an initial state localized at a given site.

Now let us discuss briefly the effect of interactions in the AA model (Eqn. 2 of the main text) and a discussion about the signatures of the mobility edge. In the interacting case, one can use the basis of single-particles states of the AA model and in this representation, the interaction act as a hopping term in energy space, allowing transitions between different single-particle states [129]. In systems with a single-particle mobility edge, like 3D Anderson model, the interaction couples localized and delocalized states[113]. This

happens because for a given strength of disorder, localized and delocalized states coexist. In the case of the AA model, as there is not mobility edge in the noninteracting case, the interaction just couples single-particle states which are either localized or delocalized. The signatures of the mobility edge observed in the experiment can be explained as a consequence of the interaction between the two particles in the lattice. When they are located at a distance smaller that the single-particle localization length, they form a bound state that spreads ballistically, as it has been reported in the literature [55]. When the particles are far apart, i.e., at a distance longer than the localization length, they remain localized. This argument explain the coexistence of localized and delocalized states in the interacting model for a fixed disorder and provides an explanation for the signatures of the mobility edge seen in Fig. (3).

Appendix F

Supplementary Information for Chapter 7

F.1 Qubit architecture

The more control a quantum platform offers, the simpler it is to embed diverse applications. For this reason, we have developed superconducting gmon qubits with tunable frequencies and tunable interactions. An optical micrograph of the device is shown in Fig. 1 of the main text and the corresponding circuit diagram is shown in Fig. F.1. The qubits consist of a capacitor (coplanar-waveguide strip), a flux-tunable DC SQUID and a shunt inductor. While the qubits are similar to typical planar transmons (unbiased frequency of 6.2 GHz, non-linearity of 180 MHz), the shunt inductor provides coupling to an RF SQUID. Flux into this RF SQUID allows for tunable coupling between neighboring

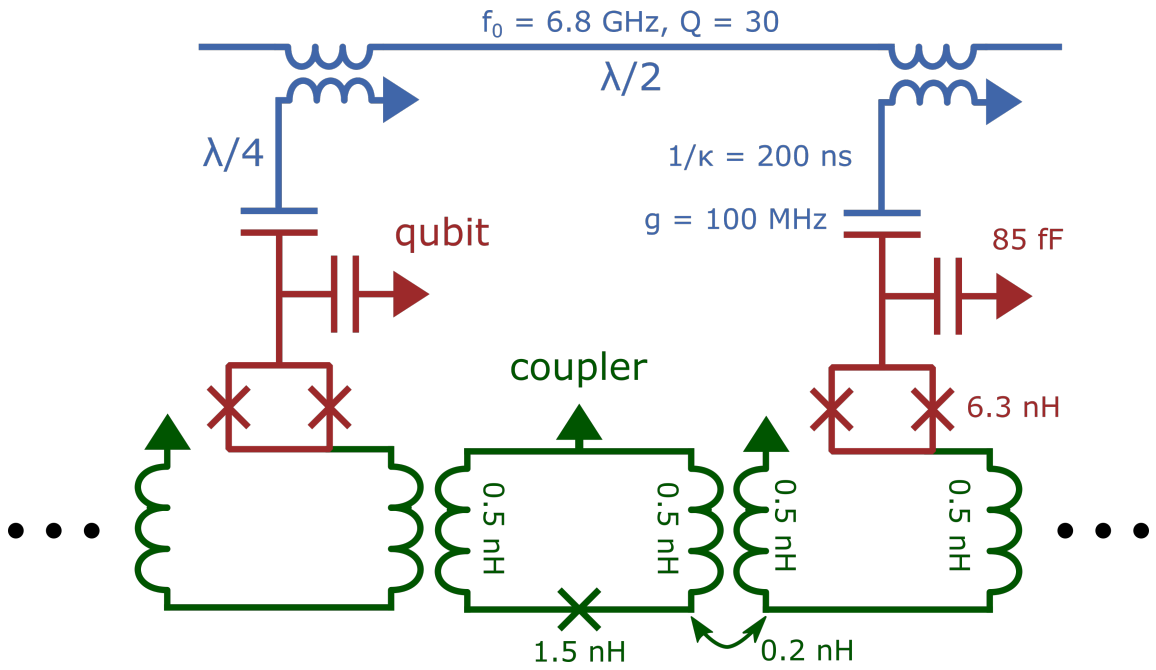

Figure F.1: **Device.** Circuit diagram for the device shown in Fig. 1 of the main text. The qubit SQUID and coupler junction inductances are the effective linear values at zero phase.

qubits. The voltage divider created by the DC SQUID and shunt inductor protect the qubit from capacitive losses in the coupling circuit. Each qubit is dispersively coupled to a readout resonator which are themselves coupled to a low-Q Purcell filter. Twenty-six control lines are used to drive microwave rotations (coupling of 50 aF), set the qubit frequencies (mutual of 1 pH), and bias the couplers (mutual of 1 pH). Interconnects and crossovers are formed using aluminum air-bridges.

F.2 Raw data with predictions

In the main-text, the cross-entropy is used to show that we are able to accurately predict the measured probabilities. Here, we show the measured probabilities with the predictions

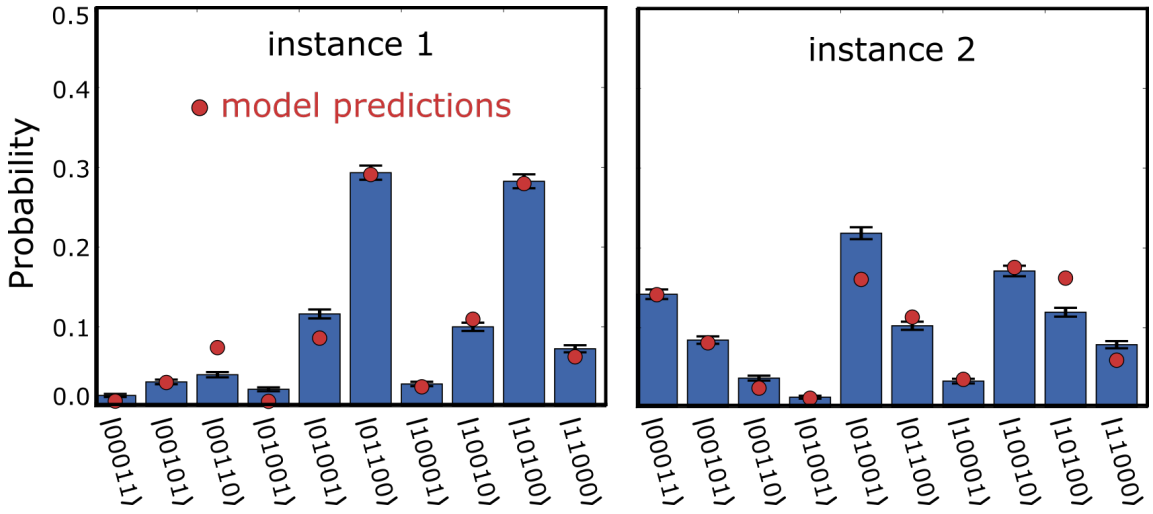

Figure F.2: **Raw data with model predictions.** Measured probabilities for two instances of a 5 qubit experiment after 10 cycles (blue bars). Error bars (3 standard deviations) represent the statistical error from 50,000 samples. This is the same data used in Fig. 1 of the main-text, however, now we overlay the expected probabilities (red circles).

overlaid onto the data (Fig. F.2). We find a strong resemblance between the data and the predictions. While less quantitative than Fig. 4a in the main-text, this provides an intuitive and visual demonstration that we have developed an accurate control model.

F.3 Histogram of probabilities without normalization

The output probabilities of interacting quantum systems (after sufficiently long evolution) all obey a single universal distribution, known as a Porter-Thomas distribution. The distribution of probabilities P has the form $e^{-P \times N_{\text{states}}}$ where N_{states} is the dimension of the state space. In the main text, we plot histograms of the measured probabilities

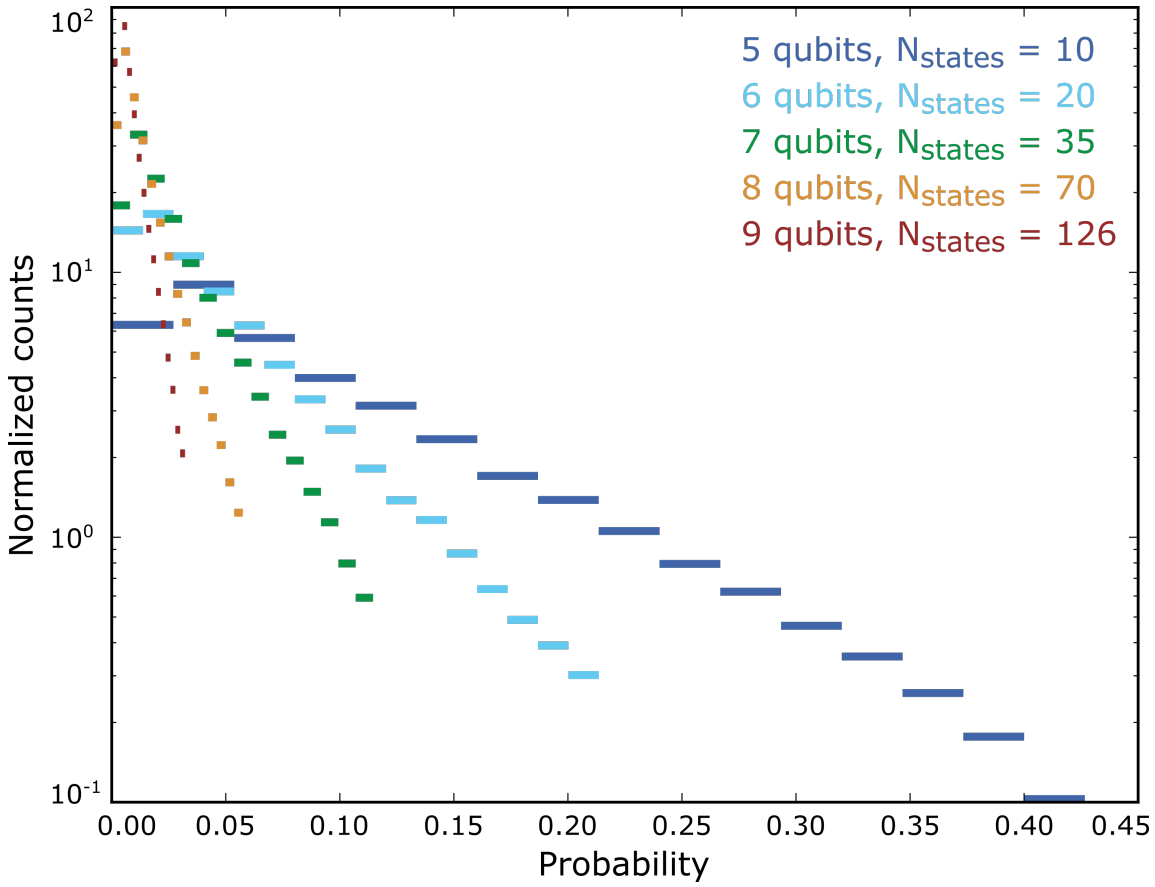

Figure F.3: **Histogram of probabilities.** Histograms of the raw output probabilities for 5 to 9 qubit experiments after 5 cycles of evolution. The width of the bars represent the size of the bins used to construct the histogram. This is the same data used in Fig. 2 of the main-text, however, here we do not normalize the probabilities by the number of states.

weighted by N_{states} - this places the data onto a universal axis. For completeness, we present histograms of the same datasets without weights (see Fig. F.3).

F.4 Hilbert-space dimension

Determining how many states are required to accurately reproduce the experimental data is key to understanding the complexity of our algorithms. In the main text, we show

that the system uniformly explores a Hilbert space that grows as $2^N/\sqrt{N}$. Therefore, this expression provides a lower bound on the complexity. However, higher states of each qubit (e.g. $|2\rangle$) do modify the dynamics and including these states in the simulations increases the computational complexity (see Appendix I for more details). It is not yet understood if these states are necessary to include or if they can be accounted for perturbatively.

In Table 1 we consider the number of states needed under various truncations schemes. The first column is the number of qubits ranging from 3 to 9. The second column is the number of states typically associated with qubit simulations (2^N) and is shown for comparison. The third column is the number of states if each qubit is treated as a 2-level system and truncated to a subspace with half the qubits excited - this scales roughly as $2^N/\sqrt{N}$. This is the lower bound on the scaling of complexity as the system uniformly explores these states (see main text). In the fourth column we consider all states where only a single qubit is in the state $|2\rangle$ - we refer to these states as single doublons. An example of such a state for 8 qubits and 4 excitation would be $|02100100\rangle$. States of this form are the closest in energy to the qubit-subspace and, consequently, most significantly modify the evolution. In the last column we consider qutrits that have been truncated to the subspace with the correct number of excitations and includes multi-doublon states.

In Fig. F.4 we plot the number of states for each of these truncation schemes for 10 to 50 gmon qubits as solid colored lines. We have taken $\log_2$ of the vertical axis so that it represents an effective number of qubits. In addition to the exact scaling, we

N	2-Levels	2-Levels truncated	Single doublon	3-Levels truncated
3	8	3	6	6
4	16	6	10	10
5	32	10	15	15
6	64	20	50	50
7	128	35	77	77
8	256	70	238	266
9	512	126	378	414

Table F.1: Hilbert-space dimension versus number of qubits N for various truncation schemes. The second column (2-levels) is simply 2^N. The next column is the number of states after truncating to a subspace with a fixed number of excitations. The third column (single doublon) includes additional states where a single qubit is in the 2-state (e.g. $|02100100\rangle$). The final column treats each qubit as a 3-level system and truncates to a fixed number of excitations. This includes all multi-doublon states such as $|02020000\rangle$.

plot approximate expressions as dashed black lines. We find that $2^N/\sqrt{N}$ is an accurate scaling for two-level systems assuming fixed number of excitations. Fitting the results for the single-doublon and qutrit subspaces, we find approximate scalings of 2.05^N and 0.15×2.42^N. For comparison, we plot the classical memory requirements as horizontal lines for a typical 16 GB home computer, a 1 TB high-performance computer, and a 1 PB super computer. A home computer may be able to simulate 33, 28 or 26 qubits depending on the truncation scheme. A super computer would be limited to 47, 44, or 37 qubits - this is the the number of qubits required to achieve quantum supremacy. For further details on the complexity of these algorithms see Appendix I.

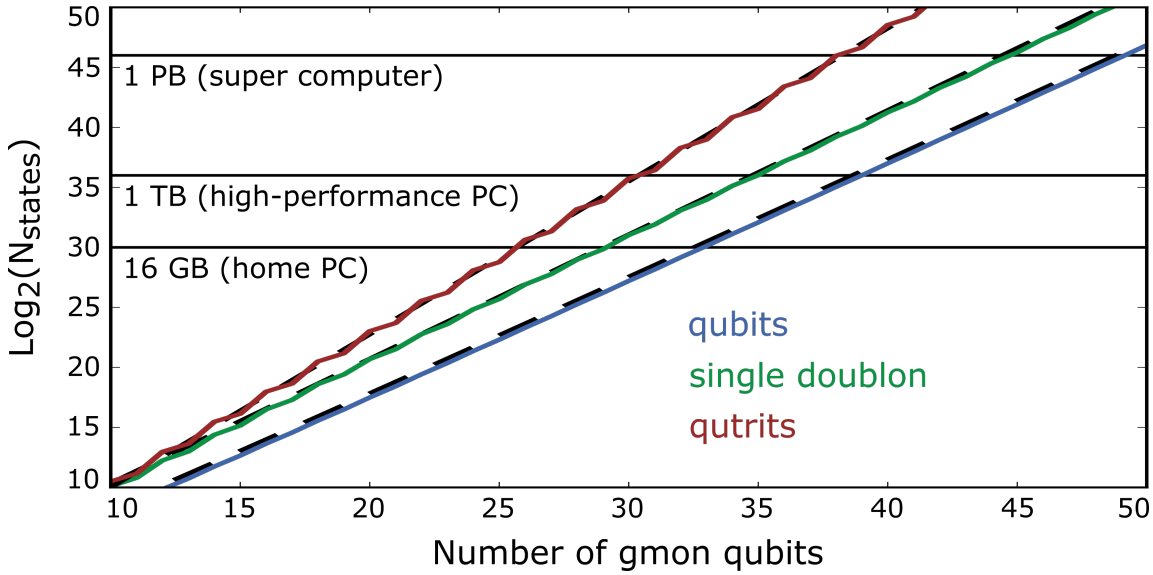

Figure F.4: **Complexity scaling.** Hilbert-space dimension versus number of qubits for 10 to 50 qubits for various truncation schemes. In every case, we only consider states with a fixed number of excitations. The exact scaling for qubits, single doublons and qutrits are shown in blue, green and red respectively. The corresponding dashed lines are approximate scalings. For qubits, this is given by $2^N/\sqrt{N}$. For the single-doublon subspace, we find that 2.05^N is an accurate approximation. For qutrits, we find that 0.15×2.42^N is an accurate approximation. Horizontal lines correspond to memory requirements on a classical computer assuming the state is represented using complex 64-bit numbers.

F.5 Post-selection

The control sequences used in this experiment are designed to conserve the total number of excitations. However, experimental imperfections, such as measurement error and photon loss, can change the number of excitations. The ability to identify and remove erroneous outcomes, while advantageous, comes at the expense of reduced data rates. In Fig. F.5 we plot the fraction of measurements that were thrown away as a function of the number of cycles for 5 to 9 qubit experiments. Initially (at 0 cycles), the number of erroneous outcomes scales as 5.0%/qubit, consistent with measurement infidelity. The number of erroneous outcomes scales linearly with the number of cycles at a rate of 0.1%/qubit/cycle, consistent with photon loss.

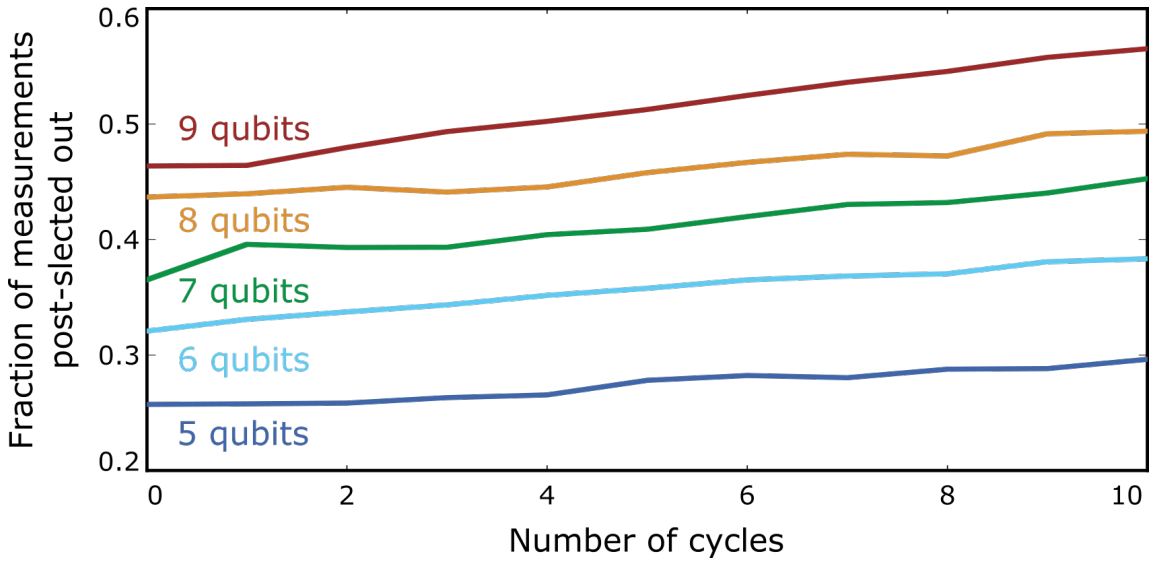

Figure F.5: **Post-selection.** The fraction of the measurements that were rejected during post-selection is plotted versus the number of cycles for 5 to 9 qubit experiments.

F.6 Calibrations

Arbitrary time-dependent control of a well-specified Hamiltonian is a staggering control problem. In the next four sections, I describe the calibration procedures used to tackle this problem. While there is still a great deal of work left before completely arbitrary control is feasible, this work represents a significant step in that direction.

Converting time-dependent pulses into time-dependent matrix elements is done in two steps. First, the signals produced at room temperature are not necessarily what reach the target device (qubit or coupler SQUID). Nonidealities include pulse-distortion, relative timings, and crosstalk (see sections 1, 2 & 3). Second, a physical model of the device is required to convert the signals at the target device to matrix-elements of a Hamiltonian (see section 4).

F.6.1 Pulse distortion

We observe that our control pulses undergo frequency-dependent attenuation. The transfer-function between room temperature and the target-device is modeled as

$$\mathrm{H}(\omega) = 1 + \epsilon \frac{i\omega\tau}{1 + i\omega\tau} \tag{F.1}$$

where ϵ is the fraction of the pulse height that undergoes distortion (typically $\epsilon \approx 1\%$) and τ is a characteristic time-scale (typical values are 10 ns and 70 ns). This expression can be derived using a simple model, treating the CPW bias-line as an inductor network with lossy asymmetric return paths. While the physical origin of the pulse-distortion is not completely understood, this model is consistent with the data.

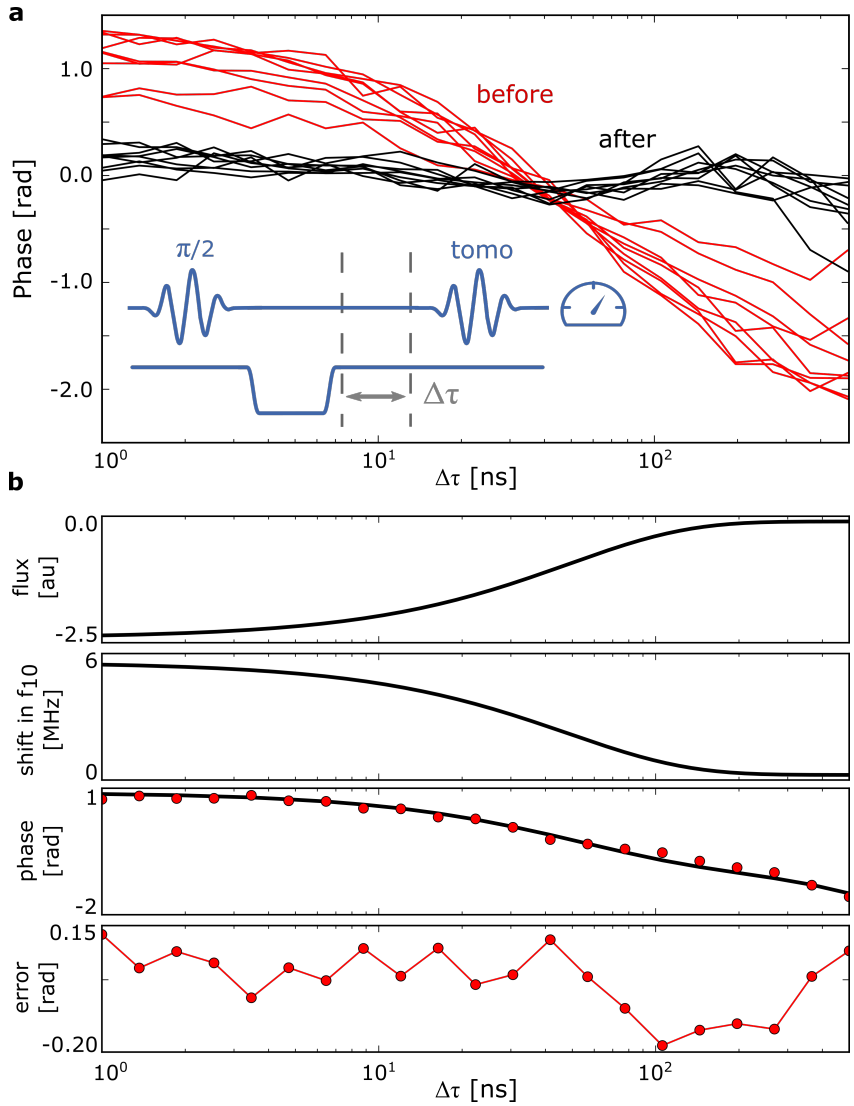

Figure F.6: **Pulse distortion. a** Qubit phase as a function of time after a pulse on the qubit flux-bias line. The ideal response is flat, however, due to imperfections in the lines, we observe the response shown in red. The data can be fit for the transfer function of the line and this can be used to flatten the response. The data after correction is shown in black. **b** Procedure for fitting the phase response data. Given a model for the transfer function, one can compute the expected flux versus time. Knowing the qubit frequency versus flux allows this to be converted to qubit frequency and then phase. This predicted phase can then be compared to the measured phase response and the difference provides a cost function for optimizing the parameters of the transfer function.

The pulse sequence used to infer the transfer function is shown inset in Fig. F.6a. First, the qubit is rotated to the equator. Next, a square pulse is applied to the qubit flux-bias line. The phase of the qubit then measured as a function of delay time after the pulse using state-tomography. Ideally, the phase should be independent of time. However, we observe that the control pulse settles over time in a manner consistent with Eq. 1. The data is shown in red for all nine qubits.

The procedure used to fit the phase response is shown in panel **b**. First, an initial guess for the parameters of the transfer function is used to predict the decay of the control pulse. Next, the control flux is converted to qubit frequency using a separate calibration (data not shown). The change in qubit-frequency can then be integrated to get the corresponding phase shift. The difference between the predicted phase response and the measured phase response provides a cost function for finding the optimal parameters in the transfer function. If one term is insufficient to flatten the response, a second amplitude and time-constant is added in order to further suppress phase accumulation. The inferred transfer function can then be used to correct for the observed distortion by dividing the output signals (in the frequency domain) by the transfer function. The phase response after correction is shown in panel **a** (black).

F.6.2 Timing

Variations in the cabling and filtering can result in the pulses arriving at the target device at different times. It is therefore important to measure these delays and offset the pulses

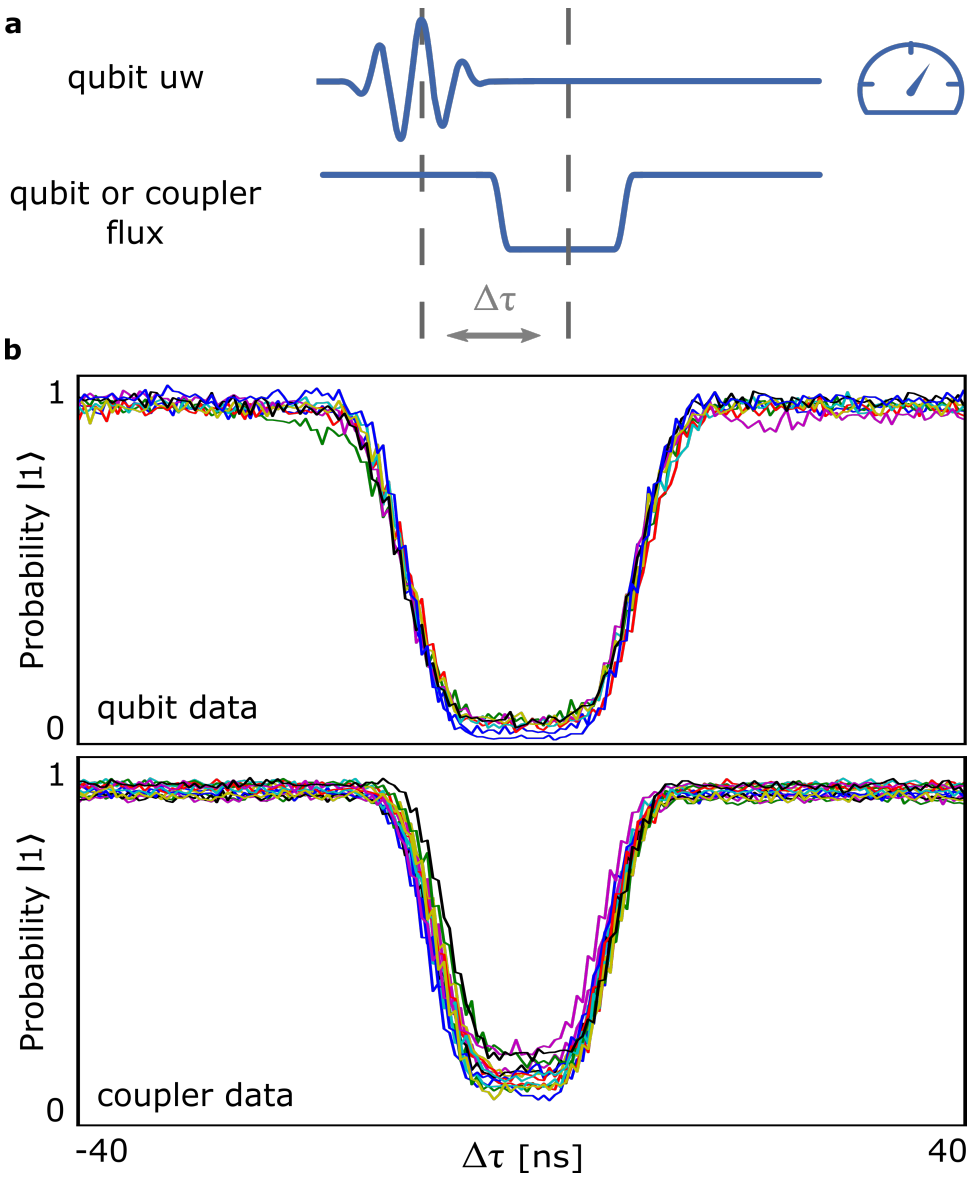

Figure F.7: **Timing delays. a** Pulse sequence used to synchronize timings for the 26 control lines. The qubit flux-bias lines and microwave lines are synchronized by varying the delay between a pi-pules and a detune pulse. When the relative timing is large, the pi-pulse excites the qubit; when the relative timing is small, the qubit is detuned from the microwave rotation and the pulse fails to excite the qubit. An identical experiment is used to synchronize the coupler flux-bias lines. This is done by using the frequency shift induced on the qubit by the coupler. **b** Experimental data for qubit and coupler experiments. Each curve is fit to a sum of two error-functions in order to determine the timing offset between pulses.

in order to compensate. Conceptually, this is done by choosing a single control line as a reference to which all other lines are synced. In this experiment, the flux-bias line of the center qubit (Q5) is chosen to be the reference. The rest of the lines are synchronized using the following steps. 1) The microwave pulses on Q5 are shifted so they align with the flux-bias pulses. 2) The flux-bias of the neighboring coupler (e.g. CP45) is shifted in order to sync with Q5's microwave line. 3) The flux-bias and microwave lines of Q4 are synchronized with one another by shifting the microwave pulse. 4) Both the flux-bias and microwave lines of Q4 are shifted in order to sync up with CP45. This procedure starts in the center and moves out towards both edges until the entire array is synced.

The pulse sequence used to carry out this procedure is shown in Fig. F.7a. The relative timing between a microwave pi-pulse and a qubit (or coupler) flux-bias pulse is varied and the probability of the qubit being in the excited state is measured. If the flux-bias pulse occurs before or after the pi-pulse, the qubit ends up in the excited state. When the flux-bias pulse occurs during the pi-pulse, the qubit frequency shifts and the pi-pulse is off-resonance with the qubit and fails to completely excite the qubit. Data for both qubit and coupler flux-bias pulses are shown in panel **b**. The data is fit in order to determine the timing offset and the result is used to correct future pulses.

F.6.3 Crosstalk

Ideally, the current from any given control line will only reach a single device. However, due to unwanted geometric coupling, a small fraction of the flux from any line will reach

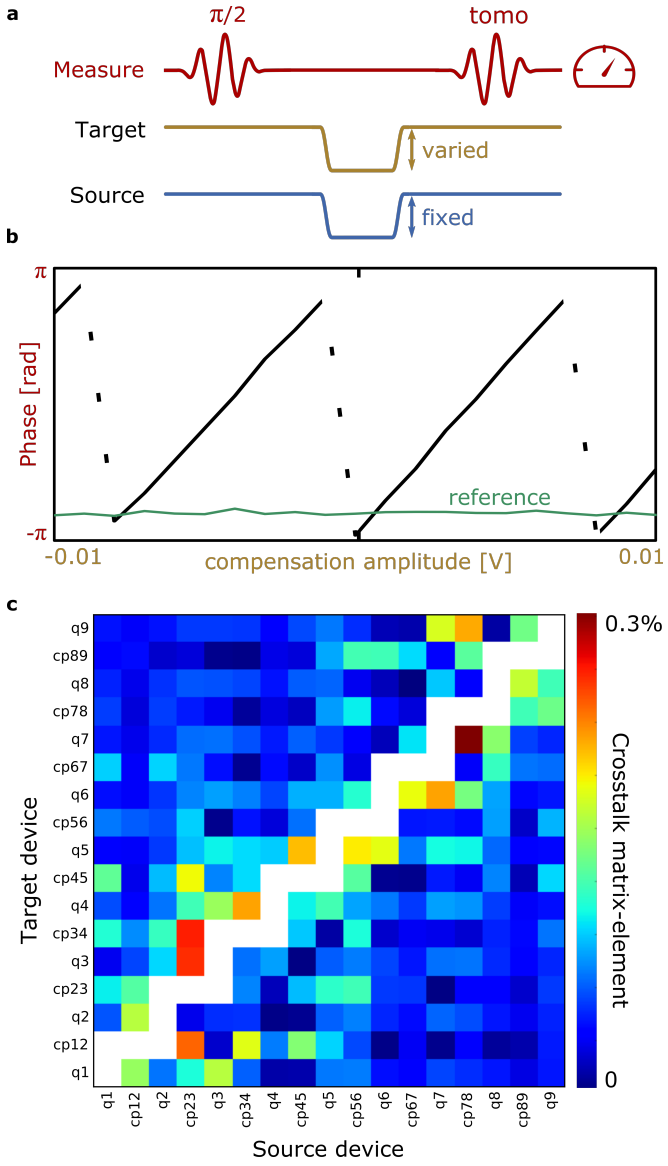

Figure F.8: **Flux-bias crosstalk. a, b** Pulse sequence and measurement used to calibrate cross-talk between flux-bias lines. This experiment is performed on all combinations of 'source' lines and 'target' qubits and couplers. For a fixed pulse height on the source line, we vary the height of a compensation pulse on the target line and measure the phase of a 'measure' qubit. The correct compensation amplitude corresponds to where the measured phase is equal to the phase without a pulse on the source line - this is the reference value (green) shown in the middle panel. The ratio of the compensation amplitude and the source pulse height is the crosstalk matrix-element. **c** The cross-talk matrix. Each pixel represent the crosstalk matrix-element from the source device to the target device. Cross-talk from from qubits to neighboring couplers are not shown as they saturate the color-scale at 4%.

several devices. The procedure used to measure and correct for this effect (linear flux crosstalk) is shown in Fig. F.8.

The pulse sequence and an example dataset are shown in panels **a** and **b**. In order to measure the crosstalk, we apply a square pulse of fixed height on the 'source' line. We then measure the phase of the 'measure' qubit versus the amplitude of the compensation pulse on the 'target' device. The target device is either the measure qubit itself or a neighboring coupler. The phase of the measure qubit in the absence of a pulse on the source line is measured as a reference. The correct compensation amplitude corresponds to when the measured phase equals the reference phase. The crosstalk matrix-element is given by the ratio of the amplitude of the compensation pulse and the source pulse. This experiment is repeated for all combinations of sources and targets.

The crosstalk matrix-elements are shown in panel **c**. Lines physically closest to one another have crosstalk around 0.1-0.3%. Crosstalk from qubits to neighboring couplers are not shown as they saturate the scale at 4%. The desired output fluxes now be multiplied by the crosstalk matrix in order to produce control fluxes with the ideal behavior.

F.6.4 Control model

In the previous three sections, we've shown how to make sure that the control pulses are orthogonal, arrive at the same time, and arrive without distortion. This should provide us with sufficient knowledge of the pulses that arrive at the target device. The next step

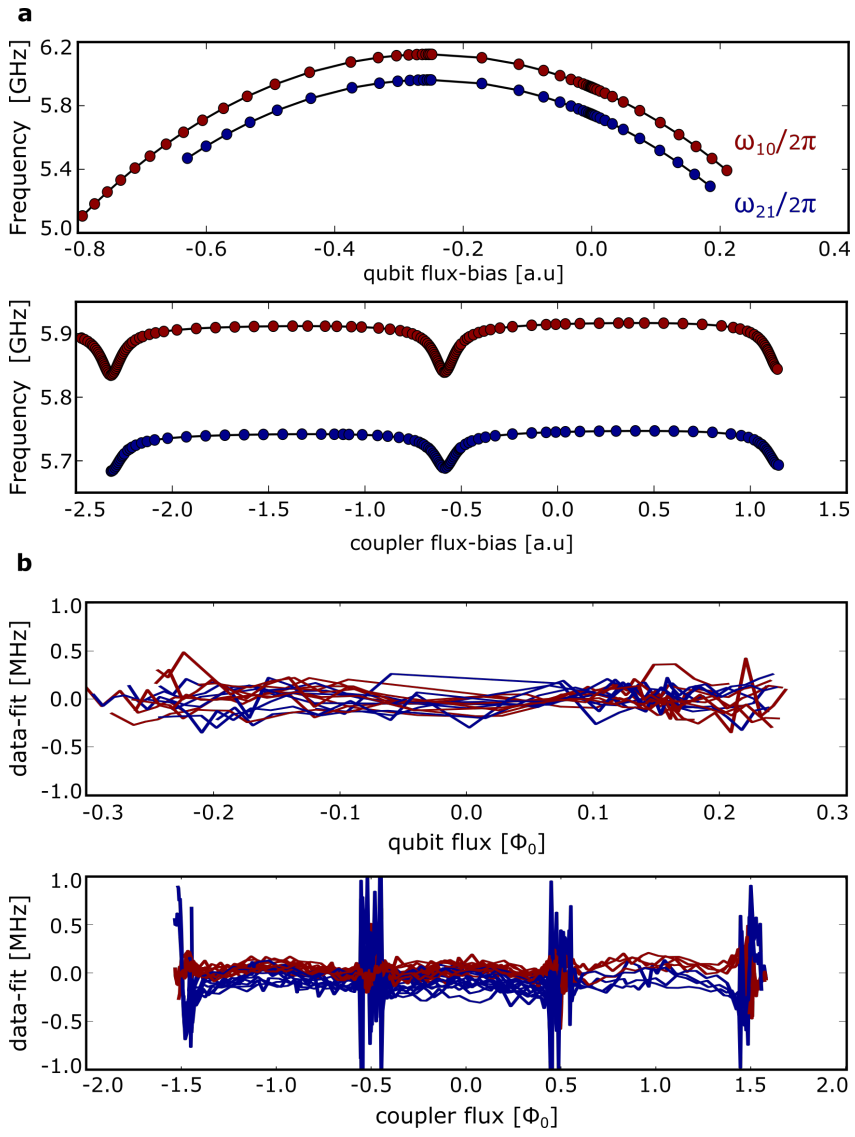

Figure F.9: **Building a physical control model. a, b** In order to convert the control pulses to Hamiltonian parameters, we construct a physical model of our qubits and couplers. The model consists of capacitors, inductors and Josephson junctions. In panel **a**, we measure the qubit transition frequencies f_{10} (ground-state to first excited state) and f_{21} (first excited to second excited state) as a function of qubit and coupler flux-biases. Fitting the datasets allows us to determine the values of model parameters. Fitting errors for all qubits and couplers are shown in panel b and are typically a few tenths of a MHz.

in converting this control pulse to matrix-elements of a known Hamiltonian.

The qubits are well approximated by a Bose-Hubbard model with three parameters: frequency, anharmonicity and coupling. The frequency and anharmonicity have a nonlinear dependence on the flux-bias of the qubit and both neighboring couplers. The coupling has a non-linear dependence on the flux-bias of the coupler, each qubit, and even the neighboring couplers (as they shift the qubit inductance).

Determining the values of these parameters as a function of the control knobs can be done in one of two ways: 1) measure every parameter versus every knob and spline the data or 2) measure cuts in the parameter space and use these cuts to construct a physical model of the device. In this experiment, we have chosen the second approach for two reasons. The first reason is that accurately measuring the individual parameters is very challenging. Given two qubits, spectroscopic probes only provide two pieces of information (the two eigenvalues) from which one cannot simultaneously determine the frequencies and couplings separately (three parameters). Time-domain approaches require accurately measuring small variations in the populations which are hard to resolve in experiments. The second reason is that the final step in calibration is often optimization. A 'measure everything and spline' approach has far too many degrees of freedom to optimize over.

A gmon qubit can be modeled as a capacitor, inductor and tunable junction, all in series. The Hamiltonian for such a circuit is given by

$$\mathcal{H} = \frac{\hat{Q}^2}{2C} - \frac{I_0 \Phi_0}{2\pi} \cos \hat{\phi}_j + \frac{1}{2} L_g \left(I_0 \sin \hat{\phi}_j \right)^2 \tag{F.2}$$

where $\hat{Q}$ is the charge on the capacitor, C is the capacitance, I_0 is the tunable critical current of the junction, $\hat{\phi}_j$ is the phase drop across the junction, and Lg is the geometric inductance. The phase drop across the junction $\hat{\phi}_j$ is related to the conjugate variable of charge (flux $\hat{\Phi}$) through the following relationship

$$\hat{\phi}_j = \hat{\phi} + 2\sum_n (-1)^n \frac{J_n(\beta n)}{n} \sin(n\hat{\phi}) \tag{F.3}$$

where $\hat{\phi} = \frac{2\pi}{\Phi_0}\hat{\Phi}$, J_n is the Bessel function of the first kind, $\beta = L_g/L_j$, and $L_j = \frac{\Phi 0}{2\pi}\frac{1}{I_0}$ is the effective inductance of the junction. The Hamiltonian can be numerically diagonalized by expressing $\hat{Q}$ and $\hat{\Phi}$ in terms of harmonic oscillator raising and lowering operators. We find that truncating these operators at 20 levels provides 1 Hz accuracy for a 5 GHz qubit with -200 MHz nonlinearity at $\beta = 0$. It is important to note that keeping too many levels (past around 60) causes this numerical approach to break down as the harmonic oscillator states start to find low energy solutions in the neighboring minima of the cosine potential.

This model is used to fit measurements of the qubit energy spectrum for C, L_j and L_g. In order to make this process computationally efficient, exact diagonilization is used to estimate coefficients in a perturbation expansion; the perturbative model is then used for fitting. This is done by expressing the Hamiltonian in terms of the harmonic oscillator frequency $\omega_0 = \frac{1}{\sqrt{C(Lg+Lj)}}$ and two small dimensionless parameters, $\beta = Lg/Lj$ and $\lambda = \frac{Z_0}{(R_k/\pi)}$ where $Z_0 = \sqrt{\frac{(Lg+Lj)}{C}}$ and $R_k = h/e^2$. The Hamiltonian was diagonalized over a 100x100 grid for $0 \leq \lambda \leq 0.04$ and $0 \leq \beta \leq 0.25$ and the results were fit for coefficients of a 2-dimensional polynomial. The following expressions for the two lowest transitions

are accurate to within 100 kHz at 5GHz

$$\omega_{10}/\omega_0 = 1 + \sum A_{nm}\beta^n\lambda^{m+1}$$

$$\omega_{21}/\omega_0 = 1 + \sum B_{nm}\beta^n\lambda^{m+1}$$

$$A = \begin{pmatrix} -0.9989185 & -1.01547902 & -3.39493789 \\ 2.92743183 & -1.15831188 & 0.0 \\ -4.93953913 & 8.17006907 & 0.0 \\ 4.03181772 & 0.0 & 0.0 \end{pmatrix}$$

$$B = \begin{pmatrix} -1.99707501 & -3.25782090 & -18.0220389 \\ 5.81558214 & -1.77830584 & 0.0 \\ -9.55174679 & 22.6985133 & 0.0 \\ 7.16401532 & 0.0 & 0.0 \end{pmatrix} \tag{F.4}$$

Note that $A_{00} \simeq -1.0$ and $B_{00} \simeq -2.0$ as expected from first-order perturbation theory. Similarly, $A_{10} \simeq 3.0$ (the coefficient of $\beta\lambda$) is also consistent with perturbation theory. Increasing the domain or improving the accuracy of this expansion is as simple as fitting to a higher degree polynomial.

Each qubit is dispersively coupled to a readout resonator. This resonator imparts a frequency dependent shift on the qubit's energy levels. The frequency shift is modeled as

$$\Delta\omega_{10} = \frac{1}{2}\left(|\delta| - \sqrt{4g_r^2 + \delta^2}\right) \tag{F.5}$$

where $\delta = \omega_{10} - \omega_r$, ω_r is the frequency of the resonator and g_r is the qubit-resonator

coupling. The shift in ω_{20} depends on the anharmonicity of the qubit and is modeled as

$$\Delta\omega_{20} = \frac{1}{2}\left(|\delta+\eta| - \sqrt{4g_r^2(1+\frac{\eta}{\omega_{10}}) + (\delta+\eta)^2}\right) \tag{F.6}$$

where $\eta = \omega_{21} - \omega_{10}$ is the qubit anharmonicity - note that we have accounted for a nonlinear correction in the two-photon coupling strength. The shift in ω_{21} is then given by $\Delta\omega_{21} = \Delta\omega_{20} - \Delta\omega_{10}$. When fitting measurements of the qubit energy spectrum, these expressions are used to find g_r given the known resonator frequency (measured independently).

Each qubit is coupled not only to a readout resonator but also to a coupler. Treating the coupler as a tunable linear inductor, one finds that the geometric inductance of the qubit is modified according to the following expression

$$Lg \rightarrow L_g - \frac{M^2}{L_c}\frac{\beta_c}{1+\beta_c} \tag{F.7}$$

where M is the mutual inductance from the qubit to the coupler, L_c is the geometric inductance of the coupler, $\beta_c = \beta_{C0}\cos\phi_c$ is the ratio of the coupler's geometric inductance to junction inductance, and ϕ_c is the phase drop across the coupler. When converting from the applied control flux to junction phase, Eq. 3 is used. When fitting measurements of the qubit energy spectrum, these expressions are used to find β_{C0} and $M_0 = M^2/L_c$.

The coupler also has a mode which dispersively pushes on the qubit energy levels (similar to the readout resonator). We find that including this mode is necessary in order to accurately reproduce the measured qubit energy spectrum. The frequency of this mode changes with the flux applied to the coupler according to $\omega_c = \omega_{C0}\sqrt{1+\beta_c}$ where ω_{C0} is the unbiased frequency of the coupler. The coupling between the qubit

and the coupler mode is given by $\frac{\sqrt{\omega_{10}\omega_c}}{2}\frac{M}{\sqrt{(Lg+Lj)Lc(1+\beta_c)}}$ which is the typical harmonic oscillator expression. The dispersive shift is then taken into account in a manner similar to the readout resonator. This effect introduces an additional fitting parameter ω_{C0}.

All of these physical parameters are determined by fitting the two lowest transition energies of each qubit (ω_{10} and ω_{21}) versus the qubit and coupler flux. The advantage of this calibration strategy is that it requires only single qubit experiments and is likely scale to much larger systems. Calibrating 9 qubits and 8 couplers takes around 24 hours to complete. During each experiment, all other qubits are biased to their minimum frequency in order to effectively remove them from the system. Ignoring the neighboring qubit could result in up to a 1 MHz error in the model at the maximum coupling (a 5 GHz detuning and a 50 MHz coupling gives a 0.5 MHz dispersive shift). Example datasets are shown in Fig. F.9**a**. The difference between the fit and the data is shown in panel **b** for all datasets. Typical errors are on the order of 0.1 MHz. Below is a table of parameters inferred from the data. M_0 left (right) refers to the mutual to the qubit on the left (right) of the coupler.

In addition to these, every control line has two more fitting parameters - a conversion from DAC amplitude to Φ_0 (2.04±0.03 for qubits and 1.82±0.04 for couplers) and a static flux offset. The data is also fit for the crosstalk from couplers to qubits as this matrix-element is difficult to infer using any other technique. Additional fitting parameters are included, when necessary, to account for the qubit being brought into resonance with two-level defects. Lastly, we find it necessary to include a factor multiplying the two-photon

Qubit	C [Ff]	L_j[nH]	L_g [nH]	$g_r/2\pi$ [MHz]
Q1	86.2	6.46	0.96	112.0
Q2	85.9	6.26	0.98	106.0
Q3	87.7	6.25	0.86	135.0
Q4	86.5	6.47	0.92	128.0
Q5	83.9	6.26	1.06	106.0
Q6	85.6	6.31	0.98	114.0
Q7	85.9	6.45	0.95	113.0
Q8	86.4	6.33	0.94	117.0
Q9	87.2	6.41	0.86	126.0
Avg.	86.1±1.0	6.35±0.08	0.95±0.06	117.4±9.5

Coupler	M_0 left [pH]	M_0 right [pH]	β_{C0}	$\omega_{C0}/2\pi$ [GHz]
CP12	43.6	40.2	0.664	14.6
CP23	42.6	41.1	0.660	14.6
CP34	42.3	41.6	0.665	14.8
CP45	43.2	41.5	0.661	14.7
CP56	46.2	40.9	0.657	15.0
CP67	44.0	41.8	0.664	14.8
CP78	43.3	39.5	0.671	14.5
CP89	43.2	37.9	0.663	14.8
Avg.	43.6±1.1	40.6±1.2	0.663±0.004	14.7±0.15

Table F.2: Model parameters for all qubits (upper table) and couplers (lower table). The last row in each table is the average over devices ± 1 standard-deviation.

interaction between the qubit and the coupler with inferred values of 0.959 ± 0.003. This 4% reduction in the 2-photon coupling is likely the result of anharmonic corrections to the coupler. Ideally, in future experiments, this parameter will be replaced by the coupler impedance and a nonlinear model of the coupler.

F.7 Appendix

F.7.1 Complexity of the time evolution in the driven Hubbard model

For a number of families of quantum circuits, such as linear optics (boson sampling) [1], commuting circuits (IQP) [34, 33] and random circuits [28, 2], it has been argued that sampling the distribution of the output of the circuit presents a hard computational task for a classical computer, see also Ref. [121] for a brief review. Also it has been suggested that these hardness arguments could be extended to a wider class of quantum circuits [121]. In this section we provide intuitive arguments in support of the computational complexity of the sampling of the output of the driven continuous evolution protocol implemented on the gmon circuit. We show that the observed probability amplitudes p_n of bitstrings $n = \{0, 1\}^{\otimes N}$ can be mapped onto a classical partition function with complex temperature which realizes an analog of the sign problem of the Quantum Monte Carlo algorithm. Computationally hard instances are likely generated in the quantum chaotic regime. To identify this regime we analyze characteristics of quantum

chaos: the wave function statistics, rapid loss of memory of the initial state and entanglement dynamics. We restrict the discussion to the Bose-Hubbard approximation. The full gmon circuit model contains additional non-integrable terms in the Hamiltonian which do not change the qualitative picture of the chaotic dynamics. Further work is needed to formally establish the complexity class of the task of computing p_n and to connect the sampling task in the gmon circuit to the collapse of the Polynomial Hierarchy, as was argued in the case of random circuits, see Ref. [28] and references therein.

Sampling amplitude as a classical partition function

We separate the diagonal and even/odd terms in the Bose-Hubbard Hamiltonian,

$$\mathcal{H} = \hat{H}_d + \hat{V}_e + \hat{V}_o, \tag{F.8}$$

$$\hat{H}_d = \sum_{i=1}^{N} \left(\delta_i \hat{a}_i^+ \hat{a}_i + \frac{\eta_i}{2} \hat{a}_i^+ \hat{a}_i \left(\hat{a}_i^+ \hat{a}_i - 1 \right) \right), \tag{F.9}$$

$$\hat{V}_e = \sum_{i\,\text{even}} g_{i,i+1}(t) \left(\hat{a}_i^+ \hat{a}_{i+1} + h.c. \right),$$

$$\hat{V}_o = \sum_{i\,\text{odd}} g_{i,i+1}(t) \left(\hat{a}_i^+ \hat{a}_{i+1} + h.c. \right), \tag{F.10}$$

where $g_{i,i+1}(t)$ is the time-dependent drive as implemented in the experiment, see main text for details. For an evolution operator $\hat{U}(T)$ we introduce a grid of discrete time points $t = 0, ..., 2M$, related to the physical time τ by $\tau = \Delta t,\ \Delta \equiv \frac{T}{2M}$. We can write a Trotter decomposition in the basis of boson occupation numbers $|\vec{n}\,(t)\rangle \equiv \otimes_{i=1}^{N} |n_{i,t}\rangle$,

where $n_{i,t}$ is the number of bosons at site i at time t,

$$Z \equiv \langle \vec{n}' | \hat{U}(T) | \vec{n} \rangle = \sum_{\{\vec{n}(t)\}} e^{-i\frac{1}{2}\Delta \sum_{t=1}^{2M} H_d(n(t))} \times \prod_{t=0,2,4\ldots} \langle \vec{n}\,(t)\,| e^{-i\Delta \hat{V}_e(t)} | \vec{n}\,(t+1)\rangle \langle \vec{n}\,(t+1)\,| e^{-i\Delta \hat{V}_o(t+1)} | \vec{n}\,(t+2)\rangle,$$

where the sum runs over all possible realizations of the set $\{\vec{n}\,(t)\}$. All even (and odd) bond operators commute among themselves resulting in the product, $\langle e^{-i\Delta \hat{V}_e(t)} \rangle = \prod_{i\,\text{even}} \Lambda_{(i,i+1);(t,t+1)}$, where each term $\Lambda_{(i,i+1);(t,t+1)}$ is

$$\langle n_{i,t} n_{i+1,t} | e^{-i\Delta g_{i,i+1}(t)(\hat{a}_i^\dagger \hat{a}_{i+1} + \hat{a}_{i+1}^\dagger \hat{a}_i)} | n_{i,t+1} n_{i+1,t+1} \rangle \ .$$

This can be calculated explicitly giving

$\mathbf{\Lambda_{(i,i+1);(t,t+1)}}$	**Condition**
1	$n_{i,t} = n_{i,t+1}$ $n_{i+1,t} = n_{i+1,t+1}$
$-i\Delta g_{i,i+1}\,(t)\,\sqrt{n_{i,t}(n_{i+1,t}+1)}$	$n_{i,t} = n_{i,t+1} + 1$ $n_{i+1,t} = n_{i+1,t+1} - 1$
$-i\Delta g_{i,i+1}\,(t)\,\sqrt{(n_{i,t}+1)n_{i+1,t}}$	$n_{i,t} = n_{i,t+1} - 1$ $n_{i+1,t} = n_{i+1,t+1} + 1$
0	other

This operator reflects a swap of one particle between the neighboring sites $n_{i,t}$ and $n_{i+1,t}$ and ensures that particle non-conserving trajectories do not contribute to the partition function. The partition function is a sum of complex amplitudes,

$$Z = \sum_{\{\vec{n}(t)\}} e^{i\phi_{\{\vec{n}(t)\}}} w_{\{\vec{n}(t)\}}. \tag{F.11}$$

Each trajectory $\{\vec{n}\,(t)\}$ is associated with a phase factor $\phi_{\{\vec{n}(t)\}}$, and a real non-negative weight $w_{\{\vec{n}(t)\}} \geq 0$,

$$w_{\{\vec{n}(t)\}} = \prod_{\text{type } I} \left| \sqrt{n_{i,t}(n_{i+1,t}+1)}\, g_{i,i+1}\,(t)\,\Delta \right| \prod_{\text{type } II} \left| \sqrt{(n_{i,t}+1)n_{i+1,t}}\, g_{i,i+1}\,(t)\,\Delta \right|,$$

where the products are over all 4-site plaquettes of type-I and type-II for which the equalities $n_{i,t} = n_{i,t+1} + 1, n_{i+1,t} = n_{i+1,t+1} - 1$ and $n_{i,t} = n_{i,t+1} - 1, n_{i+1,t} = n_{i+1,t+1} + 1$, respectively, hold for a given 2D trajectory $\{\vec{n}\,(t)\}$. According to the expressions for $\Lambda_{(i,i+1);(t,t+1)}$ the weight $w_{\{\vec{n}(t)\}}$ vanishes for any trajectory that does not conserve the number of bosons.

The phase factor, from the swaps and from the diagonal part of the Hamiltonian, is

$$\phi_{\{\vec{n}(t)\}} = -\frac{1}{2}\Delta \sum_{t=1}^{2M}\sum_{i=1}^{N}\left(\delta_i n_{i,t} + \frac{\eta}{2} n_{i,t}(n_{i,t}-1)\right) - \frac{\pi}{2}\sum_{(i,t)} J_{(i,i+1);(t,t+1)}\left(n_{i,t}-n_{i,t+1}\right)^2 \left(n_{i+1,t}-n_{i+1,t+1}\right)^2, \quad \text{(F.12)}$$

where $J_{(i,i+1);(t,t+1)} = \text{sign}\left(g_{i,i+1}(t)\right)$ when $n_{i,t} = n_{i,t+1} \pm 1$ and $n_{i+1,t} = n_{i+1,t+1} \mp 1$, but is equal to 0 otherwise.

The resulting partition function Z in Eqs. (F.11-F.12) describes a discrete classical model, a generalization of the Potts model [188] on a square lattice with 4-site interactions and complex parameters with non-zero real and imaginary parts.

Assuming a classical algorithm with overall polynomial resources, the accuracy with which each phase factor of a trajectory can be determined is polynomial in N. This means that the partition function takes the form,

$$Z = \sum_{r=0}^{R} w_r e^{2\pi i \frac{r}{R}}, \quad \text{(F.13)}$$

where r is integer, and $R \sim \mathcal{O}(N^\alpha)$ for some power α. Each weight w_r is therefore a bin containing all the trajectories corresponding to the given phase within the discretization accuracy, see Fig. F.10, i.e. w_r is a sum $w_r = \sum_{i=0}^{\kappa_r} w_r^{(i)}$ over κ_r trajectories satisfying

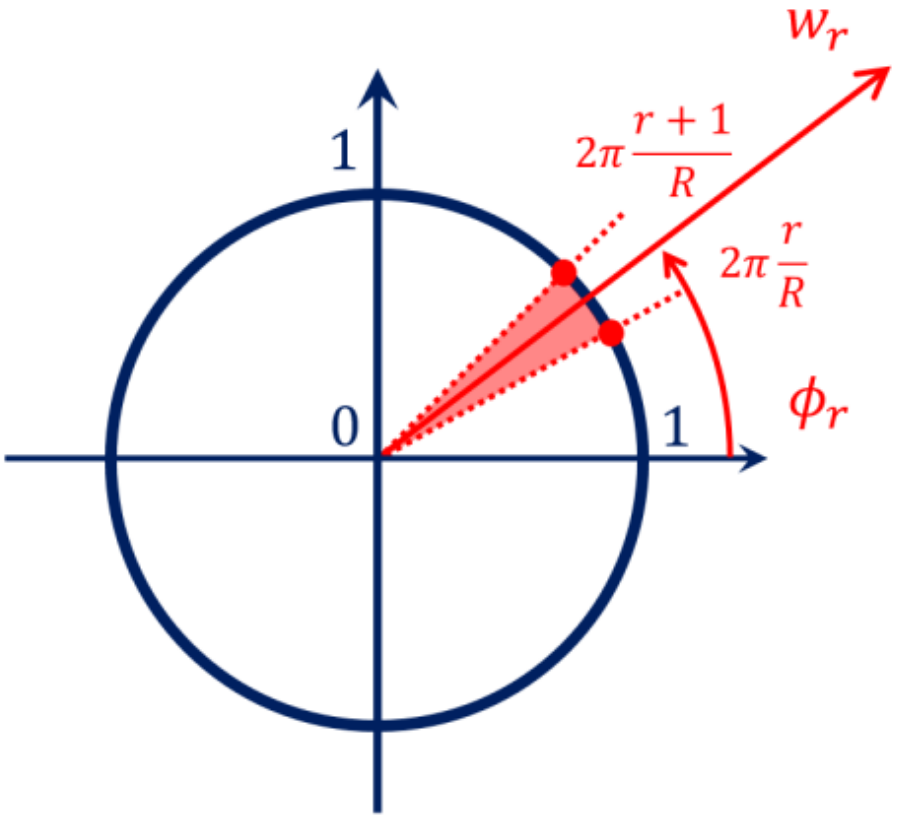

Figure F.10: Binning of the phase factors in the partition function Eq. (F.13).

the condition,

$$2\pi\frac{r}{R} < \phi_{\{\vec{n}(t)\}} < 2\pi\frac{(r+1)}{R}, \tag{F.14}$$

each trajectory weighted with $w_r^{(i)}$. The typical number of trajectories satisfying Eq. (F.14) is exponential in the number of time steps multiplied by the number of sites $M \times N$. Notice however that in the limit $M \to \infty$ the weight of each trajectory is suppressed because $w_{\{\vec{n}(t)\}} \sim \exp(-\nu \log M)$, where ν is the total number of swaps of both type-I and type-II in the trajectory. For a given realization of a trajectory $\{\vec{n}(t)\}$ containing ν swaps in a specific order there are $\binom{M}{\nu}$ ways to arrange the swaps among the M points of discrete time. This entropic factor compensates the suppression factor in the weight of the trajectory. As a result, trajectories with $\nu_{gT} \sim N\int_0^T dt g_{i,i+1}(t) \gg 1$, which does not scale with M, dominate the weight w_r. Therefore $w_{r,\nu_{gT}} \sim \exp(\text{const} \times \nu_{gT})$, which ensures that $w_r \gg 1$ scales exponentially with the number of qubits N. The partition function is therefore given by the sum of a polynomial number of phase factors each multiplied by an exponentially large weight.

In the chaotic regime the typical value of the amplitude $\left|\langle\vec{n}'|\hat{U}(T)\vec{n}\rangle\right|$ is exponentially small in the number of qubits N, and therefore the value of $|Z|$ results from the cancellation of exponentially large weights. In this regime the task of calculating the sum in Eq. (F.13) on a classical computer is analogous to estimating a partition function with a sign problem using the Quantum Monte Carlo algorithm. In Ref. [28] it was argued that a classical statistical algorithm to calculate the sum of type Eq. (F.13) in polynomial

time necessarily requires exponential accuracy, suggesting that approximating Eq. (F.13) presents a hard computational problem.

Comparison to the cases of hard core and free bosons

It is instructive to consider the case where the Hilbert space is truncated to only the ground and first excited level $n_i = \{0, 1\}$, which holds in the limit $\eta \to \infty$. This corresponds to the spin-1/2 XX model. In this case the Hubbard interaction does not contribute and therefore the evolution of the Bose-Hubbard model at half-filling can be described in terms of the dynamics of $N/2$ free particles. Moreover, the model allows a one-to-one mapping onto free fermions via the Jordan-Wigner transformation [133]. The initial state can be written in terms of fermion creation/annihilation operators $c_i^\dagger$, c_i at lattice site i,

$$|\vec{n}\rangle = \prod_{\alpha=1}^{N/2} c_{i_\alpha}^\dagger |0\rangle, \quad 1 \leq i_1 < i_2 < ... < i_{N/2} \leq N, \tag{F.15}$$

where strict ordering of indexes means Jordan-Wigner strings can be dropped. Rewriting the time-dependent Hamiltonian Eq. (F.9) in terms of fermionic operators and the time dependent $N \times N$ matrix $\hat{h}$, $\mathcal{H} = \sum_{i,j} \hat{h}_{i,j}(t) c_i^\dagger c_j$, we can find the time dependence of the

Heisenberg picture fermionic operators explicitly,

$$\tilde{c}_i(T) = \hat{U}^\dagger(T) c_j(0) \hat{U}(T) = \sum_{j=1}^{N} \left[V_{i,j}(T)\right] c_j(0), \tag{F.16}$$

$$\left[V_{i,j}\left(T\right)\right] = \left[\mathcal{T} \exp\left(-i \int_0^T dt\, \hat{h}(t)\right)\right]_{ij}, \tag{F.17}$$

where $V_{i,j}$ is an $N \times N$ matrix. The anti-commutation properties of free fermions result in the fully anti-symmetric form of the probability amplitude,

$$\begin{aligned}\langle \vec{n}' | \hat{U}(T) | \vec{n} \rangle = \langle 0 | \prod_{\beta=1}^{N/2} \tilde{c}_{j_\beta}(T) \prod_{\alpha=1}^{N/2} c_{i_\alpha}^\dagger | 0 \rangle \\ = \sum_{\mathcal{P}(i_\alpha)} (-1)^{\mathcal{P}} V_{j_1,i_1}\left(T\right) V_{j_2,i_2}\left(T\right) ... V_{j_{N/2},i_{N/2}}\left(T\right), \end{aligned} \tag{F.18}$$

where $\mathcal{P}(i_\alpha)$ stands for permutations of the site indexes i_α and the factor $(-1)^{\mathcal{P}}$ takes into account the sign change for odd number of index permutations. The sum of $\left(\frac{N}{2}\right)!$ terms in Eq. (F.18) reduces to a determinant of an $\frac{N}{2} \times \frac{N}{2}$ matrix and can be calculated efficiently. This is a very special realization of the partition function Eqs. (F.11-F.12).

In the opposite limit of $\eta \to 0$ and unlimited Hilbert space $n_i = 0, 1, ..., \frac{N}{2}$, a similar description holds in terms of free bosons. In particular, the Heisenberg equation of motion is completely analogous to Eq. (F.16) but using bosonic operators $a_j(T)$ instead of fermionic operators. Crucially, this implies that the amplitude $\langle \vec{n}' | \hat{U}(T) | \vec{n} \rangle$ does not have the form of an anti-symmetric sum, but instead it can be reduced to a permanent [168], which is known to present a hard computational problem [182, 115, 1]. Note also that

because Eq. (F.16) can swap operator indexes as part of the evolution, the restriction to 1D is not consequential for $T \in O(N)$.

In the intermediate regime of $\eta/g \in O(1)$, including the second on-site excited level $n_i = \{0, 1, 2\}$ violates the strictly anti-symmetric nature of the sum in Eq. (F.18). In the case of weak η, an intuitive picture emerges: virtual transitions through the second excited state introduce effective interactions in the fermionic representation. For random parameters, we expect the interactions to result in a chaotic evolution.

F.7.2 Estimates for the cost of simulating the Bose-Hubbard model.

Direct simulation with truncated bosons

A first attempt to estimate the cost of a direct simulation of the Bose-Hubbard model in the parameter range of interest is to truncate the Fock space of each gmon. We denote the different truncated spaces by the parameter m, with $m = 1$ corresponding to all the gmons truncated to the first excitation level $|1\rangle$ (the qubit subspace), $m = 2$ corresponding to all the gmons truncated to the second excitation level $|2\rangle$, and so for.

We integrate the time-dependent Schrödinger equation using fourth order Runge-Kutta, which is a standard numerical integration method [1]. We use the cross entropy difference after projecting the state to the qubit subspace, as explained in the main text,

[1] There are other numerical integration algorithm, such as the Lanczos method. Nevertheless, given that we are interested in a time-evolution with a time-dependent Hamiltonian, fourth order Runge-Kutta seems well suited for this task.

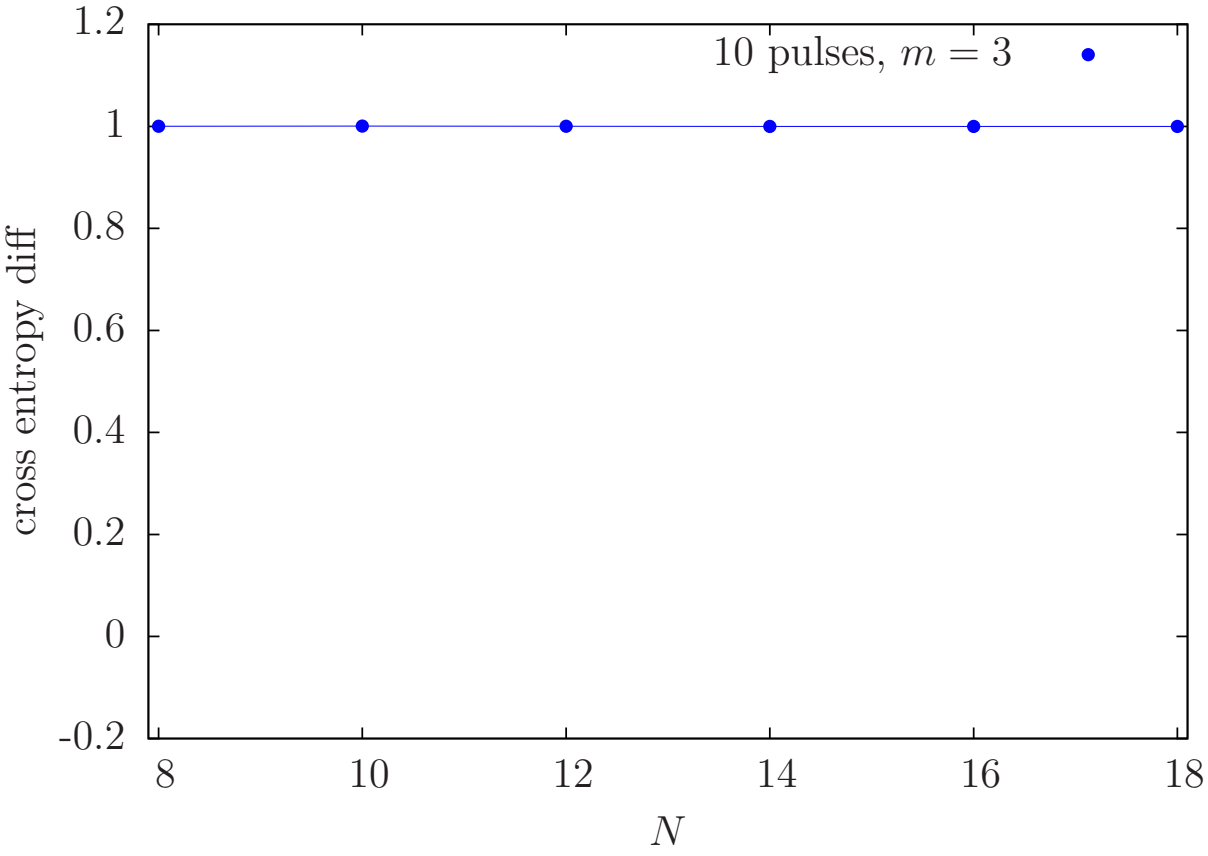

Figure F.11: We can simulate with four level systems.

as an approximation of fidelity, to quantify the fitness of the numerical integration at different levels of truncation. More explicitly, we performed numerical integration with up to $N = 18$ gmons and compute the cross entropy difference at a given truncation level m and the fiducial integration with the highest truncation level, which we choose to be $m = 4$.

Our first observation is that the cross entropy difference between $m = 3$ and $m = 4$ is exactly 1, see Fig. F.11. This implies that a direct numerical numerical integration with $m = 3$ (or $m = 4$) is sufficient to simulate the dynamics of the Bose-Hubbard model at the parameter regime of interest, because at this point including more energy levels

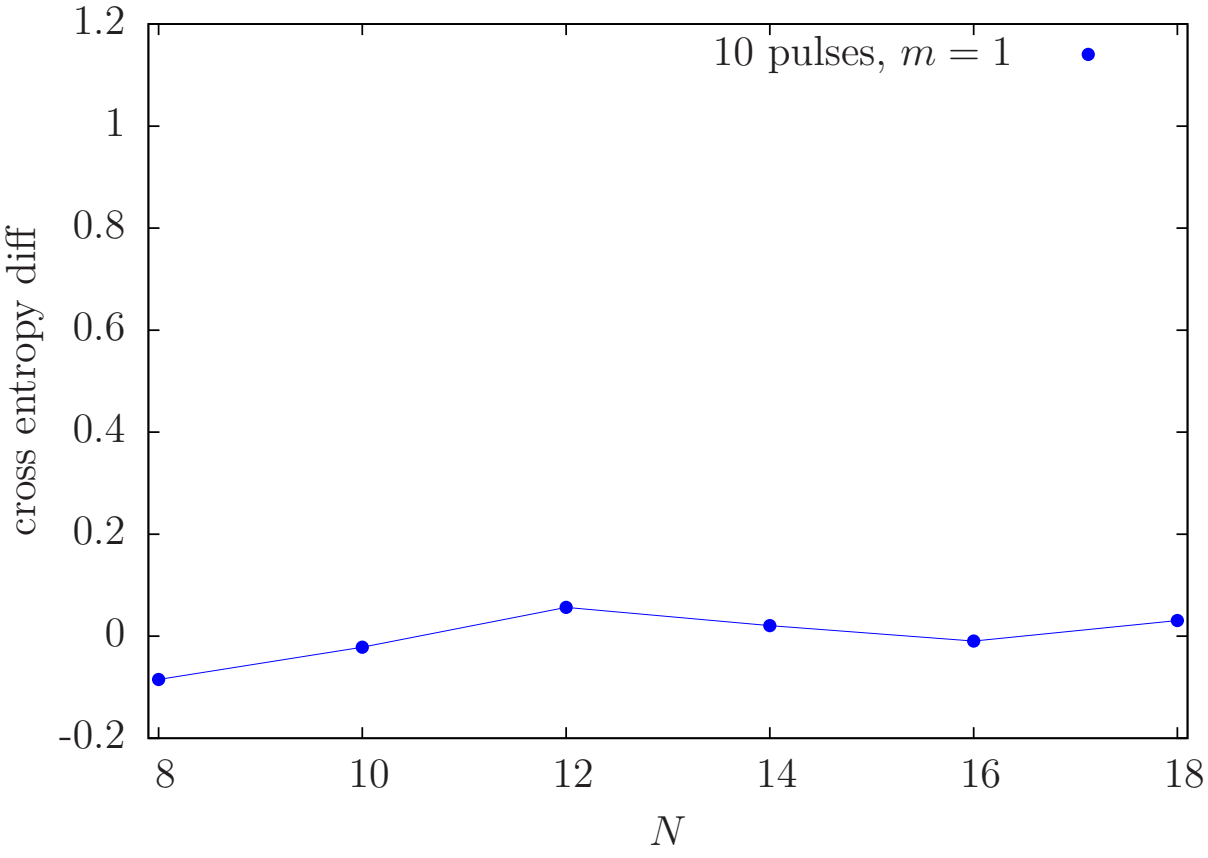

Figure F.12: We can not simulate the system with plain qubits.

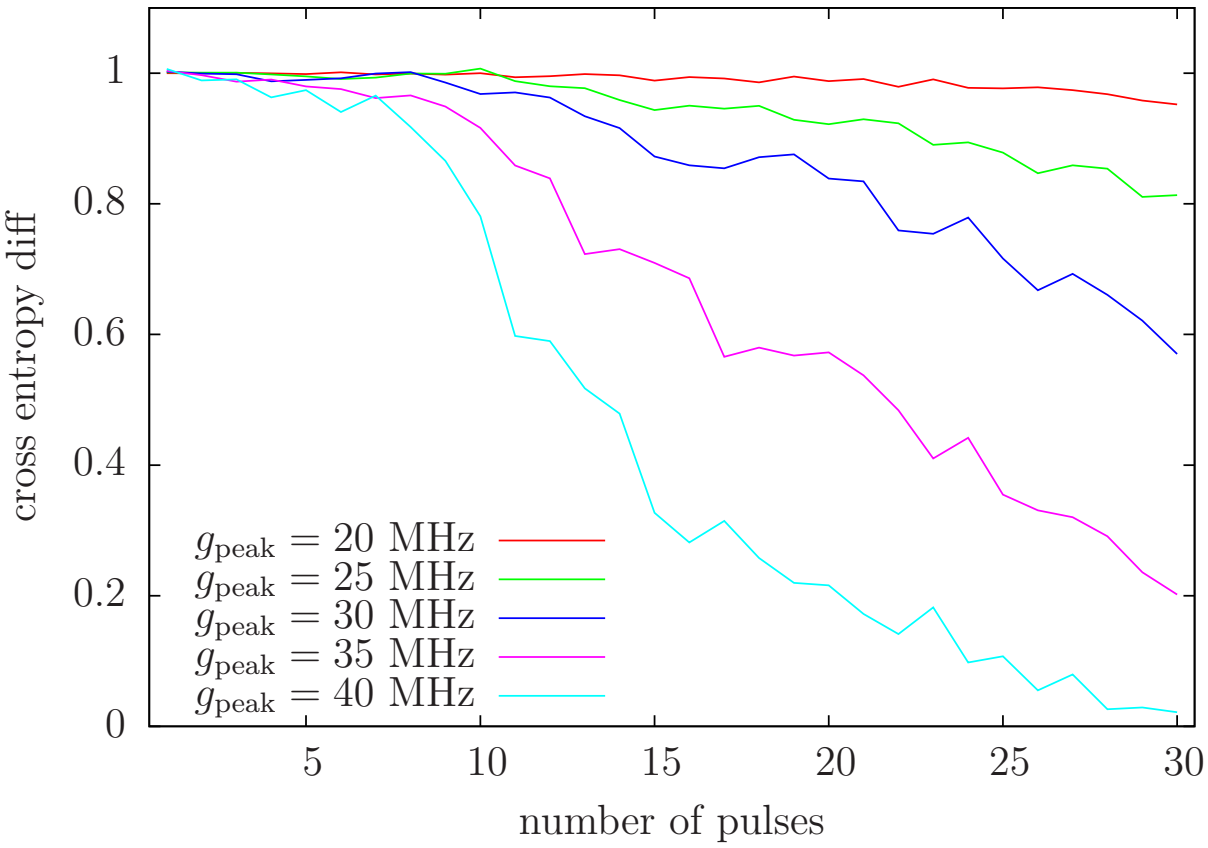

Figure F.13: Cross entropy difference with three level systems for 16 gmons, $m = 2$ and pulse duration $T_{\text{pulse}} = 20.5 \pm 4.5$ ns (the duration is chosen uniformly at random in the interval of 16 to 25 ns).

does not translate in any difference in the resulting state. Our second observation is that a direct truncation to the $m = 1$ subspace is not a valid approximation, resulting in a fidelity (cross entropy difference) ~ 0, see Fig. F.12. This is to be expected, because this approximation can be mapped to free fermions, which does not result in chaotic dynamics (see Secs. F.7.1 and F.7.3). Figure F.13 shows the cross entropy difference (fidelity) for 16 gmons as a function of the number of pulses for representative parameters with a truncation to the second excited state $|2\rangle$ of each gmon, $m = 2$. We see that the fidelity decreases as g increases, because higher energy states become increasingly important (see also Fig. F.17). Nevertheless, the decay of fidelity is likely not worse than the experimental fidelity. Therefore, this is a valid simulation method for the purposes of comparing the cost of a classical simulation against the experimental implementation.

The effective Hilbert space size of the truncation to the second excited state $|2\rangle$ of each gmon, $m = 2$, is 3^m, if we do not take into account boson number conservation. Taking into account boson number conservation, we calculate the resulting Hilbert space exactly, at half filling, for a number of gmons N between $N = 20$ and $N = 40$, which is the regime of interest for a future comparison between experiment and classical algorithms. We fit the resulting curve, an obtain a good fitting for the effective Hilbert space dimension $D \sim 2.4^N/0.14$ (see also Fig. F.21).

Estimate of Runge-Kutta integration steps

We now provide an estimate for the number of fourth order Runge-Kutta integration steps required for a numerical simulation. At the end of the integration, we project the

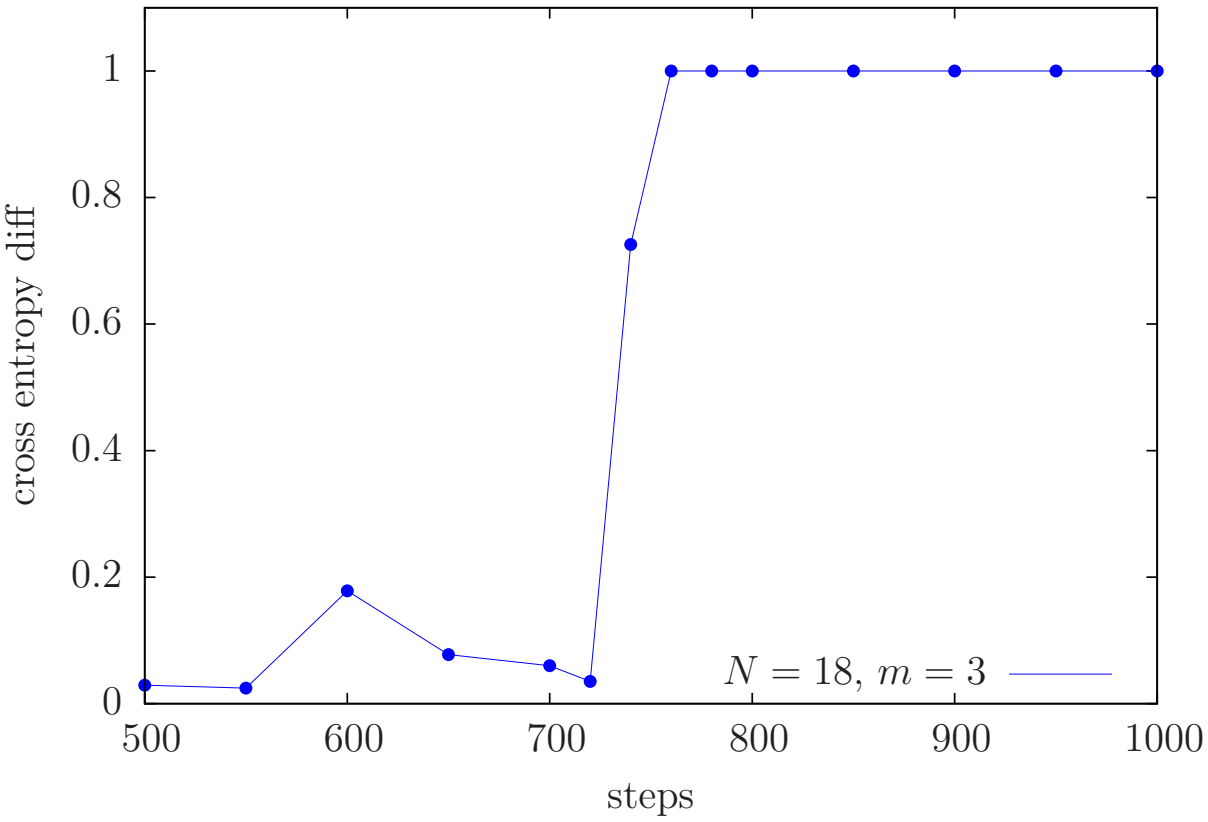

Figure F.14: Cross entropy as a function of the number of Runge-Kutta steps for 18 gmons, 5 pulses and $T_{\text{pulse}} = 30 \pm 10$ ns.

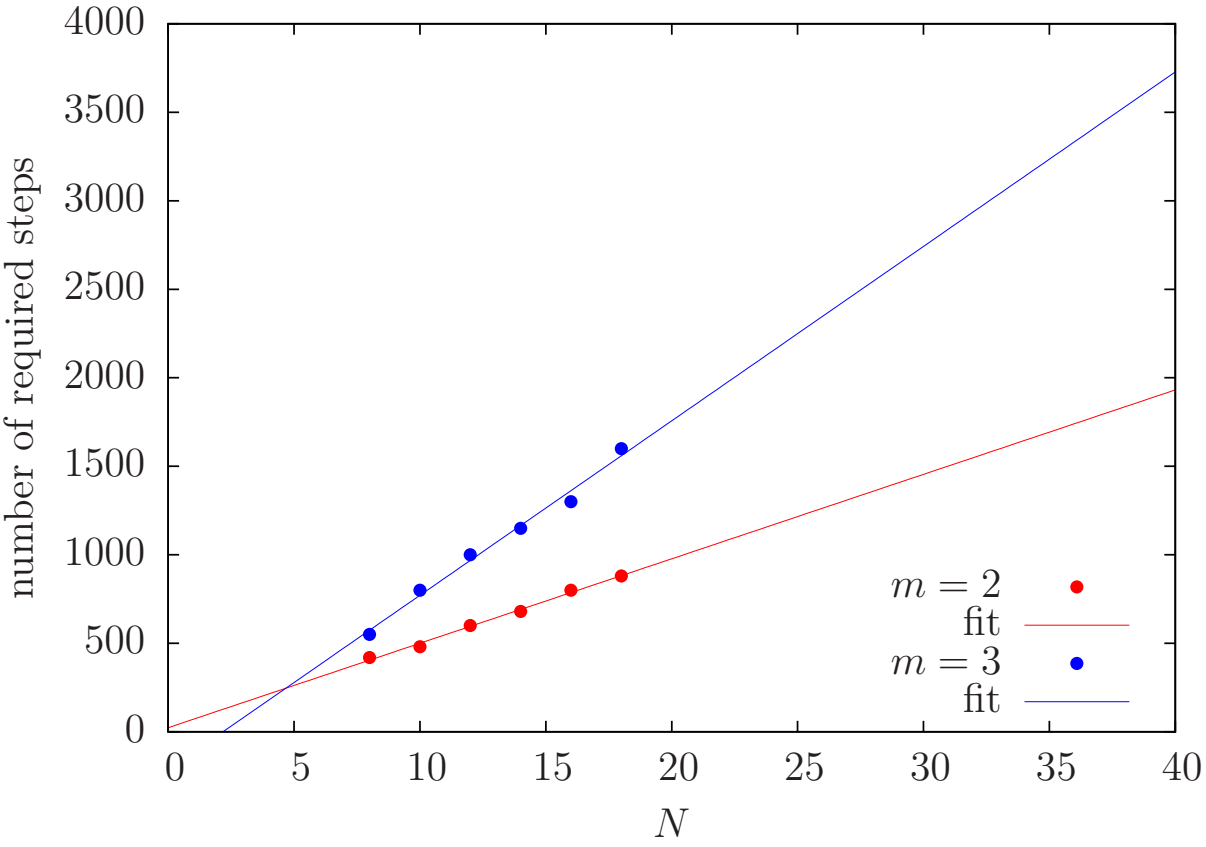

Figure F.15: Required number of Runge-Kutta integration steps for 10 pulses and $T_{\text{pulse}} = 30 \pm 10$ ns.

resulting state into the qubit subspace expanded by the states $\{|0\rangle, |1\rangle\}$ of each gmon (the first band, see Sec. F.7.2). It can be seen that we can tolerate large errors in the populations of states with higher excitation numbers (which are thrown away in the final measurement), while the populations in the qubit subspace are still accurate.

We observe a sensitive behavior of the numerical integration error in the qubit subspace for increasing number of integration steps. Figure F.14 shows the cross entropy for 18 gmons and 5 pulses ($T_{\text{pulse}} = 30 \pm 10$ ns) as a function of the number of integration steps. We see that if the number of steps is less than ~ 700 the numerical integration is completely inadequate. At the same time, we don't obtain any benefit using more than ~ 800 integration steps.

This steep behavior is used to estimate the required number of integration steps for increasing number of gmons N, instead of using an adaptive stepsize Runge-Kutta scheme. Figure F.15 gives estimates for 10 pulses ($T_{\text{pulse}} = 30 \pm 10$ ns) as a function of N. We show estimates of numerical integrations truncating at the second excited state $|2\rangle$ ($m = 2$), and the third excited state $|3\rangle$ ($m = 3$).

Band structure

In the limit $g \ll \eta$ of the swapping parameter g much smaller than the non-linearity η, the spectrum is separated by bands characterized by the occupation number of the different gmons, see Fig. F.16. The first band is the qubit subspace, with states composed by superpositions of Fock states where each gmon is either in the ground state $|0\rangle$ of the first excited state $|1\rangle$. At half filling, and using the fact that the Bose-Hubbard model

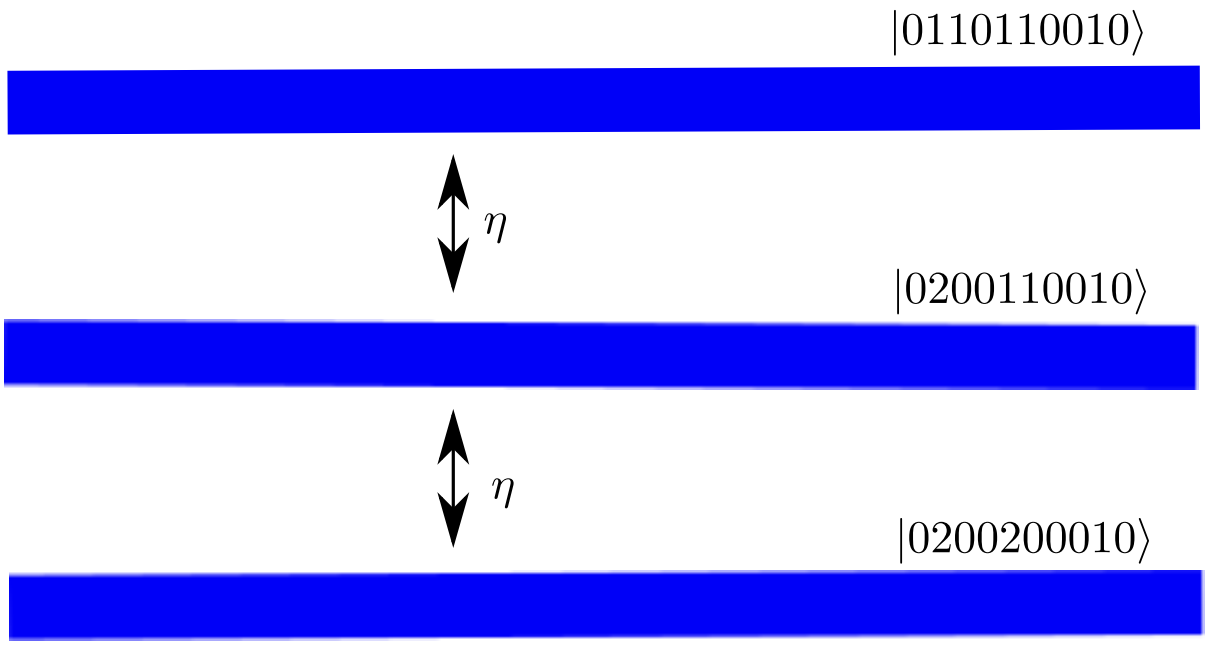

Figure F.16: Symbolic representation of state bands, separated by the non-linearity η.

conserves the total number of bosons, the Hilbert space dimension of this band is

$$\binom{N}{N/2} \sim \frac{2^N}{\sqrt{\pi N/2}} \,. \tag{F.19}$$

The next band, separated by an energy η, contains states composed by superpositions of Fock states where exactly one gmon is in the second excited state or "doublon" $|2\rangle$. At half filling, its Hilbert space dimension is given by the multinomial coefficient

$$\binom{N}{N/2-1, N/2-2, 1} \,. \tag{F.20}$$

The next band after that has states with exactly two gmons in the "doublon" state $|2\rangle$, etc...

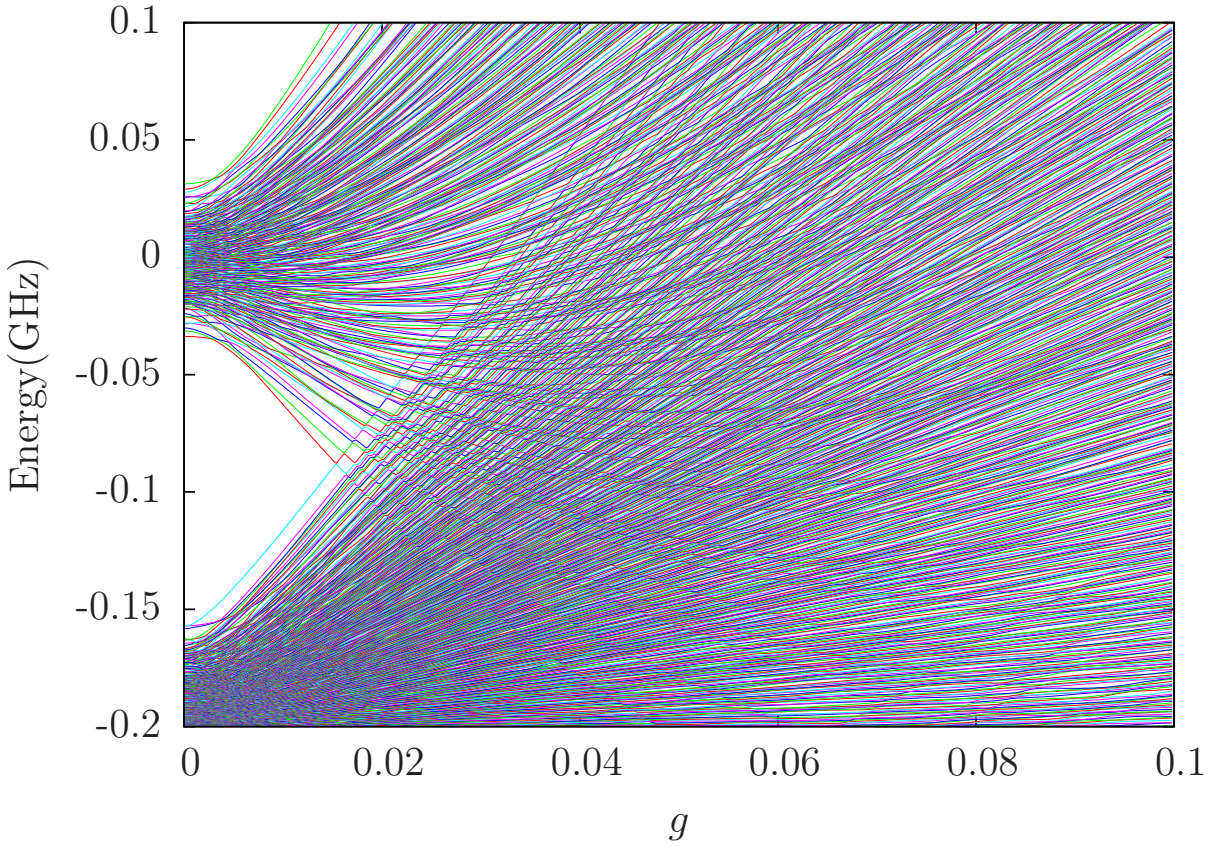

Figure F.17: Exact diagonalization with 10 gmons.

Our next observation is that the bands overlap for increasing g. Figure F.17 shows the exact spectrum for the Bose-Hubbard model and increasing g. We see that at $g \sim 20$ MHz the bands start to overlap. One implication for estimating the cost of classical simulations is that perturbation theory in the qubit subspace, such as the Schrieffer-Wolff transformation, is not expected to work. This method is an expansion in the perturbation parameter g/η, and assumes that the bands remain well separated.

Simulation with a fixed number of bands

In Sec. F.7.2 we have seen that for a direct numerical simulation it suffices to truncate each gmon to the second excited state $|2\rangle$ ($m = 2$ truncation in our notation). Using the band structure explained in the previous section, we now outline how an approximate classical simulation can be carried out more efficiently. Given that the Hilbert space in the limit of $g \ll \eta$ is divided into bands, we truncate the Hilbert space to obtain an effective Hilbert space with a fixed number of bands. We denote the resulting truncations in the notation $[d, t]$, where d is the maximun number of doublons (double excited states $|2\rangle$) allowed, and t is the maximun number of "triplons" (triple excited states $|3\rangle$) allowed. More explicitly, the effective Hilbert space $[1, 0]$ includes the first two bands: the qubit subspace band, and the band with exactly one doublon among all the gmons. The total dimension of this effective Hilbert space is

$$\binom{N}{N/2} + \binom{N}{N/2-1, N/2-2, 1} . \tag{F.21}$$

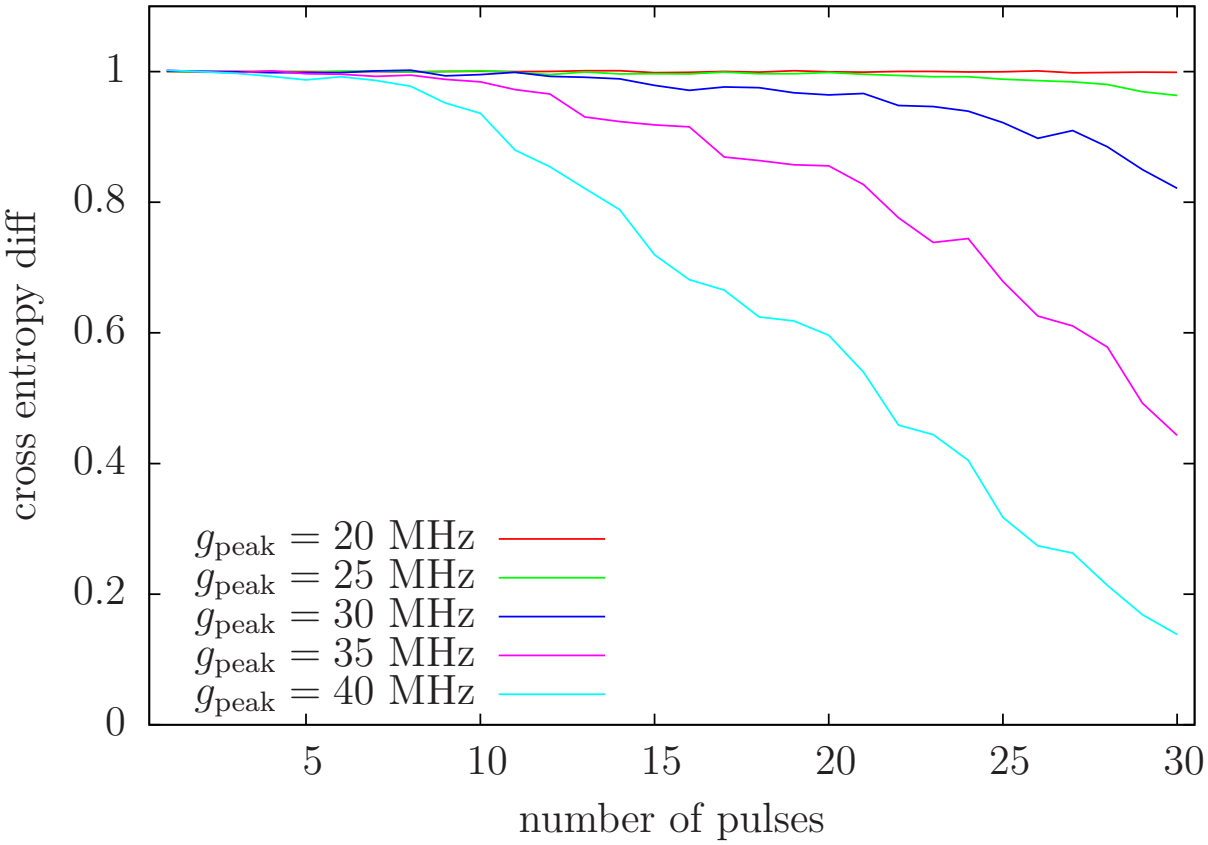

Figure F.18: Cross entropy difference with four bands for 16 gmons, the effective Hilbert space $[2, 1]$ (four bands) and $T_{\text{pulse}} = 20.5 \pm 4.5$ ns.

Analogously, the effective Hilbert space $[2, 0]$ includes the first three bands: the qubit subspace band, the band with exactly one doublon among all the gmons, and the band with exactly two doublons among all the gmons. We will also consider the effective Hilbert space $[2, 1]$, which includes four bands: the bands in the $[2, 0]$ Hilbert space, and the band with exactly one triplon among all the gmons.

Figure F.18 shows the cross entropy difference where we use the $[2, 1]$ effective Hilbert space. As in Sec. F.7.2, we calculate the cross entropy difference comparing with the $m = 4$ simulation which, as we have seen, is an accurate simulation. We observe that

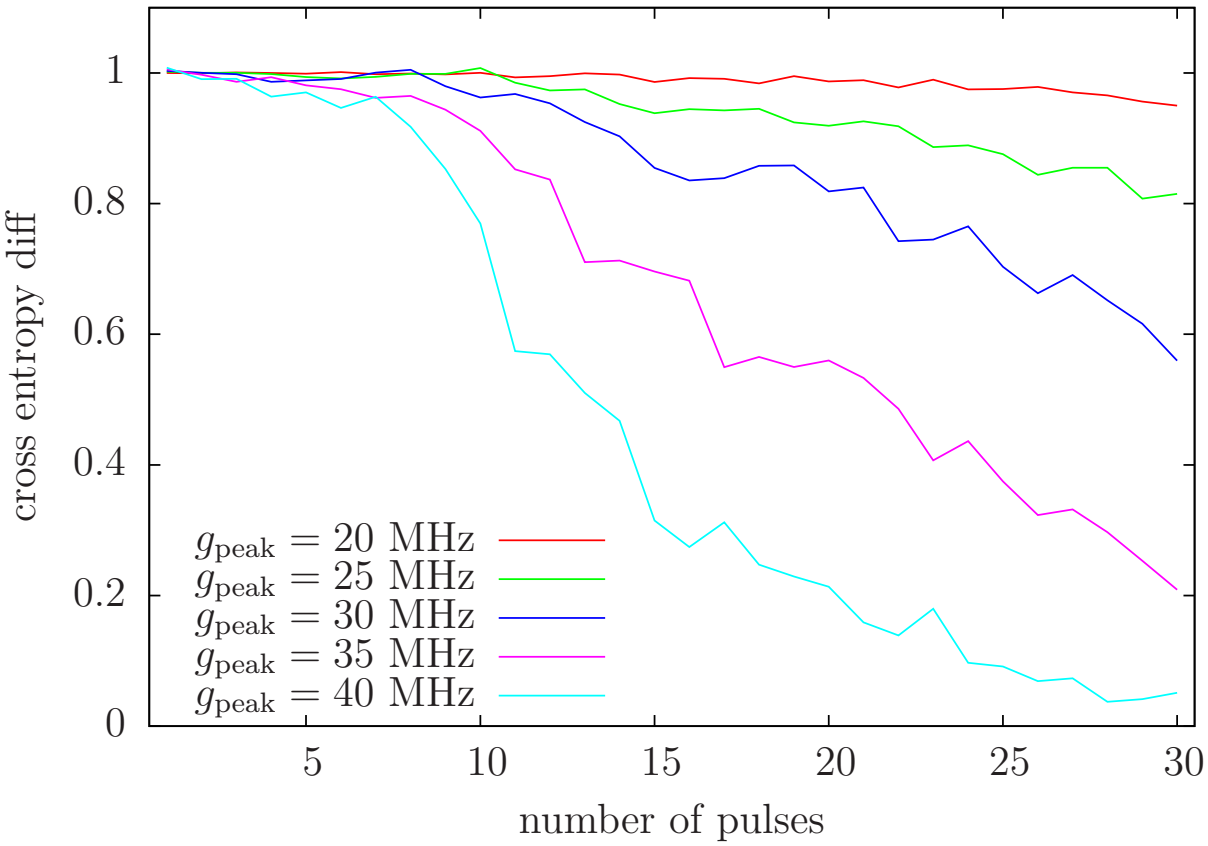

Figure F.19: Cross entropy difference with three bands for 16 gmons, the effective Hilbert space $[2, 0]$ (three bands) and $T_{\text{pulse}} = 20.5 \pm 4.5$ ns.

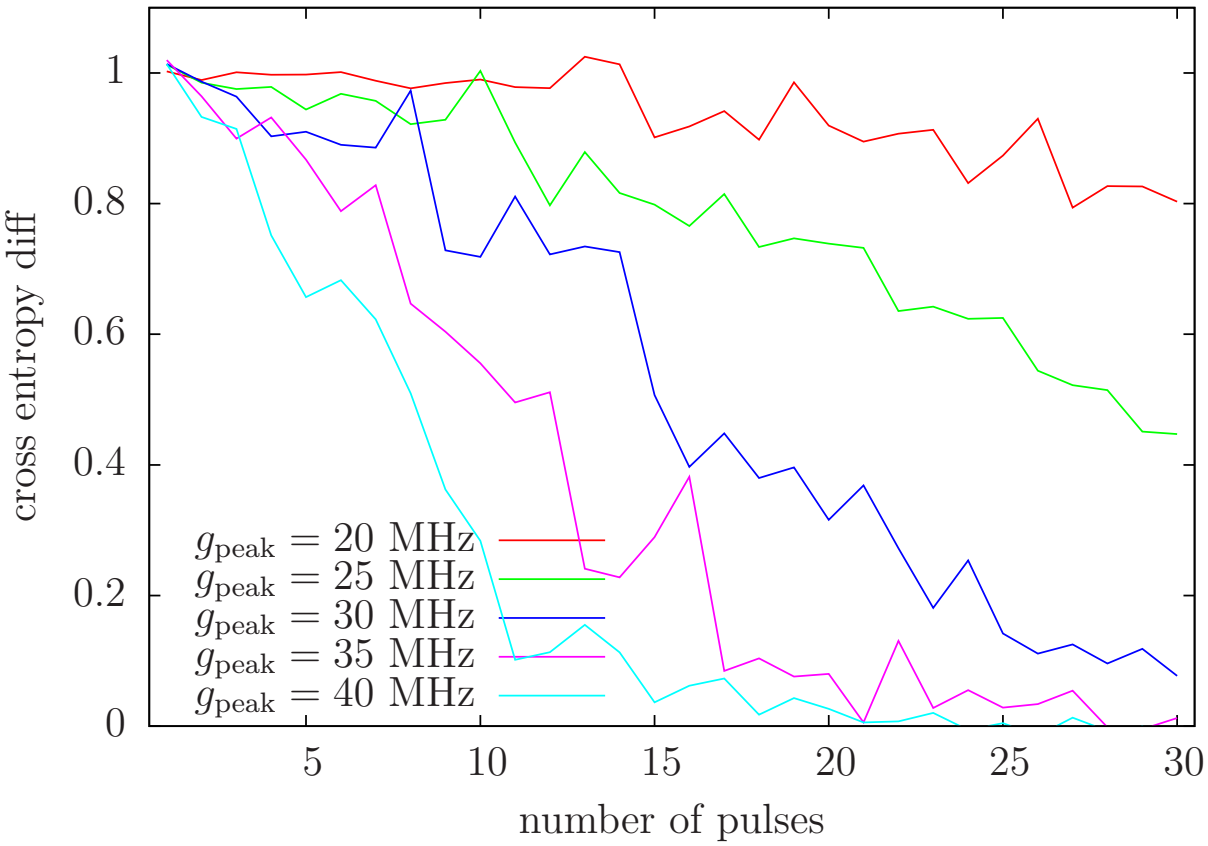

Figure F.20: Cross entropy difference with two band for 16 gmons, the effective Hilbert space $[1, 0]$ (two bands) and $T_{\text{pulse}} = 20.5 \pm 4.5$ ns.

the numerical error resulting from the truncation is less than the expected experimental error, even for fairly large maximum g and a substantial number of pulses. Therefore, this is a valid numerical method for the purpose of comparing the classical cost of simulation to a future experiment. Figure F.19 shows the cross entropy difference where we use the $[2, 0]$ effective Hilbert space. Although the errors are bigger than in the $[2, 1]$ effective Hilbert space, this remains a valid numerical method. Finally, Fig. F.20 shows the cross entropy difference where we use the $[1, 0]$ effective Hilbert space. The numerical error is in this case larger, but probably still comparable to the expected experimental errors.

Memory and time-estimate for simulations.

We now provide estimates of the memory and computational time required for an approximate classical numerical simulation from the discussion given above. Figure F.21 plots $\log_2(\mathrm{D})$, where D is the dimension of the effective Hilbert space, for increasing number of gmons N. We use this metric because, if we were studying a fully chaotic evolution in a Hilbert space composed of qubits, then $\log_2(\mathrm{D})$ would be the number of qubits. We plot the dimension of the effective space using two bands (the $[1, 0]$ subspace in the notation of Sec. F.7.2), using three bands (the $[2, 0]$ subspace), and using four bands (the $[2, 1]$ subspace). We see that for the number of gmons N experimentally relevant in the near future, both curves are well approximated by exponentials. The effective dimension is then $D \sim 2^N$ for two bands (the $[1, 0]$ subspace) $D \sim 2.1^N$ for three bands (the $[2, 0]$ subspace), and $D \sim 2.3^N$ for four bands (the $[2, 1]$ subspace). In the same figure we plot horizontal lines corresponding to 16 GB (and 1 TB) of memory required to store a

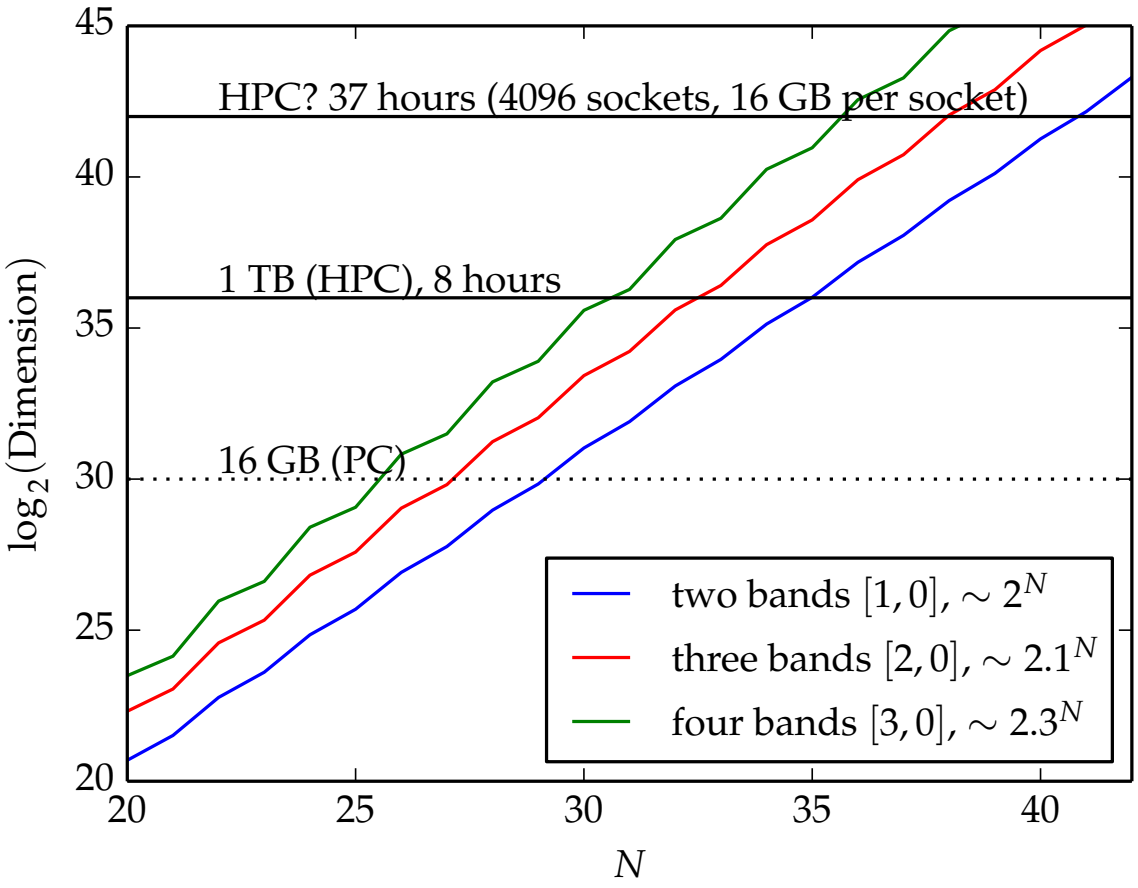

Figure F.21: Estimates of memory and computational time for a numerical simulation using fourth order Runge-Kutta and an effective Hilbert space truncated to two bands (blue) and three bands (red).

quantum state with $\log_2(D)$ qubits, using a double precision complex number to store each amplitude, so that the memory for a quantum state is $D \times 16$ bytes.

Estimating the corresponding run time is more subtle. For large scale simulations in classical supercomputers, the run time is mostly constrained by the network bandwidth between the different nodes [28, 69]. If we store the quantum state in memory, distributed among multiple nodes in a supercomputer, a single integration step in fourth order Runge-Kutta would require approximately 5 swaps between nodes (10 vector communications, taking into account that the vector amplitudes need to go out and into each node). Therefore, we expect that the total computational cost would be bandwidth bound. We label in Fig. F.21 two horizontal lines corresponding to prelimnary estimates of 8 hours and 37 hours of required communication time. To arrive at this estimates, we assume 5 memory swaps per Runge-Kutta step, and 1000 Runge-Kutta steps. For 1 TB of memory per state, we assume 64 sockets (nodes) and an effective 6 GB/s network bandwidth per socket. For $D = 2^{42}$, corresponding to 70 TB of memory per state, we assume 4096 sockets and an effective bandwidth of 1.2 GB/s per socket. These estimates are taken from the values reported in Refs. [28, 69].

F.7.3 Signatures of chaos

Quantum loss of memory

The wave functions and the spectrum of the uniform Bose-Hubbard model can be obtained via Bethe-Ansatz. This model has a regular spectrum characterized by conserved

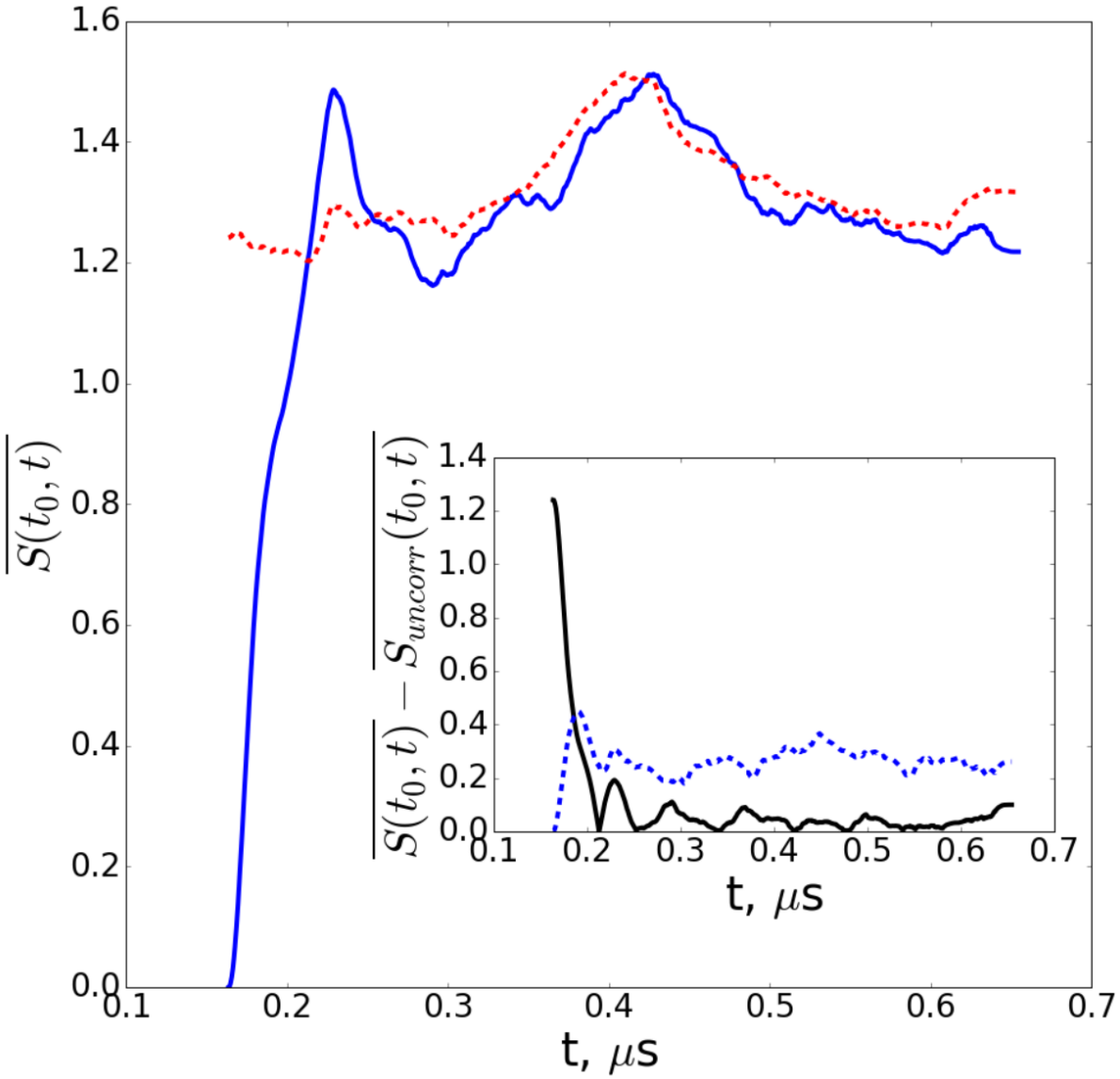

Figure F.22: Time-cross-entropy averaged over random detuning δ_i and pulse shape. The parameters in the plot are $N = 10$, $\delta = \pm 5$MHz, 22.4MHz $\leq \max\{g\} \leq$ 38.4MHz, with variable pulse length $0.042\mu s \leq T_{\text{pulse}} \leq 0.072\mu s$. Inset shows the deviation of the time-cross-entropy from the limit of uncorrelated time points, solid black line. The dashed blue line shows the root mean square of the time-cross-entropy over the ensemble of disorder realizations.

Bethe numbers [133]. In presence of disorder Bethe numbers are no longer integrals of motion and the system demonstrates quantum chaotic dynamics. As a result of chaotic dynamics the wave function amplitude spreads uniformly over the available Hilbert space. A strong indication of chaos is the Porter-Thomas wave function statistics characteristic of Haar measure. In practice the Porter-Thomas distribution is approached only approximately in the course of the shallow depth evolution (see Sec. F.7.3) and therefore it is important to check the consistency of the circuit dynamics with quantum chaos more carefully. Another characteristic of chaos is the rapid loss of memory of the initial state as a function of time. We characterize this phenomenon using statistics of the wave function over time. Consider the likelihood to observe bitstrings $z_1, ..., z_m$ at time t in the course of the evolution,

$$-\mathrm{Log}\left(\mathcal{L}_m(t)\right) \equiv -\mathrm{Log}\left(\prod_{i=1}^{m} p_{z_i}(t)\right) \tag{F.22}$$

$$= -\sum_{i=1}^{m} \mathrm{Log}\left(p_{z_i}(t)\right). \tag{F.23}$$

The likelihood has Gaussian distribution centered at $\overline{\mathrm{Log}\mathcal{L}_m} \approx m\sum_z p_z \log\left(p_z\right)$ with width of order $\sqrt{m}$. The loss of memory can be characterized by the ratio of likelihoods obtained using statistics at two different points in time,

$$S\left(t_0, t\right) \equiv -\lim_{m\to\infty} \frac{1}{m} \mathrm{Log}\left(\frac{\mathcal{L}_m(t)}{\mathcal{L}_m\left(t_0\right)}\right) \tag{F.24}$$

$$\approx -\sum_z p_z\left(t_0\right) \mathrm{Log}\left(\frac{p_z(t)}{p_z\left(t_0\right)}\right);. \tag{F.25}$$

This is the Kullback-Leibler divergence between two different times. The advantage of this characteristic is that it is directly measurable in our experiment and it quickly converges to its average for a sufficiently large number of measurements m. For perfectly correlated statistics as $t \to t_0$ the time-cross-entropy vanishes, $S(t_0, t_0) = 0$. In a chaotic system we expect the statistics of the wave function at sufficiently different moments in time to be fully uncorrelated,

$$\overline{S\left(t_0, t \gg t_0\right)} \approx \overline{S_{\text{uncorr}}}\left(t_0, t\right) \equiv -\sum_z \left(\overline{p_z\left(t_0\right)}\ \overline{\text{Log}\left(p_z(t)\right)} - \overline{p_z\left(t_0\right) \text{Log}\left(p_z(t_0)\right)}\right),$$

Fig. F.22 shows the cross-entropy $S(t_0, t)$ between t_0, taken after the first two pulses, and a later time t. $S(t_0, t)$ quickly deviates from zero (fully correlated) and approaches the uncorrelated value.

Entanglement spread in the driven system

Quantum entanglement is an important, albeit not definitive [104], metric of classical simulability of a quantum system. This is especially true in 1D as MPS and DMRG type algorithms have a computational cost exponential in the entanglement entropy. We analyze the bipartite entanglement entropy of a half chain,

$$S_{N/2} \equiv \text{Tr}\left\{\hat{\rho}_{N/2} \text{Log}\left(\hat{\rho}_{N/2}\right)\right\}, \tag{F.26}$$

where $\hat{\rho}_{N/2}$ is the reduced density matrix. A random state from the Haar measure is expected to demonstrate volume law entanglement. In our experimental protocol we need to make sure the evolution time is long enough for the entanglement to achieve the regime of volume law scaling. The character of the entanglement spread depends on the relative strength of disorder and the spectral characteristics of the drive. At low disorder entanglement spreads ballistically as expected in the ergodic phase [75], even in presence of diffusive particle transport [99]. Fig. F.23 shows the entanglement entropy $S_{N/2}$ as a function of time for different system sizes, for a pulse sequence similar to the one used in the experiment. The velocity of entanglement spread appears to be independent of the system size suggesting that for the specific drive protocol and the initial state chosen the dynamics is similar to particle transport in a spin model.

At stronger disorder there is a crossover to the regime of sublinear spread of entanglement. In general, a periodically driven system undergoes a transition to the Many-Body localized phase [30], a regime in which it does not absorb energy. In contrast, in our protocol the drive consists of a wide range of harmonics and therefore we do not expect a many-body localized phase and the system continues to absorb energy. The growth of entanglement entropy however slows down dramatically at strong disorder, see Fig. F.24, likely due to the effect of rare regions with strong fluctuations of disorder potential which have a significant effect on entanglement transport in 1D [5, 134].

Convergence to Porter-Thomas

We now study the convergence to the Porter-Thoomas (exponential) distribution. Figure F.25 shows the histogram of the output probabilities $p = \{p_z\}$ for 18 gmons after 10 pulses, at half filling. We project the output state in the qubit subspace. The Porter-Thomas distribution is the exponential function, $f(pN_{\text{states}}) = e^{-pN_{\text{states}}}$, where N_{states} is the dimension of the qubit subspace at half filling, $N_{\text{states}} = \binom{N}{N/2}$. We see a good approximation of the numerical output distribution to Porter-Thomas. Figure F.26 shows the histogram of the output probabilities $p = \{p_z\}$ for 18 gmons after 10 pulses, but with the evolution carried out using the approximation to free fermions, as explained in Sec. F.7.1. We see that in this case the distribution does not approximate the Porter-Thomas distribution, and is not chaotic (see Sec. F.7.3).

We depict in Fig. F.27 the entropy of the output distribution with $N = 12$ gmons as a function of the number of pulses and different maximun values of g for the g-pulses. We see that it approaches the Porter-Thomas distribution entropy (black line) as the number of pulses increases. Figure F.28 shows the entropy of the output distribution with increasing number of pulses using the approximation to free fermions with $N = 16$ gmons. We see again that in this case the entropy does not converge to the Porter-Thomas entropy.

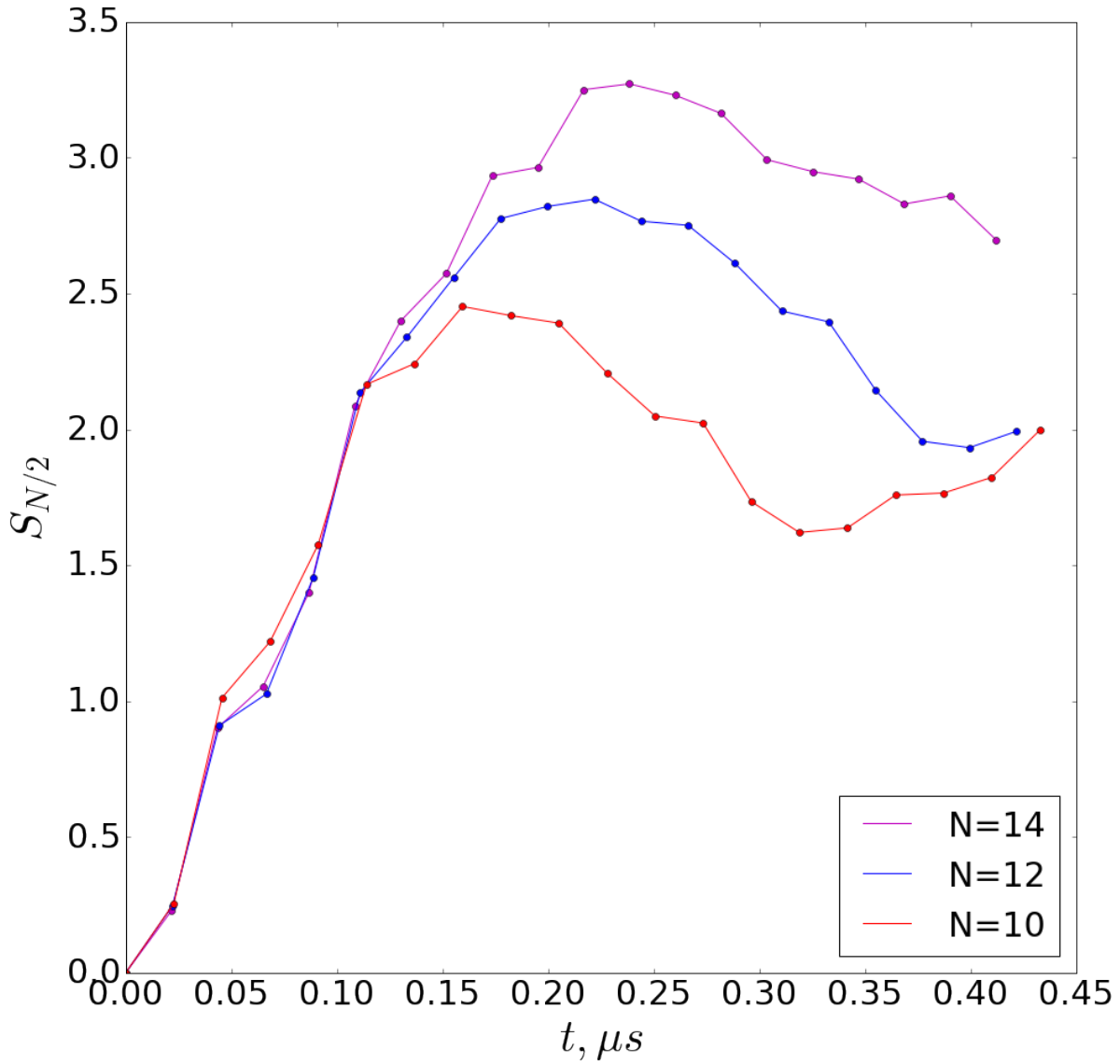

Figure F.23: Average entanglement entropy of the half-chain as a function of the system size. Parameters are $N = 10$, $\delta = \pm 5$MHz, $22.4\text{MHz} \leq \max\{g\} \leq 38.4\text{MHz}$, pulse length $0.042\mu s \leq T_{\text{pulse}} \leq 0.072\mu s$.

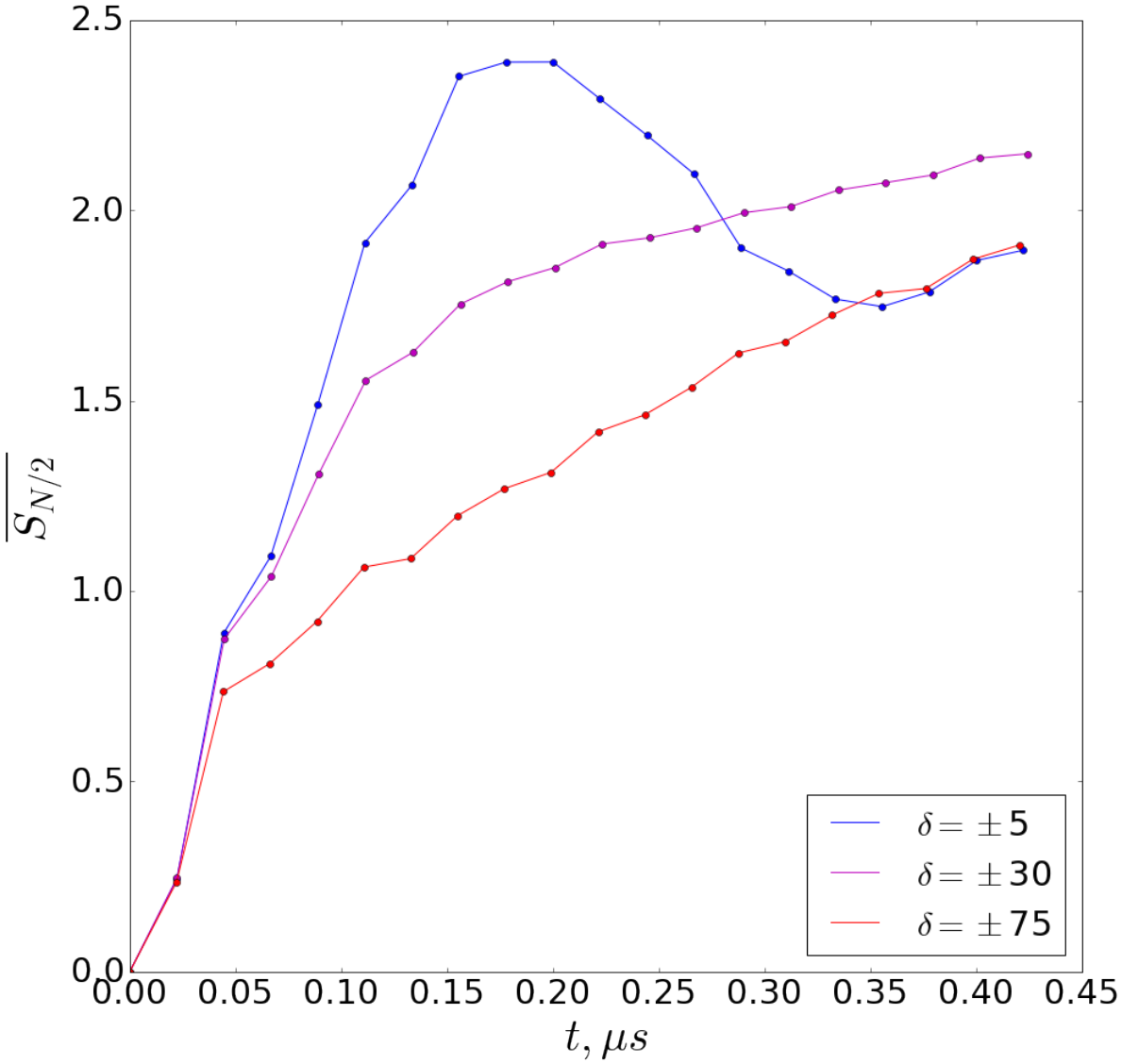

Figure F.24: Disorder strength. Same parameters as Fig. F.23.

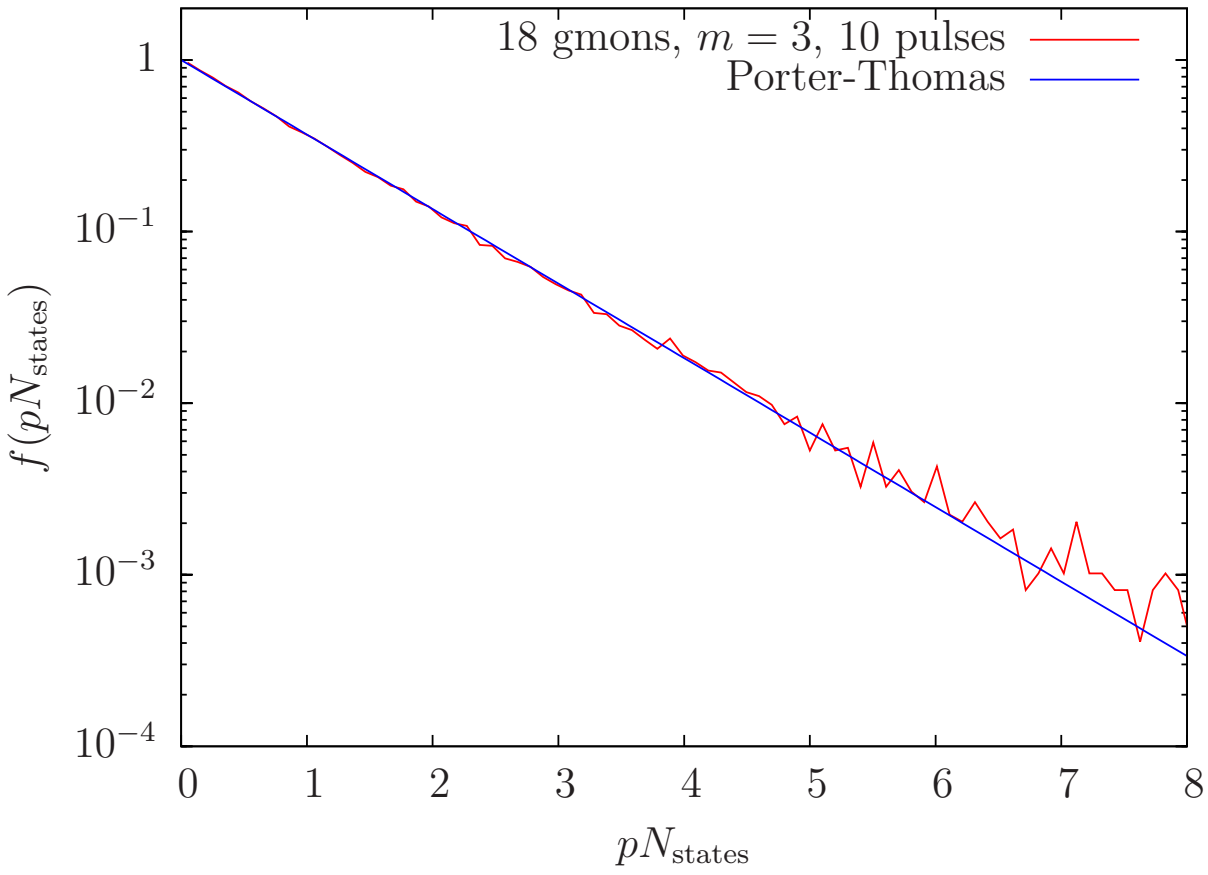

Figure F.25: Histogram of output probabilities for 18 gmons and 10 pulses of duration $T_{\text{pulse}} = 30 \pm 10$.

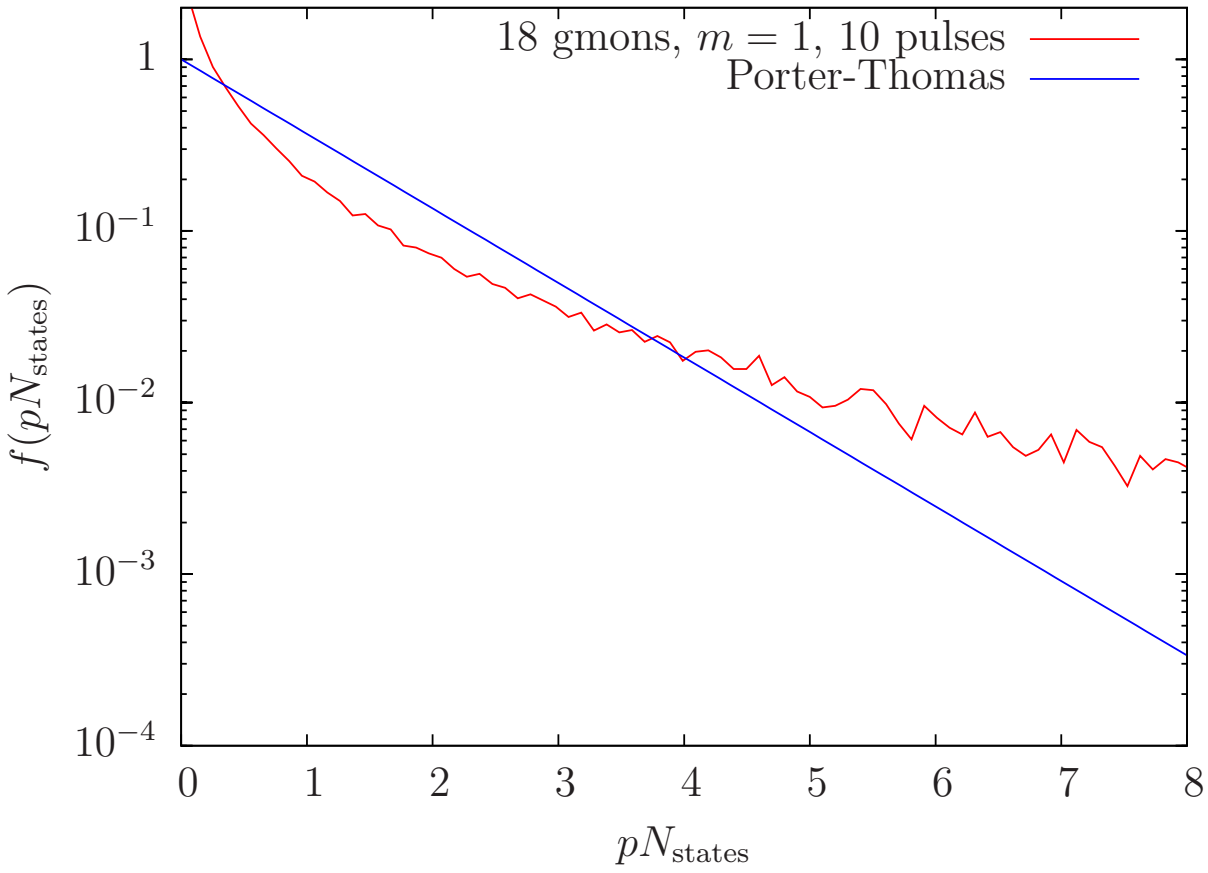

Figure F.26: Histogram of output probabilities for 18 gmons, using plain qubits, and 10 pulses.

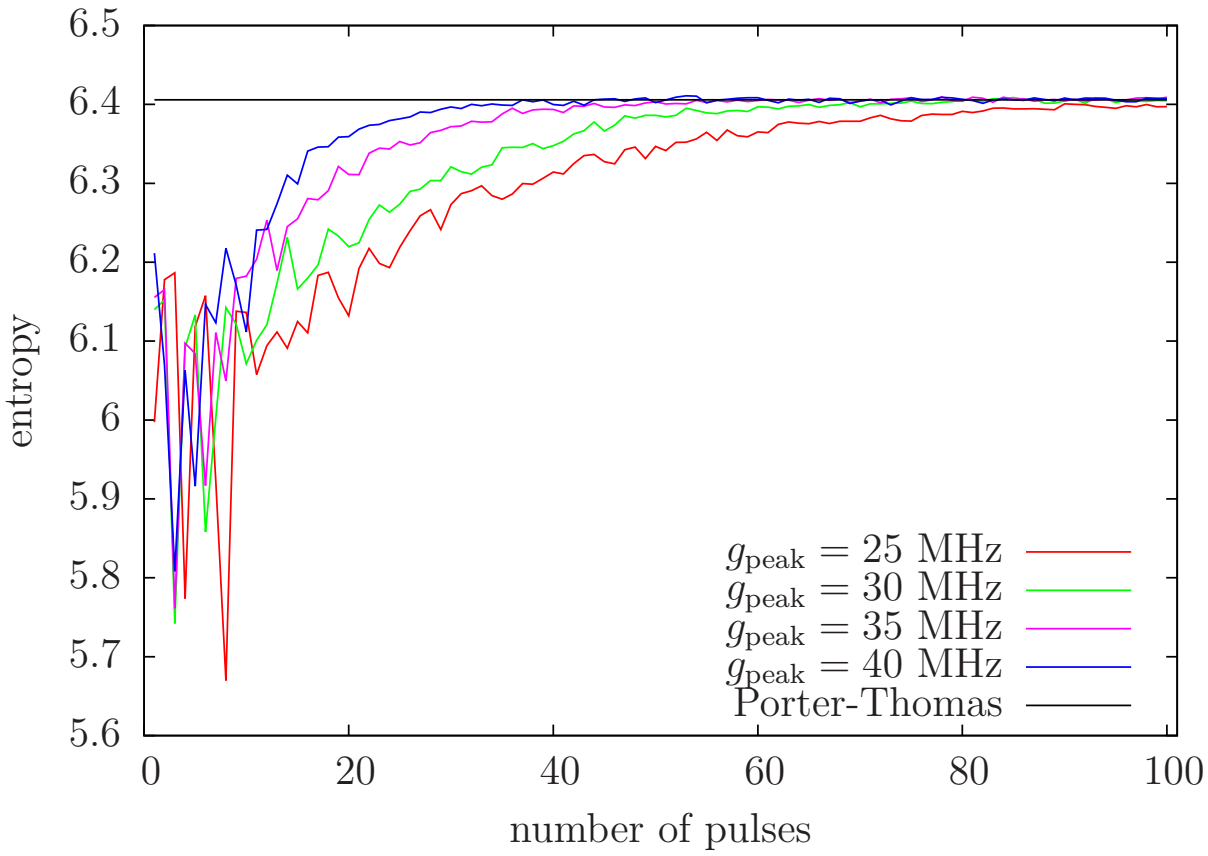

Figure F.27: The entropy of the output distribution approaches Porter-Thomas with increasing number of pulses for 12 gmons, $m = 3$ and $T_{\text{pulse}} = 20.5 \pm 4.5$ ns.

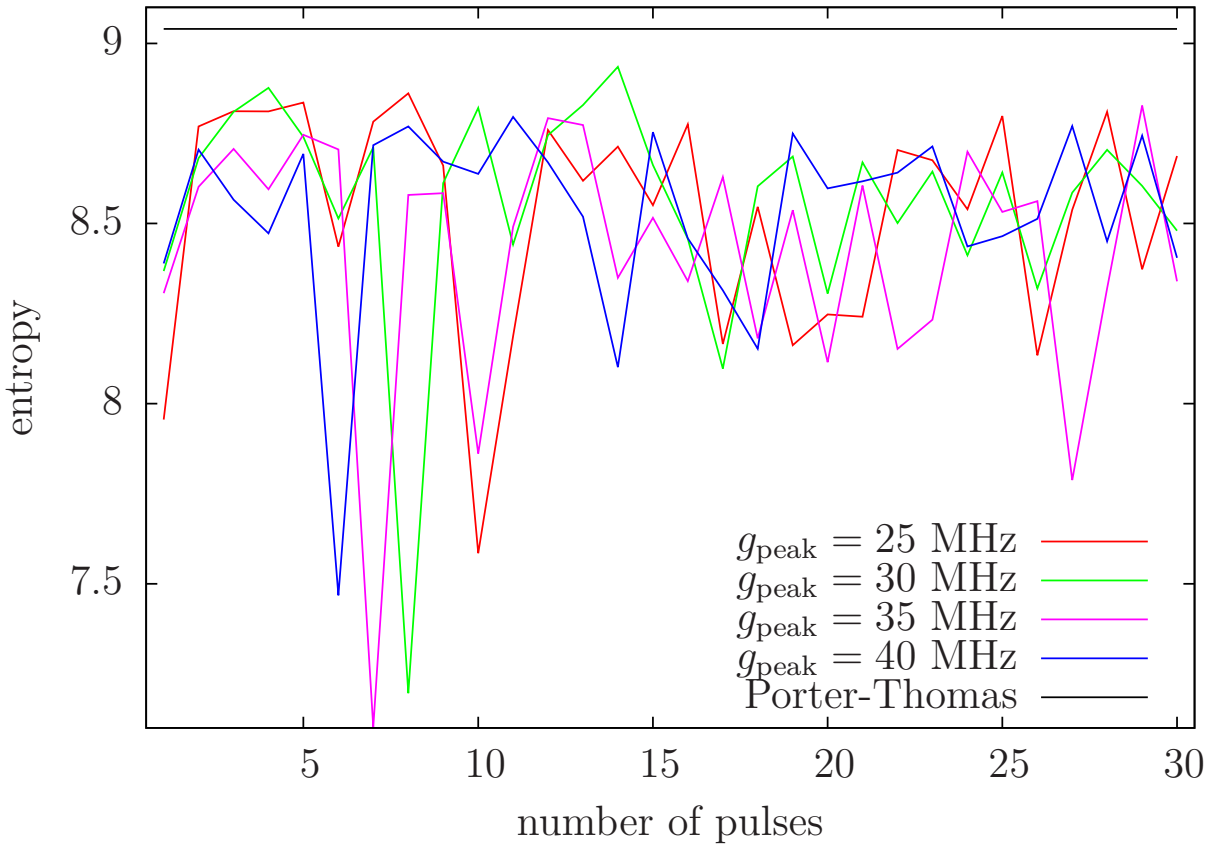

Figure F.28: The entropy of the output distribution with plain qubits does not approach Porter-Thomas with increasing number of pulses for 16 gmons, $m = 1$ and $T_{\text{pulse}} = 20.5 \pm 4.5$ ns.

Bibliography

[1] S. Aaronson and A. Arkhipov. The computational complexity of linear optics. In *Proceedings of the forty-third annual ACM symposium on Theory of computing*, pages 333–342. ACM, 2011.

[2] S. Aaronson and L. Chen. Complexity-Theoretic Foundations of Quantum Supremacy Experiments. *arXiv:1612.05903*, 2016.

[3] E. Abrahams. 50 years of anderson localization. 2010.

[4] E. Abrahams, P. W. Anderson, D. C. Licciardello, and T. V. Ramakrishnan. Scaling theory of localization: Absence of quantum diffusion in two dimensions. *Phys. Rev. Lett.*, 42:673–676, Mar 1979.

[5] K. Agarwal, E. Altman, E. Demler, S. Gopalakrishnan, D. Huse, and M. Knap. Rare-region effects and dynamics near the many-body localization transition. *Annalen der Physik*, pages 1600326–n/a, 2017.

[6] M. Aidelsburger, M. Atala, M. Lohse, J. T. Barreiro, B. Paredes, and I. Bloch. Realization of the hofstadter hamiltonian with ultracold atoms in optical lattices. *Phys. Rev. Lett.*, 111:185301, Oct 2013.

[7] M. Allman, F. Altomare, J. Whittaker, K. Cicak, D. Li, A. Sirois, J. Strong, J. Teufel, and R. Simmonds. rf-squid-mediated coherent tunable coupling between a superconducting phase qubit and a lumped-element resonator. *Phys. Rev. Lett.*, 104(17):177004–, April 2010.

[8] E. Altman and R. Vosk. Universal dynamics and renormalization in many-body-localized systems. *Annual Review of Condensed Matter Physics*, 6:383, 2015.

[9] P. W. Anderson. More is different. *Science*, 177:393–396, August 1972.

[10] A. Aspuru-Guzik and P. Walther. Photonic quantum simulators. *Nature Physics*, 8:285–291, April 2012.

[11] M Atala, M. Aidelsburger, J. T. Barreiro, D. Abanin, T. Kitagawa, E. Demler, and I. Bloch. Direct measurement of the zak phase in topological bloch bands. *Nature Physics*, 9:795–800, 2013.

[12] M. Atala, M. Aidelsburger, M. Lohse, J. Barreiro, B. Paredes, and I. Bloch. Observation of chiral currents with ultracold atoms in bosonic ladders. *Nature Physics*, 10:588–593, 2014.

[13] Y. Y. Atas, E. Bogomolny, O. Giraud, and G. Roux. Distribution of the ratio of consecutive level spacings in random matrix ensembles. *Phys. Rev. Lett.*, 110:084101, Feb 2013.

[14] D. Averin, K. Xu, Y. Zhong, C. Song, H. Wang, and S. Han. Suppression of dephasing by qubit motion in superconducting circuits. *Physical review letters*, 116(1):010501, 2016.

[15] Y. Bahri, R. Vosk, E. Altman, and A. Vishwanath. Localization and topology protected quantum coherence at the edge of hot matter. *Nature Communications*, 6:7341, 2015.

[16] J. Bandyopadhyay and A. Lakshminarayan. Testing statistical bounds on entanglement using quantum chaos. *Phys. Rev. Lett.*, 89(6):060402, 2002.

[17] R. Barends, J. Kelly, A. Megrant, D. Sank, E. Jeffrey, Y. Chen, Y. Yin, B. Chiaro, J. Mutus, C. Neill, P. O'Malley, P. Roushan, J. Wenner, T. C. White, A. N. Cleland, and John M. Martinis. Coherent josephson qubit suitable for scalable quantum integrated circuits. *Phys. Rev. Lett.*, 111(8):080502–, 2013.

[18] R. Barends, J. Kelly, A. Megrant, A. Veitia, D. Sank, E. Jeffrey, T. White, J. Mutus, A. Fowler, B. Campbell, et al. Superconducting quantum circuits at the surface code threshold for fault tolerance. *Nature*, 508(7497):500–503, 2014.

[19] D. Basko, I. Aleiner, and B. Altshuler. Metal–insulator transition in a weakly interacting many-electron system with localized single-particle states. *Annals of physics*, 321(5):1126–1205, 2006.

[20] B. A. Bernevig and T. L. Hughes. *Topological Insulators and Topological Superconductors*. Princeton University Press, 2013.

[21] B.A. Bernevig, T. L. Hughes, and S.-C Zhang. Quantum spin hall effect and topological phase transition in hgte quantum wells. *Science*, 314:1757–1761, 2006.

[22] M. Berry. Quantal phase factors accompanying adiabatic changes. *Proc. R. Soc. Lond. A*, 392:45–57, 1984.

[23] M. Berry. The bakerian lecture, 1987: quantum chaology. *Proceedings of the Royal Society of London*, 413(1844):183–198, 1987.

[24] R. Bialczak, M. Ansmann, M. Hofheinz, M. Lenander, E. Lucero, M. Neeley, A. O'Connell, D. Sank, H. Wang, M. Weides, J. Wenner, T. Yamamoto, A. Cleland, and J. Martinis. Fast tunable coupler for superconducting qubits. *Phys. Rev. Lett.*, 106(6):060501–, February 2011.

[25] A. Blais, A. Van den Brink, and A. Zagoskin. Tunable coupling of superconducting qubits. *Phys. Rev. Lett.*, 90(12):127901–, March 2003.

[26] I. Bloch, J. Dalibard, and S. Nascimbene. Quantum simulations with ultracold quantum gases. *Nature Physics*, 8:267–276, 2012.

[27] O. Bohigas, M. J. Giannoni, and C. Schmit. Characterization of chaotic quantum spectra and universality of level fluctuation laws. *Phys. Rev. Lett.*, 52:1–4, Jan 1984.

[28] S. Boixo, S. Isakov, V. Smelyanskiy, R. Babbush, N. Ding, Z. Jiang, J. Martinis, and H. Neven. Characterizing quantum supremacy in near-term devices. *arXiv preprint arXiv:1608.00263*, 2016.

[29] S. Boixo, T. Rønnow, S. Isakov, Z. Wang, D. Wecker, D. Lidar, J. Martinis, and M. Troyer. Evidence for quantum annealing with more than one hundred qubits. *Nature Physics*, 10(3):218–224, 2014.

[30] P. Bordia, H. Luschen, U. Schneider, M. Knap, and I. Bloch. Periodically driving a many-body localized quantum system. *Nat. Phys.*, 13(5):460–464, 2017.

[31] E. Boukobza, M. Chuchem, D. Cohen, and A. Vardi. Phase-diffusion dynamics in weakly coupled bose-einstein condensates. *Phys. Rev. Lett.*, 102(18):180403, 2009.

[32] E. Boukobza, M. Moore, D. Cohen, and A. Vardi. Nonlinear phase-dynamics in a driven bosonic josephson junction. *Phys. Rev. E*, 104(1):240402, 2010.

[33] M. Bremner, A. Montanaro, and D. Shepherd. Achieving quantum supremacy with sparse and noisy commuting quantum computations. *arXiv:1610.01808*, 2016.

[34] M. Bremner, A. Montanaro, and D. Shepherd. Average-case complexity versus approximate simulation of commuting quantum computations. *Phys. Rev. Lett.*, 117:080501, 2016.

[35] I. Buluta and F. Nori. Quantum simulators. *Science*, 326(5949):108–111, 2009.

[36] A. Chandran, V. Khemani, C. R. Laumann, and S. L. Sondhi. Many-body localization and symmetry-protected topological order. *Phys. Rev. B*, 89:144201, Apr 2014.

[37] S. Chaudhury, A. Smith, B. Anderson, S. Ghose, and P. Jessen. Quantum signatures of chaos in a kicked top. *Nature*, 461(7265):768–771, 2009.

[38] Y. Chen, C. Neill, P. Roushan, N. Leung, M. Fang, R. Barends, J. Kelly, B. Campbell, Z. Chen, B. Chiaro, A. Dunsworth, E. Jeffrey, A. Megrant, J. Mutus, C. Quintana, D. Sank, A. Vainsencher, J. Wenner, C. White, T., Michael R. Geller, A. Cleland, and J. Martinis. Qubit architecture with high coherence and fast tunable coupling. *Phys. Rev. Lett.*, 113:220502, Nov 2014.

[39] Z. Chen, A. Megrant, J. Kelly, R. Barends, J. Bochmann, Y. Chen, B. Chiaro, A. Dunsworth, E. Jeffrey, J. Mutus, and et. al. Fabrication and characterization of aluminum airbridges for superconducting microwave circuits. *App. Phys. Lett.*, 104(5):052602, 2014.

[40] M. Cheneau, P. Barmettler, D. Poletti, M. Endres, P. Schauß, T. Fukuhara, C. Gross, I. Bloch, C. Kollath, and S. Kuhr. Light-cone-like spreading of correlations in a quantum many-body system. *Nature*, 481(7382):484–487, 2012.

[41] J. Cho, G. Dimitris, and S. Bose. Fractional quantum hall state in coupled cavities. *Phys. Rev. Lett.*, 101:246809, Dec 2008.

[42] J. Choi, S. Hild, J. Zeiher, P. Schauss, T. Yefsah A. Rubio-Abadal1, V. Khemani, D. A. Huse, I. Bloch, and C. Gross. Exploring the many-body localization transition in two dimensions. *Science*, 352:1547–1552, 2016.

[43] J. Chow. Quantum information processing with superconducting qubits. *PhD dissertation, Yale*, 2010.

[44] J. Cirac and P. Zoller. Goals and opportunities in quantum simulation. *Nature Physics*, 8:264–266, April 2012.

[45] P. Coleman. *Introduction to many-body physics systems.* Cambrdige University Press, 2016.

[46] C. R. Dean, L. Wang, P. Maher, C. Forsythe, F. Ghahari, Y. Gao, J. Katoch, M. Ishigami, P. Moon, M. Koshino, T. Taniguchi, K. Watanabe, K. L. Shepard, J. Hone, and P. Kim. Hofstadter's butterfly and the fractal quantum hall effect in moire superlattices. *Nature*, 497:598–1430, 2013.

[47] V. Denchev, S. Boixo, S. Isakov, N. Ding, R. Babbush, V. Smelyanskiy, J. Martinis, and H. Neven. What is the computational value of finite-range tunneling? *Physical Review X*, 6(3):031015, 2016.

[48] J.M. Deutsch. Quantum statistical mechanics in a closed system. *Phys. Rev. A*, 43(4):2046, 1991.

[49] M. Devoret and R. Schoelkopf. Superconducting circuits for quantum information: An outlook. *Science*, 339(6124):1169–1174, March 2013.

[50] P. A. M. Dirac. Quantised singularities in the electromagnetic field. *Proc. R. Soc. Lond. A*, 133:60–72, 1931.

[51] N. A. Estep, D. L. Sounas, J. Soric, and A. Alu. Magnetic-free non-reciprocity and isolation based on parametrically modulated coupled-resonator loops. *Nat. Phys.*, 10:923, Nov 2014.

[52] K. Fang, Z. Yu, and S. Fan. Realizing effective magnetic field for photons by controlling the phase of dynamic modulation. *Nature Photonics*, 6:782–787, Nov 2012.

[53] K. Fang, Z. Yu, and S. Fan. Experimental demonstration of a photonic aharonov-bohm effect at radio frequencies. *Phys. Rev. B*, 87:060301, Feb 2013.

[54] R. Feynman. Simulating physics with computers. *Int. J. of Th. Phys.*, 21:467–488, 1982.

[55] S. Flach, M. Ivanchenko, and R. Khomeriki. Correlated metallic two-particle bound states in quasiperiodic chains. *EPL (Europhysics Letters)*, 98(6):66002, 2012.

[56] J. Flavin and A. Seidel. Abelian and non-abelian statistics in the coherent state representation. *Phys. Rev. X*, 1:021015, Dec 2011.

[57] Austin G Fowler, Matteo Mariantoni, John M Martinis, and Andrew N Cleland. Surface codes: Towards practical large-scale quantum computation. *Physical Review A*, 86(3):032324, 2012.

[58] M. Geller, E. Donate, Y. Chen, Michael T. Fang, N. Leung, C. Neill, P. Roushan, and J. Martinis. Tunable coupler for superconducting xmon qubits: Perturbative nonlinear model. *Phys. Rev. A*, 92:012320, Jul 2015.

[59] M. Geller, J. Martinis, A. Sornborger, P. Stancil, E. Pritchett, H. You, and A. Galiautdinov. Universal quantum simulation with prethreshold superconducting qubits: Single-excitation subspace method. *Physical Review A*, 91(6):062309, 2015.

[60] I. M. Georgescu, S. Ashhab, and F. Nori. Quantum simulation. *Rev. Mod. Phys.*, 86:153–185, Mar 2014.

[61] S. Ghose, R. Stock, P. Jessen, R. Lal, and A. Silberfarb. Chaos, entanglement, and decoherence in the quantum kicked top. *Phys. Rev. A*, 78(4):042318, 2008.

[62] D. Griffiths. *Introduction to Quantum Mechanics*. Prentice Hall, 1994.

[63] V. Gritsev and A. Polkovnikov. Dynamical quantum hall effect in the parameter space. *PNAS*, 109:6457–6462, 2012.

[64] M. Gutzwiller. *Chaos in classical and quantum mechanics*, volume 1. Springer Science & Business Media, 1990.

[65] F. Haake, M. Kuś, and R. Scharf. Classical and quantum chaos for a kicked top. *Zeitschrift für Physik B Condensed Matter*, 65(3):381–395, 1987.

[66] M. Hafezi, P. Adhikari, and J. M. Taylor. Engineering three-body interaction and pfaffian states in circuit qed systems. *Phys. Rev. B*, 90:060503, Aug 2014.

[67] M. Hafezi, S. Mittal, J. Fan, A. Migdall, and J. Taylor. Imaging topological edge states in silicon photonics. *Nature Photonics*, 7:1001–1005, 2013.

[68] F. D. M. Haldane. Model for a quantum hall effect without landau levels: Condensed-matter realization of the "parity anomaly". *Phys. Rev. Lett.*, 61:2015–2018, Oct 1988.

[69] T. Häner and D. Steiger. 0.5 petabyte simulation of a 45-qubit quantum circuit. *arXiv:1704.01127*, 2017.

[70] R. Harris, A. Berkley, M. Johnson, P. Bunyk, S. Govorkov, M. Thom, S. Uchaikin, A. Wilson, J. Chung, E. Holtham, J. Biamonte, A. Smirnov, M. Amin, and A. Maassen van den Brink. Sign- and magnitude-tunable coupler for superconducting flux qubits. *Phys. Rev. Lett.*, 98(17):177001–, April 2007.

[71] M. Z. Hasan and C. L. Kane. Colloquium: Topological insulators. *Rev. Mod. Phys.*, 82:3045–3067, Nov 2010.

[72] P. Hauke, O. Tieleman, A. Celi, C. Ölschläger, J. Simonet, J. Struck, M. Weinberg, P. Windpassinger, K. Sengstock, M. Lewenstein, and A. Eckardt. Non-abelian gauge fields and topological insulators in shaken optical lattices. *Phys. Rev. Lett.*, 109:145301, Oct 2012.

[73] A. Hayward, A. Martin, and A. Greentree. Fractional quantum hall physics in jaynes-cummings-hubbard lattices. *Phys. Rev. Lett.*, 108:223602, Jun 2012.

[74] T. Hime, P. Reichardt, B. Plourde, T. Robertson, C. Wu, A. Ustinov, and J. Clarke. Solid-state qubits with current-controlled coupling. *Science*, 314(5804):1427–1429, December 2006.

[75] W. Ho and D. Abanin. Entanglement dynamics in quantum many-body systems. *Phys. Rev. B*, 95:094302, Mar 2017.

[76] M. Hofheinz, H. Wang, M. Ansmann, R. Bialczak, E. Lucero, M. Neeley, A. O'connell, D. Sank, J. Wenner, J. Martinis, et al. Synthesizing arbitrary quantum states in a superconducting resonator. *Nature*, 459(7246):546–549, 2009.

[77] D. Hofstadter. Energy levels and wave functions of bloch electrons in rational and irrational magnetic fields. *Phys. Rev. B*, 14:2239–2249, Sep 1976.

[78] A. Houck, H. Tureci, and J. Koch. On-chip quantum simulation with superconducting circuits. *Nat Phys*, 8(4):292–299, April 2012.

[79] D. Hugel and B. Paredes. Chiral ladders and the edges of quantum hall insulators. *Phys. Rev. A*, 89:023619, Feb 2014.

[80] B. Hunt, J. D. Sanchez-Yamagishi, A. F. Young, M. Yankowitz, B. J. LeRoy, K. Watanabe, T. Taniguchi, P. Moon, M. Koshino, P. Jarillo-Herrero, and R. C. Ashoori. Massive dirac fermions and hofstadter butterfly in a van der waals heterostructure. *Science*, 340:1427–602, 2013.

[81] F. Iemini, A. Russomanno, D. Rossini, A. Scardicchio, and R. Fazio. Signatures of many-body localization in the dynamics of two-site entanglement. *Phys. Rev. B*, 94:214206, Dec 2016.

[82] J. Imbrie. Diagonalization and many-body localization for a disordered quantum spin chain. *Phys. Rev. Lett.*, 117:027201, Jul 2016.

[83] S. Iyer, V. Oganesyan, G. Refael, and D. Huse. Many-body localization in a quasiperiodic system. *Phys. Rev. B*, 87:134202, Apr 2013.

[84] J. J. Bardeen, L. Cooper, and J. Schrieffer. Theory of superconductivity. *Phys. Rev.*, 108:1175, 1957.

[85] E. J. Bergholtz and Z. LIU. Topological flat band models and fractional chern insulators. *International Journal of Modern Physics B*, 27:1330017, 2013.

[86] J. D. Jackson. *Classical electrodynamics*. John Wiley and Sons, 1998.

[87] D. Jaksch and P. Zoller. Creation of effective magnetic fields in optical lattices: the hofstadter butterfly for cold neutral atoms. *new Journal of Physics*, 5, 2003.

[88] G. Jotzu, M. Messer, R. Desbuquois, M. Lebrat, T. Uehlinger, D. Greif, and T. Esslinger. Experimental realization of the topological haldane model with ultracold fermions. *Nature*, 515:237–240, 2014.

[89] T. Kadowaki and H. Nishimori. Quantum annealing in the transverse ising model. *Physical Review E*, 58(5):5355, 1998.

[90] E. Kapit. Quantum simulation architecture for lattice bosons in arbitrary, tunable, external gauge fields. *Phys. Rev. A*, 87:062336, Jun 2013.

[91] E. Kapit. Universal two-qubit interactions, measurement, and cooling for quantum simulation and computing. *Phys. Rev. A*, 92:012302, Jul 2015.

[92] E. Kapit, M. Hafezi, and S. Simon. Induced self-stabilization in fractional quantum hall states of light. *Phys. Rev. X*, 4:031039, Sep 2014.

[93] E. Kapit and E. Mueller. Exact parent hamiltonian for the quantum hall states in a lattice. *Phys. Rev. Lett.*, 105:215303, Nov 2010.

[94] A. M. Kaufman, M. E. Tai, A. Lukin, M. Rispoli, R. Schittko, P. M. Preiss, and M. Greiner. Quantum thermalization through entanglement in an isolated many-body system. *Science*, 353:794–800, 2016.

[95] J. Kerckhoff, K. Lalumiere, B. Chapman, A. Blais, and K. Lehnert. On-chip superconducting microwave circulator from synthetic rotation. *Phys. Rev. Applied*, 4:034002, Sep 2015.

[96] S. Kessler and F. Marquardt. Single-site-resolved measurement of the current statistics in optical lattices. *Phys. Rev. A*, 89:061601, Jun 2014.

[97] A. Khanikaev, S. Hossein Mousavi, W.-K. Tse, M. Kargarian, A. MacDonald, and G. Shvets. Photonic topological insulators. *Nature materials*, 12:233–239, 2013.

[98] C. Khripkov, D. Cohen, and A. Vardi. Coherence dynamics of kicked bose-hubbard dimers: Interferometric signatures of chaos. *Phys. Rev. E*, 87(1):012910, 2013.

[99] H. Kim and D. Huse. Ballistic spreading of entanglement in a diffusive nonintegrable system. *Phys. Rev. Lett.*, 111:127205, Sep 2013.

[100] T. Kinoshita, T. Wenger, and D. Weiss. A quantum newton's cradle. *Nature*, 440(7086):900–903, 2006.

[101] J. A. Kjall, J. H. Bardarson, and F. Pollmann. Many-body localization in a disordered quantum ising chain. *Phys. Rev. Lett.*, 113:107204, Sep 2014.

[102] J. Klaers, F. Vewinger, and M. Weitz. Thermalization of a two-dimensional photonic gas in a white wall photon box. *Nature Physics*, 6(7):512–515, 2010.

[103] K. v. Klitzing, G. Dorda, and M. Pepper. New method for high-accuracy determination of the fine-structure constant based on quantized hall resistance. *Phys. Rev. Lett.*, 45:494–497, Aug 1980.

[104] E. Knill, D. Leibfried, R. Reichle, J. Britton, R. Blakestad, J. Jost, C. Langer, R. Ozeri, S. Seidelin, and D. Wineland. Randomized benchmarking of quantum gates. *Phys. Rev. A*, 77(1):012307–, January 2008.

[105] J. Koch, A. Houck, K. Hur, and S. Girvin. Time-reversal-symmetry breaking in circuit-qed-based photon lattices. *Phys. Rev. A*, 82:043811, Oct 2010.

[106] J. Koch, Y. Terri, J. Gambetta, A. Houck, D. Schuster, J. Majer, A. Blais, M. Devoret, S. Girvin, and R. Schoelkopf. Charge-insensitive qubit design derived from the cooper pair box. *Phys. Rev. A*, 76(4):042319, 2007.

[107] A. Lakshminarayan. Entangling power of quantized chaotic systems. *Phys. Rev. E*, 64(3):036207, 2001.

[108] T. Langen, R. Geiger, M. Kuhnert, B. Rauer, and J. Schmiedmayer. Local emergence of thermal correlations in an isolated quantum many-body system. *Nature Physics*, 9(10):640–643, 2013.

[109] B. Lanyon, J. Whitfield, G. Gillett, M. Goggin, M. Almeida, I. Kassal, J. Biamonte, M. Mohseni, B. Powell, M. Barbieri, A. Aspuru-Guzik, and A. White. Towards quantum chemistry on a quantum computer. *Nature Chemistry*, 2(2):106–111, 2010.

[110] R. B. Laughlin. Anomalous quantum hall effect: An incompressible quantum fluid with fractionally charged excitations. *Phys. Rev. Lett.*, 50:1395–1398, May 1983.

[111] P. J. Leek, J.M Fink, A. Blais, R. Bianchetti, M. Göppl, J. M. Gambetta, D. I. Schuster, L. Frunzio, R. J. Schoelkopf, and A. Wallraff. Observation of berry's phase in a solid-state qubit. *Science*, 318:1889–1892, Dec 2007.

[112] G. Lemos, R. Gomes, S. Walborn, P. Ribeiro, and F. Toscano. Experimental observation of quantum chaos in a beam of light. *Nature Comm.*, 3, 2012.

[113] X. Li, S. Ganeshan, J. H. Pixley, and S. Das Sarma. Many-body localization and quantum nonergodicity in a model with a single-particle mobility edge. *Phys. Rev. Lett.*, 115:186601, Oct 2015.

[114] Y.-J. Lin, R. Compton, K. Jimenez-Garcia, J. Porto, and I. Spielman. Synthetic magnetic fields for ultracold neutral atoms. *Nature*, 462:628–632, 2009.

[115] R. Lipton. New directions in testing. *Distributed Computing and Cryptography*, 2:191–202, 1989.

[116] Y. Liu, L. Wei, J. Tsai, and F. Nori. Controllable coupling between flux qubits. *Phys. Rev. Lett.*, 96(6):067003–, February 2006.

[117] S. Lloyd, M. Mohseni, and P. Rebentrost. Quantum algorithms for supervised and unsupervised machine learning. *arXiv preprint arXiv:1307.0411*, 2013.

[118] M. Lombardi and A. Matzkin. Entanglement and chaos in the kicked top. *Phys. Rev. E*, 83(1):016207, 2011.

[119] L. Lu, J. Joannopoulos, and M. Soljacic. Topological photonics. *Nature Photonics*, 8:821–829, 2014.

[120] E. Lucero, M. Hofheinz, M. Ansmann, R. Bialczak, N. Katz, M. Neeley, A. OConnell, H. Wang, A. Cleland, and J. Martinis. High-fidelity gates in a single josephson qubit. *Physical review letters*, 100(24):247001, 2008.

[121] A. P. Lund, M. Bremner, and T. C. Ralph. Quantum sampling problems, BosonSampling and quantum supremacy. *npj Quantum Information*, 3:15, 2017.

[122] V. Madhok, V. Gupta, A. Hamel, and S. Ghose. Signatures of chaos in the dynamics of quantum discord. *Phys. Rev. E*, 91:032906, 2015.

[123] E. Magesan, J. Gambetta, B. Johnson, C. Ryan, J. Chow, S. Merkel, M. Da Silva, G. Keefe, M. Rothwell, T. Ohki, M. Ketchen, and M. Steffen. Efficient measurement of quantum gate error by interleaved randomized benchmarking. *Phys. Rev. Lett.*, 109(8):080505–, August 2012.

[124] M. Mariantoni, H. Wang, T. Yamamoto, M. Neeley, R. Bialczak, Y. Chen, M. Lenander, E. Lucero, A. O'Connell, D Sank, et al. Implementing the quantum von neumann architecture with superconducting circuits. *Science*, 334(6052):61–65, 2011.

[125] J. Martinis and M. Geller. Fast adiabatic qubit gates using only σ z control. *Physical Review A*, 90(2):022307, 2014.

[126] J. Martinis, S. Nam, J. Aumentado, K. Lang, and C. Urbina. Decoherence of a superconducting qubit due to bias noise. *Physical Review B*, 67(9):094510, 2003.

[127] A. Megrant, C. Neill, R. Barends, B. Chiaro, Yu Chen, L. Feigl, J. Kelly, Erik Lucero, Matteo Mariantoni, P. J. J. O'Malley, D. Sank, A. Vainsencher, J. Wenner, T. C. White, Y. Yin, J. Zhao, C. Palmstrom, J. Martinis, and A. Cleland. Planar superconducting resonators with internal quality factors above one million. *Applied Physics Letters*, 100(11):–, 2012.

[128] A. Mezzacapo, M. Sanz, L. Lamata, I. Egusquiza, S. Succi, and E. Solano. Quantum simulator for transport phenomena in fluid flows. *Scientific Reports*, 5, 2015.

[129] V. P. Michal, B. L. Altshuler, and G. V. Shlyapnikov. Delocalization of weakly interacting bosons in a 1d quasiperiodic potential. *Phys. Rev. Lett.*, 113:045304, Jul 2014.

[130] P. Miller and S. Sarkar. Signatures of chaos in the entanglement of two coupled quantum kicked tops. *Phys. Rev. E*, 60(2):1542, 1999.

[131] H. Miyake, G. A. Siviloglou, C. J. Kennedy, W. Burton, and W. Ketterle. Realizing the harper hamiltonian with laser-assisted tunneling in optical lattices. *Phys. Rev. Lett.*, 111:185302, Oct 2013.

[132] J.E. Moore. The birth of topological insulators. *Nature*, 464:194–198, 2010.

[133] Naoto Nagaosa. *Quantum Field Theory in Strongly Correlated Electronic Systems*. Springer, 1999.

[134] A. Nahum, J. Ruhman, and D. A. Huse. Dynamics of entanglement and transport in 1D systems with quenched randomness. *arXiv:1705.10364*, 2017.

[135] R. Nandkishore and D. A. Huse. Many-body localization and thermalization in quantum statistical mechanics. *Annual Review of Condensed Matter Physics*, 6:15–38, 2015.

[136] C. Nayak, S. Simon, A. Stern, M. Freedman, and S. Das Sarma. Non-abelian anyons and topological quantum computation. *Rev. Mod. Phys.*, 80:1083–1159, Sep 2008.

[137] M. Neeley, M. Ansmann, R. C. Bialczak, M. Hofheinz, E. Lucero, A. D. O'Connell, D. Sank, H. Wang, J. Wenner, A. N. Cleland, M. R. Geller, and J. M. Martinis. Emulation of a quantum spin with a superconducting phase qudit. *Science*, 325:722–725, 2009.

[138] M. Neeley, R. C Bialczak, M. Lenander, E. Lucero, M. Mariantoni, A. O'Connell, D. Sank, H. Wang, M. Weides, J. Wenner, et al. Generation of three-qubit entangled states using superconducting phase qubits. *Nature*, 467(7315):570–573, 2010.

[139] M. A. Nielsen and I. L. Chuang. *Quantum Computation and Quantum Information*. Cambridge University Press, 2000.

[140] J. Ningyuan, C. Owens, A. Sommer, D. Schuster, and J. Simon. Time- and site-resolved dynamics in a topological circuit. *Phys. Rev. X*, 5:021031, Jun 2015.

[141] A. Niskanen, K. Harrabi, F. Yoshihara, Y. Nakamura, S. Lloyd, and J. Tsai. Quantum coherent tunable coupling of superconducting qubits. *Science*, 316(5825):723–726, May 2007.

[142] A. Nunnenkamp, J. Koch, and S.M. Girvin. Synthetic gauge fields and homodyne transmission in jaynes cummings lattices. *New J. of Phys.*, 13(095008), 2011.

[143] V. Oganesyan and D. Huse. Localization of interacting fermions at high temperature. *Phys. Rev. B*, 75:155111, Apr 2007.

[144] E. Ott. *Chaos in dynamical systems*. Cambridge university press, 2002.

[145] D. Page. Average entropy of a subsystem. *Phys. Rev. Lett.*, 71(9):1291, 1993.

[146] H. Paik, D. Schuster, L. Bishop, G. Kirchmair, G. Catelani, A. Sears, B. Johnson, M. Reagor, L. Frunzio, L. Glazman, S. Girvin, M. Devoret, and R. Schoelkopf. Observation of high coherence in josephson junction qubits measured in a three-dimensional circuit qed architecture. *Phys. Rev. Lett.*, 107(24):240501–, December 2011.

[147] A. Pal and D. Huse. Many-body localization phase transition. *Physical Review B*, 82(17):174411, 2010.

[148] B. Paredes, P. Zoller, and J.I. Cirac. Fractional quantum hall regime of a gas of ultracold atoms. *Solid State Communications*, 127:155–162, 2003.

[149] B. Peropadre, G. Guerreschi, J. Huh, and A. Aspuru-Guzik. Proposal for microwave boson sampling. *Physical Review Letters*, 117(14):140505, 2016.

[150] A. Peruzzo, J. McClean, P. Shadbolt, M. Yung, X. Zhou, P. Love, A. Aspuru-Guzik, and J. O'brien. A variational eigenvalue solver on a quantum processor. *Nature Communications*, 5, 2014.

[151] A. Petrescu, A. Houck, and K. Le Hur. Anomalous hall effects of light and chiral edge modes on the kagomé lattice. *Phys. Rev. A*, 86:053804, Nov 2012.

[152] R. Pinto, A. Korotkov, M. Geller, V. Shumeiko, and J. Martinis. Analysis of a tunable coupler for superconducting phase qubits. *Phys. Rev. B*, 82(10):104522–, September 2010.

[153] A. Polkovnikov. Microscopic diagonal entropy and its connection to basic thermodynamic relations. *Ann. of Phys.*, 326(2):486–499, 2011.

[154] A. Polkovnikov, K. Sengupta, A. Silva, and M. Vengalattore. Colloquium: Nonequilibrium dynamics of closed interacting quantum systems. *Reviews of Modern Physics*, 83(3):863, 2011.

[155] L. A. Ponomarenko, R. V. Gorbachev, G. L. Yu, D. C. Elias, R. Jalil, A.A. Patel, A. Mishchenko, A. S. Mayorov, C. R. Woods, J. R. Wallbank, M. Mucha-Kruczynski, B. A. Piot, M. Potemski, I. V. Grigorieva, K. S. Novoselov, F. Guinea, V. I. Falko, and A. K. Geim. Cloning of dirac fermions in graphene superlattices. *Nature*, 497:594–597, 2013.

[156] C. Porter and R. Thomas. Fluctuations of nuclear reaction widths. *Physical Review*, 104(2):483, 1956.

[157] David M Pozar. *Microwave engineering*. John Wiley & Sons, 2009.

[158] J. Preskill. Quantum computing and the entanglement frontier. 2012. 25th Solvay Conf. arXiv:1203.5813.

[159] S. Raghu and F. Haldane. Analogs of quantum-hall-effect edge states in photonic crystals. *Phys. Rev. A*, 78:033834, Sep 2008.

[160] M. Rechtsman, J. Zeuner, Y. Plotnik, Y. Lumer, D. Podolsky, F. Dreisow, S. Nolte, M. Segev, and A. Szameit. Photonic floquet topological insulators. *Nature*, 496:196–200, 2013.

[161] P. Richerme, Z. Gong, A. Lee, C. Senko, J. Smith, M. Foss-Feig, S. Michalakis, A. Gorshkov, and C. Monroe. Non-local propagation of correlations in quantum systems with long-range interactions. *Nature*, 511(7508):198–201, 2014.

[162] M. Rigol, V. Dunjko, and M. Olshanii. Thermalization and its mechanism for generic isolated quantum systems. *Nature*, 452(7189):854–858, 2008.

[163] P. Roushan, C. Neill, Y. Chen, M. Kolodrubetz, C. Quintana, N. Leung, M. Fang, R. Barends, B. Campbell, Z. Chen, et al. Observation of topological transitions in interacting quantum circuits. *Nature*, 515(7526):241–244, 2014.

[164] J. Sakurai. *Modern Quantum Mechanics*. Addison-Wesley, 1994.

[165] D. Sank, R. Barends, R. Bialczak, Y. Chen, J. Kelly, M. Lenander, E. Lucero, M. Mariantoni, A. Megrant, M. Neeley, et al. Flux noise probed with real time qubit tomography in a josephson phase qubit. *Physical review letters*, 109(6):067001, 2012.

[166] L. Santos, A. Polkovnikov, and M. Rigol. Entropy of isolated quantum systems after a quench. *Physical Review Letters*, 107(4):040601, 2011.

[167] L. Santos, A. Polkovnikov, and M. Rigol. Weak and strong typicality in quantum systems. *Phys. Rev. E*, 86(1):010102, 2012.

[168] S. Scheel. Permanents in linear optical networks. *arXiv:quant-ph/0406127*, 2004.

[169] M. Schreiber, S. Hodgman, P. Bordia, H. Lüschen, M. Fischer, R. Vosk, E. Altman, U. Schneider, and I. Bloch. Observation of many-body localization of interacting fermions in a quasi-random optical lattice. *Science*, 349:842, 2015.

[170] M. D. Schroer, M. H. Kolodrubetz, W. F. Kindel, M. Sandberg, J. Gao, M. R. Vissers, D. P. Pappas, Anatoli Polkovnikov, and K. W. Lehnert. Measuring a topological transition in an artificial spin-1/2 system. *Phys. Rev. Lett.*, 113:050402, Jul 2014.

[171] M. Serbyn, M. Knap, S. Gopalakrishnan, Z. Papic, N. Y. Yao, C. R. Laumann, D. A. Abanin, M. D. Lukin, and E. A. Demler. Interferometric probes of many-body localization. *Phys. Rev. Lett.*, 113:147204, Oct 2014.

[172] M. Serbyn, Z. Papic, and D.A. Abanin. Criterion for many-body localization-delocalization phase transition. *Phys. Rev. X*, 5:041047, Dec 2015.

[173] J. Smith, A. Lee, P. Richerme, B. Neyenhuis, P. W. Hess, P. Hauke, M. Heyl, D. A. Huse, and C. Monroe. Many-body localization in a quantum simulator with programmable random disorder. *Nature Physics*, 12, 2016.

[174] M. Srednicki. Chaos and quantum thermalization. *Phys. Rev. E*, 50(2):888, 1994.

[175] S. Srinivasan, A. Hoffman, J. Gambetta, and A. Houck. Tunable coupling in circuit quantum electrodynamics using a superconducting charge qubit with a v-shaped energy level diagram. *Phys. Rev. Lett.*, 106(8):083601–, February 2011.

[176] John R Taylor. *Classical mechanics*. University Science Books, 2005.

[177] D. J. Thouless, M. Kohmoto, M. P. Nightingale, and M. den Nijs. Quantized hall conductance in a two-dimensional periodic potential. *Phys. Rev. Lett.*, 49:405–408, Aug 1982.

[178] Michael Tinkham. *Introduction to superconductivity*. Courier Corporation, 1996.

[179] S. Trotzky, Y. Chen, A. Flesch, I. McCulloch, U. Schollwöck, J. Eisert, and I. Bloch. Probing the relaxation towards equilibrium in an isolated strongly correlated one-dimensional bose gas. *Nature Physics*, 8(4):325–330, 2012.

[180] D. C. Tsui, H. L. Stormer, and A. C. Gossard. Two-dimensional magnetotransport in the extreme quantum limit. *Phys. Rev. Lett.*, 48:1559–1562, May 1982.

[181] L. Tzuang, K. Fang, P. Nussenzveig, S. Fan, and M. Lipson. Non-reciprocal phase shift induced by an effective magnetic flux for light. *Nature Photonics*, 8:701–705, 2014.

[182] L. Valiant. The complexity of computing the permanent. *Theor. Comput. Sci.*, 8(2):189–201, 1979.

[183] S. Van der Ploeg, A. Izmalkov, A. Van den Brink, U. Hubner, M. Grajcar, E. Il'ichev, H. Meyer, and A. Zagoskin. Controllable coupling of superconducting flux qubits. *Phys. Rev. Lett.*, 98(5):057004–, February 2007.

[184] X. Wang, S. Ghose, B. C Sanders, and B. Hu. Entanglement as a signature of quantum chaos. *Phys. Rev. E*, 70(1):016217, 2004.

[185] Z. Wang, Y. Chong, J. Joannopoulos, and M. Soljacic. Observation of unidirectional backscattering-immune topological electromagnetic states. *Nature*, 461:772–775, 2009.

[186] Xiao-Gang Wen. *Quantum Field Theory of Many-body systems*. Oxford, 2004.

[187] F. Wilczek and A. Shapere. *Geometric Phases in Physics*. World Scientific, 1989.

[188] F. Y. Wu. The potts model. *Rev. Mod. Phys.*, 54:235–268, Jan 1982.

[189] C. Xu, A. Poudel, and M. G. Vavilov. Nonadiabatic dynamics of a slowly driven dissipative two-level system. *Phys. Rev. A*, 89:052102, May 2014.

[190] T. Yamamoto, M. Neeley, E. Lucero, R. Bialczak, J. Kelly, M. Lenander, M. Mariantoni, A. O'Connell, D. Sank, H. Wang, M. Weides, J. Wenner, Y. Yin, A. Cleland, and J. Martinis. Quantum process tomography of two-qubit controlled-z and controlled-not gates using superconducting phase qubits. *Phys. Rev. B*, 82(18):184515–, November 2010.

[191] N. Y. Yao, C. R. Laumann, S. Gopalakrishnan, M. Knap, M. Muller, E. A. Demler, and M. D. Lukin. Many-body localization in dipolar systems. *Phys. Rev. Lett.*, 113:243002, Dec 2014.